TECHNISCHE UNIVERSITÄT MÜNCHEN

TUM School of Engineering and Design

Dissertation

Hierarchical Distributed Control to Integrate Prosumer Flexibility in Smart Grids

Michael Alexander Kramer

TECHNISCHE UNIVERSITÄT MÜNCHEN

TUM School of Engineering and Design

Hierarchical Distributed Control to Integrate Prosumer Flexibility in Smart Grids

Michael Alexander Kramer, M.Sc.

Vollständiger Abdruck der von der TUM School of Engineering and Design der Technischen Universität München zur Erlangung des akademischen Grades eines

Doktors der Ingenieurwissenschaften

genehmigten Dissertation.

Vorsitzender:		Prof. Thomas Auer
Prüfer der Dissertation:	1.	Dr. Vicky Albert-Seifried
	2.	Prof. Dr. Thomas Hamacher

Die Dissertation wurde am 28.08.2020 bei der Technischen Universität München eingereicht und durch die TUM School of Engineering and Design am 08.11.2021 angenommen.

Acknowledgment

This thesis is the result of my work as a researcher at the Technical University of Munich. During my time I have met many people from inside and outside of the university who have contributed to the productive, supportive and encouraging environment I found myself in. I want to use this opportunity to thank them.

First of all, I would like to thank my supervisor Dr. Vicky Albert-Seifried for giving me the opportunity to work in the research group on "Energy Efficient and Smart Cities" at the Munich School of Engineering. I am grateful for the freedom and support she provided to find my direction of research, to connect with people from other research groups and to facilitate the interdisciplinary exchange this thesis required.

My sincere thanks goes to Professor Thomas Hamacher for being my mentor over the last years and for his willingness to examine this thesis. His guidance together with his encouraging and humorous ways contributed a lot to my motivation and the finish of this thesis. I am grateful for his support of the "MEMAP" project and the opportunity he gave me to lead the research group for the last two years.

I am particularly grateful to Akhila Jambagi, who joined me on the PhD journey and not only helped with teamwork and fruitful discussions, but also became a true friend. I thank Daniel Beckenbauer, Mathias Ehrenwirth and the "Hackls" and "Herzigs" for the open and fun community among the first generation of MSE-PhDs. A special thanks goes to Alex Capone and Thomas Lickleder for filling the "MEMAP" project with life and for the great atmosphere in our small research group. I would like to thank Maximilian Irlbeck from the former Software- and Systems Engineering research group and Center Digitisation.Bavaria for our early joint efforts and fun times of proposal writing.

I am grateful for the good times with the many great colleagues, scientists and students at the Munich School of Engineering, the Chair of Renewable and Sustainable Energy Systems, the Center for Combined Smart Energy Systems, the Centre of Sustainable Building, the Grid Integration Group at Lawrence Berkeley National Laboratories and TUM CREATE in Singapore.

I want to thank the partners of the "ESOSEG" and "MEMAP" projects for the successful cooperations and valuable insights from other academic disciplines and the industry. The Bavarian State Ministry of Science, Research and the Arts is gratefully acknowledged for funding within the research program "Energy Valley Bavaria". The Federal Ministry for Economic Affairs and Energy is gratefully acknowledged for funding the projects "ESOSEG" and "MEMAP".

Heartfelt thanks go to my parents Angelika and Michael for their love and unlimited support throughout the years. I thank my brother Max for his positive nature and for always being there with an open ear. Finally, my deepest gratitude goes to Emilie, for your incredible patience, optimism and strength to see the beauty in things. Thank you for being by my side.

Munich, July 2020 Michael Kramer

Abstract

A higher share of renewable energies in heating and enhanced energy efficiency through better thermal insulation and modern heating systems in buildings is required to decarbonize Germany's heating sector. Electricity-based systems like heat pumps allow for a direct integration of renewable electricity generation and offer operational flexibility due to the thermal storage systems they are connected to. This allows decoupling of the heating demand from the heat pump's electricity demand for a period of time in order to operate the system during times of low prices, favorable ambient conditions or when the grid operator requires it. Grid operators face the challenge to connect increasing numbers of electrical flexible loads and to maintain current and voltage limits during grid operation. A smart grid utilizes the flexibility of buildings with heat pump heating systems and electric vehicles in order to integrate renewables, to guarantee feasible grid operation and to prevent grid expansion. The identification of a desired and feasible operational schedule of a single building is already a complex task which requires forecasts of weather and occupancy and a mathematical representation of the system's underlying storage dynamics. This becomes even more challenging when possibly hundreds of physically coupled systems are involved and have to be coordinated in a large-scale power system.
This thesis proposes a scalable algorithm to coordinate the operation of multiple residential prosumers equipped with heat pump heating systems and photovoltaic plants in a distribution grid. A hierarchical distributed controller is designed based on methods from predictive control and distributed optimization. The control algorithm works with reduced exchange of information, system and state knowledge of the buildings and distribution grid remains at the respective entity and needs not to be communicated. Only residual load schedules and dual variables are communicated iteratively between the grid operator and the prosumers to converge to a solution. Several models are developed in this thesis to represent the thermal and electrical systems in the controller. A thermal building model is developed to represent the dynamics of a single family house and then validated. The low-order model can be parameterized based on building typology data and shows satisfying accuracy with respect to temperature and energy demand predictions. Together with a heat pump and domestic hot water model, the resulting state-space model is used for the design of a model predictive controller for energy management of a single prosumer. For the distribution grid, a linearized power flow model is introduced and applied to German reference low-voltage grids. Both the model error and the sensitivities of the grids to congestion and undervoltages are investigated in preparation for the later simulations. Finally, the above models are combined to formulate the central coordination problem and a mathematical decomposition is carried out to obtain the hierarchical distributed control algorithm. Simulation studies on voltage stability, valley-filling and community photovoltaic self-consumption demonstrate the effectiveness of the distributed control algorithm to coordinate the operation of prosumers in a distribution grid online. The algorithm allows prosumers to exploit their flexibility to minimize their local costs, but coordinates the operation when a shared or global cost function has to be minimized or distribution grid constraints are violated. Closed-loop simulations over a week are presented for different building energy standards. A central optimization is used to benchmark the effectiveness of the distributed optimization algorithm. The change in costs due to coordination is investigated in a comparison with the uncoordinated reference operation of the prosumers. Prosumers located at buses with strong undervoltages face above average cost increases. It is further shown how the volatility of the power flow over the transformer can be reduced with only a marginal increase in operational costs and little impact on the comfort of building occupants. Finally, the algorithm also manages to increase the communities photovoltaic self-consumption to achieve lower total costs.

Kurzzusammenfassung

Ein höherer Anteil erneuerbarer Energien im Wärmebereich sowie eine verbesserte Energieeffizienz durch Wärmedämmung und moderne Heizsysteme sind zur Dekarbonisierung des deutschen Wärmesektors erforderlich. Elektrische Wärmepumpen mit thermischen Speichersystemen ermöglichen die Integration erneuerbarer Stromerzeugung und bieten betriebliche Flexibilität. Diese ermöglicht die zeitliche Entkopplung des Wärmebedarfs von der Stromnachfrage zur Ausnutzung von Perioden mit niedrigen Preisen, günstigen Wetterbedingungen oder für einen netzdienlichen Betrieb. Netzbetreiber sehen sich mit der Herausforderung konfrontiert, eine zunehmende Anzahl elektrischer Lasten anzuschließen und weiterhin Strom- und Spannungsgrenzen des Netzes einzuhalten. Im *Smart Grid* werden Flexibilitäten in Gebäuden und Elektroautos zur Integration der Erzeugung, zur Unterstützung des Netzbetriebs und zur Vermeidung des Netzausbaus genutzt. Die Ermittlung des optimalen und im Rahmen der Betriebsgrenzen möglichen Fahrplans eines Gebäudes ist bereits komplex und erfordert Wetter- und Anwesenheitsprognosen sowie eine mathematische Abbildung der Speicherdynamik des zugrundeliegenden Systems. Die Koordination einer Vielzahl physikalisch gekoppelter Systeme im Stromnetz ist eine Herausforderung.
Diese Arbeit präsentiert einen skalierbaren Algorithmus zur Koordination des Betriebs mehrerer Wohngebäude mit Wärmepumpen und Photovoltaikanlagen im Verteilnetz. Basierend auf Methoden der modellprädiktiven Regelung und der verteilten Optimierung wird eine verteilte Regelung mit hierarchischer Struktur entwickelt. Der Regelungsalgorithmus ermöglicht einen reduzierten Informationsaustausch. System- und Zustandswissen über einzelne Gebäude und das Verteilnetz verbleibt bei den jeweiligen Teilnehmern und wird nicht zwischen diesen kommuniziert. Lediglich Fahrpläne der Residuallasten und Dualvariablen werden zwischen den Prosumern und dem Netzbetreiber iterativ bis zur Konvergenz zu einer gemeinsamen Lösung kommuniziert. Mehrere Modelle der dem Regler zugrundeliegenden thermischen und elektrischen Systeme werden entwickelt. Ein thermisches Gebäudemodell wird zur Abbildung der Dynamik eines Einfamilienhauses entwickelt und validiert. Das ordnungsreduzierte Modell kann durch Gebäudetypologiedaten parametrisiert werden. Es erzielt eine ausreichende Genauigkeit bei Temperatur- und Energiebedarfsprognosen. Das Gebäudemodell wird dann mit einem Wärmepumpen- und Trinkwarmwassermodell im Entwurf eines modellprädiktiven Reglers für das Energiemanagement eines Prosumers verwendet. Das Niederspannungsnetz wird entsprechend deutscher Referenznetze parametrisiert und durch ein linearisiertes Lastflussmodell abgebildet. Der Modellfehler wird quantifiziert und die Empfindlichkeit der Referenznetze im Hinblick auf Betriebsmittelüberlastungen und Unterspannungen untersucht. Anschließend werden alle Modelle in der Formulierung des zentralen Optimierungsproblems zusammengeführt und der verteilte Regelungsalgorithmus durch eine mathematische Dekomposition entwickelt. Zur Demonstration der Effektivität des Algorithmus zur Koordination der Prosumer im Verteilnetz werden abschließend drei Simulationsstudien zur Spannungsstabilität, Lastglättung und der Eigenverbrauchsoptimierung durchgeführt. Der Algorithmus erlaubt den Prosumern Flexibilität zur Minimierung individueller Kosten auszunutzen, koordiniert den Betrieb aber, wenn gemeinsame oder globale Kostenfunktionen zu berücksichtigen sind oder Betriebsgrenzen des Netzes verletzt werden. Closed-Loop Simulationen über eine Woche werden für verschiedene energetische Gebäudestandards gezeigt. Durch Koordination verursachte Kostenänderungen werden im Vergleich mit dem unkoordinierten Betrieb ermittelt. Prosumer an Netzknoten mit starker Unterspannung erfahren eine überdurchschnittliche Kostensteigerung durch Koordination. Im Weiteren wird gezeigt, wie die Transformatorlast unter geringer Kostensteigerung und Auswirkung auf den Nutzerkomfort geglättet werden kann. Der Eigenverbrauch der Nachbarschaft kann zur Reduzierung der Gesamtkosten durch den Algorithmus gesteigert werden.

List of Publications

D. Bytschkow, A. Capone, J. Mayer, M. Kramer, T. Lickleder, An OPC UA-based Energy Management Platform for Multi-Energy Prosumers in Districts, In *2019 IEEE PES Innovative Smart Grid Technologies Conference Europe (ISGT-Europe)*, 2019, Bucharest.

R. Kuniyoshi, M. Kramer, M. Lindauer, Validation of RC Building Models for Applications in Energy and Demand Side Management, *Proceedings of eSim 2018, the 10th conference of IBPSA-Canada*, 2018, Montréal.

M. Kramer, A. Jambagi, V. Cheng, Distributed Model Predictive Control for Building Energy Systems in Distribution Grids, In *2017 IEEE PES Innovative Smart Grid Technologies Conference Europe (ISGT-Europe)*, 2017, Torino.

M. Kramer, A. Jambagi, V. Cheng, Bottom-up Modeling of Residential Heating Systems for Demand Side Management in District Energy System Analysis and Distribution Grid Planning, *Proceedings of BS2017: 15th Conference of International Building Performance Simulation Association*, 2017, San Francisco.

M. Kramer, D. Bytschkow, D. Ascher, V. Koutsoumpas, A. Jambagi, M. Irlbeck, Entwicklung eines Analyseframeworks zur Unterstützung der Verteilnetzbetreiber im Projekt ESOSEG, *VDE Kongress 2016 IoT - Internet der Dinge*, 2016, Mannheim.

M. Kramer, A. Jambagi, V. Cheng, A Model Predictive Control Approach for Demand Side Management of Residential Power to Heat Technologies, In *2016 IEEE International Energy Conference (ENERGYCON)*, 2016, Leuven.

A. Jambagi, M. Kramer, V. Cheng, Energy Storage within a Multi-Energy Carrier Optimisation Framework, In *2016 IEEE International Energy Conference (ENERGYCON)*, 2016, Leuven.

A. Jambagi, M. Kramer, V. Cheng, Residential Electricity Demand Modelling: Activity based modelling for a model with high time and spatial resolution, *Proceedings of 2015 IEEE International Renewable and Sustainable Energy Conference (IRSEC'15)*, 2015, Marrakech.

C. Ben Ammar, V. Cheng, M. Kramer, A Study of Building Thermal Models for Use in the Analysis of Energy Sector Coupling, *8th International Scientific Conference on Energy and Climate Change*, 2015, Athens.

A. Jambagi, M. Kramer, Electricity and Heat Sector Coupling for Domestic Energy Systems, *2015 International Conference on Smart Cities and Green ICT Systems (SMARTGREENS)*, 2015, Lisbon.

Contents

List of Figures

List of Tables

List of Acronyms and Abbreviations

AB	Apartment Building
ACPF	Alternating Current Power Flow
ADMM	Alternating Direction Method of Multipliers
BDI	Federation of German Industries
BRP	Balancing Responsible Party
CHP	Combined Heat and Power
CO	Central Optimization
CoSES	Center for Combined Smart Energy Systems
DCPF	Direct Current Power Flow
$D(+)$	Default RC-model, with radiative heat transfer coefficients (+)
DENA	German Energy Agency
DER	Distributed Energy Resources
DHW	Domestic Hot Water
DIN	German Institute for Standardization
DLMP	Distribution Locational Marginal Price
DMPC	Distributed Model Predictive Control
DSM	Demand Side Management
DSO	Distribution System Operator
E	TABULA building type $E(2)$, old building refurbished
EnEV	German Energy Saving Ordinance
F	RC-model with fitted f-factors
GEG	Gebäudeenergiegesetz
GHG	Greenhouse Gas
HP	Heat Pump
HVAC	Heating, Ventilation and Air Conditioning
IPCC	Intergovernmental Panel on Climate Change
ISO	International Organization for Standardization
J	TABULA building type EnEV 2002 $J(1)$, unrefurbished
K	TABULA buiding type EnEV 2009 $K(1)$, unrefurbished
KfW	Kreditanstalt für Wiederaufbau
L	TABULA modern passive house $L(3)$ with advanced insulation
LinDistFlow	Linearized Dist Flow
MFH	Multiy Family House
MPC	Model Predictive Control
nZEB	nearly Zero-Energy Building
OPF	Optimal Power Flow
pf	power factor
PF	Performance Factor
PI(D)	Proportional Integral (Derivative)

p.u.	per unit
PV	Photovoltaic
R^2	Coefficient of Determination
R	RC-model with radiative resistance
RBC	Rule Based Control
RC	Resistance Capacitance
REM	Residential Electricity Demand Model
RES	Renewable Energy Sources
RMSE	Root-Mean-Square Error
SFH	Single Family House
SPF	Seasonal Performance Factor
TABULA	Typology Approach for Building Stock Energy Assessment
TFH	Two Family House
TH	Terraced House
TUS	Time Use Survey
VDI	Association of German Engineers
WSVO	Thermal Insulation Ordinance

Nomenclature

Notation and Operators

$\mathbb{N}$	Set of natural numbers
$\mathbb{R}$	Set of real numbers
$\in$	Element of
$\exists$	There exists
$\forall$	For all
$\cup, \cap, \subset$	Union, intersection and subset respectively
$\otimes$	Kronecker product
Δ	Difference of two variables
j	Imaginary unit: $\mathrm{j} = \sqrt{-1}$
$\dot{x}$	Time derivative of x
$\hat{x}$	Prediction of x
x^*	Optimal point, (complex conjugate in Chapter 4)
$\overline{x}, \underline{x}$	Upper and lower limit of x
$\lvert X \rvert$	Number of elements in set X
$\lVert x \rVert$	Euclidean norm of vector x: $\lVert x \rVert = \sqrt{x_1^2 + x_2^2 + \ldots + x_N^2}$
$\mathrm{diag}(x)$	Diagonal matrix of the elements of x
$\max(\cdot)$	Maximum
$\min(\cdot)$	Minimum
$\mu(\cdot)$	Arithmetic mean
$\sigma(\cdot)$	Standard deviation
$Re(\cdot)$	Real part
$Im(\cdot)$	Imaginary part
$U(min, max)$	Uniform distribution in interval $[min, max]$
$X \in \mathbb{R}^{n \times m}$	Matrix X of real numbers with n rows and m columns
$\mathbf{X}$	Matrix X in multi-period notation
$\mathbf{x}$	Multi-period vector stacked over N_P time instants: $(x_1^T, \ldots, x_{N_P}^T)^T$
$I_n \in \mathbb{R}^{n \times n}$	Identity matrix of size n
$\mathbf{0}_{n \times m} \in \mathbb{R}^{n \times m}$	Zero matrix
$\mathbf{1}_{n \times m} \in \mathbb{R}^{n \times m}$	Ones matrix

Building Energy Modeling

α	Heat transfer coefficient	$W/(m^2K)$
Δt	Discretization step in time	s
ε	Emissivity	
ε_{hr}	Efficiency of the heat recovery system	
η	Coefficient of performance	
$\eta_{inf/vent/mec}$	Air change rate of infiltration, natural and mechanical ventilation	h^{-1}
λ	Conductivity	W/(mK)
λ_i	Eigenvalue corresponding to state i	
ξ	Loss factor	
π	Slack variable price	
$\rho_{w/air}$	Density (water/air)	kg/m^3
σ	Stefan-Boltzmann constant $\sigma = 5.67 \cdot 10^{-8} W/(m^2K^4)$	
τ	Time constant	s
φ	Thermal gain as model input	W
ω	Angular frequency	rad/s
A	Area	m^2
A_{comp}	Heat transfer matrix of a component	
A_v	Chain marix of material layer v	
a	Absorptivity	
C	Capacity	$Ws/(m^2K)$
$c_{(w/air)}$	Specific heat capacity (water/air)	Ws/(kgK)
d	Vector of disturbances	
d_{dhw}	DHW model day counter	
$f_\square$	Heating system power distribution factor	
$g_\square$	Internal gains distribution factor	
H	Number of household members	
$I_{dir/diff/H}$	Direct/diffuse/global horizontal radiation	W/m^2
n	Number of material layers in a component	
N	Sample size	
$o(t)$	Occupancy profile	
$P_{bh,sh}$	Electrical demand of the back-up heater for space heating	W
$P_{bh,dhw}$	Electrical demand of the back-up heater for domestic hot water	W
$P_{hp,sh}$	Electrical demand of the heat pump for space heating	W
$P_{hp,dhw}$	Electrical demand of the heat pump for domestic hot water	W
$\dot{Q}$	Heat flow	W
$\dot{Q}_{bh,dhw}$	Back-up heater power supplied to domestic hot water storage	W
$\dot{Q}_{bh,sh}$	Back-up heater power supplied to space heating	W
$\dot{Q}_{dhw}$	Domestic hot water demand in power drawn	W
$\dot{Q}_{hp,dhw}$	Heat pump power supplied to domestic hot water storage	W
$\dot{Q}_{hp,sh}$	Heat pump power supplied to space heating	W
$\dot{Q}_{sto}$	Thermal load of the building supplied by the storage	W
$\dot{q}$	Heat flux	W/m^2
R	Resistance	m^2K/W
$R_{se/si}$	External/internal surface resistance	m^2K/W
R_{vent}	Resistance for losses from ventilation and thermal bridges	m^2K/W
s	Slack variable	°C

Building Energy Modeling

$s_{\square}$	Solar gains distribution factor	
T	Temperature	°C
$T_{a(,eq)}$	(Equivalent) ambient temperature	°C
T_{cold}	Cold water temperature	°C
T_{env}	Temperature of the water storage surrounding	°C
T_g	Ground temperature	°C
T_m	Mean temperature	°C
T_P	Period in days	
$T_{service}$	Temperature of tapped water	°C
t	Time or time index	s, [ ]
U	U-value, thermal transmittance	$W/(m^2K)$
V	Matrix of Eigenvectors	
V_{air}	Air volume	m^3
$\dot{V}$	Flow rate	l/min
v	Number of material layer, Eigenvector	
x	Position, length	m
x_{E+}	EnergyPlus temperature vector	°C
x_{RC}	RC-model temperature vector	°C

Subscripts

$\square_{1+}$	One time step prediction
$\square_{dhw}$	Domestic hot water storage
$\square_{E+}$	EnergyPlus result
$\square_{RC}$	RC-model result
$\square_{fl}$	Floor
$\square_{h}$	Heating input
$\square_{ig}$	Internal gains
$\square_{,s}$	At the surface
$\square_{sg}$	Solar gains
$\square_{sto}$	Storage
$\square_{wi}$	Inner wall
$\square_{wo}$	Outer wall
$\square_{z}$	Zone

Prosumer Energy Management

π	Electricity price	
Δ_t	sample time	s
A	System matrix	
$\mathcal{A}$	System matrix over prediction horizon	
B	Controllable input matrix	
$\mathcal{B}$	Input matrix over prediction horizon	
$\mathcal{B}^C(k)$	Matrix to map the controllable inputs to the electric load at time k	
$\overline{\mathcal{B}}$	Matrix to couple the controllable inputs w.r.t. constraints of operation	
C	Output matrix	
$\mathbf{c}$	Cost vector	
d	Disturbance vector	
E	Uncontrollable input or disturbance matrix	
$\mathcal{E}$	Disturbance matrix over prediction horizon	
g	Photovoltaic generation	W
j	Index for time instant in the prediction horizon	
k	Discrete time sample number	
l	Fixed electricity load	W
N_P	Length of the prediction horizon	
n_d	Dimension disturbance vector	
n_u	Dimension controllable input vector	
n_x	Dimension states vector	
P_{el}	Electrical demand of the heating system	W
r	Residual load	W
r^+	Positive part of residual load r	W
u	Controllable input vector	W
x	States vector	°C
x_0	States measurement	°C

Subscripts

$\square_c$	Complete continuous-time state-space model
$\square_k$	Indicates a vector stacked in time defined at time k
$\square_{RC-R}$	Continuous-time RC-model R
$\square_{sto,dhw}$	Continuous-time domestic hot water storage model
$\square_{sto,sh}$	Continuous-time buffer storage model

Power Flow Model

δ	*LinDistFlow* model vector of constants	
ϵ	Voltage tolerance	p.u.
θ_i	Voltage angle at bus i	rad
Π	*LinDistFlow* model matrix	
$\tilde{\Pi}$	Matrix to couple participating residual loads to the nodal balance and voltage equations	
φ	Angle between active and apparent power	rad
Ω_i^+	Set of neighbor buses of bus i including i	
B_{ij}	Susceptance between buses i and j	S
$\mathcal{C}_j$	Child buses of j	
C_P	Active power connectivity matrix	
C_Q	Reactive power connectivity matrix	
C_U	Voltage connectivity matrix	
c_u	Vector of voltage constants	
E_i	Complex voltage at bus i	V
$\mathcal{E}$	Set of branches	
e	Number of branches	
G_{ij}	Conductance between buses i and j	S
I_i	Complex current injection at bus i	A
$\mathcal{L}_{LinDistFlow}$	Resistive losses of the *LinDistFlow* model	W
l_{ij}	Squared current magnitude from bus i to j	A^2
$\mathcal{N}$	Set of buses	
$\mathcal{N}^+$	Set of buses without substation bus	
n	Number of buses	
P	Vector of active power flows	W
$P_{(i)j}$	Active power flow from bus i to j	W
p	Vector of active power loads	W
p_i	Active power injection at bus i	W
Q	Vector of reactive power flows	var
$Q_{(i)j}$	Reactive power flow from bus i to j	var
q	Vector of reactive power loads	var
q_i	Reactive power injection at bus i	var
R	Resistance matrix	Ω
R_{ij}	Resistance between buses i and j	Ω
S	Vector of apparent power flows	VA
s_i	Apparent power injection at bus i	VA
U_i	Squared voltage magnitude at bus i	V^2
V_i	Voltage amplitude at bus i	V
X	Reactance matrix	Ω
X_{ij}	Reactance between buses i and j	Ω
Y_{ij}	Admittance between buses i and j	S
Z_{ij}	Impedance between buses i and j	Ω

Superscripts

$\square^{(c)}$	consumed
$\square^{(g)}$	generated

Power Flow Model

Subscripts

$\square_{i,j,(k)}$	(Child) bus index
$\square_{ref}$	Reference

Hierarchical Distributed MPC

$\Delta_{dual}^{\ell+1}$	Dual residual after iteration	
$\Delta_{prim}^{\ell+1}$	Primal residual after iteration	
ϵ_{dual}	Dual residual tolerance	
ϵ_{prim}	Primal residual tolerance	
λ	Vector of dual variables	
ν	Scaled dual variable	
ρ	Penalty parameter	
Ω	PV self-consumption rate of the community	
ω	Weighting factor local prosumer costs vs. shared costs	
a	Vector of auxiliary variables, copy of z	W
a_i	Vector of auxiliary variables, copy of z_i for prosumer i	W
$C_{\mathcal{I}}$	Participation matrix	
$\mathbb{D}$	Set of feasible points of operation at the global system level (DSO)	
e_g	Global level disturbances	
e_i	Disturbances on coupling variables of prosumer i	
$\mathcal{F}(\cdot)$	Central optimization complete cost function	
$\mathcal{F}^*$	Objective function value of $\mathcal{F}$ at the optimal solution	
$\mathcal{F}^{\ell^*}$	Objective function value of $\mathcal{F}$ after ℓ^* iterations	
$\mathcal{F}_i(\cdot)$	Prosumer or subsystem running cost	
$f_i(\cdot)$	Prosumer or subsystem cost function over the prediction horizon	
$f_{i,f}(\cdot)$	Prosumer slack variables cost function over the prediction horizon	
$\mathcal{G}_g(\cdot)$	Global system running cost	
$\mathcal{G}_s(\cdot)$	Shared running cost	
$g_f(\cdot)$	Global system slack variables cost function over the prediction horizon	
$g_g(\cdot)$	Global system cost function over the prediction horizon	
$g_s(\cdot)$	Shared cost function over the prediction horizon	
$\mathcal{I}$	Number of prosumers	
$\mathcal{L}(\cdot)$	Lagrangian function	
$\mathcal{L}_\rho(\cdot)$	The augmented Lagrangian function	
ℓ	ADMM iteration	
ℓ^*	ADMM iteration when a termination criteria is met	
$\overline{\ell}$	Maximum number of ADMM iterations	
M_g	Global (DSO) slack variables cost parameter	
M_i	Slack variables cost parameter of prosumer i	
$\mathcal{N}_c$	Set of participating buses available for coordination	
$\mathcal{N}_{\not c}$	Set of non-participating buses	
n_{z_i}	Dimension of coupling variable vector of prosumer i	
$\mathbb{P}_i$	Set of feasible trajectories of prosumer i	
s_g	DSO slack variables	
s_i	Slack variables of prosumer i	
T	Simulation period	
$\mathbb{U}_i$	Controllable inputs constraint set of prosumer i	
$\mathbb{X}_i$	State variable constraint set of prosumer i	
$\mathbb{X}_g$	Global state variables constraint set	
x_g	Vector of global system state variables	
x_i	Vector of state variables of prosumer i	°C
z	Vector of coupling variables	W

Hierarchical Distributed MPC

z_i	Vector of coupling variables of prosumer i	W

Superscript

$\square^{\ell}$	ADMM iteration
$\square^{*}$	Indicates the optimal parameter, variable or optimum of a function

Subscripts

$\square_i$	Prosumer or subsystem i
$\square_k$	At time k, includes decisions or predictions over prediction horizon from k to $k+N_P-1$ ($k+1$ to $k+N_P$)

Chapter 1

Introduction

The aim of the first chapter is to provide an overview of international and national measures to reduce global greenhouse gas emissions and to motivate the ongoing transformation of the energy system. Literature reviews on the electrification of the heating sector, the use of operational flexibility provided by buildings and technological requirements to optimally integrate buildings in future power systems are given to define points of reference for the contributions of this thesis.

1.1 Motivation

The physical science basis presented in the fifth assessment report of the Intergovernmental Panel on Climate Change (IPCC) confirms the human influence on the climate system. The IPCC states a 95% certainty that humans are the main cause for current global warming, with many climatic changes since the 1950s being unprecedented over decades to millennia [SQP+13]. Several emission pathways exist to limit the global temperature increase below 2 °C relative to preindustrial levels, but intensive and urgent mitigation efforts are required in order to avoid higher costs and even greater technological, economic and institutional challenges [EPMS+14, CM14]. The aim of the 2015 international Paris Agreement is to keep the increase in the global average temperature to "well below 2 °C" above preindustrial levels and to pursue efforts to limit the temperature increase to 1.5 °C above preindustrial levels [Uni15]. The authors in [RGR+17] translate the goals of the Paris Agreement into a global roadmap for decarbonization. A modeled reduction scenario with a chance larger than 66% to achieve the 2 °C target and a 50% chance of limiting the temperature increase to 1.5 °C by the end of the century requires the annual global emissions to peak at around 40 $GtCO_2$/a in year 2020 and to then decrease to 5 $GtCO_2$/a in 2050. The authors suggest a climate law to halve emissions every decade, leading to net-zero emissions in 2050 and leaving a total remaining budget of 700 $GtCO_2$ until the end of the century. Such a reduction could be, among other measures, achieved by a transition of the energy system with a doubling of the share of zero-carbon generation resources in primary energy every five to seven years[1], and an upscaling of CO_2 removal technologies [RGR+17].
Germany intends to reduce its greenhouse gas emissions by at least 40% in 2020 and by 80-95% in 2050, relative to the level of emissions in 1990. Key sectors expected to contribute are the energy industry, the industry, households and transport [BMU14]. The energy industry has already undergone a significant change. Major fossil-fuel power and heating plants are included in the European emissions trading scheme and renewable energies have been expanded significantly in the last two decades. In 2018, renewable energies had a share of 37.8% in gross electricity consumption, but only a share of 14.2% and 5.7% in final energy consumption for heating/cooling and transport, respectively [BMW19]. Special emphasis is given to those sectors, since the shares of renewables have stagnated over the last years. One third of the final energy consumption alone

[1] Doubling time for renewables was 5.5 years in the past decade, the energy system would be carbon free around year 2040 [RGR+17].

is associated to space heating and hot water. Including further process heat, heat accounted for 54% of the final energy consumption in 2016 [BMW18]. Heat is of high relevance in private households: space heating (70.7%) and hot water (13.9%) accounted for almost 85% of the sector specific final energy consumption in 2016. The associated total emissions accounted for 74% of the private households' emissions for living [Fed19].
Looking at the final energy demand associated with buildings (residential and non-residential) across all sectors underlines the relevance of heat and the importance of buildings as a lever for energy efficiency. Buildings accounted for 35.3% of the final energy demand in 2016, with space heating accounting for almost 80% of that demand alone and leading to 66% of the related emissions [BMW18].

1.2 Sector Coupling, Flexibility and the Smart Grid

Increasing energy efficiency and expanding the use of renewable energies in heating and transport is required to achieve Germany's climate goals. Several studies have investigated optimal pathways for the transition of the energy system and identify a strong electrification of the sectors as necessary in order to replace fossil fuels with renewables.

1.2.1 Sector Coupling and Electrification

The study in [DEN18b] estimates that an average net expansion of renewable energies of up to 8.5 GW per year is required until 2050, with main contributions from onshore wind and photovoltaic (PV). Independent of the investigated scenario (strong or moderate electrification, 80% or 95% reduction of emissions), the installed capacity of renewable energies in 2050 exceeds 300 GW, which is more than a tripling of the capacity stated for 2015. In parallel, the energy efficiency in the building sector has to be increased through higher refurbishment rates to upgrade the insulation standard of the existing building stock. Electrical heat pumps are mentioned as an important technology to integrate more renewables in the building sector. Depending on the degree of electrification, the authors state a total number of residential heat pump systems ranging between 7 and 17 million in 2050 compared to near to one million systems installed today [DEN18b]. Other studies confirm the relevance of residential heat pump systems to enable sector coupling, see e.g. [Fra17,BDI18]. A detailed discussion of heat pump penetration scenarios is provided in Chapter 2.1.3.
Electrifying the heating sector with heat pumps and electrical heaters is also found beneficial in energy system optimization studies. The study in [SSH13] examines how the significant temporary excess generation resulting from high shares of wind and PV could be integrated in a cost-optimal way in Germany. The authors find coupling of the electricity and heat sectors to be more beneficial than integrating the excess in the hydrogen or natural gas sectors due to flexible and low-cost electrical heaters. Battery costs are found not to be competitive for large-scale deployment. Expansion of the transmission grid is required to facilitate sector coupling at higher shares of variable renewable energies. The thesis in [Hei15] investigated the cost-optimal structure and operation of the electricity and heat supply for Germany to achieve national climate goals. Electrified heating options, especially optimally operated heat pumps, lead the way to supply heat at low costs. Heat pumps are found to be complementary to combined heat and power (CHP) plants, which are predominantly used to supply heating grids. The additional electricity generation from CHPs during times of high heat demand coincides with the increased electricity demand of the heat pumps. A similar effect was observed for the interaction of heat pumps and CHPs in low voltage grids in [Arn16]. Simple electric heating elements are mentioned in [Hei15] as another low-cost option to supply heat and are found to be useful to better integrate short-

term generation peaks of renewables. The author argues that the geographically distributed nature of the electric heaters helps to alleviate issues of grid congestion during excess generation, although the details of electricity grids are not covered in the optimization model used in the thesis. Operational flexibility is mainly provided by thermal storage systems which allow heat pumps, heating elements and CHPs to achieve higher operating times and a better integration of renewables. Thermal storages reduce overall costs and higher emission targets lead to a higher demand for thermal storages. A stronger coupling between the electricity and heating sectors also reduces the demand for hydrogen as a storage option, which is in line with the results of the previous study in [SSH13].

1.2.2 Operational Flexibility

In addition to a stronger electrification through electric heat pumps and electromobility, technological solutions like storages and load management are needed to decouple demand from generation in a more renewable and volatile energy system [BMW18]. Increasing shares of renewable energy sources (RES) will result in more non-controllable stochastic in-feed into power systems and generation will have limited capabilities to follow the demand. The latter needs to be flexible in operation to adapt to the volatility in generation [DEN18b].
[UA12] investigates general operational flexibility in power systems and finds it on both the generation and demand side. Sources include fast responding conventional power plants or RES curtailment, stationary storage capacities or load management to change the shape of the demand curve. The authors define operational flexibility as the ability of units in the power system to modulate power and energy in-feed and out-feed. Operational flexibility can be characterized by the metrics power capability for up- or down-regulation measured in [W], power ramping rate in [W/s] and energy storage capability in [Ws] [UA12, MLMdM09]. The metrics differ among different sources of flexibility and depend in the operational constraints of the unit. Activities that allow for a change of the time pattern and magnitude of the electricity customer are not new to the energy industry and are also summarized under the term Demand Side Management (DSM) [Gel85].
The focus of this thesis lies on the optimal integration of operational flexibility provided from residential buildings in power systems. The heating sector provides multiple sources of flexibility in addition to the obvious flexibility from electrical battery storage systems to decouple electrical supply and demand. The electricity demand of an electrified heating system can be decoupled from the heating demand by use of a thermal storage system. A detailed discussion of different thermal storage systems and their DSM potential is given in [AHP12]. The structural building mass has been of great interest as a thermal storage in recent years, besides commonly available water tanks and buffer storages. The basic idea is to benefit from the thermal inertia of a building by temporary overheating parts of the structural thermal mass, e.g. floor, walls, ceilings and concrete elements. Also the zone air can be overheated within a comfort temperature range. The literature addresses modeling and control of concrete core activation in office buildings [Sou12, Jun14], the impact of the type of building and structural thermal mass on the potential of DSM [HAS+14, Rey15] and the potential of a single family house equipped with an air-to-water heat pump and floor heating or a radiator heat emission system to integrate local PV generation [RNS13]. The latter finds significant short-term flexibility to shift the electricity demand of a heat pump from peak demand to peak supply times whilst maintaining thermal comfort. Several studies try to quantify the flexibility beyond single building cases, i.e. the flexibility from aggregations of buildings or even the total provided on the national level. [SHM16] introduces a methodology to compute the above flexibility metrics for a single building energy system. The approach allows for upscaling to investigate the flexibility on city or even regional

and national levels. The works in [PH14,RS14,RDS17] develop bottom-up models to characterize and quantify the potential from typology buildings of the residential Belgian building stock. In contrast, [KH17] presents a top-down approach to quantify the flexibility from residential and non-residential heating and cooling in Germany based on the rated power of devices and the approximated thermal capacity of buildings, explicitly including the thermal building mass. A potential capacity of 200 GWh and 20 GW up- and down-regulation power are estimated for the status quo. Finally, the Annex 67 program of the International Energy Agency was an international initiative to acquire more insights into the flexibility potential of different building types, its usefulness for energy system services and appropriate control strategies, see [JMPL+17] and the many subsequent publications of the working group[2]. Even though the working group states grid supportive building operation as an important use case of flexibility, none of the publications addresses the actual impact on power grids in terms of line power flows and voltages.
Operational flexibility is a complex technological option since it has use cases and impacts on different levels of the energy system, involving different stakeholders. The authors in [SHM16] name three exemplary use cases of flexibility for:

- increase of building level or city quarter/district self-consumption,
- balancing RES fluctuations on the level of the national power system,
- power system support, e.g. mitigation of grid congestion.

Studies on the building level self-consumption with heat pumps and local PV systems are for example carried out in [VGC+14, TSWB15, BKHB17]. Average autarky rates between 20% and 40% for a 10 kW PV plant and optimized heat pump operation are stated in [TSWB15] for residential buildings of different thermal standards. The authors underline the requirement of an interface to enable optimal control of the heat pump. Potential benefits on the city district level are discussed in [MMS+15] and the authors of [JAL+18] develop a flexibility index to communicate the available flexibility of single or multiple buildings to a grid operator to participate in balancing or day-ahead markets.
Other studies address the impact of DSM from buildings on the national power system level. [PBA+15] derives an approach to integrate DSM of heat pumps and electrical resistance heaters in a national power system model and tries to include the price elasticity of the flexible systems in a merit order model. The same authors use the model to investigate increasing shares of demand response participants in [APB+16]. More customers participating in load shifting leads to lower total operational costs of the energy system due to the additional flexibility in operation, but also to a decrease of the per participant reward. [PH16] presents an integrated framework to optimize both residential building energy system design (investments) and operation for nine energy mix scenarios in Belgium. Investing in heat pumps with floor heating and local PV systems results in lowest emissions for additional annual costs of 350 EUR when compared with the status quo fossil fuel heating system. The authors in [AHW+17] investigate the impact of DSM on the German energy mix and power plant dispatch until the year 2050. Electrification of the building sector leads to a higher electrical load, which is mainly covered by RES, and reduced CO_2 emissions. Flexibilization of the new load allows for a better utilization of combined cycle power plants and reduces emissions further. Two different heat pump penetration scenarios lead to a strong reduction of emissions, i.e. a tenth of the emission associated with a conventional heating scenario.

[2]Project website: http://www.annex67.org/.

1.2.3 Smart Grid

The electrical peak load of the whole building sector in Germany is expected to double from 33 GW to 65 GW in the electrification scenarios for year 2050 in [DEN18b]. Necessary investments in low voltage grids to integrate new loads and generators are expected to exceed those in medium and high voltage grids in all 2050 scenarios, ranging between 68 and 150 bn EUR depending on the degree of electrification and emissions reduction. The use of grid-supportive flexibility options is assumed to reduce the costs from 150 to 103 bn EUR in the ambitious electrification scenario. Additionally exploiting the inertia of buildings was not considered in the study and might offer a further cost reduction [DEN18b].
Increasing numbers of RES, electrified heating systems and electric vehicles will pose challenges for distribution grids and change the way future power systems are planned and operated. While the authors in [BKF+14] find the combination of curtailment and on-load tap changers favorable to limit distribution grid expansion costs associated with local RES integration, integrated sector studies like in [DEN18b,Fra17] highlight the importance of DSM to actively control heat pumps and electric vehicle charging. Enabled by enhanced capabilities in measurement and automation, innovative concepts for the operational management of power grids are, besides the benefits discussed above, required to reduce costs of grid expansion [DEN18b].
Distribution system operators (DSO) face multiple challenges. As the interface to higher level grids, distribution grids must host many of the new electrical loads which are required to adapt their operation to available RES generation and market price signals. At the same time, operational limits of distribution grids must be maintained. In the light of increasing wind generation capacity the study in [SKP+,PKG+17] investigates the cost optimal thermal standard and heating system design to integrate electricity generation from strong wind events which occur with a 95% probability every 13 days during the heating period and last in average for 9 hours. A residential single-family house should have a tight insulation, a low temperature emissions system like floor heating, a large thermal water storage and an operational zone temperature range from 20 °C to 25 °C in order to maximize the stored wind energy in the building to bridge calm wind days and to avoid use of fossil back-up generation. Since the heating demand of two weeks has to be stored in only a couple of hours, direct electrical heating is suggested to avoid expensive overdimensioning of the heat pump. The total rated power of the building is found to be significantly higher than what is commonly assumed in grid planning. The authors recommend to "adjust" distribution grids to the new peak load. In this case, grid-supportive operation is limited to the integration of excess generation from wind and the impact on local grid operation is beyond the scope of the study. The authors also highlight the need for prediction-based control algorithms to enable wind-oriented operation.
The simulation study in [Arn16] assumes less extreme system designs but finds undervoltages caused by heat pumps as the limiting factor in a suburban distribution grid scenario for year 2020. The author assumes an air-to-water heat pump with an electrical power rating of 4 kW and a heating rod of the same size[3]. DSM is implemented in form of a simple local proportional controller which limits the maximum power of a heat pump linearly when the local bus voltage is between 0.91 p.u.[4] and the lower limit of 0.9 p.u.. Since undervoltages often occur at the ends of grid feeders, the majority of heat pump controllers do not see the undervoltages, and the overall power reduction is not sufficient to support the voltage. Even worse, DSM also causes a loss in end-user comfort due to the simple hysteresis heating system control. On-load tap changers are

[3] [NMB+12] reports of a distribution grid design of a German DSO which assumes a total connection of 3.5 kVA per house including the heat pump.

[4] The per-unit system is used in power systems analysis to express and compare technical quantities. The dimensionless value is obtained from dividing a physical quantity by a base reference value used for all components, i.e. for voltages $V_{p.u.} = \frac{V}{V_{base}} = \frac{0.36\text{kV}}{0.4\text{kV}} = 0.9\,\text{p.u.}$.

found to be effective and the most cost-effective solution among others, but DSM could become viable when information exchange enables a more sophisticated and coordinated control of the heat pumps [Arn16]. Extensive simulation studies to assess the impact of building/neighborhood properties, air-to-water heat pump and PV system penetrations rates in Belgian low-voltage distribution grids are carried out in [PS17]. Modelica-based simulations show that especially rural grids face violations of operational grid limits. Already heat pump penetrations rates between 20% and 30% cause line overloading in larger rural grids, undervoltages occur at slightly higher rates. Coincidence in demand, especially caused by electrical back-up heaters, poses a major problem and the authors point out that DSM and a smarter operation of the grid could be beneficial. Issues related to the use of auxiliary heaters are confirmed in [NMB+12] based on a smart meter data study. The authors further investigate the effect of a synchronized reaction of heat pumps to a price signal in order to use DSM to reduce individual costs. The required investments in grid reinforcement overcompensate the total cost benefit of the customers. This incentivices solutions for intelligent grid operation to simultaneously facilitate DSM and the consideration of power system constraints from a welfare-economic point of view. High coincidence in demand due to reactions on market prices must be avoided [Fra17].

The idea of an intelligently operated distribution grid which integrates new loads and generators but also optimally exploits local flexibility to the extent that its own operational limits are maintained, is conceptualized in the so-called *Smart Grid*. The need of a smart grid to tackle challenges in future energy systems is stated in [LHM+07, BLHP09, RGR+17]. "Smart" refers to the circumstance that enhanced sensing, automation and control enables the grid to optimally operate a system of increasing complexity. [UA12] provides a control-theoretical perspective, understanding the term as "the sum of all efforts that improve observability and controllability over individual power system processes happening on the transmission and distribution grid level". The smart grid also has the task to "empower its stakeholders to define and realize new ways of engaging with each other and performing energy transactions across the system" [Far10]. This aspect is, among other things, motivated by a transition of small-scale electricity customers: previous passive *consumers* become active *producers* who sell locally generated electricity, often referred to as *prosumers*[5] [LVK10]. Improved communication infrastructure and metering of devices together with controllability and predictability over various distributed energy resources are key elements of a smart grid. Missing communication and metering infrastructure is seen as an important reason for limited deployment of DSM so far [Str08]. A review of communication technologies and standards used in different domains (e.g. grid operation, building automation) is provided in [GSK+11]. A wider use of monitoring solutions also raises concerns of data privacy. Metering close to the private customer involves the risk of revealing behavior, activities and occupancy [MM09, LXL+12]. This concerns not only smart meters tracking the household electricity consumption, but also advanced energy management solutions to operate heating systems. As will be shown in the next section, state-of-the-art control approaches base optimal scheduling decisions on multiple forecasts, potentially including occupancy.

Assuming availability of communication technologies, suitable control strategies have to be developed to integrate and enable the use of flexibility in distribution grids. The authors in [DEMM17] highlight characterizing factors that influence the development of such real-time control strategies in the context of distribution grids. Flexibility stems from non-electrical storages and coupling of the sectors results in so-called multi-energy systems with significantly different time constants of physical processes in power systems and thermodynamics. Previously independently developed and applied control and optimization strategies used e.g. in power systems and heating, ventilation and air conditioning (HVAC) have to be combined now. In order to integrate flexible

[5] The term is used in this thesis for a residential customer whose building is equipped with an electrical heat pump and a PV plant.

operation of buildings in distribution grids, a non-exhaustive set of tasks and aspects can be given which seems to be relevant and is addressed in the context of this thesis:

- *Economic dispatch and cost optimal use of flexibility*:
  The control strategy must allow the computation of set-points for the local systems (prosumer, HVAC system) to meet individual subsystem objectives, e.g. minimal energy costs or maximum comfort, but must also allow for consideration of global objectives of the community or DSO to match overall demand and supply targets [DEMM17]. The strategy should be able to find a cost-minimal selection among multiple flexibility options.

- *Local and global feasible operation*:
  Operational schedules must account for intertemporal dependencies of storages and satisfy both operational constraints of the subsystems (e.g. individual temperature and power limits) and of the distribution grid (e.g. voltage and current limits). Modeling constraints of systems is crucial to assess and optimally exploit flexibility [UA12].

- *Predictability and uncertainty treatment*:
  The control strategy must account for the volatility of RES generation profiles and the impact of non-controllable disturbances on systems and their flexibility through predictions. Especially building operation is driven by ambient conditions and user behavior. The authors in [OMSE+14] hint at the higher uncertainty of load profiles in smaller microgrids compared to the bulk power systems due to a smaller number of systems and a weaker averaging effect.

- *Information exchange:*
  The necessity of a certain degree of information exchange between the subsystems and the DSO is evident. Price signals or information on grid conditions could be revealed to the subsystems to make independent local decisions. Conversely, DSOs could monitor and directly control subsystems in order to steer demand profiles [IA09]. Since DSOs might be unwilling to share topological and operational data with electricity customers, and customers might have privacy concerns when sharing detailed operational data of their subsystems, data protection and minimum information exchange are desired features. Reduced communication requirements might also be of importance for critical tasks in grid operation [OMSE+14].

- *Adaptability and scalability*:
  The number of subsystems and the composition by type might change over time, and with this the overall system model used in a controller. Thus a control strategy should facilitate seamless integration and removal (the "plug-and-play" feature, see [Sto09]) and be able to deal with topological changes in the grid [OMSE+14]. In addition, the size and type of optimization problems to solve may become a challenge. Nonconvexity resulting from the underlying power flow physics, non-linear efficiency models, binary decision variables of HVAC systems, increasing system size and optimization horizon can lead to models of high and possibly prohibitive computational complexity [DEMM17].[6]

1.3 Smart Grid Control

This section gives an introduction to standard and advanced control methods and architectures applied to problems in building controls and power systems. Different methods are briefly discussed with respect to the aspects described above and a literature review on building controls

[6] A short introduction to convex optimization is provided in Appendix A.1.

for heat pumps and large-scale systems given. The goal is to motivate the development of a distributed hierarchical model predictive controller for the coordination of prosumers in distribution grids in this thesis.

1.3.1 Rule-based Control and Model Predictive Control

Multiple conventional controllers are applied to operate building HVAC systems. [SNN+14] provides a review of common controllers and names thermostats, proportional-integral (PI) and proportional-integral-derivative (PID) controllers among others. Besides classical feedback controllers used for setpoint tracking, so-called *Rule-based Control* (RBC) schemes are frequently applied in building automation to steer overall system behavior. In RBC, inputs for actuators are determined based on a set of rules stated in a structure such as *if* (condition) - *then* (action 1) - *else* (action 2) [VLOA13], e.g. a thermal storage is recharged when the temperature falls below a certain threshold and charging stops after a predefined amount of time. To find a set of rules which achieves the best possible operation with respect to costs or comfort might be difficult, the task might become even more challenging in complex systems with hundreds of actuators.
The task to optimally control a physical process of a system is a standard dynamic optimization problem, e.g. the decision when to optimally charge or discharge a thermal storage system over time can be found by solving such a problem. Core element is a model representation of the physical process, stated as a discrete-time (time index k) dynamic model:

$$x(k+1) = h(x(k), u(k), d(k)), \quad x(0) = x_0. \tag{1.1}$$

x is the state of the system (e.g. temperature in the storage), u is the controllable input (e.g. power injection from an electrical heater and/or controlled discharge) and d is a predicted, non-controllable disturbance influencing the process (e.g. random discharge of the storage, surrounding temperature driving heat loss). All variables might be vectors. The evolution of the state of the system over time is defined by the possibly nonlinear function h and the initialization of the model with $x(0) = x_0$ where x_0 is the latest measurement of the state. The dynamic optimization then solves for the optimal vector $\boldsymbol{u}_{N_P} = (u(0)^T, u(1)^T, \dots, u(N_P-1)^T)^T$ to minimize the stage cost function $\mathcal{F}$ and the terminal cost function $\mathcal{F}_x$ over the prediction horizon N_P:

$$\min_{\boldsymbol{u}_{N_P}} \sum_{k=0}^{N_P-1} \mathcal{F}(x(k), u(k)) + \mathcal{F}_x(x(N_P)). \tag{1.2}$$

The optimal sequence of controllable inputs (e.g. values of charging and discharging power) is computed with techniques from numerical optimization to attain the minimum aggregated cost over the finite prediction horizon. $\mathcal{F}$ might be linear or nonlinear and depends on either of the variables, depending on the control objective chosen. Minimizing cost of the use of the heater or tracking a predefined trajectory with the storage temperature are possible applications. A weighted combination of linear and/or quadratic terms can also be implemented.
Computing the optimal sequence $\boldsymbol{u}^*_{N_P}$ once and applying the solution to the system over the length of the predicted time steps might result in bad operation and the actual progress of the state might deviate from the predicted trajectory. The process model h might be inaccurate and forecasts of disturbances erroneous. In addition, predictions for a fixed future time step usually become better the closer one is to it. One might also benefit from taking a new measurement of the system into account. Instead of applying the whole sequence $\boldsymbol{u}^*_{N_P}$ on the system, only a part of it, e.g. the first element $u(0)^*$, is used. The dynamic process of the system advances and a new measurement for $x(1)$ and updated predictions of d are used to repeat the optimization.

This online procedure is referred to as *Model Predictive Control*[7] (MPC), see [BBM15, RM09] and the introductions therein.
MPC evolved from the chemical process industry in the 1970s and has since then found application in many other industries [QB03]. A crucial advantage over other control methods lies in the explicit consideration of interdependencies and operational constraints on multiple model inputs and outputs, which helps to avoid their violation during operation. The dynamic model can be extended by such constraints in the optimization problem [BBM15]. While MPC is often used to perform setpoint tracking and economic objectives are only considered in a steady-state optimization layer located above the actual MPC controller, so-called *Economic MPC* considers economic objectives directly in the objective function (1.2) [RAB12].
The ability of MPC to schedule operation with respect to different performance criteria in real-time, to take process dynamics and physical constraints into account and to make use of predictions and treat uncertainty, make MPC attractive also for applications in building controls. [MKDB12] provides a thorough introduction on MPC for thermal storage operation of commercial HVAC systems and demonstrates how MPC can be used for energy efficient operation and demand response services. [KK16] describes how in contrast to a standard PID controller implementation, MPC is able to anticipate a severe drop in the ambient temperature, takes the delayed response in the zone temperature of the building into account and finally operates the heating system with only a minimal loss in comfort. Multiple works have addressed control problems in both commercial and residential buildings, addressing energy efficiency, occupant comfort or the response to price signals. Publications have covered different settings and control tasks, with a focus on energy efficient building operation for radiator heating systems [HGP12a, HGP12b], water-based cooling systems [MBH+10], control of multizone buildings [AH16] or the minimization of discomfort from thermal stratification in shopping centers [MF15]. [OPJ+12] investigates the impact of MPC on energy efficiency and occupant comfort and controls blind positions and lighting in addition to the HVAC system. A stochastic MPC approach to deal with uncertainty in weather predictions was introduced and found to be superior with respect to energy consumption and comfort compared with the standard deterministic formulation. Stochastic MPC for large HVAC systems is also addressed in [MMB15]. Robust MPC for disturbance uncertainty is investigated in [MSV13].
In modern systems MPC is implemented as a part of a multi-level control hierarchy where the higher level MPC determines setpoints for basic field level controls [QB03]. This allows for integration of MPC as supervisory control with existing PID and rule-based controllers, see the exemplary structure in a building automation system in [KK16] or the experimental HVAC setup with a three-level control hierarchy to accomplish energy reserve scheduling and frequency regulation signal tracking in [VKM+16a, VKM+16b].

1.3.2 MPC for Residential Buildings

An early contribution in optimal control (not MPC) for heat pump scheduling with respect to time-of-use tariffs can be found in [RGZ88]. The authors derive the optimal trajectories of operation for a bilinear system model for the case of periodic boundary conditions, i.e. the price profile and ambient temperature are assumed to have a period of 24 hours. The work in [Wim04] designs and successfully tests a linear-quadratic MPC implementation for a residential heat pump in a real single-family house. [Bia06] extends the work and develops online parameter identification techniques to automatically adapt parameters of the system model. The works in [VDL+12, VLvH12] investigate the impact of different nonlinear and convex problem formulations for the 24 hours optimal control problem, to schedule a residential heat pump on model accuracy,

[7] *Receeding Horizon Control* is another term frequently used in the literature.

costs and comfort. The use of a simplified linearized model for the heat pump efficiency seems valid when power peaks are penalized in the cost function.
Several works investigate financial benefits of economic MPC for residential heating systems and the impact on comfort. [ZMPK+12] demonstrates how MPC is used to increase PV self-consumption and to exploit low spot prices in a building with electrical heaters. [HBP+12] achieves annual electricity cost reductions between 25% and 30% compared with a thermostat control when using MPC for spot price optimized control of a water storage tank. A cost reduction in the range of 25% to 35% (depending on the zone temperature constraint) over a five day simulation is reported in [HPMJ12] when operating MPC on day-ahead prices instead of a constant price. [KMW+13] estimates a house model based on measurements and optimizes the heat pump operation against spot prices from the Nord Pool power exchange. A cost reduction by 7% together with a slight increase in the standard deviation of the zone temperature resulted from a simulation of a winter month. MPC is also simulated for different price signals in [VLOA13] for a residential building with a heat pump, slab cooling, a domestic hot water heater, PV and a battery. Simulations show a good response of the building system to day-ahead and real-time prices, which qualifies for energy market oriented demand response services. Depending on the building and price scenarios, a cost reduction between 18% and 28% can be achieved against a rule-based reference implementation. The author of this thesis designs a predictive controller for a residential ground-source heat pump in [KJC16] based on the thermal model from [HPMJ12] to investigate the trade-off between minimizing electricity costs and discomfort. A seven day closed-loop simulation with a 24 hours prediction horizon reveals a possible cost reduction of 62% when the controller must no longer maintain a 22 °C zone temperature and is allowed to exploit spot price differences while keeping the average zone temperature at 22 °C. A benchmark optimization with perfect predictions over the whole simulation period demonstrates the impact of the limited prediction horizon in MPC.
Cost saving results must be interpreted in the context of often simplified building and heating system models. Such estimates heavily depend on the quality of the benchmark controller when compared with standard control methods. [FBMW17] tests RBC implementations of different sophistication against a convex MPC for an air-to-water heat pump heating system in a multi-family house. MPC outperforms all RBC solutions with respect to annual costs (reduction between 6%-16%), energy efficiency and comfort in all scenarios, but requires significant modeling effort and is computationally more expensive. RBC is initially easier to design, but satisfying results require much fine-tuning and the derived rules are not robust to changing boundary conditions. This is also an important result with respect to the parallel operation of multiple buildings, i.e. defining rules for a close to optimal operation of an aggregations of systems might be impossible with RBC.
To conclude, RBC has limited applicability for load shifting in buildings and MPC offers many of the features required in the context of building operation in smart grids. [KK16] argues that there is no other control strategy comparable to MPC with similar suitability to integrate buildings in smart grids. MPC computes an operational dispatch with respect to technical or economic objectives, assures feasible system operation and is able to take forecasts and uncertainty into account. The above literature review supports the view that MPC could be the primary candidate to enable DSM of buildings for services in power systems, due to the ability to shift electrical loads in response to price signals. Finally, this section has revealed two important limitations: Studies with price signals focus on prices from market places such as European energy exchanges or time-of-use tariffs provided by local utilities. The studies are limited to the assessment of the general flexibility to change a building's load profile. The actual impact of price responsive operation on distribution grids is not investigated further. The perspective from the single optimized building needs to be extended by the view of the DSO. In addition, multiple buildings

must be controlled to enable coordination in distribution grids, which requires a method reaching further than single building MPC.

1.3.3 Control Architectures

Independent of the methods used to control complex dynamic systems, control architectures are commonly distinguished with respect to the distribution of information, the distribution of computational power and the required communication infrastructure.
Centrality requires all information to be available at a central control unit where all decisions are made, including complete process knowledge, i.e. dynamic models of all systems but also sensor measurements of all states. Centralized architectures fail in large-scale systems due to limits of costly information gathering and central computation capability [BB10]. Geographically dispersed power systems with many connected subsystems are one example where centrality fails [SVAS78, VHRW08]. Extensive communication would be required between a central controller and the executing units [OMSE+14].
In contrast, *decentralized* architectures assume that the large-scale system is in fact a composition of many autonomous subsystems, each one of them able to perform control tasks on its own [NdSH04, Sca09]. No communication between the systems exists. All subsystem information remains local and all decisive power is given to the subsystems, which requires local computational power. It finally depends on the degree of interactions, i.e. the physical *coupling* between the subsystem, whether or not a decentralized architecture is sufficient to guarantee overall performance and feasible operation [Sca09]. See [SVAS78] for analysis of weak and strong coupling in decentralized systems. Coupling may exit between states of subsystems or their controllable inputs. In the context of this thesis, coupling among the building and prosumer subsystems exists in the shared use of the distribution grid through the residual loads. Coupling may further exist in a shared cost function of the controllable inputs. Assuming selfishly operating MPCs in multiple buildings without further coordination is an instance of a totally decentralized architecture.
Coordination is better achieved in a *distributed* architecture, where a certain iterative or non-iterative exchange of information between subsystem controllers is possible. A further distinction is made between *fully* and *partially* distributed architectures, referring to communication network topologies where a subsystem has information exchange with all other subsystems or only a subset [Sca09]. The latter results in reduced communication and might be favorable where not all subsystems share interdependencies/coupling with one another. The basic idea of a distributed architecture is to decompose the overall system model of a central coordinator into smaller subproblems solved by local controllers[8]. Depending on the type of information exchange, distributed architectures are also categorized by the extent of cooperation between the subsystems. While *communication based/independent* settings assume that competing subsystems are unaware about the cost functions of other subsystems, *cooperative* settings assume that such knowledge is available and the subsystems operate towards a systemwide objective. On algorithm convergence, cooperative settings can achieve global optimal performance like in a centralized setting. In contrast, even if convergence is possible, an optimal solution is not guaranteed in the non-cooperative setting, one obtains the so called Nash equilibrium which might not lie on the Pareto optimal surface, i.e. the set of optimal trade-offs between the subsystems' objectives. See [Sca09] and the works in [VRW05, VRW06] for distributed MPC and a discussion of its relationship to the cooperative/non-cooperative game theory.
Distributed architectures can further have a *hierarchical* structure to achieve coordination,

[8] Autonomous "local controllers" or just "subsystems" have similarity to "agents", a term used in computer science [Sca09], see also [NdSH04] referring to "Multi-agent MPC".

see [Sca09]. In a two level structure a central entity or "coordinator" on the top level coordinates the operation among all subsystems on the lower level by exchange of communication variables. The global optimization problem has to be reformulated in order to decompose it into separate subproblems [SVAS78]. The subsystems take prices communicated by the coordinator into account when solving for their local optimal operation and then communicate a part of the local solution back to the coordinator. The iterative procedure is repeated until global feasible operation is achieved, i.e. consensus in the coupled variables exists. Conditions for convergence and optimality depend on the overall optimization problem and algorithm chosen to solve the distributed problem. In order to break a central problem, e.g. the minimization in (1.2) subject to (1.1), into smaller distributed subproblems, a mathematical decomposition of the initial problem has to be carried out and specific algorithms are used to calculate a solution. Methods frequently applied in the smart grid literature are the dual decomposition and the alternating direction method of multipliers (ADMM), but many others exist. The choice of algorithm depends on the mathematical properties of the underlying optimization problem, associated convergence properties and the speed of convergence. As will be shown in the next section, some publications propose algorithms that are not supported with proofs of convergence and optimality. A motivation for the use of ADMM in this thesis is given in Chapter 5.
Architectures for hierarchical control are attractive where the distribution of knowledge is important. Since neither the central coordinator nor the local controllers of the subsystems need to know the global problem, i.e. the overall system model including all cost functions, knowledge is decentralized [SVAS78]. This is highly applicable in the context of this thesis, where it is desirable to keep knowledge of internal building system states, occupancy predictions and cost functions with the local system controller. Simultaneously it can be assumed that a DSO is not willing to share any topological, asset and operational distribution system information with customers.
A further advantage of a hierarchical architecture in the context of MPC may lie in computational requirements. Depending on the model and objective, MPC requires the solving a linear or nonlinear optimization problem online. Even though linear or quadratic problems are easy to solve with today's methods, large-scale problems with many variables and long prediction horizons can still become computationally demanding [MH99]. Computational complexity is reported to be a potential challenge in building controls where inexpensive computing platforms have limited computational resources [MKDB12][9] and problem specific optimization methods are designed to enable fast computation on embedded systems [BBM15]. Obviously, limited memory can be a reason for a distributed solution. Since computation time often increases at a greater than linear rate with problem size (often polynomial growth for MPC problems [ESJ09, HVP+16]), solving smaller subproblems in parallel instead of one large central problem might be beneficial. However, the time needed to iterate could outweigh savings and a final judgement is problem specific [SVAS78]. Nevertheless, previous works on DSM carried out through distributed optimization found better scalability in terms of computation time and peak memory use for instances with many subsystems when compared with centralized implementations [HVP+16,RGJ17]. The latter found superior performance when more than 100 electric vehicles are controlled.

1.4 Literature Review on Coordination of Distributed Systems in Power Grids

This section provides an overview of different control strategies and architectures applied to coordination problems including buildings and power systems.

[9] The author is aware that this argument must be put into perspective by applications in cloud computing.

1.4.1 Central Strategies

The study in [dCBS+14] investigates how residential buildings equipped with air-to-water heat pumps and domestic hot water storages can help to reduce curtailment of local PV generation in order to avoid overvoltages. The Modelica-based simulation study tests different rule-based control strategies for the domestic hot water loop, i.e. the set point temperature of the water tank is temporarily increased, triggered by a timer, an active power measurement or a voltage measurement at each house. A central control architecture is tested in addition to the simple decentral solutions. Here, a coordinator has access to all building voltages and storage temperatures and triggers a temperature increase in all storages as soon as a single bus voltage violates the limit. All strategies help to reduce curtailment losses and the most complex central strategy leads only to a small improvement compared to the simpler solutions. The authors find best results when the whole neighborhood participates in a DSM strategy. MPC to operate the whole neighborhood is expected to outperform the rule-based strategies. [TBSH15] solve a central optimization problem to investigate the potential of electrical heat pumps with buffer storages of a group of residential buildings to help integrate PV generation and to mitigate voltage increase. The distribution grid (IEEE European Low Voltage Test Feeder) is not part of the optimization, only the aggregated residual load of the buildings is optimized. The study uses low-order dynamic models to forecast the heating demand of buildings with different energy efficiency standards and includes the domestic hot water demand. Shifting charging times of the buffer storages helps to integrate PV and leads to lower maximum voltage peaks. The domestic hot water demand helps to integrate PV during the summer months. The authors of [MSSVP14] propose a central MPC framework on top of the classical PI-controlled generation control to provide up- and down-regulation power from commercial building HVAC systems for frequency regulation in the transmission system. Control areas with buildings, frequency dependent loads and generators are coupled through a simple power system model, i.e. no losses, voltages and reactive power flows are considered.

1.4.2 Distributed Coordination of Flexibility

A general hierarchical control architecture to coordinate houses and distributed appliances towards a global objective is presented in [MBB+10]. [LvS13] presents a distributed MPC approach to coordinate the power imbalance with small-scale CHPs based on a dual decomposition algorithm. In the partially distributed setting, a system only communicates with a subset of all systems depending on the typology. Both a relaxed and a nonconvex problem formulation with binary decision variables to account for on-off switching are tested. In [CGB+13], a distributed MPC algorithm is presented to coordinate the aggregate peak load of a cluster of buildings, PV plants, batteries and electric vehicles at their single point of common coupling to the grid. The local controllers of the units take the shared coupling constraint into account and asynchronously access a central "blackboard" to retrieve the total operation plan and publish their schedules. No central coordinator optimization problem has to be solved, but the authors do not provide formal guarantees on convergence and optimality for the proposed algorithm. A third-order model of an office building from the literature is used to represent more realistic building dynamics. A similar, asynchronous approach is used in [SAM16] to coordinate DERs including residential heating systems in order to shape the aggregated load profile. The control scheme's impact on a distribution grid is briefly investigated for an IEEE benchmark grid, but local operational grid constraints are not explicitly considered in the coordination. The works in [WKGW14, WKB+15] present a hierarchical distributed MPC approach to flatten the aggregated power profile of residential energy systems equipped with electric batteries. The distributed mechanism is enabled through a central coordinator, the "market maker", who iteratively adjusts buying and selling prices for

electricity based on the schedules received from the subsystems. In [WKB+15], the algorithm is compared with a simple rule-based, a centralized MPC and a decentralized MPC approach in which the individual subsystems penalize their deviation from the average demand and neither communicate with each other nor with the coordinator. The simple decentralized rule-based controllers fail to exploit storage flexibility in order to reduce the peak-to-peak variation in the aggregated profile. The distributed MPC achieves the performance results of the centralized MPC in some cases and always outperforms the decentralized implementation. Unfortunately, an investigation of the convergence properties of the distributed MPC algorithm is left for future work.
Many publications propose distributed control frameworks including single or multiple aggregators as interfaces between energy markets and the many subsystems. [TBS11] propose a hierarchical distributed MPC scheme where possibly multiple aggregators subsume a group of flexible consumers and steer them to achieve top level power balancing. Single aggregator settings and optimal electric vehicle charging have been studied in e.g. [MDP13] and [RWH+13]. The latter presents a decomposition to hierarchically coordinate between an aggregator and a fleet of electric vehicles based on ADMM. Objectives are minimum cost or valley-filling, i.e. charging when the aggregated load is low in order to prevent new peaks in the total electricity profile. A dual decomposition and ADMM are applied in [DVM14, DSM16] to coordinate heat pumps coupled to a simple thermal storage in a day-ahead optimization with respect to different local and global cost functions, no building dynamics are modeled. [HJP+13, HVP+16] propose hierarchical distributed MPC based on Douglas-Rachford splitting to coordinate thermal storage systems in order to achieve cost-minimal tracking of a predefined consumption profile the aggregator has committed to. [HVP+16] presents closed-loop MPC simulation results for exemplary second-order systems parameterized with time constants from a typical range of refrigerators and heat pumps.
[BFG+18] proposes a hierarchical distributed MPC algorithm based on ADMM for physically decoupled subsystems with a coupling in a shared objective function handled by the grid operator. Convergence is guaranteed for convex MPC problems, i.e. the minimization of (1.2) subject to constraints in (1.1) form a convex optimization problem. The size of the problem solved by the central coordinator can be made independent of the number of subsystems through an averaging procedure and the communication to the subsystems at each iteration reduces to a single vector of information transmitted to all participating systems. Case studies with simple models for residential battery systems investigate closed-loop valley-filling, operation with respect to a time-varying aggregate power grid constraint and islanding of a micro grid. The paper provides a mathematically rigorous treatment of the decomposition for linear time-varying dynamic systems and the thesis in [BFG+16] by the same author provides a proof of convergence adapted to the context of MPC. The author of this thesis has adapted the hierarchical distributed MPC algorithm from [BFG+18] to the setting of a cluster of residential buildings equipped with heat pumps in the publication in [KJC17b]. The objective is to flatten the electrical demand of the heat pumps, which adds to the non-flexible profile of remaining electrical loads, at minimum costs. In a closed-loop simulation study with 20 well insulated buildings, the variance of the aggregate demand profile is reduced by over 70% while the overall energy consumption increases by around 3%, since the buildings have to deviate from their local optimal schedules.

1.4.3 Distributed Coordination in Distribution Grids

Beyond simple limits on aggregate power capacities, the above works on distributed control do not consider operational limits of the distribution grid, i.e. topology, line flow and voltage limits are not taken into account in the problem statements. With respect to the contributions in

distributed control, this generally means that coupling is limited to a shared cost function or an aggregated variable constraint. A number of publications address power system constraints in distributed settings, e.g. [BGHL16] investigates decomposition approaches for the nonlinear AC optimal power flow problem to coordinate power exchange between control areas in a distributed MPC setting. Multiple methods exist to manage congestion in distribution grids, i.e. to alleviate line overloading or voltage issues related to the operation of DERs. [AHH12] gives a more generic discussion of grid capacity markets, capacity allocation or dynamic tariffs as strategies to coordinate high penetrations of electric vehicles in distribution grids. The review in [HWLN14] distinguishes between indirect ("market") and direct control methods for congestion management. The former includes all methods where a price signal is used to influence the operation of flexible loads, while the latter refers to measures exclusively taken by the DSO to directly access and manipulate controllable inputs in order to prevent blackouts. The authors suggest to DSOs to first make use of close to cost free direct methods (network reconfiguration, on-load tap changers, reactive power control), then to use market methods to achieve welfare optimal and feasible operation and finally to apply direct control of active power as a last resort, since significant losses in customer comfort are expected by the author. Several methods exist to establish a price on grid constraints in order to avoid congestion. The authors in [BASB12] propose a hierarchical distributed MPC to coordinate consumers grouped under different balancing responsible parties (BRP) with respect to simple line flow capacities in a distribution grid. The central optimization problem, initially formulated in [BSBA12] is decomposed based on dual decomposition and the communication takes place between the DSO and the BRPs in the form of shadow prices for each branch of the simple grid. Congestion management is also addressed in [NSB17], where a multi-level structure is proposed to coordinate BRPs, aggregators and flexible loads. Simple DSO line flow limits are considered in a neighbor-to-neighbor optimization. Lagrange multipliers of the dual decomposition are used in [MT13] to coordinate customers in a 24 hours day-ahead optimization with respect to three-phase nodal balance constraints, voltages are not considered. The authors suggest the use of ADMM as an alternative in case not strictly convex cost/utility functions are used. ADMM is used in [JAW14] to coordinate electric vehicles and heat pumps to reduce grid losses in a simplified distribution grid model neglecting voltages. The concept of distribution locational marginal prices (DLMP) introduces node specific congestion prices with respect to grid constraints. DLMPs are used in [LWO14] to coordinate electric vehicle charging between a DSO and an aggregator. The DLMPs are computed by the DSO in a central optimization including a DC power flow representation of the grid, i.e. the voltage is assumed to be constant 1 p.u. at all nodes for simplicity. The approach is enhanced in [HWO+15] to guarantee uniqueness of the solution in order to prevent divergence of the DSO and aggregator solutions. A case study includes a literature-based parameterization for a second-order dynamic model of a house with a heat pump. Line flow limits are the only grid constraints considered. The work in [HMG+17] extends the concept through a dual decomposition algorithm in order to compute the DLMPs in a distributed fashion while preserving privacy of the DSO and aggregators/customers. The formulation contains line flow limits and a test case with commercial building HVAC systems is presented. Demand uncertainty is treated in [HGM+17] with the introduction of day-ahead robust DLMPs and the resulting conservatism is alleviated with a real-time adjustment method.

In contrast to the simple power flow models used above, the full non-convex optimal power flow problem is solved by ADMM for varying degrees of decomposition (TSO-level, DSO-level, Microgrid-level) for different IEEE test grids in [LBD15], see also [LDB16]. Even though convergence of ADMM is not guaranteed for non-convex problems, the algorithm was found to converge for a certain selection of penalty parameters, suggesting applicability in practice. In [DZG13], a relaxed convex semidefinite programming reformulation of the non-convex optimal power flow

problem is solved with ADMM to coordinate multiple areas of unbalanced microgrids. In contrast to the iterative methods above, [WDCD14] suggests a one time information exchange heuristic including transformer and voltage limits (linear model) to coordinate electric vehicles in distribution grids.

1.5 Contributions

This thesis hopes to make a contribution to the approaches to coordinate residential prosumers equipped with electrical heat pump systems in distribution grids to enable sector coupling on a technological level. Gaps with respect to the optimal coordination and closed-loop operation of heat pump systems can be identified based on the previous literature review. Many works focus on the coordination of electric vehicles and heat pumps, but the full potential of flexible, electrified heating system operation is not addressed due to simple literature-based parameterizations or completely neglected building dynamics. In addition, closed-loop behavior is usually not investigated since most works focus on single open-loop or day-ahead optimizations. This concerns the efficiency of the multi-period operation of thermal systems but also the performance of the decomposition algorithm, which has to be sequentially executed at different time steps with updated measurements and predictions. Furthermore, distribution grid limits are only selectively addressed, i.e. voltages are neglected in works that have investigated distributed control schemes to coordinate heat pumps.
This thesis demonstrates how residential prosumers with electrical heat pumps can help to mitigate grid congestion and support voltage stability in low voltage distribution grids and simultaneously achieve both global and local level objectives. As a result, prosumers can still react to price differences on energy markets to minimize their costs, but only to the extent that a secure operation of the distribution grid is maintained. In order to show how the complete flexibility of the prosumers can be exploited to achieve feasible distribution grid operation and at what cost this is achieved, a hierarchical distributed model predictive controller is designed and simulated. Different thermal and electrical models with parameterizations typical for Germany are combined to facilitate the final simulation studies. The following contributions are presented in the scope of this thesis, references to previous publications of the author are indicated:

- **Prosumer Thermal Energy Models**:
  A **linear thermal building model** is developed to represent the most important dynamics of a residential single family house equipped with a floor heating system. The model is parameterized based on the German building typology and three different energy standards are implemented to represent the range of thermal behavior from old refurbished to modern highly insulated buildings. The model is validated against a reference model implemented in the complex energy simulation software EnergyPlus. The fourth-order model accounts for conductive, convective and radiative heat transfer mechanisms and predicts the zone temperature with satisfying accuracy. Furthermore, the dynamic response and the specific energy demand of the model are investigated. A first version of the thermal building model was presented by the author of this thesis in [KJC17a].
  A **heat pump model** based on manufacturer data is developed. The model maintains linearity of the thermal building model and results in a time-varying coefficient of performance, which depends both on the ambient and the supply temperature.
  A **domestic hot water demand model** is developed based on German time use survey statistics to model time series for hot water draws taken from a storage.
  An **internal gains model** is introduced to account for internal gains from occupants in the thermal building model. The same underlying time use survey statistics are used to achieve consistency in occupancy and user activity dependent time series.

- **Prosumer MPC for Energy Management**:
  A **model predictive controller** is designed for a prosumer including the above thermal models. The convex optimal control problem is formulated to minimize electricity costs and, if available, integrate local PV generation, while maintaining temperature limits to guarantee thermal comfort of the occupants. The controller is not aware of distribution grid constraints and is as such an exemplary implementation for a decentralized control architecture. A single building MPC design for a different and less complex building model was presented by the author of this thesis in [KJC16].

- **Distribution Grid Model**:
  A linear **power flow model** from the literature is used to model active and reactive power flows and bus voltages in distribution grids. The model is parameterized based on German reference distribution grids and the accuracy of the model is validated against a non-convex AC power flow simulation. Furthermore, the sensitivity of line overloading and undervoltages caused by coincident load behavior is investigated for five German reference distribution grids. The non-flexible residential electricity load is modeled through time series generated from a model presented in a previous publication of the author in [JKC15].

- **Hierarchical Distributed MPC**:
  A general **central MPC** problem formulation to coordinate multiple physically coupled dynamic systems is presented. The central control problem is decomposed based on ADMM to construct a scalable **hierarchical distributed MPC** architecture. The problem formulation is then adapted to the setting of a distribution grid hosting multiple prosumers equipped with heat pumps. Physical coupling exists through the residual loads of the prosumers causing power flows in the distribution grid. The grid operator functions as the top level central entity to coordinate the residual loads with respect to the distribution grid constraints. The final algorithm accounts for both local and global objective functions and constraints. Additional slack variables are introduced for distribution grid and prosumer constraints in order to guarantee feasibility of the overall optimization problem at all times. Finally, all distribution grid information remains in the domain of the DSO and any information regarding local prosumer cost functions, models and predictions (occupancy, temperatures) remains in the private domain of the prosumers. This contribution is an extension of the previous work of the author presented in [KJC17b].

- **Simulation Studies**:
  Finally, **three simulation studies** on voltage stability, valley-filling and community cost reduction through optimized self-consumption demonstrate the mechanism and effectiveness of the distributed MPC algorithm to coordinate the operation of prosumers or building energy management systems in a distribution grid online. The distributed hierarchical MPC algorithm allows prosumers to exploit their flexibility in order to minimize their local costs, but coordinates the operation when a global cost function has to be minimized or distribution grid constraints are violated. Closed-loop simulation results of the distributed MPC algorithm over one week are presented for all three studies including different building energy standards. A central MPC solution is computed as a benchmark to guarantee effectiveness of the distributed optimization algorithm. The change in costs due to coordination is investigated in a comparison with the uncoordinated reference operation of the prosumers. The effect of stricter voltage constraints on the required number of iterations to converge is investigated. A dynamic scaling algorithm for ADMM is applied to the problem of valley-filling with different weight factors in order to speed up convergence of the hierarchical distributed MPC.

1.6 Structure of the Thesis

Chapter 2 provides an introduction on the German residential building stock and heat pump scenarios to motivate the use of three different types of insulation standard for the buildings. Afterwards, the thermal building model is developed and validated, followed by the heat pump, domestic hot water and internal gains models. The prosumer MPC controller is designed in Chapter 3. The linearized power flow model is introduced in Chapter 4, including a short validation and its application to German reference distribution grids. The hierarchical distributed MPC algorithm is developed in Chapter 5 and finally validated in the three simulation studies of Chapter 6. Chapter 7 concludes the thesis and gives an outlook on future research questions.

Chapter 2

Building Energy Modeling

The second chapter first motivates the use of three different types of insulation standard for the representative residential building parameterizations used in this thesis. Afterwards a dynamic thermal building model is developed and validated, followed by the heat pump, domestic hot water and internal gains models.

2.1 German Building Stock and Typology

This section gives an overview of the German building stock and current regulative efforts to manage thermal protection. Possible future heat pump penetration scenarios are investigated and the shares of systems in buildings of different age analyzed in order to reduce the selection of representative building parameterizations worth considering in the context of this thesis.

2.1.1 Regulation and Status Quo of Thermal Protection

The European research project Typology Approach for Building Stock Energy Assessment (TABULA[1]) investigated the national residential building stocks in Europe with a harmonized approach to develop a comparable assessment for energy efficiency measures [LSDB15]. The typology is organized by age classes and further distinguishes between detached single-family (SFH), multi-family (MFH), terraced houses (TH) and apartment buildings (AB). A detached single-family house can contain up to two dwellings by definition. The periods of the typology were chosen with respect to the availability of statistical surveys, historical events and building regulations of relevance for thermal characteristics. A characterization of the periods is given in [LDSB12, LSDB15]. The first technical post-war regulation was introduced in 1952 with the norm DIN 4108. The first thermal protection ordinance (Wärmeschutzverordnung/WSVO) was issued in 1977 in response to the oil crisis and was amended twice in 1984 and 1995. The previous ordinance was replaced by the German Energy Saving Ordinance (EnEV) in 2002 to combine both the thermal protection and heating system ordinances. The EnEV defines the maximum annual primary energy demand and transmission heat loss for new buildings and refurbishments in the existing stock. It was updated several times to harmonize the national ordinance with the European energy efficiency directives. As a result, constructions built after 2009 must at least meet the requirements of the EnEV 2009, but may also face stricter requirements of the EnEV 2014/2016, depending on the year of construction. The new Gebäudeenergiegesetz (GEG) passed in 2020 combines the Energieeinsparungsgesetz (EnEG), which provides the legal authorization of the EnEV, and the Erneuerbare-Energien-Wärmegesetz (EEWärmeG), which defines requirements for the use of renewable energies for heating in buildings, in a single law to enforce standards for the so called nearly zero-energy buildings (nZEB). Germany will keep the current

[1] http://webtool.building-typology.eu

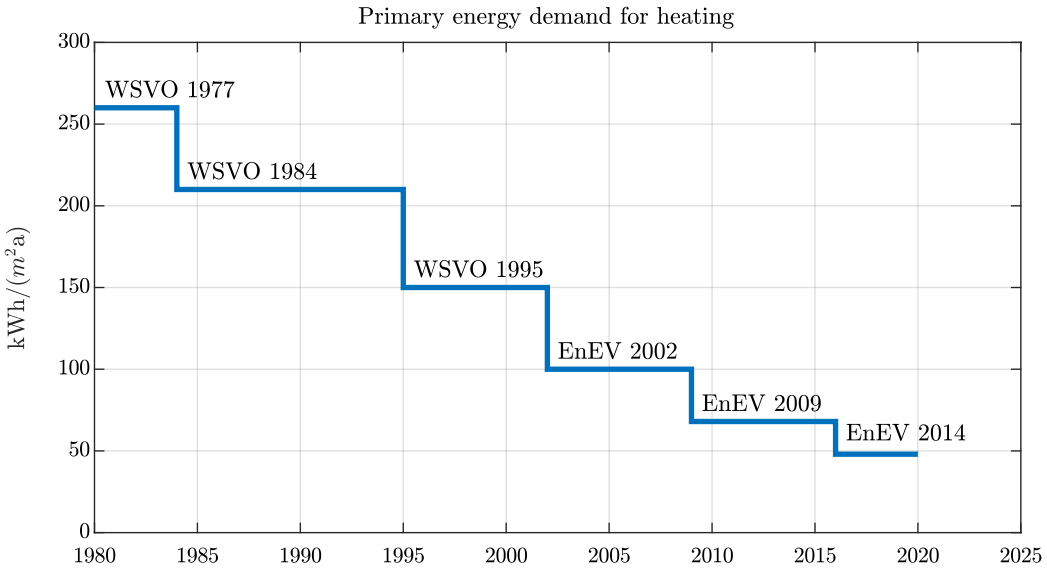

Figure 2.1: *Development of the maximum primary energy demand requirement for energy efficient construction in Germany. Drawing based on [Hau09].*

EnEV 2014/2016 requirements for future new residential buildings. Figure 2.1 shows the decrease of the allowed primary energy demand for heating in accordance with the development of the building regulation.
Figure 2.2 shows the distribution of building types for the German national building stock for constructions until the end of 2009. Approximately two thirds of all buildings (and the total residential living space) were constructed before the first thermal protection ordinance came into effect and thus were built without any requirement on the heating demand. With almost 10 million buildings out of 18 million in total, detached single-family houses represent 55% of all residential buildings. Approximately 63% of all SFHs were constructed before 1979, a third of them were constructed during the active period from 1958 to 1978.
Table 2.1 shows the status of the thermal insulation among German SFHs. Latest survey data from [CD18][2] reveals that the share of old buildings (before 1979) with a thermal insulation is below average for all components, with less then 50% of them having an insulated outer wall. The quarter of new buildings (after 2009) without an outer wall insulation can be explained by brick insulation, which could not be identified by the survey [CD18]. The values in brackets state the share of single- and two-family (TFH) houses which received the insulated component after the construction of the building. Some older buildings were initially equipped with insulated components which not necessarily resulted in a better thermal insulation compared to constructions of that time. The numbers show how the majority of older buildings with an insulated component received the update in later years. An exterior insulation is the dominating measure among insulation options for the outer wall. The quality of the insulation is measured by the thickness of the insulation layer. The shares of layer thicknesses below 10 cm in buildings before 1979 account for almost two thirds, half of that share is contributed by thicknesses up to 5 cm only. In contrast, two thirds of the buildings constructed after 2009 have a minimum outer wall insulation of 14 cm [CD18].
The authors of [CD18] estimate the annual area-weighted refurbishment rates for the German building stock over the period from 2010 to 2016. The building stock's total area at the end of

[2]The survey from 2016/2017 was based on questionnaires sent out to building owners and resulted in 17,000 building profiles.

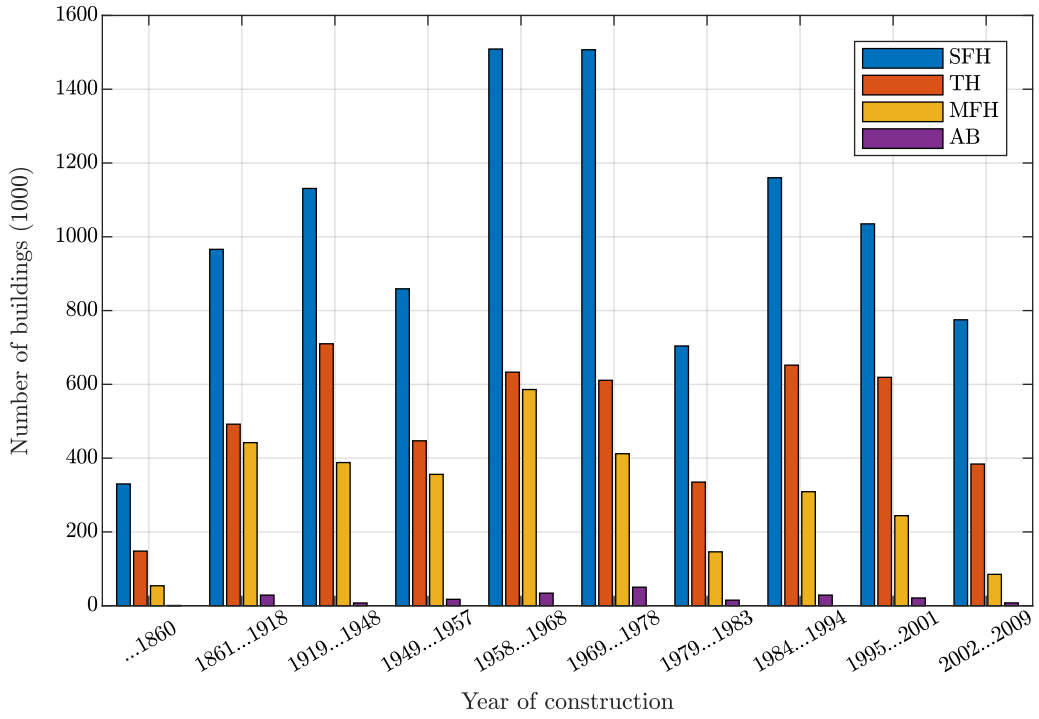

Figure 2.2: *Distribution of the German national residential building stock based on data from [LSDB15].*

2016 is used as a reference and the results represent a total refurbishment rate per year with generalized weights for the outer wall, roof, ground floor and windows as 40%, 28%, 23% and 9% respectively.[3] The refurbishment rates are approximated as 0.99% per year for the area of all buildings and 1.43% for buildings constructed before 1979. The German Energy Agency (DENA) criticizes the low rate and demands a doubling of the refurbishment rate for the whole building stock to reach the national targets in terms of energy policy. Special emphasis should be put on buildings constructed before 1979 [DEN18a].

Table 2.1: *SFHs/TFHs with thermal insulation, data from [CD18].*

	Outer wall	**Roof/upper story ceiling**	**Floor/basement ceiling**
	Share of SFHs/TFHs with the insulated component (Share of SFHs/TFHs which received the component's insulation after construction)		
All buildings	49.6% (22.8%)	84.3% (39.0%)	41.1% (10.8%)
Before 1979	43.8% (35.1%)	76.9% (59.1%)	26.2% (16.3%)
After 2009	76.6%	97.9%	83.4%

[3] This rough approximation is used to combine individual component measures, the area-weighting might differ within the building groups of different construction periods, see [CD18].

2.1.2 Residential Heating by Energy Carrier in Germany

The left bar chart in Figure 2.3 shows the shares of energy carriers for residential heating by age class and the situation for existing SFHs/TFHs. Heating by natural gas dominates in buildings constructed before 2010, followed by oil. The situation is similar for single- and two-family houses. The majority of residential buildings constructed after 2009 have natural gas- or electricity-based heating, followed by biomass and district heating. The high share of electricity-based heating in new buildings is attributed to electrical heat pumps. In 2015, a third of all new build SFHs in Germany were equipped with heat pumps [Fed16]. Besides remaining electrical night storage heaters from the 1950s and 1960s, heat pumps are the most frequently appearing electro-thermal technology. Electricity-based heating accounts for 6.9% among all single- and two-family houses, with 3.7% for heat pumps and 3.2% for night storage heaters and other direct electric heating [CD18].
The right bar chart in Figure 2.3 shows that natural gas also dominates as the energy carrier chosen after a refurbishment of the heating system in the existing residential building stock. Still, around a fifth of the buildings constructed before 2010 are upgraded with oil-based heating. Electricity as an energy carrier for residential heating plays only a minor role in refurbishment of the heating system in older buildings. The average annual heating system refurbishment rate of all residential buildings measured over the period from 2010 to 2016 was 3.05%. A similar rate of 3.09% was found for SFHs and TFHs. Buildings constructed before 1979 were slightly more likely to receive an upgrade compared to buildings constructed after that period (3.27% vs. 2.69%) [CD18].

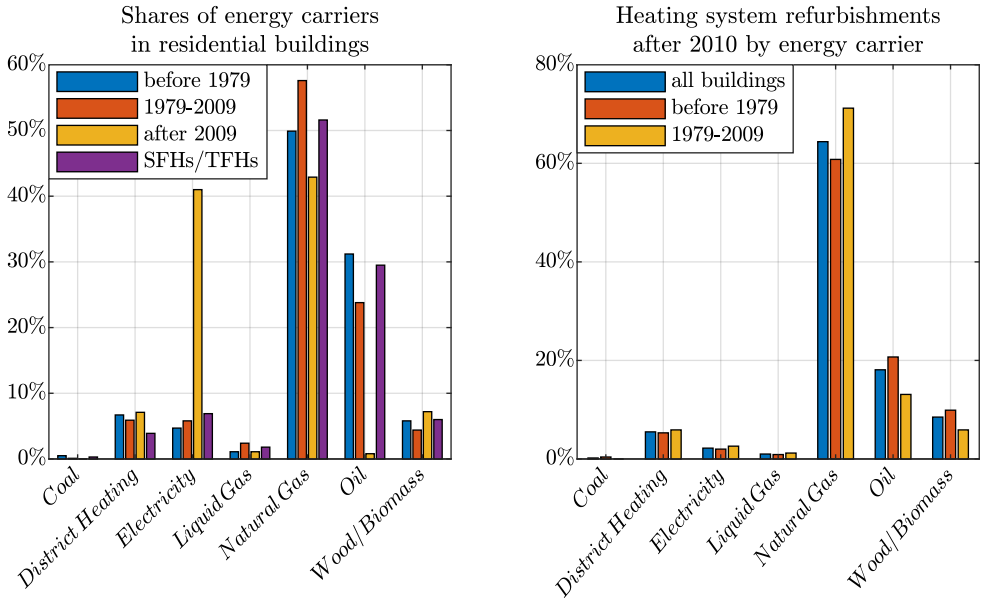

Figure 2.3: *Shares of energy carriers in the existing residential building stock and chosen energy carriers after heating system refurbishment, data from [CD18].*

2.1.3 Heat Pump Penetration Scenarios

Based on the statistics of the national building stock and average refurbishment rates, four simple penetration scenarios for heat pumps are developed to better estimate their possible relevance for the energy system up to the year 2050.

Building Stock Update Until 2020

[Fed18b] states 15.7 million residential buildings exist with one or two flats by the end of 2017.[4] New constructions in this category from the period 2010-2017 account for a total of 5%. Assuming a split of the existing building stock of SFHs constructed before 2010 with a ratio of two to one, the total distribution in 2017 can be approximated as 63%, 32% and 5% for constructions before 1979, between 1979-2009 and between 2010-2017. Statistics from [Fed16, Fed18a] are used to adjust the national building stock distribution for single-family houses by new constructions and demolitions up to 2020. The average annual rate of new constructions is assumed to be 1% of the residential building stock. Building demolitions are assumed to be 0.1% for the residential building stock per year and are equally distributed over the oldest buildings constructed before 1979.

Heat Pump Stock Update Until 2020

The study in [Int17] analyses the heat pump sales for space heating applications until 2016 and estimates that 94% of all systems are installed in residential buildings and a further 96% of those in SFHs. The resulting cumulated heat pump sales from 1990 to 2017 leads to an estimate of 690.000 systems. Calculating with the upper end of the range of shares of electrical heat pumps per age category from [CD18] results in 640.000 systems when applied to the building stock estimation presented above, which is close to the presented sales estimation. The overall share of heat pumps in SFHs in 2017 results in 4%, which is in proximity to the statistical value of 3.7% measured for the 2016 survey in [CD18]. The heat pump stock is updated until 2020 under the assumptions for demolitions and new construction as described above. An annual refurbishment rate of 1.5% is assumed for buildings constructed before 1979 and a rate of 1% for buildings from 1979-2009 ([CD18] states 1.43% for old buildings and 0.99% for all buildings).
A building refurbishment is assumed to be required for a heat pump installation since the majority of old buildings has a poor insulation standard, as was shown in Table 2.1. Older buildings usually have relatively high design heat loads together with high supply temperatures as a consequence and thus fail to meet the requirements of low-temperature systems. According to [Bru06], common refurbishment options are better thermal insulation, glazing and ventilation systems with heat recovery, which result in lower required supply temperatures and a possible utilization of radiators if a new installation of a floor heating system is not an option. Modern radiators achieve a higher heat transmission per area compared to older systems from the 70s and 80s. A reduction of the supply temperature from 70 °C to 60 °C is possible. Buildings from the 90s already have a better insulation standard, and common refurbishment measures are the increase of the heating surface or the installation of a heat recovery system, since ventilation losses are dominant in well insulated buildings. Finally, air-to-water heat pumps are a popular option for updates in the existing building stock since they can be installed outside or inside a house and their installation is often less difficult and restricted than for water- or ground-source heat pumps [Bru06]. In a study on heat pump implementation scenarios in Europe, [BOB+13] expect a growing market for heat pumps in Germany and assume an increasing share of air-to-water heat pumps to up to 59% of total annual heat pump sales, due to relatively low investment costs and limited available space for ground-source heat pumps. The German industry association for heat pumps estimates the share of air-to-water heat pumps to be over 70% in 2030 [Bun15].
[CD18] provides statistics for the percentage of refurbishments per age category and the share of heat pumps in heating system upgrades per category. To account for the higher share of heat pumps in a heating system upgrade after a refurbishment of the insulation, 2.5% of the

[4] In accordance with the federal statisctics, a SFH is defined as a residential building with up to two flats in the remainder of this section.

Table 2.2: *Heat pump penetration scenarios.*

	Building stock development [%/a]			**Chance of HP installation [%]**		
	Demolition	Refurbishment	New	After ref./new		
	(-1978)	(-1978)/(1979-2009)	(2020-)	(-1978)	(1979-2009)	(2020-)
Baseline	0.1	1.5/1	1	2.5	5	33
HP	0.1	3/2	1	33	33	50
HP+	0.1	3/2	1	50	50	100
HP++	0.1	3/2	1	100	100	100

refurbished buildings before 1979 are assumed to receive a heat pump and 5% of the buildings from 1979-2009 to match the overall heating system refurbishment statistic. Younger buildings from that category might allow for a heat pump installation without a refurbishment, but their share is rather small according to Figure 2.2, which justifies this assumption. Finally, 33% of all new buildings (2020-) are assumed to be equipped with a heat pump.

Scenarios 2020-2050

After year 2020, the development in the SFH stock is projected until the year 2050 and examined every 10 years. From 2020 to 2050, four different scenarios are considered: Baseline, HP, HP+ and HP++. The annual rates for demolitions, refurbishments and new constructions and shares of heat pump systems remain at the values assumed until 2020 in the baseline scenario. 2020 is the reference year.

Scenario HP is characterized by an equal share of 33% for both heat pump installations in buildings after a refurbishment of the building envelope (-1978, 1979-2009). The share in new constructions (2020-) is assumed to be 50% (44% for 2018 stated by the German industry association for heat pumps [Bun19]). In addition, the refurbishment rate in the old existing building stock is assumed to increase to 3% and 2% per year. Finally, the scenarios HP+ and HP++ describe an ambitious and an extreme penetration scenario, with heat pumps being chosen in 50% (100%) of the cases for old buildings and 100% (100%) in new buildings. Buildings constructed during the period 2010-2020 are assumed to neither be demolished, nor to receive a refurbishment of the insulation or heating system. Thus, the number of heat pumps from that period is assumed to remain constant until 2050.

Figure 2.4 shows the development of the stock of SFHs for the scenarios Baseline and HP (equal to HP+/++, same building stock development). In both scenarios, demolitions lead only to a slow reduction of the number of old buildings constructed before 1979. New buildings are constructed according to the nearly zero-energy standard and already outweigh the constructions from 2010-2020 with a standard complying with the EnEV 2009 or better in year 2030. The relatively high annual rate of new constructions leads to a net growth in the SFH stock. Buildings constructed after 2010 account for approximately 30% in 2050. By that time, less than half of the buildings constructed before 2010 have been refurbished in the Baseline scenario. In contrast, only a small number of buildings without a refurbishment remains in 2050 in scenarios HP/+/++, due to the increased refurbishment rates.

The share of heat pumps in SFHs changes with the building stock, as shown in Figure 2.5. The Baseline scenario leads to a share of heat pumps of 13% in 2050. The majority of the systems is installed in modern buildings constructed after 2020. The share increases to 35% in 2050 in the scenario HP, where heat pumps in older buildings (-2009) account for almost two thirds of that share, driven by the increased refurbishment rate and higher share in system choice.

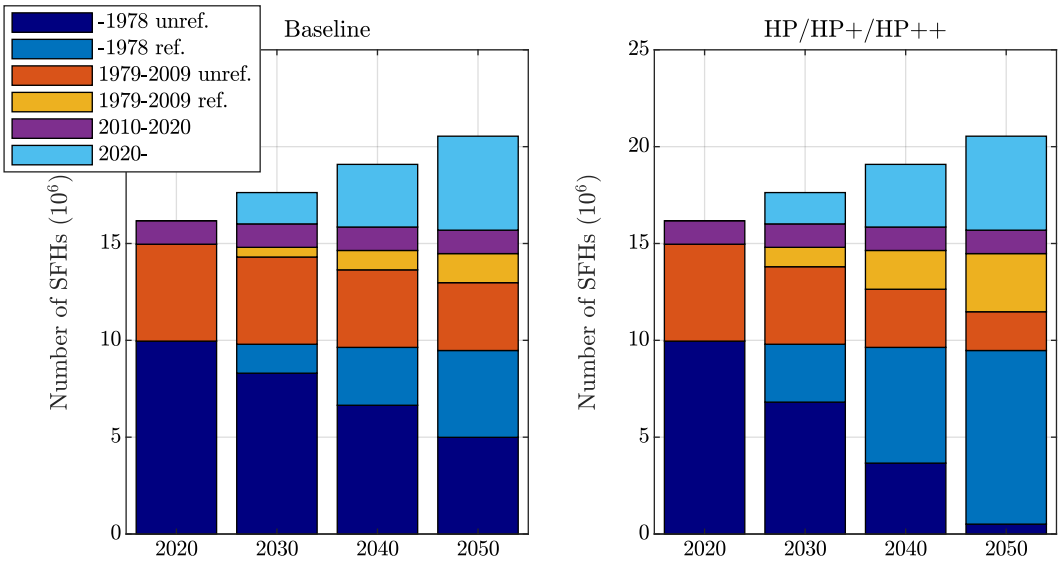

Figure 2.4: *Development of the German SFH building stock in the scenarios Baseline and HP/+/++, distinguished by shares of refurbished and unrefurbished buildings.*

The ambitious scenario HP+ leads to a high share of heat pumps in SFHs with almost 60%. Both, heat pumps in modern buildings and in old but refurbished buildings dominate the pool of systems. While a heat pump is installed in every fourth SFH in 2040 in scenario HP, this share is reached 10 years earlier in scenario HP+. The scenarios show that significant shares of heat pumps are not likely to occur if the current statistics are assumed for the projections. In contrast, an extreme heat pump penetration rate of 86% in all SFHs can be achieved in 2050 in scenario HP++, where the system of choice is always a heat pump. In such a scenario, over two thirds of all heat pumps are located in old refurbished buildings (-2009). The range of heat pump shares in 2050 is similar to results from the literature.

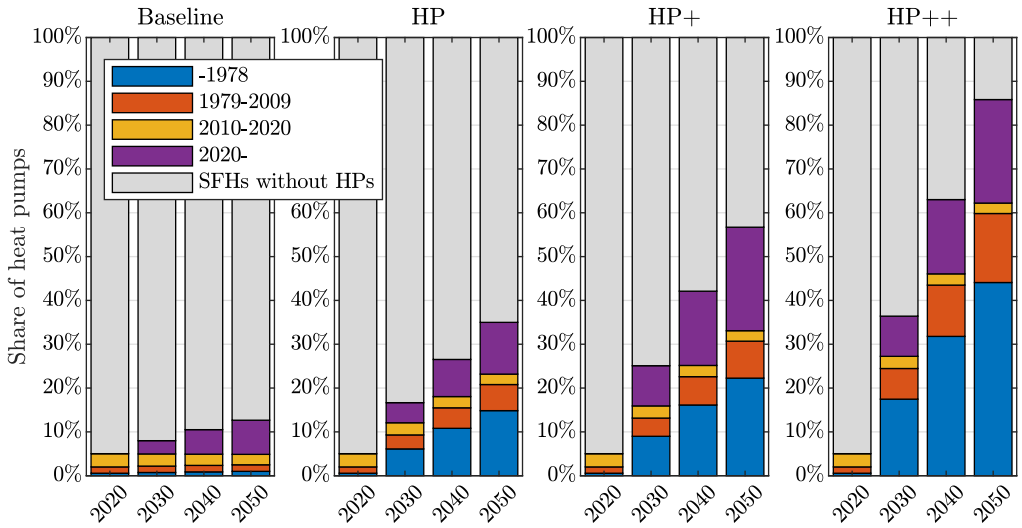

Figure 2.5: *Heat pump penetration in the scenarios Baseline, HP, HP+ and HP++.*

The study [HP15] published by Fraunhofer ISE estimates a share of heat pumps in the whole building sector ranging from two-thirds to 90% in all considered climate policy scenarios for 2050.

The BDI study in [BDI18] estimates a heat pump share of 70-80% in SFHs in their scenarios. Figure 2.6 shows the resulting total numbers from the presented scenarios with estimates from the studies in [Fra17, DEN18b, BDI18] and the 2030 sales estimate of the German industry association for heat pumps [Bun15]. Values from the literature state heat pumps for the whole residential building sector or the whole building sector in contrast to the SFH focus of the scenarios in Table 2.2. All considered studies from the literature achieve a 95% reduction of the 1990 levels of GHG emissions by year 2050. Feasible scenarios result in a total number between 7 and 17 million systems in 2050, today's amount of systems increasing nine to twenty-fold. Even the technology mix scenario (TM95) from [DEN18b], which is an alternative to the strong electrification scenario (EL95), results in a high number of heat pumps compared to today. The importance of increased refurbishment rates and incentives for heat pump installations is obvious. Also a substantial amount of heat pump systems must already be installed in year 2030 to maintain the 95% reduction paths with given refurbishment rates, resulting in a four- to a tenfold increase of the number of systems within the next decade.

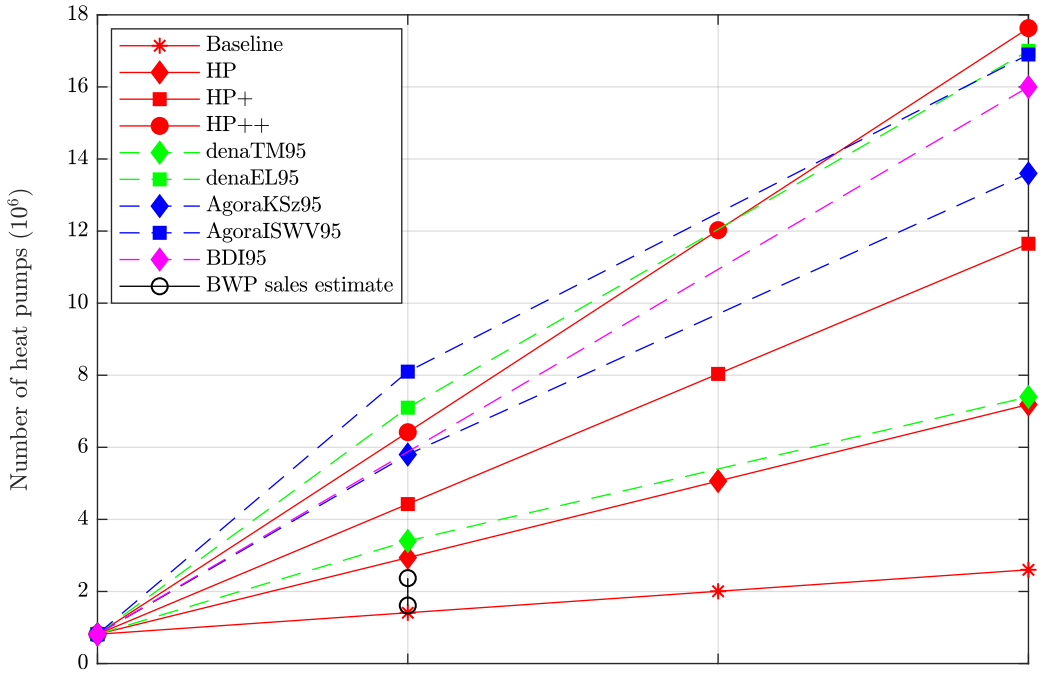

Figure 2.6: *Projections of the total number of heat pumps in the German building sector from different studies with a 95% GHG emissions reduction target in 2050. Details of the scenarios Agora, dena and BDI are given in [Fra17, DEN18b, BDI18].*

In summary, scenarios with high penetration rates will only be achieved through higher refurbishment rates and stronger incentives to install a heat pump. Financial incentives can be given by market incentive programs for subsidies or changes in price structure of different energy carriers. The German heat pump industry explains the current stagnation in heat pump sales with high tax-induced prices for electricity compared to the prices for gas and oil [Bun15].

2.1.4 Building Type Selection for Thermal Models

Based on the previous sections, relevant building types are selected from the TABULA typology to create realistic scenarios of buildings equipped with heat pumps. The typology is used as a

starting point to generate representative datasets to parameterize the building models used in this thesis. A representative building description is given for each building type.
In general, each identified building type of the TABULA typology is described in three variants to account for different levels of refurbishment or standards of construction. All variants specify exemplary compositions of components of the building envelope (outer walls, floor, roof, window, door) and their overall value of thermal transmittance per square meter (U-value). The first variant describes the *existing state (1)* with respect to the building regulation when the building was constructed. The variant *usual (2)* refurbishment reflects the minimum requirements for refurbishments according to the regulation of the German Energy Saving Ordinance. This is currently the EnEV 2009 since the following ordinances did not tighten the requirements for refurbishments substantially. Finally, variant *advanced (3)* reflects ambitious refurbishments or new buildings to achieve a low energy or passive house standard.
The TABULA study assumes electrical heat pumps as a heating system option in the usual refurbishment variant for all SFHs constructed before 1995 and as an option in the existing state for SFHs constructed after 1995. The authors in [TBSH15] argue, that in general only buildings constructed after 1995 should be considered as realistic candidates for heat pumps to supply low-temperature floor heating systems due to otherwise high design heat loads and supply temperatures. However, the authors consider SFHs from the period 1958-1968 for floor heating after a refurbishment to represent old buildings in their analysis.
A selection from the TABULA types and refurbishment variants has been made to limit this thesis to few representative and meaningful building types. In accordance with the categorization of the previous section, types to represent buildings constructed before 1979, 2010, 2020 and after 2020 are selected. A possible selection is summarized in Table 2.3 with exemplary space heating demands from the TABULA typology and resulting U-values of the components. Three out of the four selected types are chosen in the minimum viable standard for a heat pump with floor heating to not underestimate the load impact on the power grid. The generalized modeling approach for a single zone building equipped with underfloor heating and a heat pump system is always the same, independent of the building type selected. Details are given in Chapter 2.2.

Table 2.3: *Selection of building types and refurbishment variants based on the TABULA typology*

Building type	***E*** SFH.05	***J*** SFH.10	***K*** SFH.11	***L*** SFH.12
Period	1958-1968	2002-2009	2010-2015	2016-
Refurbishment	usual (2)	existing state (1)	existing state (1)	advanced (3)
Net heating demand [kWh/(m^{2}a)]	133	80.9	72.8	21.1
		U-value [W/(m^{2}K)]		
Outer all	0.23	0.30	0.24	0.11
Inner wall	2.33	0.36	0.36	0.36
Floor	0.31	0.28	0.35	0.13
Roof	0.42	0.25	0.22	0.11
Window	1.30	1.40	1.10	0.70
Door	1.31	1.99	1.75	0.80
Thermal bridges	0.1	0.05	0.05	0.02

Building type ***E*** in the variant of usual refurbishment is chosen to represent old existing buildings with improved but not ambitious thermal properties due to additional insulation and replaced windows. The type can be seen as a conservative, minimum example for measures to be taken

to meet requirements by a modernization complying with the EnEV 2009. Depending on the incentivisation for refurbishments in old buildings and the efficiency of refurbishment measures, the implemented standard might be better in future years. The authors of the study in [BDI18] assume a total space heating demand ranging from 45 to 75 kWh/(m²a) for the average refurbished SFH in their scenarios until 2050. ***E***(2) is kept as a worst-case implementation for an old but refurbished SFH.

Types ***J*** and ***K*** represent newer SFHs constructed before and after the EnEV 2009/2014 which fulfill only the required minimum standard. While the space heating demand of a building constructed (and calculated) according to the EnEV 2002 should be below 70 kWh/(m²a), typical implementations from the building praxis can result in the range from 75 to up to 120 kWh/(m²a). The difference mainly results from different boundary conditions assumed for heating and larger approximated heated areas in the EnEV [Log02]. Since type ***K***(1) has rather similar thermal properties compared to type ***J***(1), this parameterization is neglected in the upcoming analysis.

Building type ***L*** represents new constructions in an advanced standard with an airtight envelope and a mechanical ventilation system including heat recovery. This building type is comparable to a nearly zero-energy building. The nearly zero-energy building (nZEB) standard was introduced by the European Union with the directive 2010/31/EU and defines a nZEB as a building that requires (almost) zero energy, largely covered by local production of renewables [The10]. A possible interpretation of the new standard was developed in the European COHERENO[5] project. The status of a nZEB can be achieved by refurbishment if the new primary energy demand is below 40 kWh/(m²a) and the building envelope has a maximum overall transmission heat loss of 0.28 W/(m²K) [DEN]. Numerical requirements for new constructions are likely to be defined according to the funding standards used by the KfW funding bank to incentivize new constructions which achieve primary energy demands below the current legislative requirement. The KfW efficiency house 40 would be considered a nZEB [LSDB15].[6] The next better standard, not yet defined but often considered a passive house, requires a further reduction of the demand from below 25 kWh/(m²a) for the KfW 40 house to a demand below 15 kWh/(m²a) [BDI18].

Several measurement campaigns carried out by Fraunhofer ISE investigated the performance of heat pumps in both the older building stock and new buildings. New single-family houses were mainly equipped with floor heating systems, older buildings often used radiators or combinations of both systems. Figure 2.7 shows the range of seasonal performance factors (SPF)[7] and space heating demands for a sample of heat pump systems in modern and old buildings monitored in the Fraunhofer projects *WP Monitor* and *WPsmart im Bestand*, the majority equipped with floor heating. Modern systems (2006-2011) before and after the EnEV 2009 often achieve specific annual space heating demands below 75 kWh/(m²a), while demands in old buildings (1930-1992) are often above 100 kWh/(m²a) when no or only a partial refurbishment was carried out. The project *WP im Bestand* measured 73 buildings constructed during the period 1919-1996 in the years 2008/2009 after old oil heating systems were replaced by a heat pump. A building refurbishment was not a necessary requirement. The average total demand including space heating and domestic hot water was 177 kWh/(m²a), ranging from 85 to 340 kWh/(m²a) depending on the standard of insulation. Air-source heat pumps achieved an average SPF of 2.6 compared to a SPF of 3.3 for ground-source systems [RMP+10]. Currently, the measurement campaign *WPsmart im Bestand* is carried out to reinvestigate the performance in the old building stock. The projects *WP Effizienz* and *WP Monitor* monitored heat pumps installed in

[5] COHERENO: Collaboration for housing nearly zero energy renovation.

[6] The KfW grant program incentivizes constructions which outperform the current efficiency standards. The efficiency house 40 has a 60% lower primary energy demand than the reference building. Even though the EnEV 2016 is currently in force, the grant program's reference level of requirement is defined by the EnEV 2009.

[7] The SPF is defined as the ratio between heating energy provided by the heating system to the electrical energy supplied to it.

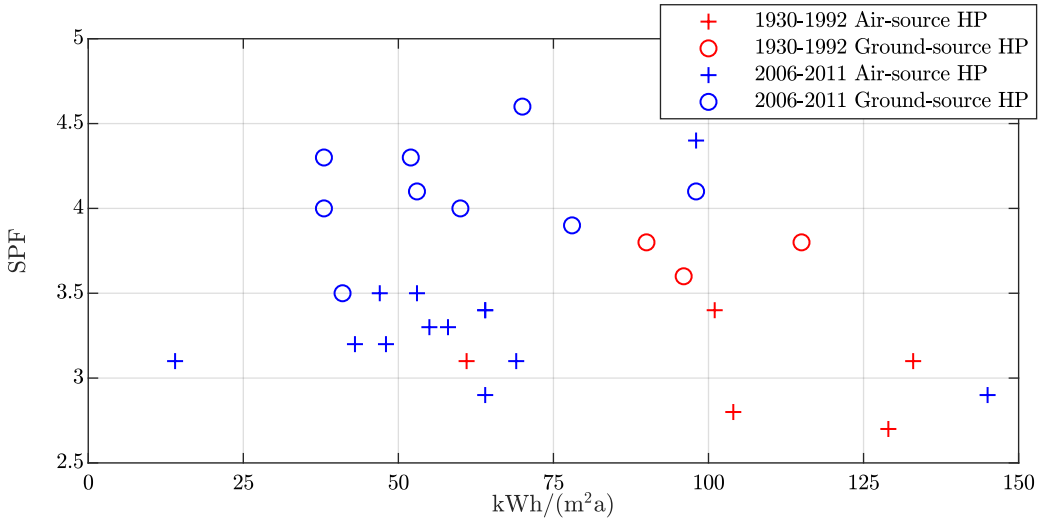

Figure 2.7: *Seasonal performance factor (SPF) and space heating demand from field measurements, data from [Fra13, Fra18].*

the years 2006/2007 and 2010/2011, respectively. The average space heating demand for 90% of the 87 systems in 2013 was 69 kWh/(m²a), with a range from 29 to 127 kWh/(m²a). Including outliers, the average demand increased to 78 kWh/(m²a) with the worst system demanding 202 kWh/(m²a). The SPF for air-source heat pumps was 3.1 (range: 2.3-4.3), with younger systems achieving a slightly better performance of 3.2 (2.5-4.3) compared to the older systems 3.0 (2.3-3.5). The same was observed for ground-source systems with an average SPF of 4.0 (3.0-5.4), 4.3 (3.5-5.4) for newer and 3.9 (3.0-5.1) for older systems [MGK+11, GML+14].
To conclude, a realistic range of space heating demands in old and new SFHs can be represented by the selected TABULA types. With the exception of building type ***K***, which has very similar thermal properties to type ***J***, do the remaining types represent the possible range from rather weakly refurbished buildings to advanced modern constructions that are not yet defined as a required standard.

2.1.5 Conclusion

Around two thirds of all German SFHs were constructed before the first thermal protection ordinance with no restriction on the space heating demand. In addition, those buildings have often not or only weakly been refurbished. A doubling of the current annual refurbishment rate is required to meet the national targets on carbon emissions. While natural gas is first choice as heating system energy carrier in old and refurbished buildings, electricity-based systems like heat pumps have already a share of over one third in new build SFHs. The investigation of possible heat pump penetration scenarios in the future shows that an increase of today's less than a million heat pumps to 7 to 17 million systems is required in scenarios aligned with Germany's carbon emission targets. Heat pumps in older buildings will have a significant share in all scenarios and years, except the Baseline scenario. The total share of heat pumps and the age of the supplied buildings in a local neighborhood will heavily depend on the type of residential area. New areas of development will lead to high shares of heat pumps in nearly zero-energy buildings, whereas existing residential areas might face substantial shares of heat pumps to supply old refurbished buildings.
Representative buildings have been selected from the TABULA typology as a starting point for the single building parameterization and modeling approach presented in the next section. The

approach is not restricted to the building types identified in Table 2.3 and can be extended to any typology as long as the necessary set of parameters is available.

2.2 Thermal Building Model

Single zone resistance and capacitance models are created in this thesis to capture the thermal dynamics of a single building. The thermal building physics depend on the construction, component materials and thermal gains from the heating system, disturbances and occupants. By modeling the building itself as a dynamic system, one is able to exploit the thermal storage in the thermal mass of the construction in addition to water-based storage tanks of the heating system in a control strategy. The low-order model is a compromise between the accurate representation of the most important dynamics and the computational costs to solve the system's progression in time. Due to the limited complexity of a single building, multiple models can be used to represent an aggregation of buildings in a neighborhood in a bottom-up approach. The program is implemented in MATLAB[8] and a set of ordinary differential equations for a single building is returned for controller design. It is favorable to use a discretized linear system representation in a convex optimal control problem since convex optimization problems can be solved efficiently for global optimal solutions by a range of algorithms [BV04][9]. Convexity of the resulting problem is further motivated by the convexity requirement for convergence of to the distributed optimization algorithm presented in Chapter 5.1.

2.2.1 Literature Review

A variety of tools exists for the detailed transient simulation of physical processes in building zones, construction and heating system components. The paper [CHKG05] provides an overview over key features of twenty major building energy performance simulation programs such as EnergyPlus[10], TRNSYS[11] or IDA ICE[12], among the possibly hundreds of tools developed over the last decades. A high level of detail, such as three-dimensional time-dependent temperature distributions in components, comes at the cost of a high effort for parameterization and computation. The authors of [KR07] classify three main categories of techniques to model the transient heat transfer in physical models. The techniques differ in possible spatial and temporal resolution, necessary input data and computational cost. As the first technique, the solution of the heat transfer equations can be found through methods from computational fluid dynamics, e.g. finite difference, volume or element methods, often used in software mentioned above. As a second approach, model reduction techniques reduce the model complexity of reference models to achieve similar accuracy at less computational cost, but lack generality due to the limitation to the reference they relate to. In district or city quarter energy simulations a model must be applicable to a range of instances of buildings with limited information for parameterization. For such applications, within the third category of so-called simplified models, low-order thermal network models are first choice and a good compromise [KR07, LTF+14]. Composed of thermal resistances and capacitances (RC), such RC-models result in circuits that represent the thermal behavior in analogy to electrical circuits. Their use is motivated by

- limited input data requirement for parameterization,

[8] www.mathworks.com

[9] A convex optimization problem requires a convex cost function, convex inequality constraint functions and affine equality constraint functions [BV04].

[10] https://energyplus.net/

[11] https://trnsys.de

[12] https://www.equa.se

- best option for generality,
- sufficient accuracy w.r.t. temperature and energy demand predictions,
- simplicity of the modeling approach (one-dimensional heat transfer) leading to a set of few, often first-order linear differential equations and thus
- low computational cost.

Simplified models as such can be further distinguished in white-, grey- and black-box models [KvS12]. RC-models completely parameterized on physical principles are referred to as white-box models, since their structure and parameters allow for a physical interpretation. In contrast, black-box models such as neural networks provide an input-to-output relationship without its components (e.g. the hidden layer) giving direct physical meaning. No prior system knowledge is required. Grey-box models lie between white- and black-box models. Their model structure can be derived from knowledge of physics like in white-box models, but the model parameters are result of an identification process using measured data, see e.g. [MH95,BCC+11]. The results allow for direct physical interpretation where parameters have a physically determined counterpart. Further details on grey-box models as part of hybrid approaches, besides white-box and purely data-driven approaches, are given in [AH16].
In a review paper from 2012, the authors [KvS12] state a decreased interest in simplified models due to the rapid increase of computational power allowing for higher model complexity. However, in the research communities of control and energy system optimization, simplified models are widely applied to represent thermal systems. Especially grey-box models are used in optimal model-based control to achieve sufficient paramterizations from experimental data, see e.g. [Wim04, Bia06, BCC+11, HGP12a, HGP12b]. Identification processes can be automated and may require less expert knowledge compared to white-box modeling. This is of particular interest in model-based control, where projects have shown that the modeling task can take between 55 and 80% of the total time spent on modeling, controller development and communications & signal processing tasks in practice [CGŠ+13]. While there might be experimental data available for single buildings, sufficient data of multiple buildings on district level are usually not available. The authors of [RDS14] circumvented this issue by creating Modelica[13]-based emulator models to generate time-series for later identification of low order grey-box models. The detailed reference models were partially parameterized from data sets of the Belgian TABULA typology. One of the low-order models was later replicated with varying user behavior in an aggregation model to represent 100 buildings performing demand side management with heat pumps [PH14]. In a further study in [PBA+15] the models were scaled and used to assess demand and supply side interactions in a national power market model. To conclude, in absence of experimental data RC-network models can either be directly parameterized from data sheets or derived from more detailed reference models implemented in simulation environments.
Since multiple thermal zones or walls are often summarized in one representative element in RC-models to reduce the model's complexity, they are also referred to as lumped parameter models [RGEC13]. In the maximum reduction case, a lumped model results in a single capacitance model with only one time constant. The grey-box model study in [MH95] suggests at least two capacities to capture short and long-term variation in the room air of a residential building supplied by electrical heaters. A similar observation was made in [LMB12] for HVAC supplied zone models, where a second-order model reproduced the thermal behavior almost as accurately as the 13th order reference model. A model predictive controller for a single family house supplied by a heat pump was successfully demonstrated with fitted second- and third-order models

[13] https://www.modelica.org/

in [Wim04, Bia06]. The authors in [RDS14] concluded that models of similar structure can be used for different types of SFHs.
Since experimental building data is not available for the range of possible building types introduced in Chapter 2.1.4 and it is not intended to create complex reference simulation models for each type to generate simulated data, this work uses white-box simplified low-order thermal network models. The models are parameterized with representative material and construction data from the TABULA typology. In a second step, the general white-box modeling approach is validated and refined against two exemplary implementations in EnergyPlus.
In a publication from 1972, Rouvel developed representative white-box RC-models for walls and thermal zones. The simplified models reproduced the thermal behavior with satisfying accuracy, even for multi-layer, asymmetrically loaded walls exposed to excitations from non-sinusoidal temperatures or impulse-like heat gains [Rou72]. Similar, well established first and second-order thermal network representations of whole buildings are described in the international standard ISO 13790 [DIN08] and German guideline VDI 6007 [VDI15b], the latter based on the approach from [Rou72]. Since the VDI 6007 offers a validated approach for transient simulations and has been successfully applied to works in the field of district or urban scale energy analysis (see e.g. [FLTM12, LTF+14, LBL+14]), the approach in [Rou72] is used as a starting point to model individual components of the building model in this work. The resulting fourth-order building model created for this thesis is a compromise between model complexity and the possibility to validate single component surface temperatures. Especially the floor heating system in exchange with it's surrounding can be addressed separately. Obviously, the latter is not possible with the lumped first- or second-order models in [DIN08, Rou72, VDI15b]. In contrast to the solution procedures applied there, in this thesis a state-space model is derived from the RC-model for application in a discrete-time optimal control framework.
The first implementation of the author's fourth-order model was published in the conference paper [KJC17a]. A first validation of the initial model and it's variants against reference simulation models for types J and L in EnergyPlus was documented in the master's thesis in [Kun17] and published in [KKL18]. After a short introduction to standard heat transfer modeling approaches applied here, different variants of the RC-model used in this thesis are defined and validated w.r.t. the accuracy of temperature and heating demand predictions. The temperature predictions are validated for types J and L in accordance with the available reference data from EnergyPlus simulations.

2.2.2 Mechanisms of Heat Transfer

Heat transfer is the transport of thermal energy due to a temperature difference between two thermodynamic systems. Three heat transfer mechanisms are distinguished, namely transfer by conduction, radiation and convection. The following paragraphs are based on [BS11], where the heat transfer mechanisms are discussed in detail.
The total heat flow as the sum of the three heat transfer mechanisms is stated as

$$\dot{Q} = \dot{Q}_{cond} + \dot{Q}_{conv} + \dot{Q}_{rad} \qquad [\mathrm{W}], \tag{2.1}$$

measured in energy per time.
Conduction is the transport of energy in a conductive material or substance between its molecules due to a temperature gradient. Fourier's basic law for the conduction of heat is

$$\dot{\boldsymbol{q}}(t, \boldsymbol{x}) = -\lambda \ \mathrm{grad}\ T(t, \boldsymbol{x}) \qquad [\mathrm{W/m^2}]. \tag{2.2}$$

$\dot{\boldsymbol{q}}$ is the vector field of the heat flux (heat flow per surface area) and T the temperature, both quantities can depend on the position in the body x and time t. The heat flux is defined over the heat flow $d\dot{Q}_{cond} = \dot{\boldsymbol{q}}(t, \boldsymbol{x})\boldsymbol{n}\, dA$ through area dA with its normal $\boldsymbol{n}$. The negative sign in Equation (2.2) directs the heat flux from the higher to the lower temperature. The conductivity λ is a material property[14] and is quantified in [W/(mK)]. The heat transfer by conduction through multi-layered building walls is discussed in the next section.
Convection transfers heat between a surface and a moving fluid through the movement of molecules. The convective heat flow between a solid surface with an area A of temperature T_s (at the surface) and the moving air of temperature T_{air} can be described as

$$\dot{Q}_{conv} = \alpha_{conv} A(T_{air} - T_s). \tag{2.3}$$

The convective heat transfer coefficient α_{conv} relates the specific heat flux to the driving temperature difference:

$$\alpha_{conv} := \frac{\dot{q}_{conv}}{T_{air} - T_s} \qquad [\mathrm{W/(m^2K)}]. \tag{2.4}$$

The proportional factor defines the intensity of the heat transfer in the boundary layer. The convective heat transfer depends among others on the velocity and direction of the fluid and the roughness of the surface. α_{conv} is used in this work to model the convective heat transfer between the building walls or (heated) floor and the air in the building's zone.
Radiation describes the emission of electromagnetic waves from a body of a certain temperature. Radiative heat transfer between two bodies of different temperatures results in a heat flow emitted from the warmer to the colder body, but the colder body also radiates towards the warmer body. The total radiative exchange between a radiator with area A of temperature T and the surrounding of that body which absorbs all radiation[15] at temperature T_{sur} is given by

$$\dot{Q}_{rad} = \dot{Q}_{em} - \dot{Q}_{abs} = A\varepsilon\sigma T^4 - Aa\sigma T_{sur}^4. \tag{2.5}$$

The emissivity $\varepsilon[-]$ depends on the temperature, material and roughness of a body. It scales the emissive power of the body relative to an ideal black body with maximum emissivity. The absorptivity $a[-]$ scales how much radiation from the surrounding is absorbed. $\sigma = 5.67 \cdot 10^{-8}\mathrm{W/(m^2K^4)}$ is the Stefan-Boltzmann constant. The surfaces in practical applications are often assumed to be grey radiators, with $0 < \varepsilon < 1$ and a constant $a = \varepsilon$. The latter follows from Kirchoff's law of radiation, the absorptivity of the body equals its emissivity. The radiative net heat flow of the grey radiator in the black surrounding then simplifies to

$$\dot{Q}_{rad} = A\varepsilon\sigma(T^4 - T_{sur}^4). \tag{2.6}$$

This nonlinear relationship complicates the integration of radiative processes in a linear thermal building model. A common solution is to linearize the radiation's dependency on the temperature and to define a constant heat transfer coefficient to account for both radiation and convection. This is discussed in more detail in Section 2.2.4.

2.2.3 Thermal Electrical Analogy for Conduction

The heat flow by conduction can be modeled by analogy to an electrical circuit, with voltages representing temperatures and currents representing heat flows by conduction. The model for thermal conduction developed by Beuken in [Beu36] is based on the similar differential equations

[14] For now λ is assumed to be constant.
[15] The surrounding is assumed to be a black body: An ideal absorber and emitter.

as for an idealized cable derived from the telegraph equations. The telegraph equations describe voltage u and current i depending on location x and time t on an electrical transmission line with resistance R', conductance G', inductance L' and capacitance C', all defined in per unit length. For the homogeneous, lossy case, the telegraph equations are [Beu36, Rou72]:

$$\frac{\partial}{\partial x}u(t,x) = -L'\frac{\partial}{\partial t}i(t,x) - R'i(t,x) \tag{2.7}$$

$$\frac{\partial}{\partial x}i(t,x) = -C'\frac{\partial}{\partial t}u(t,x) - G'u(t,x). \tag{2.8}$$

Differentiating Equation (2.7) with respect to x and Equation (2.8) with respect to t and replacing leads to

$$\frac{\partial^2}{\partial x^2}u(t,x) = L'C'\frac{\partial^2}{\partial t^2}u(t,x) + (L'G' + R'C')\frac{\partial}{\partial t}u(t,x) + R'G'u(t,x). \tag{2.9}$$

Neglecting L' and G' and rearranging leads to

$$\frac{\partial}{\partial t}u(t,x) = \frac{1}{R'C'}\frac{\partial^2}{\partial x^2}u(t,x), \tag{2.10}$$

which is of similar form like the temporal and spatial one-dimensional temperature distribution in a homogeneous wall layer with thermal conductivity λ, specific heat capacity c and density ρ derived from from Equation (2.2):

$$\frac{\partial}{\partial t}T(t,x) = \frac{\lambda}{c\rho}\frac{\partial^2}{\partial x^2}T(t,x). \tag{2.11}$$

No additional heat sources are assumed in this case. x refers to the dimension in direction of the layer's thickness. Figure 2.8 shows the analogy of the Beuken model for a homogeneous wall layer with thickness Δx.

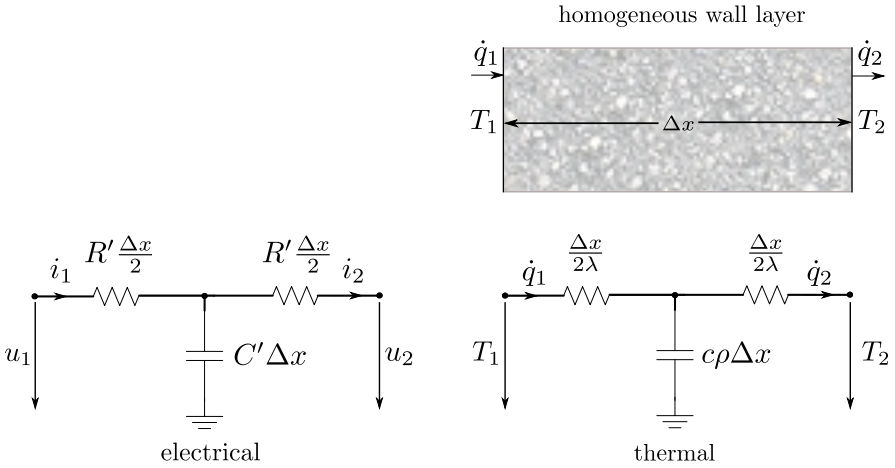

Figure 2.8: *Electrical and thermal analogy of Beuken, drawing based on [Rou72].*

The Beuken model discretizes a wall in multiple equivalent T-circuits and facilitates modeling a thermal zone surrounded by multiple walls. The complexity of the total model increases quickly, since the accuracy depends on the discretization step in the wall layers and thus the total number of equivalent T-circuits used. Approaches like the Fourier analysis or Laplace transform applied to the Beuken model to solve for the non-stationary thermal behavior of a wall layer under dynamic load conditions are discussed in [Rou72]. Rouvel developed further equivalent circuits

of reduced complexity based on the Beuken analogy to allow a simplified computation of the dynamic behavior of a multi-layer component for application in climate control. The equivalent circuits are based on the matrix representation of the thermal two-port network of a single layer and then extended and further simplified for asymmetrical and symmetrical load conditions of complete walls. The significantly simplified models allow computation of analytic solutions with sufficient accuracy at low computational costs.
The relationship between the temperatures and heat fluxes in a slab of finite thickness is the starting point of further simplifications. With the one-dimensional heat flux equation in direction of x

$$\dot{q}(t,x) = -\lambda \frac{\partial}{\partial x} T(t,x), \tag{2.12}$$

and the general solution to the differential Equation (2.11), a frequency domain solution can be derived for the heat fluxes and temperatures of the thermal network for a single layer, see Appendix A.2. For the periodic excitation case, the one-dimensional distribution of the heat flux $\dot{q}$ and the temperature T in a homogeneous wall layer v for a coordinate x perpendicular to the wall can then be expressed as

$$\begin{pmatrix} T(\omega, x=0) \\ \dot{q}(\omega, x=0) \end{pmatrix} = A_v \begin{pmatrix} T(\omega,x) \\ \dot{q}(\omega,x) \end{pmatrix}, \tag{2.13}$$

with

$$A_v = \begin{pmatrix} \cosh\left(x\sqrt{j\omega\frac{c\rho}{\lambda}}\right) & \frac{1}{\lambda\sqrt{j\omega\frac{c\rho}{\lambda}}} \sinh\left(x\sqrt{j\omega\frac{c\rho}{\lambda}}\right) \\ \lambda\sqrt{j\omega\frac{c\rho}{\lambda}} \sinh\left(x\sqrt{j\omega\frac{c\rho}{\lambda}}\right) & \cosh\left(x\sqrt{j\omega\frac{c\rho}{\lambda}}\right) \end{pmatrix}. \tag{2.14}$$

The real and imaginary parts of the complex coefficients can be separated and are given in Appendix A.2. In addition to the fixed material properties the transient response of a wall layer depends on the angular frequency ω in [rad/s] of the excitation signal applied to a surface. Frequencies of interest for building components or a thermal zone are usually $\omega = 0$ for the stationary heat flow and the ground frequency with a period of 24 hours and the multiples thereof [Rou72]. Recommendations to parameterize the building components are given in the next section. The chain matrix allows connection of multiple wall layers in series and further model reductions are possible to simplify whole building components. Similar to the transfer function of voltage and current in electrical two-port networks, the analogous model represents the frequency-dependent temperature and heat flow distribution in a wall.

2.2.4 Component Model

The building model implemented in this work lumps the main building components such as walls, the floor, the roof and windows together to a limited set of components, which results in a model with few differential equations but acceptable accuracy. In the process towards the single zone model, the individual components are modeled first and then lumped together to keep the number of states in the RC-model low.
The thermal resistance per unit area, heat capacity per unit area and the assumed period of the layer are inputs for the equations of chain matrix A_v. In the case of multiple wall or component layers ($v = 1, \ldots, n$), matrix A_{comp} for the entire wall or component can be calculated by matrix multiplication

$$A_{comp} = \prod_{v=1}^{n} A_v. \tag{2.15}$$

The sequence of multiple different material layers must not be changed, since A_{comp} depends on the direction. Indexing in this thesis is from the thermal zone towards the outside.
According to the approach in [Rou72], every component of a building can be represented by the $3R2C$ model depicted in Figure 2.9. The parameters R_1, R_2, R_3, C_1, C_2 can be directly calculated from the coefficients of matrix A_{comp} and area A of the component. The final equations to obtain the parameters in Figure 2.9 are given in Appendix A.3. Further reductions are possible in the case of [Rou72]:

- asymmetrically loaded components (outer walls, walls to zones of different temperatures): $2R1C$,
- symmetrically loaded walls (inner walls): $1R1C$.

Symmetrically loaded walls are assumed to have equal temperatures on both sides of the wall. The equations to compute the reduced equivalent circuits for the asymmetrically and symmetrically loaded components again depend on the coefficients of the component's chain matrix A_{comp} and are presented in Appendix A.3. The parameters for a symmetrically loaded component reduce to just R_1 and $\tilde{C}_1$ from Figure 2.10. For an asymmetrically loaded component, the resistances remain and a corrected capacity $\tilde{C}_1$ is computed. In the case of asymmetrically loaded components, the effective thermal mass must be carefully chosen to not overestimate the capacitance of the component model. The authors of [RDS14] suggest to only take into account the material layers within the insulation barrier as a rule of thumb, since usually only the first centimeters of an envelope wall are excited by a heating system. The study in [Rou72] distinguishes between thermotechnical thick and thin walls and defines a criteria for an assessment of single layer walls. The length of the thermally active layer is inversely proportional to the frequency ω of the excitation signal at the surface. Thus the size of the capacity considered in the equivalent models $3R2C$, $2R1C$ and $1R1C$ depends on the choice of the frequency assumed. The guideline VDI 6007 recommends to fix $\omega = \frac{2\pi}{86400 s T_P}$ to the frequency corresponding to a period of $T_p = 7$ days for standard components. The modeling approach in this work finally follows this practical suggestion.

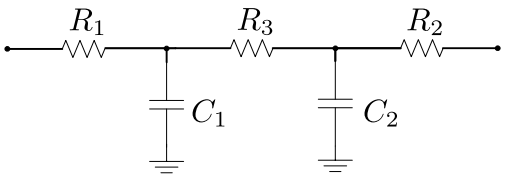

Figure 2.9: *3R2C model for a wall component from [Rou72].*

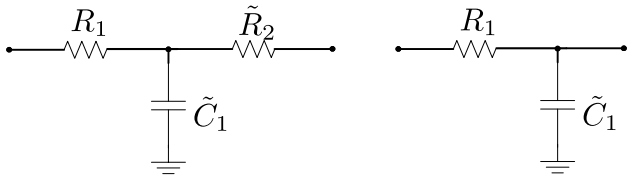

Figure 2.10: *2R1C and 1R1C model for a wall component based on [Rou72].*

The thermal capacity of the windows is negligible and not considered in the corresponding component model. Simple window models are given in [Rou72, VDI15b]. This work finally uses the exterior and interior film coefficients from [AKG09] to use equal values in the RC-model and the reference simulation in EnergyPlus. Details are given in [Kun17].
The workflow implemented in MATLAB calls a function *component(materials, area)* for every building component presented in the final model. The function itself calls a function *layer(material)* for every wall layer in the component to create the corresponding chain matrix A_v depending on the density ρ, specific heat capacity c, thermal conductivity λ and thickness x of the material of layer v. The above parameters and wall composition are stored for every building type and component shown in Table 2.3 in a database. Because the TABULA typology does not specify the exact building construction, common wall and material compositions are based on examples from [Aro14, TBSH15] for types J, L and an own parameterization is carried out for type E based on values from the ISO 10456 [DIN10]. The physical properties of all material layers and their selection and composition for the building types are stated in Appendix A.4.

2.2.5 Single Zone Model

The building is represented by a single zone model with a uniform air temperature in the whole zone. The function *building(typology, geometry)* generates a parameter set for the final low-order representation of the building. For a given geometry of a building, the function accesses the typology database and generates components for inner and outer walls, floors, windows, the door and the roof as described above. The editable geometry file includes among others the ground floor, outer wall and window areas, number of floors and floor height. The final structure of the resulting RC-model is shown in Figure 2.11.
The parameters $R_{wo,1}, R_{wo,2}$ and C_{wo} are the thermal resistances and capacitance for all outer walls, obtained from a consecutive parallel connection of the complex impedances of the envelope walls, roof, windows and door. A period of $T_P = 5$ days is chosen for the parallel connection of multiple individual components, as recommended in the VDI 6007. R_{wi} and C_{wi} represent the inner walls modeled as a symmetrically loaded component, with an area facing the zone equal to the outer walls. $R_{fl,1}$, $R_{fl,2}$ and C_{fl} represent the floor connected to the ground temperature T_g.

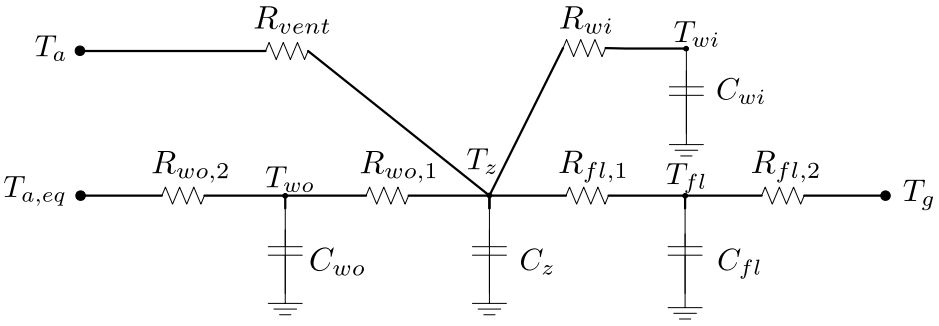

Figure 2.11: *Default structure for a single zone building model.*

The final model considers a capacitance of the zone C_z to summarize the heat capacity of the air volume at the zone temperature T_z. C_z is simply calculated by the volume of the zone V_z in

m^3, the density of air $\rho_{air} = 1.23 \frac{kg}{m^3}$ and its specific heat capacity c_{air} =1 008 Ws/(kgK) as

$$C_z = V_z \rho_{air} c_{air}. \tag{2.16}$$

Optionally, the capacity can be scaled by a factor of 5 to account for furniture in the zone [RDS14]. Furniture modeling is neglected here to not overestimate the thermal inertia of the zone and to keep the reference model for the validation simple. In contrast to the VDI 6007, where the final model order has only two capacitances for outer and inner walls, the additional capacitances of the zone air and floor of the developed RC-model are kept for simulation and validation purposes in this thesis. A study in [RDS15] found that due to the low-pass filtering effect of the high thermal mass, even a single capacitance model can provide a good approximation in the case of floor heating systems. In the case of modeling from building typologies and the absence of dynamic measurements, the presented structure is a reasonable starting point. A similar model structure to create low-order building models from Belgian typology data was employed in [RS14] and compared to both a reference and a grey-box model based on parameter fitting. The two zone model (night and day zone) showed acceptable accuracy.

Thermal Bridges and Ventilation

Thermal bridges are considered for the total envelope area in resistance $R_{bridges}$ and lumped together with the ventilation and infiltration losses in the parameter R_{vent}. According to [Nie05], the losses can be calculated as

$$\frac{1}{R_{vent,loss}} = V_z \rho_{air} c_{air} (\eta_{vent} + \eta_{inf} + \eta_{mec}(1 - \varepsilon_{hr})), \tag{2.17}$$

based on the heat capacity of air in the zone and the change rates η in $[h^{-1}]$ for natural ventilation, infiltration and, if present, mechanical ventilation with the efficiency of heat recovery factor ε_{hr}. Equation (2.17) implies that the heat loss due to mechanical ventilation can be approximated with an equivalent change rate for natural ventilation. The lumped resistance R_{vent} finally becomes

$$R_{vent} = \frac{1}{\frac{1}{R_{bridges}} + \frac{1}{R_{vent,loss}}}. \tag{2.18}$$

Only 1.4% (2.6%) of all German residential buildings are equipped with a ventilation system (including heat recovery), but approximately 30% of all new buildings constructed after 2009 are equipped with an active ventilation and heat recovery system [CD18]. This is often the case for modern airtight constructions. Table 2.4 shows the parameters assumed for the RC-models in this work.

Table 2.4: *Thermal bridges and ventilation parameters per building type based on TABULA and [Aro14].*

	$U_{therm.bridges}$ $[\frac{W}{m^2 K}]$	$\eta_{vent} + \eta_{inf}$ $[\frac{1}{h}]$	η_{mec} $[\frac{1}{h}]$	ε_{hr} [ ]
E	0.1	0.6	/	/
J	0.05	0.5	/	/
L	0.02	/	0.55 [Aro14]	0.84

Radiation and Convection

All final resistances in the RC-model must include surface resistances for convection and, if modeled, radiation. A wall or floor at a certain temperature exchanges heat by radiation with

the other components in the surrounding. In addition, heat is released to the air of the zone by convection. The two parallel processes are often approximated and aggregated in one total linearized heat exchange process for simplicity. The total heat flux from convection and radiation based on Equations (2.3) and (2.6) is

$$\dot{q} = \dot{q}_{conv} + \dot{q}_{rad} = \alpha_{conv}(T - T_z) + \varepsilon\sigma(T^4 - T_{sur}^4). \tag{2.19}$$

The total heat transfer at the surface of temperature T can be simplified when the surrounding and air temperatures are assumed to be similar, i.e. $T_z \approx T_{sur}$[16] [BS11, DB13] leading to

$$\dot{q} = (\alpha_{conv} + \alpha_{rad})(T - T_z) \tag{2.20}$$

with

$$\alpha_{rad} = \frac{\dot{q}_{rad}}{(T - T_z)} = \varepsilon\sigma\frac{T^4 - T_z^4}{(T - T_z)}. \tag{2.21}$$

Equation (2.21) can be approximated with

$$\begin{aligned} T^4 - T_z^4 &= (T^2 - T_z^2)(T^2 + T_z^2) && (2.22)\\ &= (T - T_z)(T + T_z)(T^2 + T_z^2) && (2.23)\\ &= (T - T_z)(T^3 + T^2T_z + T_z^2T + T_z^3) && (2.24)\\ &= (T - T_z)4T_m^3 && (2.25) \end{aligned}$$

for small temperature differences $T_z \approx T$. The coefficient becomes

$$\alpha_{rad} = 4\varepsilon\sigma T_m^3 \tag{2.26}$$

and T_m can be estimated by the mean $T_m \approx \frac{T+T_z}{2}$. α_{rad} is then predefined depending on the operative temperature conditions. The linearization allows the parallel heat transfers by convection and radiation to be lumped together in one coefficient $\alpha = \alpha_{conv} + \alpha_{rad}$, with T_z as the reference temperature for the total thermal transfer

$$\dot{q} = \alpha(T - T_z). \tag{2.27}$$

The literature provides standard heat transfer coefficients for radiation and convection at a component's surfaces towards the inside and outside of a building. Table 2.5 shows exemplary values. The overall resistance needed in the modeling process can be computed as

$$R_{se/si} = \frac{1}{\alpha_{rad} + \alpha_{conv}}. \tag{2.28}$$

[16] This also includes an approximation of the surrounding areas to a space with similar temperatures, neglecting view factors between the surfaces from the geometry of the zone. To be exact, resulting T_z in such a model is the operative perceived or sensation temperature, a combination of the air and radiation temperature.

Table 2.5: *External (se) and internal (si) surface resistances calculated based on [DIN15b, VDI15a] with indication of the orientation of the convective heat transfer.*

	$\alpha_{conv}[\frac{\mathrm{W}}{\mathrm{m^2\,K}}]$	$\alpha_{rad}[\frac{\mathrm{W}}{\mathrm{m^2\,K}}]$
$R_{se} = 0.04\frac{\mathrm{m^2\,K}}{\mathrm{W}}$ (vertical and horizontal)	20	4.63
$R_{si} = 0.13\frac{\mathrm{m^2\,K}}{\mathrm{W}}$ (horizontal)	2.5	5.14
$R_{si} = 0.083\frac{\mathrm{m^2\,K}}{\mathrm{W}}$ (panel heating)	7	5

The standard external and internal radiative heat transfer coefficients from [DIN15b] are computed with $\varepsilon = 0.9$ at $T_m = 10\,°\mathrm{C}$ and $T_m = 20\,°\mathrm{C}$ respectively by use of Equation (2.26)[17]. The external convective heat transfer coefficient is computed for a constant speed of wind of $4\,\mathrm{m/s}$. Since the heat transfer coefficients are predetermined and correspond to an average operative temperature, the approach might have limitations when heated surfaces face varying operating temperatures like a heated floor.
$\dot{q} = 8.92(T - T_z)^{1.1}$ is an empirical function for the maximum system-independent heat transfer used in the planning of floor heating systems which exchanges power with its surrounding. It is also known as the *basic characteristic* [DIN13]. T is the surface temperature of the floor and $T_z = 20\,°\mathrm{C}$ is the room temperature, a combination of both the air and radiative temperature of the surrounding. The resulting heat transfer for both the empirical model and the calculation based on Equation (2.19) are depicted in the first graph in Figure 2.12. The resulting heat transfers are close to each other. One observes the strong change in power by change in Kelvin overtemperature.

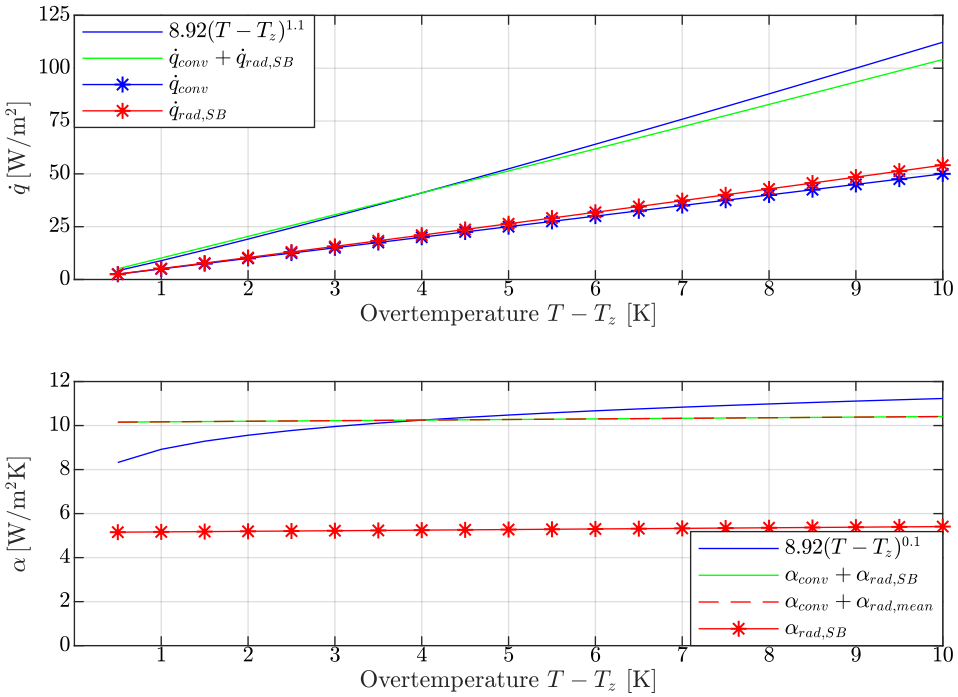

Figure 2.12: *Heat transfers and heat transfer coefficients resulting from the Stefan-Boltzmann law (SB) and the mean (mean) temperature approach compared to the empirical basic characteristic used in the planning of floor heating systems.* $\alpha_{conv} = 5\,\mathrm{W/(m^2K)}, \varepsilon = 0.9, \sigma = 5.67 * 10^{-8}\mathrm{W/(m^2K^4)}$.

[17] International norms often use h instead of α as the heat transfer coefficient.

The second graph in Figure 2.12 shows the corresponding heat transfer coefficients of the models. $\alpha_{rad,SB}$ is the coefficient for radiation according to the Stefan-Boltzmann law from Equation (2.21). The value ranges between 5.2 and 5.4 $\mathrm{W/(m^2K)}$ for an overtemperature up to 10 K. The maximum allowed temperature of a heated floor is limited to 29 °C in living areas due to physiological reasons [DIN13]. Adding a constant convective heat transfer coefficient of $\alpha_{conv} = 5\,\mathrm{W/(m^2K)}$ results in a total value around $10\,\mathrm{W/(m^2K)}$ over the overtemperature range. Using Equation (2.26) is a sufficient approximation for Equation (2.21). The error induced by predetermining α_{rad} with T_m (indicated as $\alpha_{rad,mean}$ in the figure) for the case of $T_z = 20\,°\mathrm{C}$ at an operative point and using it elsewhere is small. A detailed discussion of the approximation for different panel heating and cooling systems is given in [Glü08].
Finally, the values from Table 2.5 are used in the RC-model when either convection or both radiation and convection are modeled. Parameters $R_{si,wi/wo/fl}$ are used for the total surface resistance of the areas $A_{wi/wo/fl}$. The convective and radiative heat transfers are proportional to the surface area of a component.

Thermal Gains

The short and long-wave radiative heat exchange of the exterior building components with the outside environment can be taken into account by the introduction of a modified equivalent ambient temperature at each surface. The equivalent temperature incorporates a relative temperature increase due to the radiation between the surface and the environment. The approach is used in [VDI15b] and showed sufficient accuracy in a comparison with more sophisticated models carried out in [LRF+14]. The building model in this thesis neglects the long-wave radiation. The contribution to the temperature increase by the short-wave radiation on an exterior component i is weighted by the component's surface area A_i and thermal transmittance U_i. The equivalent ambient temperature for the lumped outer wall component is computed as

$$T_{a,eq} = T_a + \sum_i \frac{U_i A_i}{\sum_i U_i A_i} (I_{dir,i} + I_{diff,i}) \frac{\alpha_F}{\alpha_A}, \tag{2.29}$$

with ambient temperature T_a, direct and diffuse radiation I_{dir} and I_{diff} on the opaque outer wall areas, short-wave absorption coefficient $\alpha_F = 0.5$ and the external heat transfer coefficient $\alpha_A = \frac{1}{R_{se}}$ at the exterior surfaces. The roof is approximated as a horizontal surface.
According to the ISO 13790 [DIN08] the solar gains φ_{sg} through windows can be assumed to have a convective share of 9%, which is added to the zone temperature T_z in this model. The remaining fraction is initially split up according to an area-weighted distribution to the inner walls, outer walls and floor by the factors $s_{z/wi/wo/fl}$. φ_{sg} is computed as

$$\varphi_{sg} = \sum_i (I_{dir,i} + I_{diff,i}) A_{window,i} g_{window}, \tag{2.30}$$

based on the radiation through window i with area $A_{window,i}$ and the dimensionless window permeability factor $g_{window} = 0.6$.
Likewise, the distribution of internal gains φ_{ig} from occupants and devices is carried out via the factors $g_{z/wi/wo/fl}$ with a convective share of 50%. The equations to determine the distribution factors for the solar and internal gains are given in Appendix A.5
The shares of the heat transfer mechanisms vary and depend on the type of heat emission system to supply the thermal zone. Convective shares from 50% up to 70% are stated for radiator heating systems. In contrast, area and especially ceiling and floor heating systems emit a larger share by radiation, with typical values for the radiative share up to 70% [RS14, VDI15b]. The heated floor

exchanges heat with the other walls in the thermal zone by radiation, which in return partially transfer heat to other surfaces by radiation and to the zone by convection.
Similar as for the solar and internal gains, the radiative fraction of the heat input φ_h is distributed among the capacities of the components with the distribution factors f_{wi}, f_{wo} and f_{fl}. It must be noted that the distribution of the radiative heat transfer directly to the respective capacities is an approximation and not in line with the physical mechanism. The radiation absorbed by a component enters at the surface and not within the component. The initial zone model neglects this to avoid the introduction of additional temperature states. Possible corrections and extensions to avoid related inaccuracies of the initial RC-model are discussed in the validation Chapter 2.2.7.

Default RC-model *D*

Finally, the building function of the workflow returns an individual set of parameters for the building components and heating system parameters for the structure in Figure 2.11. Temperatures T_z, T_{wi}, T_{wo} and T_{fl} are defined at the capacitances. The differential equations of the low-order default RC-model lead to the Equations (2.31)-(2.34):

$$\frac{dT_z}{dt} = \frac{1}{R_{vent}C_z}(T_a - T_z) + \frac{1}{R_{wi}C_z}(T_{wi} - T_z) + \frac{1}{R_{wo,1}C_z}(T_{wo} - T_z) + \frac{1}{R_{fl,1}C_z}(T_{fl} - T_z) + \frac{s_z}{C_z}\varphi_{sg} + \frac{g_z}{C_z}\varphi_{ig} + \frac{f_z}{C_z}\varphi_h \tag{2.31}$$

$$\frac{dT_{wi}}{dt} = \frac{1}{R_{wi}C_{wi}}(T_z - T_{wi}) + \frac{s_{wi}}{C_{wi}}\varphi_{sg} + \frac{g_{wi}}{C_{wi}}\varphi_{ig} + \frac{f_{wi}}{C_{wi}}\varphi_h \tag{2.32}$$

$$\frac{dT_{wo}}{dt} = \frac{1}{R_{wo,2}C_{wo}}(T_{a,eq} - T_{wo}) + \frac{1}{R_{wo,1}C_{wo}}(T_z - T_{wo}) + \frac{s_{wo}}{C_{wo}}\varphi_{sg} + \frac{g_{wo}}{C_{wo}}\varphi_{ig} + \frac{f_{wo}}{C_{wo}}\varphi_h \tag{2.33}$$

$$\frac{dT_{fl}}{dt} = \frac{1}{R_{fl,2}C_{fl}}(T_g - T_{fl}) + \frac{1}{R_{fl,1}C_{fl}}(T_z - T_{fl}) + \frac{s_{fl}}{C_{fl}}\varphi_{sg} + \frac{g_{fl}}{C_{fl}}\varphi_{ig} + \frac{f_{fl}}{C_{fl}}\varphi_h. \tag{2.34}$$

The next paragraph discusses limitations of the default model and possible adjustments to enhance its accuracy. All discussed refinements maintain the above low-order model structure of four states.

Model Limitations and Refinement

The default single zone model provides a starting point for temperature and energy demand predictions based on a model with reduced complexity. Obviously, this leads to certain limitations with respect to the representation of the actual physical processes:

- The long-wave radiation exchange between the building and it's environment is neglected in both the RC and the EnergyPlus reference validation model for simplicity. Optional linearization approaches can be found in [DIN08] and [VDI15b] and are discussed in [LRF+14].

- The dependency of the convective heat transfer coefficient on the wind velocity or surface roughness is not considered. The constant values from Table 2.5 are used in both the RC-model and the EnergyPlus reference model.

- The magnitude of the solar gains through the windows depends on the time-dependent incident angle. The solar gains enter the components based on fixed distribution factors in

the RC-model. The actual internal distribution depends on the incident angle and varies with time, which is not covered in the one-dimensional RC-model.

- The uniform air and component temperatures result from modeling only one-dimensional heat transfer. Lumped components like the outer wall comprise individual components like the external wall, roof, door and windows. Thus, resulting temperatures for the lumped component must be interpreted as an averaged temperature over multiple components with different material properties.
- The distribution of the radiative thermal gains at component capacities is just a rough approximation of the actual radiative heat transfer according to the Stefan-Boltzmann law. When modeled, the long-wave radiation exchange between the components within the thermal zone can only be taken into account with linearized heat transfer coefficients in the default RC-model.
- Simply adding the heat gains at the component capacities introduces a potential inaccuracy with respect to the actual location of entry. The RC-representation of the floor defines a floor temperature which must not necessarily match with the position of the hydronic tube system. The derivation for the wall components assumed no internal heat sources in Equation (2.11), which disagrees when thermally active components are modeled. Nevertheless, the approximation is kept for the floor heating system, since sufficient accuracy was achieved with a similar procedure for panel cooling and heating systems in [Rou16].

Since the radiative heat transfers from thermal gains are only distributed among the components in the default RC-model, two modifications are tested in addition to the initial model to investigate the heat transfer from the floor for the case of a floor heating system. The default model is abbreviated as model D, the model refinements are referred to as models F and R.
The default model D neglects the internal long-wave radiation exchange between the surfaces for simplicity. It is intuitive to start with convective heat transfer coefficients from Table 2.5 only. Also T_z remains the pure air temperature in this approach.
The first modification of the RC-model substitutes the initial area-weighted distribution factors $f_{z/wi/wo/fl}$ by fitted values to achieve a better approximation of the zone temperature T_z. An accurate prediction of the zone temperature is of great importance, since it is closely related to the comfort of occupants. The quadratic program (2.35)[18] to solve over the fitting period is

$$\begin{aligned} \underset{f_z, f_{wi}, f_{wo}, f_{fl}}{\text{minimize}} \quad & \sum_{t=1}^{T} (T_{z,RC}(t) - T_{z,E+}(t))^2 \\ \text{subject to} \quad & (2.31), (2.32), (2.33), (2.34) \quad \forall t = 1, \dots, T \\ & f_{wi} + f_{wo} + f_{fl} = 1 - f_z. \end{aligned} \tag{2.35}$$

$T_{z,E+}$ is obtained from the detailed reference simulation in EnergyPlus. The equality constraint assures that the distributed radiative plus the convective share of the heat gain must be equal to the total heat input φ_h taken from EnergyPlus. A period of two weeks in February was chosen as the fitting period. This model is referred to as model F. Model F can be considered a grey-box model since it partially results from a fitting process based on simulated data.
The second modification of the default model introduces a radiant resistance $R_{rad,wo-fl}$ between the floor and the lumped outer walls:

$$R_{rad,wo-fl} = \frac{1}{\alpha_{rad} \min\{A_{wo}, A_{fl}\}}. \tag{2.36}$$

[18] The continuous-time dynamics in (2.31)-(2.34) are discretized to solve the optimization problem.

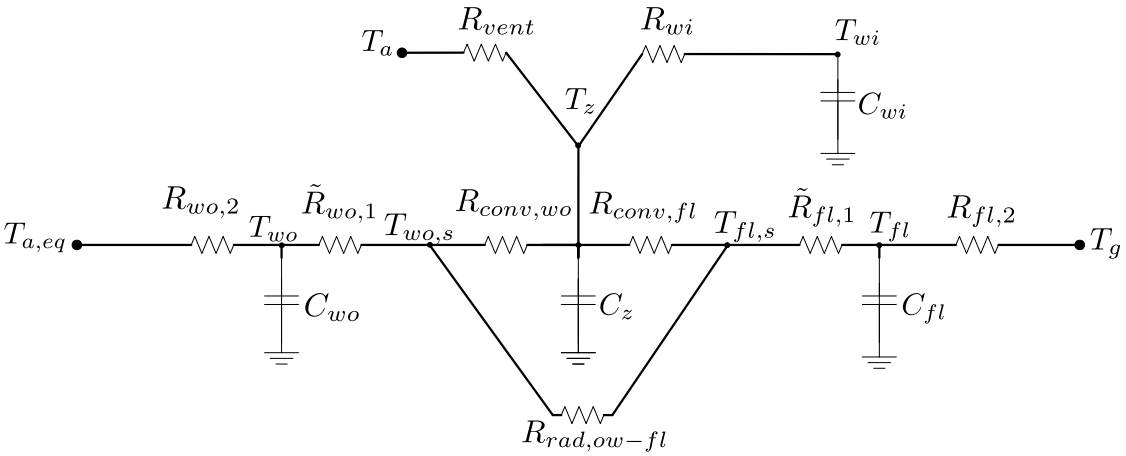

Figure 2.13: *The modified RC-model R with a radiative resistance between the floor and the outer wall. The radiative heat transfer between the other components is not considered.*

Figure 2.13 shows the additional resistance for radiation to explicitly consider the radiative heat exchange between the floor and the outer wall. The smaller of the two surfaces is chosen and the radiative heat transfer coefficient is set to $5\,\mathrm{W/(m^2K)}$, in accordance with Table 2.5. The long-wave radiation between the other components is still neglected. The remaining structure contains a delta circuit including the radiative and the two convective resistances. A delta-star transformation can be applied to avoid the introduction of additional temperature nodes, see also [VDI15b]. The resulting final structure is depicted in Figure 2.14. The formulas for the resistances $R_{starA/B/C}$ together with a derivation for the model with four temperatures based on adjustments in Equations (2.31)-(2.34) are given in Appendix A.6[19]. The surface temperatures $T_{wo,s}$ and $T_{fl,s}$ have to be considered in the derivation, but the final model states remain T_z, T_{wi} T_{wo} and T_{fl} such that the resulting state-space model does not change in complexity.

[19]It will be referred to Equations (2.31)-(2.34) in the remainder of this chapter for simplicity, keeping in mind that Equations (A.51)-(A.54) are used whenever model R is used.

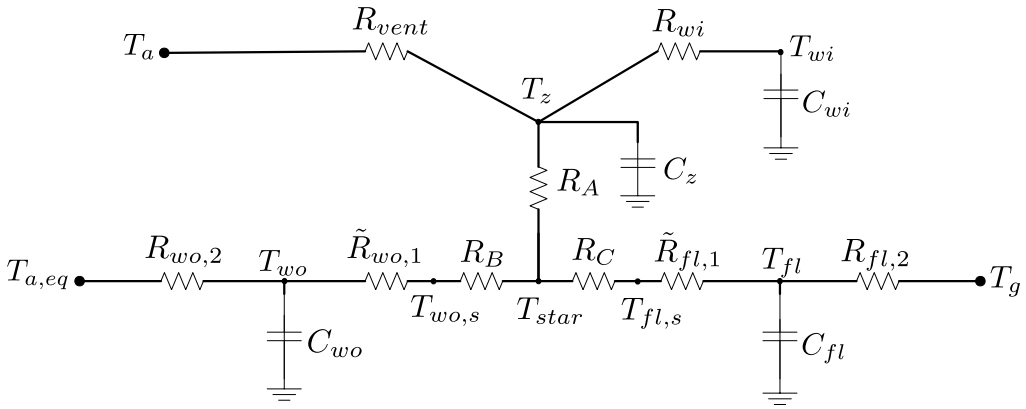

Figure 2.14: *The modified RC-model R after the delta-star transformation with* $R_{(star)A/B/C}$.

Both model *F* and model *R* work with updated *s*-factors for the distribution of the solar gains entering through the windows on the surfaces. The validation of the default model in [Kun17] revealed inconsistencies between the solar gains on surfaces measured in EnergyPlus and the resulting gains in model *D*. Especially the gains on the floor were underestimated by model *D*. The distribution factors $s_{wi/wo/fl}$ were optimized such that the resulting solar gains match with those of the reference simulation in EnergyPlus to overcome the insufficiency of the area-weighted initial guess. The parameters were again fitted over the same period and were well applicable to other weeks of the heating period. Even though an improvement of T_z was not part of the optimization, the updated factors already lead to a better prediction of the zone temperature. A detailed discussion can be found in [Kun17]. Table 2.6 shows the distribution factors for solar gains, internal gains from occupants and the heat gains used in models *D*, *F* and *R* for the further analysis in this work.

Table 2.6: *Thermal gains distribution factors for the RC-models D, F and R by validated building type (L and J).*

	Solar gains φ_{sg}				**Internal gains** φ_{ig}				**Heat gains** φ_h			
	s_z	s_{wi}	s_{wo}	s_{fl}	g_z	g_{wi}	g_{wo}	g_{fl}	f_z	f_{wi}	f_{wo}	f_{fl}
D-J/L	0.09	0.32	0.46	0.13	0.5	0.18	0.25	0.07	0.05	0.33	0.48	0.14
F-J	0.09	0.2	0.21	0.5	0.5	0.18	0.25	0.07	0.0	0.11	0.46	0.43
F-L	0.09	0.2	0.21	0.5	0.5	0.18	0.25	0.07	0.0	0.1	0.43	0.47
R-J/L	0.09	0.2	0.21	0.5	0.5	0.18	0.25	0.07	0	0	0	1

The *g*-weighting factors for the distribution of the convective and radiative shares from occupants and appliances remain the same for all three models. In [Kun17] the area-weighted approach led to satisfying results to model the sensible heat gain.

2.2.6 EnergyPlus Reference Building Model

A reference building model to validate RC-models was created in the master's thesis in [Kun17] for types *J* and *L*. The thesis investigated the effects of the ambient temperature, solar radiation, internal gains and heating system input for the default model in sequential order to distinguish

the impact of modeling options in EnergyPlus from flaws of the RC-model. As an example, the first analysis investigated the impact of convection and conduction under free-floating conditions without any solar or heating gains. The fitting of the s-factors was done before an investigation of the impact of the floor heating system to not compensate for modeling errors of the heating input. This procedure enabled the analysis of different physical phenomena. A graphical representation of the building with a single zone is given in Figure 2.15. The building geometry used to parameterize both the RC-models and the EnergyPlus model is given in Table 2.7. In order to allow for a convenient comparability of the transient behavior and power profiles of different energy standards, the building type J geometry was also assumed for building type L.

Table 2.7: *Building geometry used in EnergyPlus and the RC-models.*

Component	**Area** [m^2]
Outer wall	188.9
(N/S/E/W)	54.3/40.1/46.25/48.25
Inner wall	188.9
Floor	79.8
Roof	85.9
Window	28.2
(N/S/E/W)	3.1/17.3/3.9/3.9
Door	2

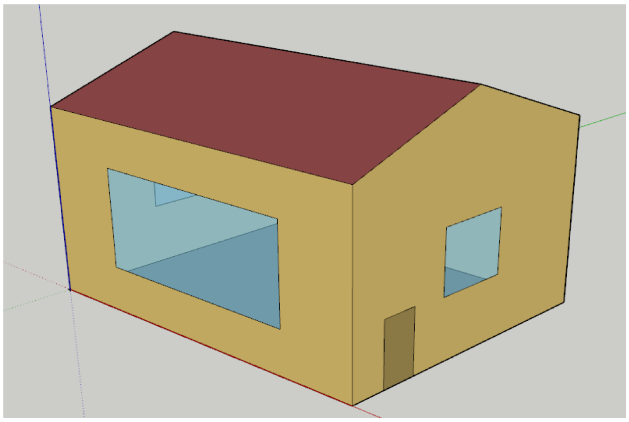

Figure 2.15: *EnergyPlus building geometry. Drawing from [Kun17].*

The building components were defined with the exact same material layers used in the RC-model parameterization, based on the material properties stated in Appendix A.4 for either building type L or J. The thickness of the outer components' insulation layer was corrected to account for the effect of the thermal bridges, since it is not possible to model thermal bridges as a separate component in EnergyPlus. The dependency of convective heat transfer coefficients on the speed of wind is disregarded in EnergyPlus. The coefficients were set to the constant values used in the RC-models.
The reference building was equipped with a hydronic underfloor heating system as the heat emission system. The water circuit is located between the layers of cement screed and the tiles. Hot water for the tubes is supplied from a buffer storage tank connected to an air-to-water heat pump. The simple temperature control in EnergyPlus computes the power input provided to the floor to maintain the zone temperature above 19 °C. EnergyPlus applies an iterative heat

balance algorithm to compute a solution for the current time step, details can be found in [U.S15]. The dynamic behavior of the heat pump and the buffer storage are not part of the validation, since they are not part of the building RC-model considered here. The floor input power from EnergyPlus is taken as input φ_h in the simulation of the RC-models.
The simulation period in EnergyPlus covers the months January and February to include the most challenging weeks of the heating period. Weather data is taken for Munich in the epw weather format, including the ambient dry bulb temperature and the direct and diffuse radiation. The ground temperature is assumed to be constant 10 °C throughout the simulation. The same value is used in EnergyPlus simulations models in [Lin17], more complex ground models can be found in [DIN15a].

2.2.7 Thermal Building Model Validation

The thermal building model implemented in EnergyPlus is assumed to represent a realistic approximation of a heated single family house of a certain typology. A more detailed representation could consist of a multi-zone building, with some zones equipped with a heat emission system, maybe even of different type (floor heating and radiators) and temperature set-points (bathroom and living room). The scope and conclusions of this work are thus limited to the example building described in Chapter 2.2.6.
The simulated temperatures from EnergyPlus are taken as a reference output to compare with the RC-models' output. With the temperature states x, the heating system input φ_h and the disturbances d, the validation evaluates if the RC-models' dynamics represented in Equations (2.31)-(2.34) are a sufficient approximation of the EnergyPlus functional f_{E+}:

$$\dot{x}_{E+} = f_{E+}(x_{E+}, \varphi_h, d) \approx Ax_{RC} + B\varphi_h + Ed = \dot{x}_{RC}. \tag{2.37}$$

A, B and E are the general system, input and disturbance matrices of the corresponding state-space model, discussed in detail in Chapter 3. The simulation time step in EnergyPlus is set to 15 minutes and the system matrices of the RC-models are discretized accordingly. The computation time increases with higher temporal resolutions for a fixed simulation period. [U.S18] recommends time steps lower than 60 minutes when thermal simulations include HVAC systems, best below 10 minutes to obtain a less damped dynamic response. A temporal resolution of 15 minutes is a compromise between computation time and accuracy. In addition, a thermal model validated at 15 minutes time steps fits well to energy market processes, since they are often settled at 15 minutes intervals.

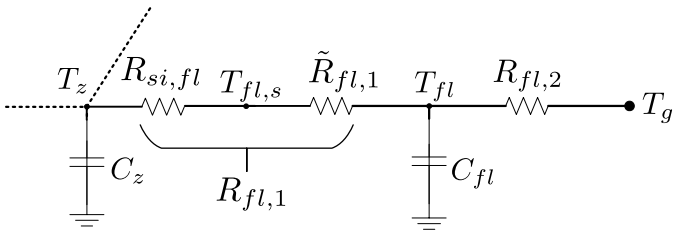

Figure 2.16: *Location of the floor's surface temperature with respect to the initial parameters.*

The RC-models are assessed for $x_{RC} = (T_z, T_{wi,s}, T_{wo,s}, T_{fl,s})^T$. $T_{z,E+}$ refers to the zone air temperature from EnergyPlus. While EnergyPlus can provide temperatures at defined positions

in a building component, it is difficult to estimate the exact position of the temperature in a building component modeled with the RC-model. Therefore, the surface temperatures are compared. Equating the heat flows at $T_{fl,s}$ in Figure 2.16 leads to

$$\frac{1}{R_{si,fl}}(T_z - T_{fl,s}) = -\frac{1}{\tilde{R}_{fl,1}}(T_{fl} - T_{fl,s}) \tag{2.38}$$

$$T_{fl,s} = \frac{R_{si,fl}T_{fl} + \tilde{R}_{fl,1}T_z}{R_{fl,1}} \tag{2.39}$$

with

$$\tilde{R}_{fl,1} = R_{fl,1} - R_{si,fl}. \tag{2.40}$$

The equations for the computation of all surface temperatures for RC-models D, F and R are given in Appendix A.7.

Simulation Error

Figure 2.17 shows the temperature trajectories for T_z, $T_{wi,s}$, $T_{wo,s}$ and $T_{fl,s}$ for the EnergyPlus simulation of the reference building and the models D, F and R for building type J over the period of February 14-28. The ambient temperature (T_a) and global horizontal solar radiation (I_H) disturbances are shown in the fifth subplot. This particular period was chosen for validation since it exhibits strongly varying climatic conditions during the heating period. The same heat input φ_h is used in the EnergyPlus and RC-models. The first half of the simulation period is dominated by cold ambient temperatures reaching below $-15\,°C$, followed by slightly milder conditions between $-5\,°C$ and $5\,°C$. The cold temperatures are accompanied by clear sky conditions with stronger solar gains in the first half of the simulation period. The peak power of the heating input increases with colder temperatures and pauses during periods of solar gains during the day. This can be seen in the charging pattern of the floor temperature from EnergyPlus, e.g. during day 5. The floor's temperature increases over night until the ambient temperature and solar gains increase again and φ_h remains zero for almost 6 hours.
The default model D approximates the zone temperature well during times of high solar radiation, but overestimates the temperature when the floor heating system is operating at high load. The surface temperature of the inner walls is overly sensitive to the thermal gains, leading to a steady overestimation of the temperature compared with the reference from EnergyPlus. The opposite is the case for the floor temperature, which is not adequately represented and shows a weak sensitivity to thermal gains. The typical charging profile as seen for the floor's temperature in the EnergyPlus reference is lost. It can be concluded that the purely parameterized first-guess model D achieves a tolerable approximation of the zone's air temperature, but fails to explain the floor and inner wall temperatures due to the simple area-weighted distribution factors. This is partially corrected with model F, where the solar gains distribution factors where corrected with respect to the actual physical solar gains on the inner surfaces and the f-factors were optimized to minimize the error of T_z. T_z and $T_{wi,s}$ are approximated better, but the approach still fails to accurately predict the temperature of the floor. The higher sensitivity of the floor to solar gains and heating input (see the change in the distribution factors in Table 2.6) helps to better explain the zone temperature, but now overestimates the floor's temperatures due to the selective optimization. Explicitly modeling the radiative exchange between the outer walls and the floor in model R solves this and shows that the applied linearization proves successful. $T_{fl,s}$ is accurately reproduced, explaining the temperature increase due to charging of the floor heating system well. A similar good result is achieved for the zone temperature.

Similar observations can be made for building type L in Figure 2.18. Default model D is overly sensitive with respect to the ambient temperature and solar gains. This can be seen in the systematic overestimation of T_z, $T_{wi,s}$ and $T_{wo,s}$ during an increase in outside temperature and solar gains, followed by an underestimation when the disturbances decline, e.g. seen during the free-floating period from noon of day 7 to day 10. The floor temperature is less sensitive, exhibiting weakly pronounced charging peaks. Nevertheless, a better approximation compared to building type J is achieved. Model F corrects the oversensitivity, especially the inner and outer walls receive less solar gains in favor of the floor. Due to the updated distribution factors in Table 2.6, the heat gains are mainly attributed to the floor and outer walls and the direct convective share of the heating input to the zone is reduced to zero when the error of T_z is optimized. This leads to a better approximation of the zone temperature, but again leads to a systematic overestimation of $T_{fl,s}$.[20] Again, the best results with respect to T_z and $T_{fl,s}$ were achieved by explicitly modeling the radiative exchange in model R. Still, a slight overestimation of the floor's temperature during the second half of the simulation period can be observed. The floor's temperature is operated at a lower average value compared to building type J and the charging peaks are less pronounced due to lower power levels of φ_h. In contrast to building type J, the larger part of the variation in $T_{fl,s}$ can be explained by the solar gains. The modern building standard L results in a higher average zone temperature and less heating demand. The relatively high temperatures can be explained by the large south-facing window in combination with the airtight envelope (as seen in Table 2.3, building type L has less than half of the U-values of type J for the outer wall and roof). Obviously, a ventilation system is highly required in such a building to manage summer conditions.

[20] An equally weighted optimization with respect to all states instead of T_z only was tested too, but resulted only in a minor improvement of the components' state errors and worsening of the error of T_z.

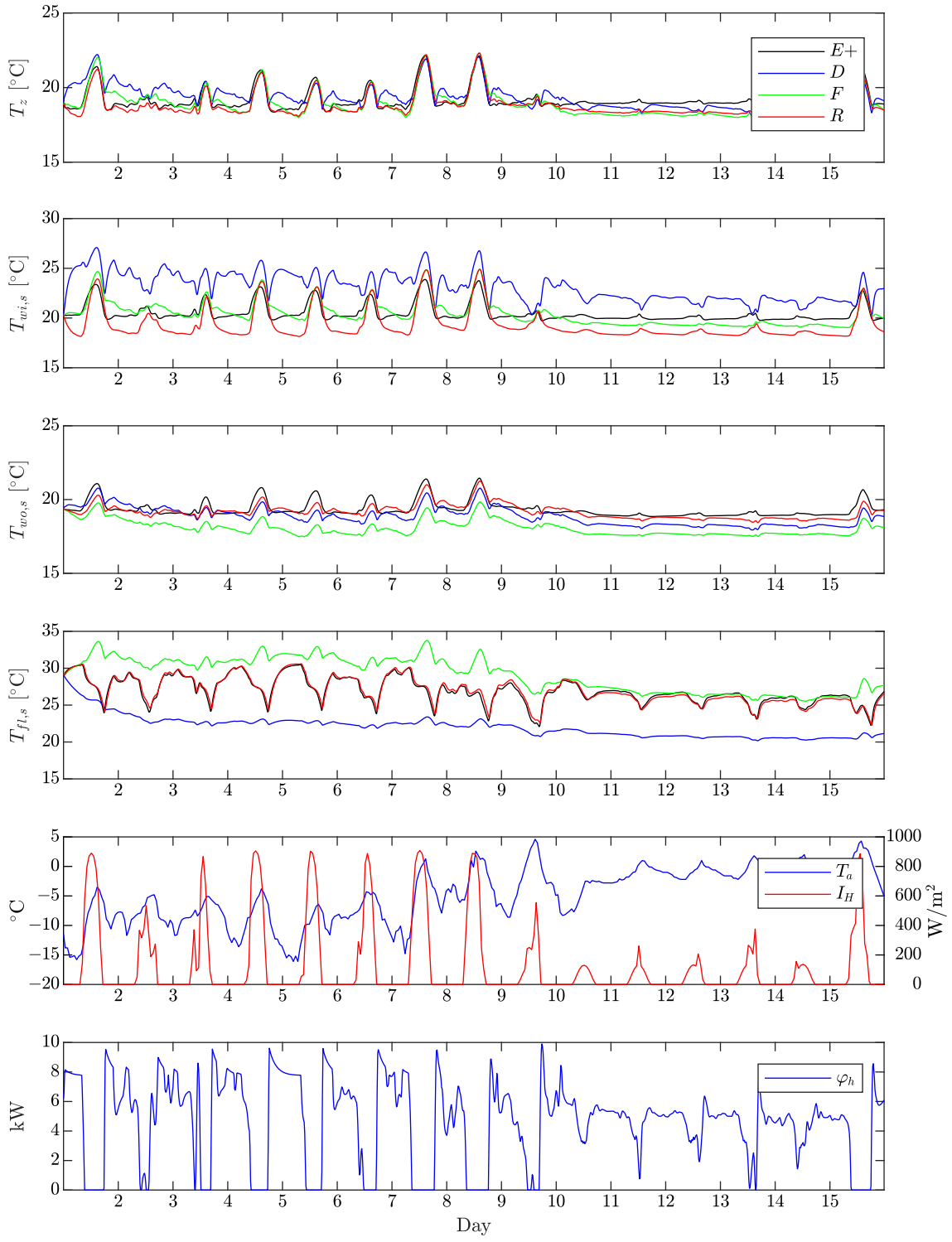

Figure 2.17: *Simulation results for the RC-models D,F, and R compared to the EnergyPlus(E+) reference for building type J.*

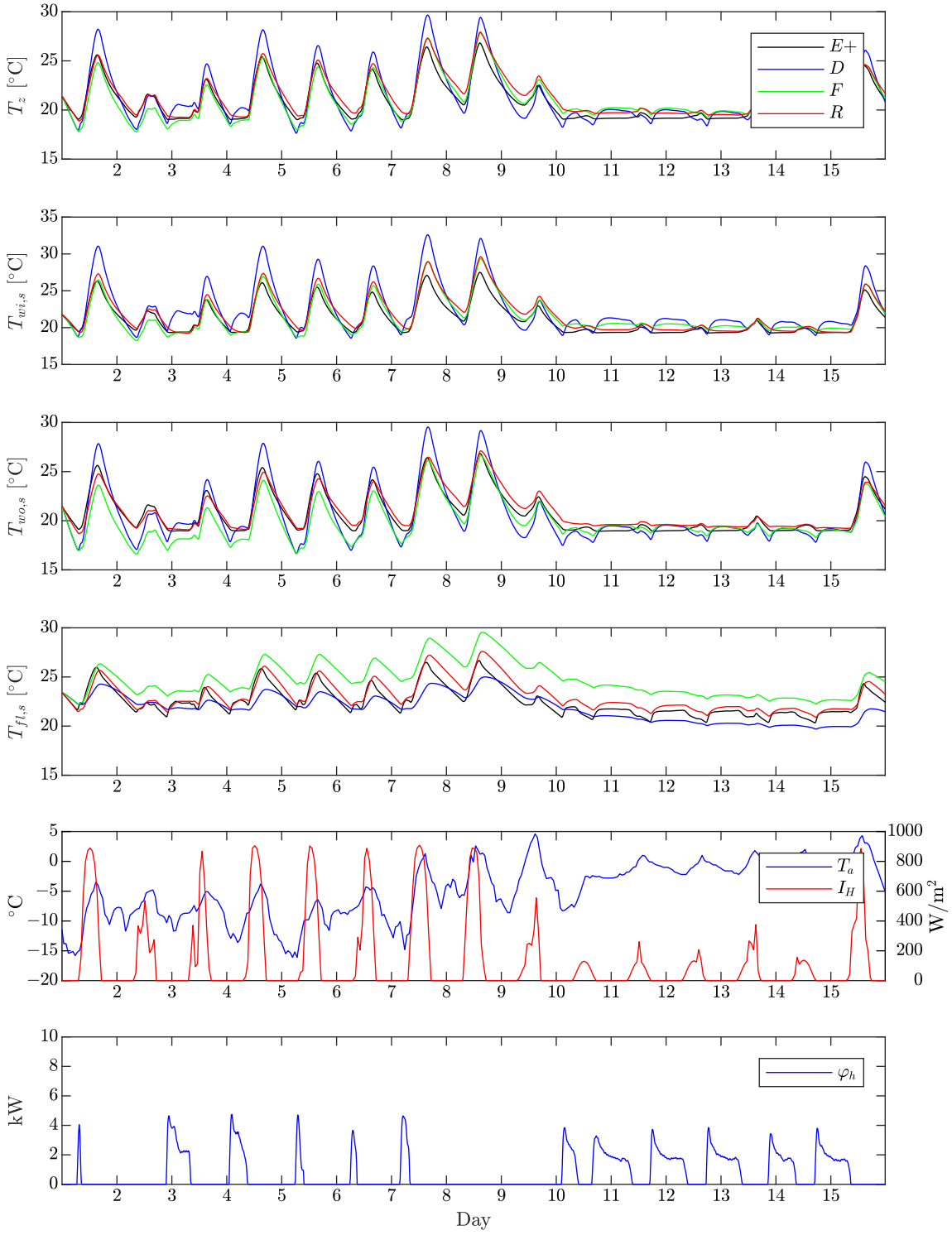

Figure 2.18: *Simulation results for the RC-models D,F, and R compared to the EnergyPlus(E+) reference for building type L.*

Figure 2.19 shows the root-mean-square error ($RMSE$) for the states and RC-models over the

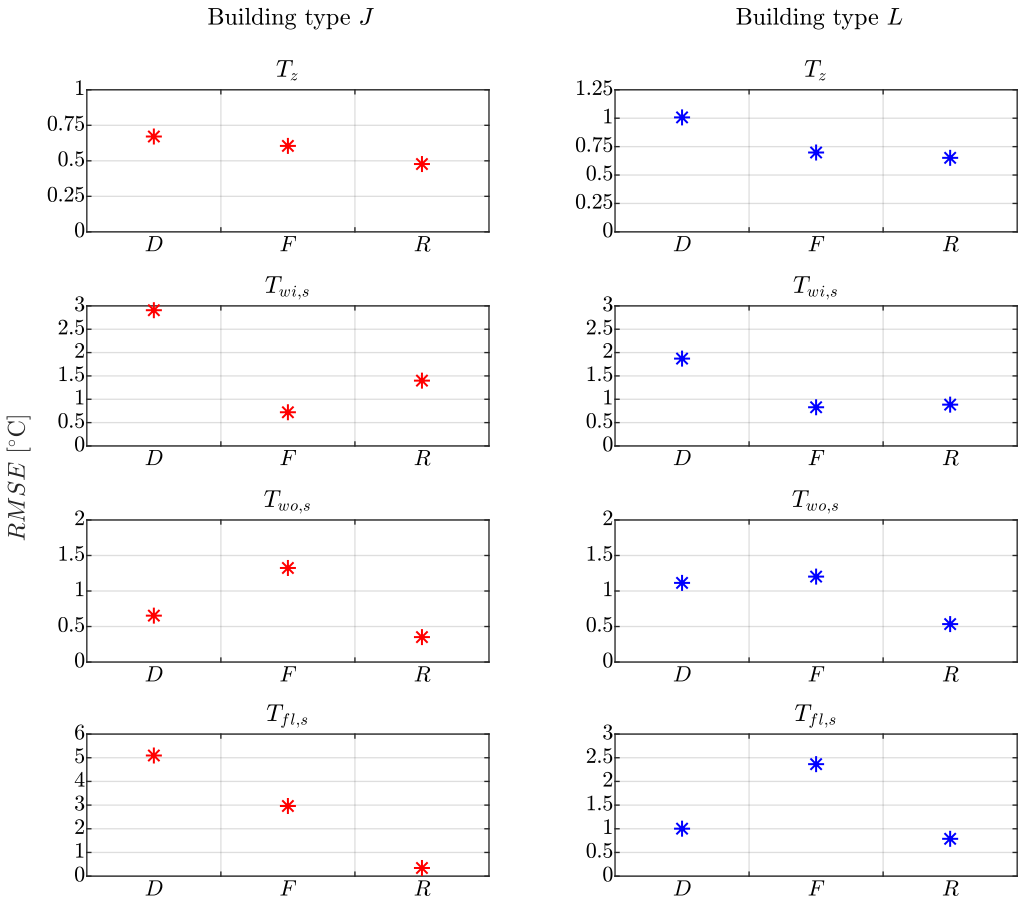

Figure 2.19: *RMSE of the RC-models D,F, and R over the period February 14-28.*

simulation period from 14th to 28th of February.

$$RMSE = \sqrt{\frac{1}{N}\sum_{i=1}^{N}(x_{i,RC} - x_{i,E+})^2} \tag{2.41}$$

In line with the observations above, model D already achieves a relatively small $RMSE$ below 1 °C in T_z for both building types, but leads to higher deviations for $T_{wi,s}$ and $T_{fl,s}$ for building type J. Model F results in small improvements for T_z and $T_{wi,s}$, while deteriorating $T_{wo,s}$ for both buildings and $T_{fl,s}$ for type J. Despite the inner wall surface temperature, model R outperforms the other models in all states for both buildings.

The superior accuracy of model R is in general confirmed when a cross-validation is performed over different periods of the heating period. Figure 2.20 shows the $RMSE$ of the three models over periods of 14/15 days in January and February.

Beginning with building type J, the results for each state are slightly more diverse compared to building type L. While model R achieves the smallest $RMSE$ of T_z during the period from February 14-28 examined above, this is not the case for the other periods, where model D achieves the best results for building type J. $T_{wi,s}$ is best approximated by model F throughout all periods. The errors for $T_{wo,s}$ and $T_{fl,s}$ are smallest with model R for all considered periods. The good results of model R are even more robust for building type L, where it achieves the smallest $RMSE$s in T_z, $T_{wo,s}$ and $T_{fl,s}$ for all periods. The only case in which another model

accomplishes similar or superior results occurs for $T_{wi,s}$, where model F achieves slightly better results for two periods.[21]
In summary, model R is superior in 9 out of 16 comparisons (four states over four different periods) for building type J and in 14 out of 16 comparisons for building type L. It achieves a $RMSE$ below 1 °C in all states for all considered periods with the exception of $T_{wi,s}$ in building type J.

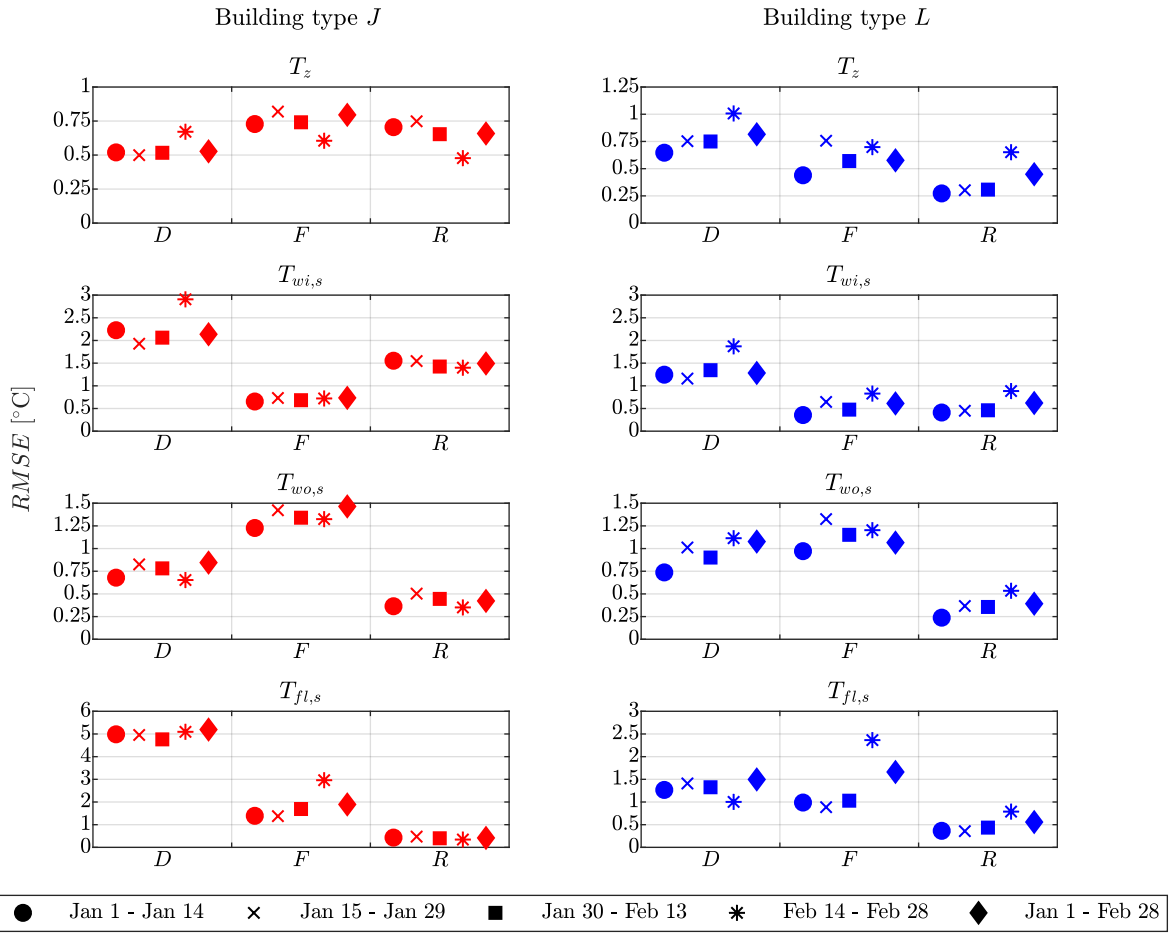

Figure 2.20: *RMSEs for the RC-models D, F, and R over different simulation periods for cross-validation.*

The different performances of the models lead to the question, whether some simple adjustments based on the results of model R can be applied to the default model D to increase it's accuracy without a further modeling effort. The idea is to find the best initial guess possible without the need of further fitting or more complex modeling. The results have shown, that a redistribution of the heat gains through modified f-factors and the integration of the radiative heat exchange between the floor and the outer wall have increased the performance significantly. Model F did not consider internal radiation, but optimized the f-factors with respect to T_z. Thus it is the optimal model to approximate T_z without modeling radiation. Figure 2.20 shows that the results for T_z are only slightly better and the fitted values are not necessarily robust to different simulation periods (see worse $RMSE$s of T_z in the other periods for building J with model F

[21] An alternative measure to compare the $RMSE$s of two different periods is the standardized $RMSE$, where the model's error is divided by the standard deviation of the underlying reference time series. The results are similar and given in Appendix A.8.

due to possible over-fitting). An obvious adjustment of model D is to use the f-factors of model R, i.e. allocating all heat gain on the floor ($f_{fl} = 1$). A test showed that for building type J, T_z and $T_{wi,s}$ were slightly improved, while $T_{wo,s}$ and $T_{fl,s}$ were considerably worse. The approximation of the dynamic behavior of the floor was not enhanced. A similar picture was obtained for building type L, with deteriorated results for T_z in addition. Working with updated solar radiation factors did not change the results for neither of the buildings.
A second, intuitive approach for model D is to include radiation by using the total heat transfer coefficient with α_{rad} from Table 2.5 and the f-factors of model R. Thus, radiation is not modeled explicitly with a separate resistance, but is at least integrated in the components surface resistances $R_{si,wi/wo/fl}$. As discussed earlier, in this case T_z approximates a combination of the air and surrounding radiation temperature. This enhanced initial guess model is introduced as model $D+$.

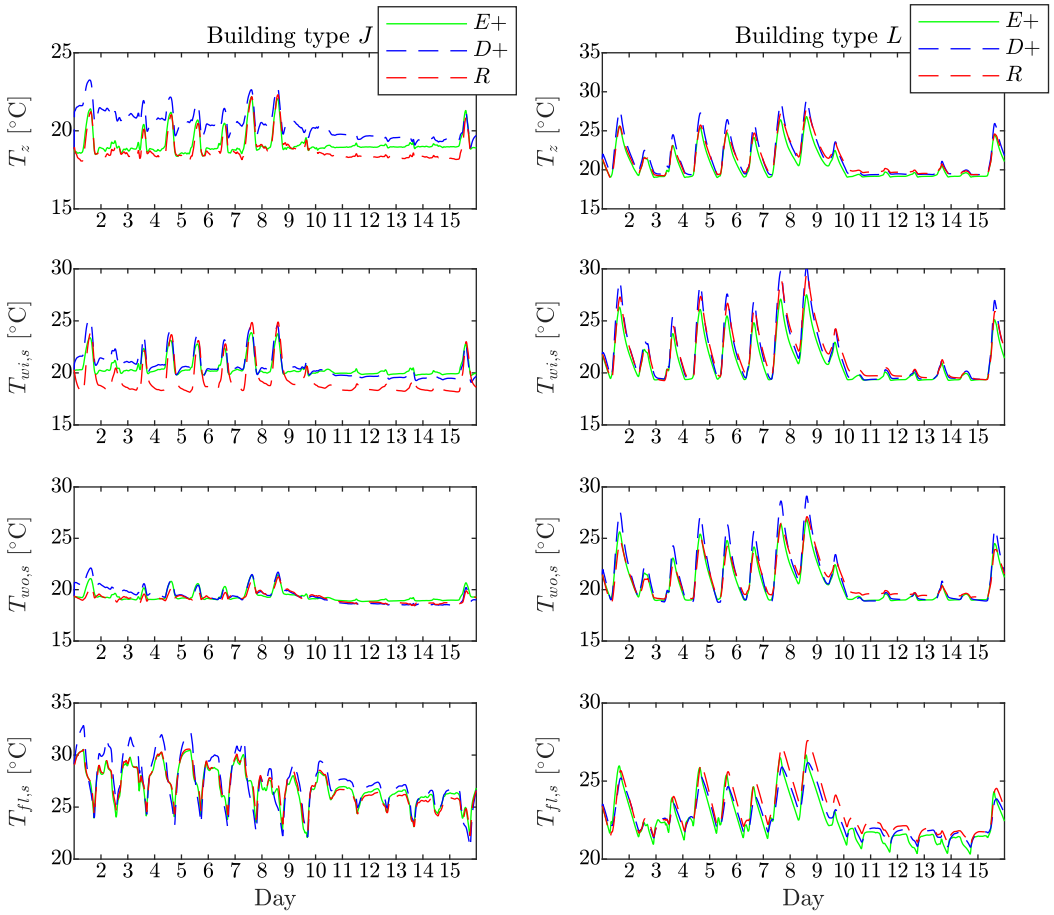

Figure 2.21: *Simulation results for the RC-models D+ and R compared to the EnergyPlus(E+) reference.*

Figure 2.21 shows the temperature trajectories for the models $D+$ and R for both building types. The results of model $D+$ for the component temperatures are significantly improved compared to model D. The initial solar s-factors were used in model $D+$ to assume no prior knowledge and a simple parameterization. R_{si} =0.13 $(\mathrm{m^2K})/\mathrm{W}$ was used for all components in model $D+$ despite the orientation, to assume the same convective and radiative coefficients as in model R. As mentioned earlier, T_z in model $D+$ includes a radiative zone temperature, therefore a direct comparison to the air temperature from the EnergyPlus model has limited validity. Thus, it is not surprising that T_z is estimated higher, especially for building type J. The three surface

temperatures are approximated with sufficient accuracy and the dynamics are better captured in contrast to the models D and F.
Figure 2.22 shows the $RMSE$s of the improved default model $D+$ in comparison with model D and R. The improved default mode $D+$ achieves lower $RMSE$s for all component temperatures for both buildings compared to model D. This finding is robust for all considered simulation periods. The results are close to those of model R, even partially outperforming them for certain simulation periods. The $RMSE$s for T_z improve slightly for type L while they deteriorate for type J. T_z is overestimated in both cases. As mentioned before, a direct comparison to the air temperature from EnergyPlus is no longer accurate, since model $D+$ approximates the operative temperature. Finally, fine tuning of model $D+$ by increasing α_{conv} from 2.5 to $7\,\mathrm{W/(m^2K)}$ as stated for panel heating systems in Table 2.5 did not improve the results.
It can be concluded from the additional investigation that a similarly good approximation can be obtained when radiation is considered in the total heat transfer coefficients at the component surfaces and all heating system input φ_h is assigned to the floor. An area-weighted distribution of the internal solar gains can remain. The resulting model $D+$ needs neither fitting nor increased model complexity and can be used as an initial guess.

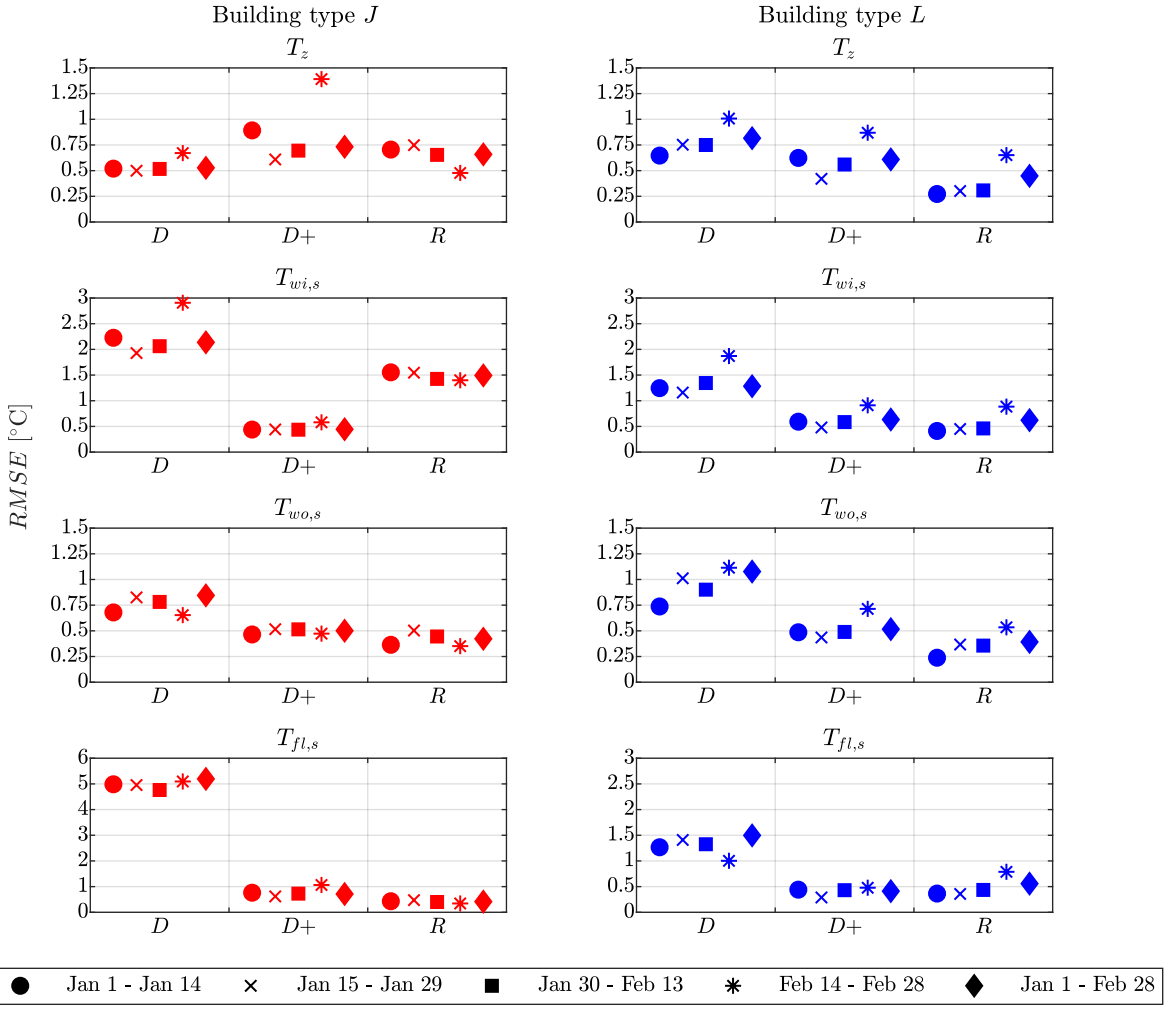

Figure 2.22: *$RMSE$ of the improved model $D+$ compared to the models D and R.*

Finally, after a visual validation and an assessment of the $RMSE$s over different simulation periods, Figure 2.23 shows the box-plots of the errors $(x_{RC} - x_{E+})$ in all states for all RC-

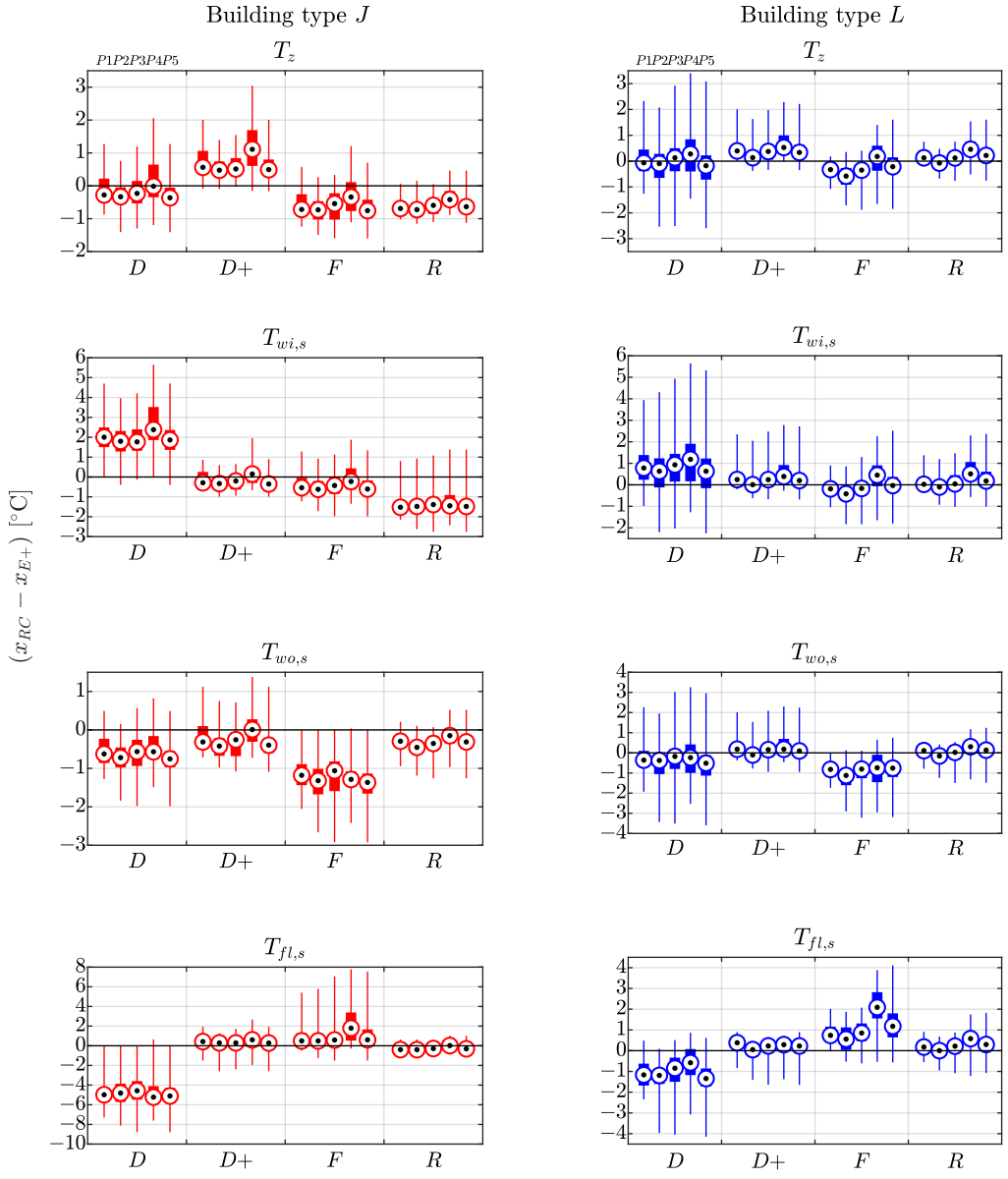

Figure 2.23: *Box-plots of the errors of the RC-models D, D+, F, and R over the simulation periods P1 (Jan 1-Jan 14), P2 (Jan 15-Jan 29), P3 (Jan 30-Feb 13), P4 (Feb 14-Feb 28) and P5 (Jan 1-Feb 28).*

models. The median of the errors is indicated by the midpoint, the bottom and top edges of the box indicate the 25th and 75th percentiles and the whiskers reach to the maximum negative and positive errors. Model R is able to reduce the worst case error range, especially for T_z and $T_{fl,s}$ for building type J and for all states for building type L. The low $RMSE$s of model R in T_z corresponds to possible maximum errors between $-1.15\,°C$ and $0.46\,°C$ for type J and $-0.76\,°C$ and $1.6\,°C$ for type L. While single underestimations of $T_{fl,s}$ to up to $-8.8\,°C$ are possible with the default model D for building J, deviations are considerably more limited when using model R.[22] For building type L, the medians indicate that model R is rather balanced between over- and underestimation of the state temperatures, depending on the simulated period. Although in a tolerable range, model R for type J tends to systematically underestimate T_z, $T_{wi,s}$ and $T_{wo,s}$. The enhanced default model $D+$ leads to an improvement for all temperatures for building type L, compared to model D. The results are similar to those of model R. The improvement from D to $D+$ for building type J is mainly achieved in the floor and inner wall temperatures.

Error Propagation versus 1-Step Prediction

The previous validation considered the RC-models' errors over longer simulation periods, where the progression of the temperatures was in part dependent on the previous output of the models. Based on Equation (2.37), the temperatures for the next time step were computed as

$$x_{t+1,RC} = Ax_{t,RC} + B\varphi_{t,h} + Ed_t. \tag{2.42}$$

Since the RC-models will be used for the purpose of simulation, a quantification of the errors including their propagation over the simulation time is justified. In the application of a realistic operation, one can use the linear RC-model to predict the next time step and then update the states with the measured values instead of the prediction of the subsequent time step:

$$x_{t+1,RC} = Ax_{t,E+} + B\varphi_{t,h} + Ed_t. \tag{2.43}$$

The error-prone simulation procedure based on Equation (2.42) is referred to as the simulation with error propagation, the prediction based on the actual reference measurements is referred to as the 1-step prediction (1+). The latter uses the zone and surface temperatures' reference values from EnergyPlus and recalculates the surface temperatures based on the relationships in Appendix A.9 to be applied in the RC-models, which define the temperatures in the components. An accurate prediction of the next time step is of great importance in predictive control [VKM+16a], since it is the last chance to adjust the controllable input.
Figure 2.24 shows the simulation results of model D for the zone and floor temperatures for both building types. The 1-step prediction achieves a relatively accurate approximation of the reference values in comparison to the simulation with error-propagation. Especially $T_{fl,s}$ can be predicted close to the actual value. The difference can be explained by the strong dependency of the floor's temperature on it's previous time step's value, expressed by the corresponding coefficients in system matrix A of the linear model.

[22] One might wonder why the extreme values of the full simulation period ($P5$) are not necessarily determined by those from the consecutive periods $P1$-$P4$. This results from the fact that $P1$-$P4$ are each initialized with the EnergPlus reference values in contrast to $P5$, which continues with deviating state values from the simulation with error propagation.

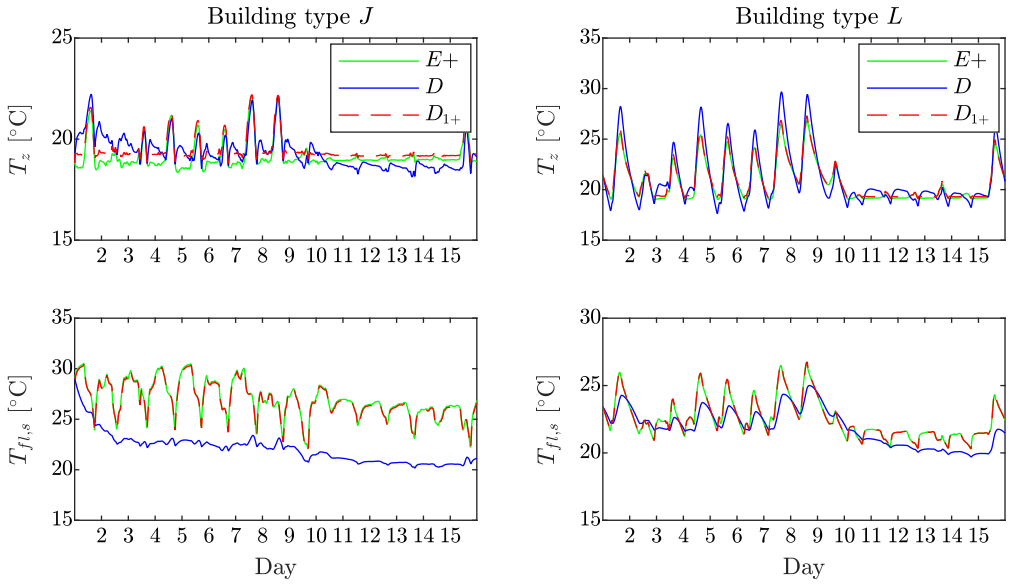

Figure 2.24: *Results for the simulation with error propagation and 1-step prediction* (1+) *over the period Feb 14-Feb 28 for default model D.*

Table 2.8 states the $RMSE$ and coefficient of determination R^2, here defined as

$$R^2 = \frac{\sum_{i=1}^{N}(x_{i,RC} - \bar{x}_{E+})^2}{\sum_{i=1}^{N}(x_{i,E+} - \bar{x}_{E+})^2} = 1 - \frac{\sum_{i=1}^{N}(x_{i,RC} - x_{i,E+})^2}{\sum_{i=1}^{N}(x_{i,E+} - \bar{x}_{E+})^2} \tag{2.44}$$

for both the simulations with error propagation and 1-step prediction for models D and R. R^2 measures the proportion of the variance of the temperatures explained by the RC-models and is used as a measure to quantify the model fit. The RC-models exhibit a structure like a multiple linear regression model, but their coefficients are not result of a least squares regression method. $R^2 = 1$ means that all variance in the reference data obtained from EnergyPlus can be explained by the RC-model. $R^2 < 0$ indicates that the RC-model performs worse than using the mean $\bar{x}_{E+}$ as a predictor.

The 1-step prediction results in lower $RMSEs$ and a higher R^2 for all states and models for both building types compared to the simulation with error propagation. Even the default model D achieves a relatively low $RMSE$ and high explanatory power for the 1-step prediction. Model R improves the results further, with all values of R^2 above 0.97 for building type J and 0.99 for type L. The negative results for R^2 of some component temperatures underscore the limitation of the models to accurately track the temperatures when the simulation is carried out with error propagation. This is in line with the observations made in the previous paragraphs. With the exception of $T_{wi,s}$ does model R provide the best model fit for the simulation with error propagation for both building types. The results for model $D+$ and F are given in Appendix A.10.

It can be concluded that the temperature errors of the RC-models may reduce significantly when the prediction horizon is limited to the next step and the model is updated with reference measurements of the states. Even a simple initial guess model like model D yields a reasonable approximation, when the linear model exhibits a strong dependency on the states of the previous time step.

Table 2.8: *Accuracy of the simulation with error propagation (Sim.) versus 1-step prediction error (1+) of models D and R for building types J and L over the period Feb 14-Feb 28.*

		D				***R***			
		$RMSE$ [°C]		R^2 [ ]		$RMSE$ [°C]		R^2 [ ]	
		Sim.	1+	Sim.	1+	Sim.	1+	Sim.	1+
J	T_z	0.7	0.4	0.083	0.748	0.5	0.1	0.536	0.978
	$T_{wi,s}$	3.0	0.4	-9.529	0.769	1.4	0.2	-1.438	0.973
	$T_{wo,s}$	0.7	0.1	-0.465	0.960	0.4	0.0	0.577	0.995
	$T_{fl,s}$	5.1	0.2	-7.476	0.990	0.3	0.1	0.961	0.998
L	T_z	1.0	0.2	0.727	0.987	0.7	0.2	0.886	0.993
	$T_{wi,s}$	1.9	0.2	0.167	0.991	0.9	0.1	0.814	0.998
	$T_{wo,s}$	1.1	0.2	0.684	0.994	0.5	0.1	0.927	0.999
	$T_{fl,s}$	1.0	0.1	0.495	0.998	0.8	0.1	0.691	0.998

Power and Energy Demand

So far, the temperature trajectories of the RC-models have been simulated with the power input from EnergyPlus. Finally, the power and energy demand from an optimization with the RC-models are assessed to quantify the impact of the models on the power profiles. At each time step $t = 1, \dots, T$ of the simulation period, the optimization problem (2.45)[23], here stated for model D, is solved to compute the minimum required power φ_h over the next 15 minutes to keep T_z above the temperature from EnergyPlus. The mean of the zone temperature from EnergyPlus is above the predefined threshold, but the zone temperature falls below the threshold in some cases due to the rule-based control in EnergyPlus. Thus, the optimization uses the EnergyPlus reference $T_{z,E+}$ rather than a fix minimum temperature to not bias the comparison. The heating power φ_h is limited to the maximum value observed over the reference simulation in EnergyPlus. The slack variable s is introduced to guarantee feasibility of the problem with respect to the temperature constraint and is penalized by the scalar π. A relatively high price of e.g. $\pi = 10^6$ forces the solver to avoid excessive use of the slack variable.

$$\begin{aligned} \underset{\varphi_h, s}{\text{minimize}} \quad & \varphi_h + \pi s \\ \text{subject to} \quad & (2.31), (2.32), (2.33), (2.34) \\ & T_z \geq T_{z,E+} - s \\ & 0 \leq \varphi_h \leq \varphi_{h,max,E+} \\ & 0 \leq s \leq s_{max} \end{aligned} \tag{2.45}$$

Each of the simulations is carried out with error-propagation, thus the temperatures computed with the RC-model are used to initialize the next time step. Table 2.9 shows the total energy demand, the relative percentage deviation from the energy demand obtained from EnergyPlus and the RMSEs of the power and zone temperature over the period Jan 1-Feb 28 for all RC-models investigated. The total energy demands of the RC-models are close to the demands from EnergyPlus. Model F for building type J results in the largest deviation of 4.86%, the best result in terms of energy demand is achieved by model R for type L with an underestimation of just 1.05%. While the models D ($D+$) and F tend to overestimate (underestimate) the required

[23] The continuous-time dynamics in (2.31)-(2.34) are discretized to solve the optimization problem. The dynamics in problem (2.45) are adapted for the other models, accordingly.

energy demand independent of the building type, model R leads to over- or underestimation depending on the standard. This is confirmed for the most part when the four shorter simulation periods $P1$ to $P4$ are looked at. D (exception in $P4$) and F overestimate the demand for both building types, $D+$ underestimates. Model R always overestimates for building type J, while both over- and underestimation occur for type L depending on the period. The varying energy demands can be explained by the nature of the different modeling approaches of the RC-models, since they differ in the distribution of the heating input and the heat transfers between the components. The zone temperatures obtained from solving (2.45) are close to the reference values from EnergyPlus, with a slightly higher error for building type L.

Table 2.9: *Results for the power simulation over the period Jan 1-Feb 28.* $\Delta t = 0.25\,\mathrm{h}$ *by discretization.*

		Energy Demand		*RMSE*	
		$\sum \varphi_{h,RC} \Delta t$ [kWh]	$(\frac{\sum \varphi_{h,RC}}{\sum \varphi_{h,E+}} - 1)100\%$ [%]	$\varphi_h - \varphi_{h,E+}$ [kW]	$T_z - T_{z,E+}$ [°C]
J	D	6,129.6	1.82	1.065	0.05
	$D+$	5,794.3	-3.76	0.944	0.08
	F	6,312.8	4.86	1.293	0.17
	R	6,267.1	4.1	0.864	0.11
L	D	1,336.0	4.15	0.646	0.58
	$D+$	1,259.3	-1.83	0.675	0.49
	F	1.313.2	2.37	0.558	0.24
	R	1.269.3	-1.05	0.800	0.31

Rather high deviations in the range of $0.6-1.3\,\mathrm{kW}$ occur in the difference between the power profiles computed with problem (2.45) and those from EnergyPlus. Especially model R for building type L exhibits a difference similarly large as for building type J, even though the latter has an almost twice as high maximum power of φ_h. Figure 2.25 shows the zone temperature and heating power from EnergyPlus and RC-model R over the last 15 days of February to analyze the power profiles in more detail. The simulation with problem (2.45) achieves a good approximation of the temperature reference from EnergyPlus for both building types, with only minor use of the slack variable to relax the problem. Three observations can be made for φ_h of type J. Firstly, the operation time resulting from the optimization with the RC-model is very close to the reference. It covers 98% of the on-time in EnergyPlus, which corresponds to a total time of approximately 12 days. Secondly, the magnitude of φ_h follows the operation in EnergyPlus in general, with the slight tendency to overestimate the demand. This is in line with the corresponding result from Table 2.9. Thirdly, the power profile of the RC-model is more volatile, with maximum peaks not always being coincident with those from the reference. This is also observable for building type L, where the optimization sometimes results in operation where the reference system in EnergyPlus does not provide power to the floor. This can be explained with a difference in the propagation of the states due to model errors and the freedom of the solver to correct for a solution which is both energy minimal and above the zone temperature of the reference.

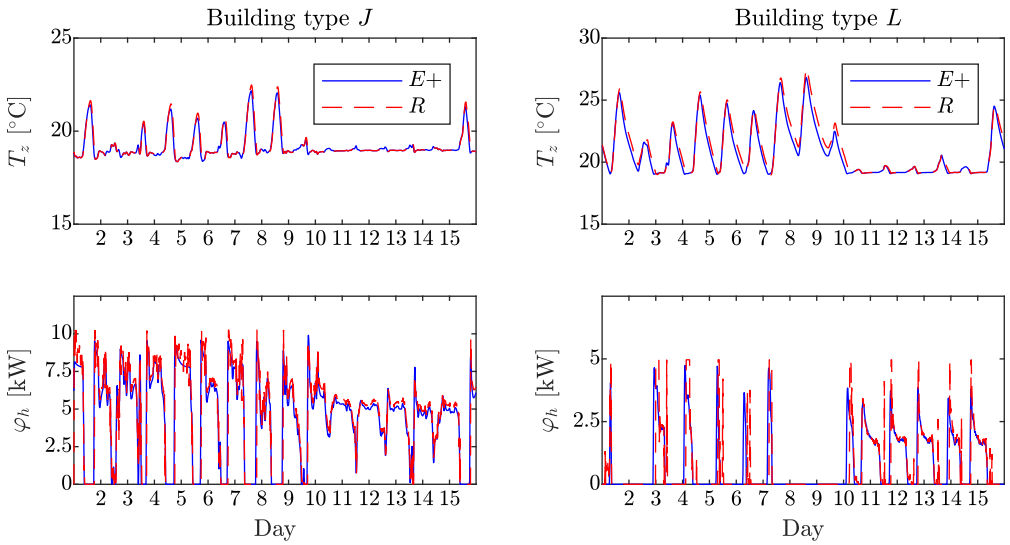

Figure 2.25: *Results for the power optimization simulated over the period Feb 14-Feb 28 for model R.*

Applying problem (2.45) on model R leads to partial overestimations of the peak power. Further fine tuning of the optimization can achieve an even closer tracking of the power trajectories from EnergyPlus, e.g. by use of time specific limits on φ_h from EnergyPlus and inter-temporal constraints and penalties to flatten the resulting profiles. A model predictive controller offers a convenient approach to account for such restrictions and is introduced in Chapter 3.

Energy Demand vs. TABULA Estimates

Finally, an annual simulation of the RC-model R is carried out for types L, J and also type E. Even though the latter has not been validated in the previous section, it is assumed that the validated modeling approach can be applied to other SFH types. The specific annual heat demand is calculated and compared to the TABULA reference values. In order to compare simulation results with values from the TABULA typology, boundary conditions in the simulation of the RC-models have been partially changed to approximate those from the standard TABULA calculation. The one-step optimization has to keep the zone temperature above 20 °C, which is the same comfort temperature used in the TABULA calculation. A heating limit of 12 °C is assumed and the mean of the ambient temperature time-series is shifted to obtain a similar amount of degree days as used by TABULA. The solar gains through each of the windows are scaled to the heating period values assumed in TABULA and further reductions through shadowing and window frames are considered. Internal gains are taken into account with constant $3\,\frac{\mathrm{W}}{\mathrm{m}^2}$ in contrast to the time-varying model introduced in Section 2.6, which is used in the remaining parts of this work. Finally, each of the three building types are geometrically parameterized as given in the typology, leading to different surface areas, e.g. floor, outer wall or window areas per cardinal direction. This is in contrast to the previous validation section, where the geometry of building J was also assumed for type L for comparability of the modeling approaches.

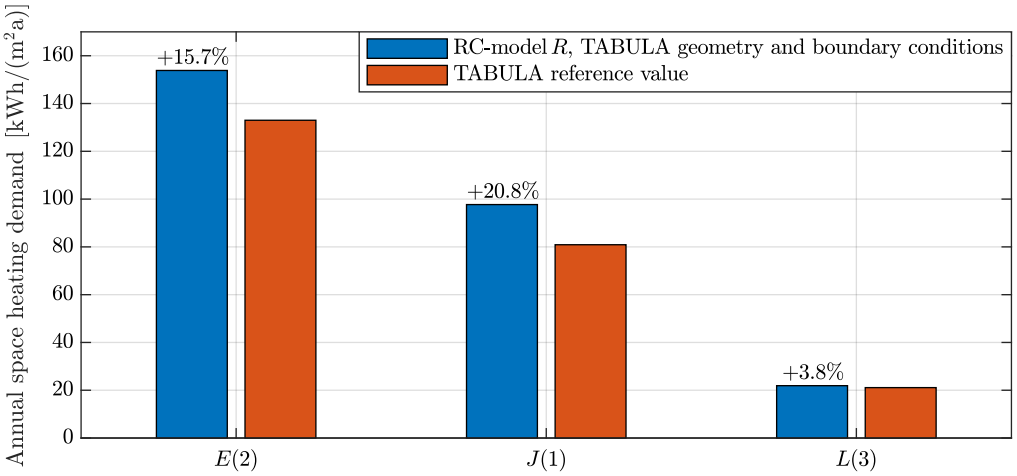

Figure 2.26: *Annual specific space heating demand of RC-model R and the TABULA standard calculation reference value*

For simplicity the single zone RC-modeling approach takes into account the whole volume enclosed by the envelope for ventilation losses, including the attic volume. This was a reasonable assumption for the validation against the single zone reference model implemented in EnergyPlus. In contrast, the TABULA calculation considers only the net living area multiplied with the standard floor height. Since the simulation results were rather sensitive to ventilation losses, the ventilation coefficients were corrected to assume similar air volumes and system efficiencies as used in the TABULA typology. Finally, the annual energy demand values are related to the reference area from TABULA. Figure 2.26 shows the different energy demands among the three building types. The RC-model R manages to reproduce the differences in energy demand due to different insulation standards but estimates the demand higher compared to the reference values from TABULA. Since the static TABULA calculation is a simplified approximation of the demand itself, there is no final answer to which final value is more accurate.

2.2.8 Conclusion

The presented single zone model remains a strong simplification of multi-zonal constructions in real buildings, including e.g. bathrooms with different set-points and highly user-dependent temperatures. The validation section has shown that it is possible to approximate the transient simulation of an exemplary single zone SFH based on a set of four first-order differential equations. A further model reduction might be possible but was not tested. The validation of the variants of the RC-model shows the importance of accounting for radiation in the model. Initial model D showed a reasonable accuracy to predict T_z, but failed to track component temperatures such as the surface temperature of the floor. Modeling radiation by either the use of lumped heat transfer coefficients at surfaces or an explicit resistance between the floor and the outer walls improved the results significantly and allows to simulate the progression of the states with high accuracy. In a cross-validation over different periods, a RMSE below 1 °C was achieved by model R for all temperature states in building L and all but the inner wall temperature for building J for all considered simulation periods. Model R shows not only satisfying results for T_z and $T_{fl,s}$ but also leads to reasonable close energy demand values and power profiles. It is used as the model structure in the remaining chapters. If only the 1-step ahead prediction is considered and states are continuously updated by measurements from a reference system, even a simple initial guess model D shows sufficient accuracy since model errors do not propagate with time.

It is important to note that the validation is restricted to the given temperature, disturbance and heating input time-series from EnergyPlus compared to a simple model with predefined resistances and capacitances. To completely capture the dynamics of a system including the active thermal mass, pseudorandom binary excitation signals are commonly used for the heating system input in experiments to identify the system's response over the full range of frequencies, see e.g. [MH95, LMB12]. As a consequence, there is no guarantee that the RC-model gives a correct response to strongly different control signals as they will occur in the coordination problems analysed in Chapter 5.

2.3 Thermal Model Dynamic Response

Figure 2.27 shows the final RC- model parameters obtained from the previously described modeling approach. While the floor has the largest thermal capacity in modern building L, the older buildings J and E have a high thermal mass located in the outer walls. The contribution by the air volume of the zone is small compared to the other capacities. The resistances reflect the difference in insulation standard. Especially the resistances in direct connection to ambient disturbances ($R_{wo,2}$, $R_{fl,2}$ and R_{vent}) are significantly higher for building L. The lower inward resistances allow for a higher heat transfer to the capacities of the components. The third subplot shows the multiple time constants $\tau_i = -\frac{1}{\lambda_i}$ computed based on the eigenvalues λ_i of the system matrix A of each building.[24] The values range from below an hour for the zone to over 100 hours for the outer walls in building L corresponding to both slow and fast dynamics. In contrast to a first-order model with one distinct time constant, the state response of the fourth-order model results from a weighted sum of exponential components with the corresponding eigenvalues.

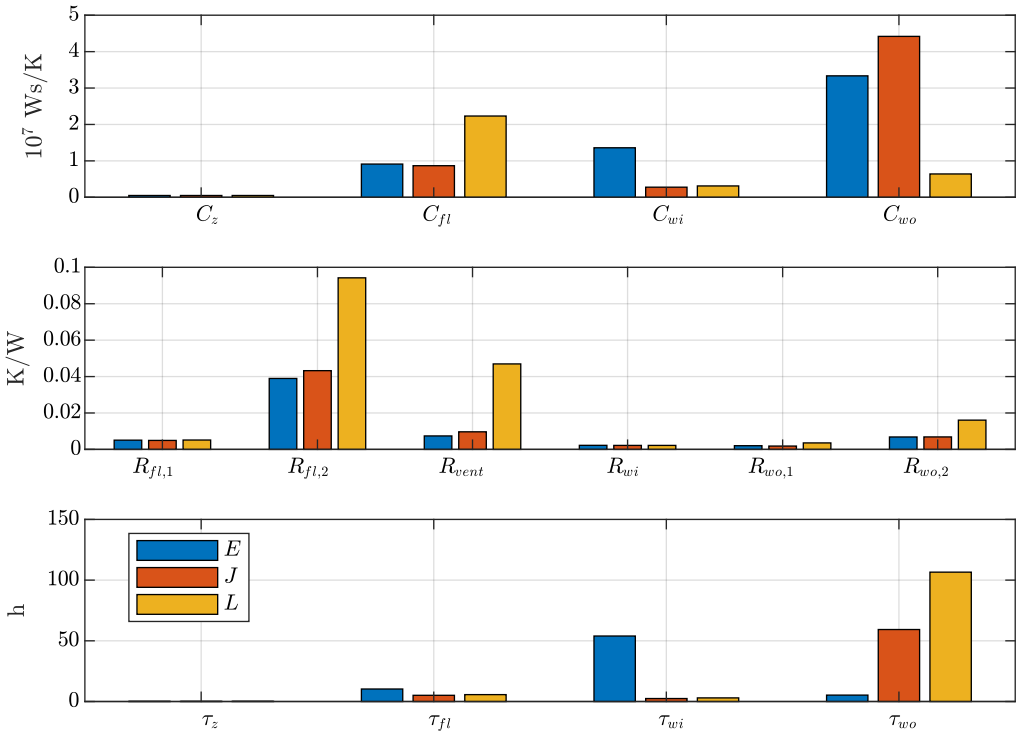

Figure 2.27: *Parameters of RC-model R.*

[24] All eigenvalues of matrices A for all buildings are real and negative. The systems are asymptotically stable.

Figure 2.28 shows the transition of the states over 24 hours when all temperatures in the building are initialized at 22 °C and for a case where the floor is preheated to 29 °C. All inputs to the model (heating, disturbances) are assumed to be zero. While all states cool down in the first case, this happens faster for buildings E and J compared to building type L where the zone temperature stays above 20 °C for almost 6 hours. When the floor is preheated to 29 °C, building L shows an increase in the zone temperature for the first 2.5 hours, followed by a decrease for 12.5 hours to return back to the initial 22 °C. One can observe how the direction and change in temperature per time are governed by different time constants and differences between component temperatures. Fundamentals of the so-called homogeneous response are given in Appendix A.11.

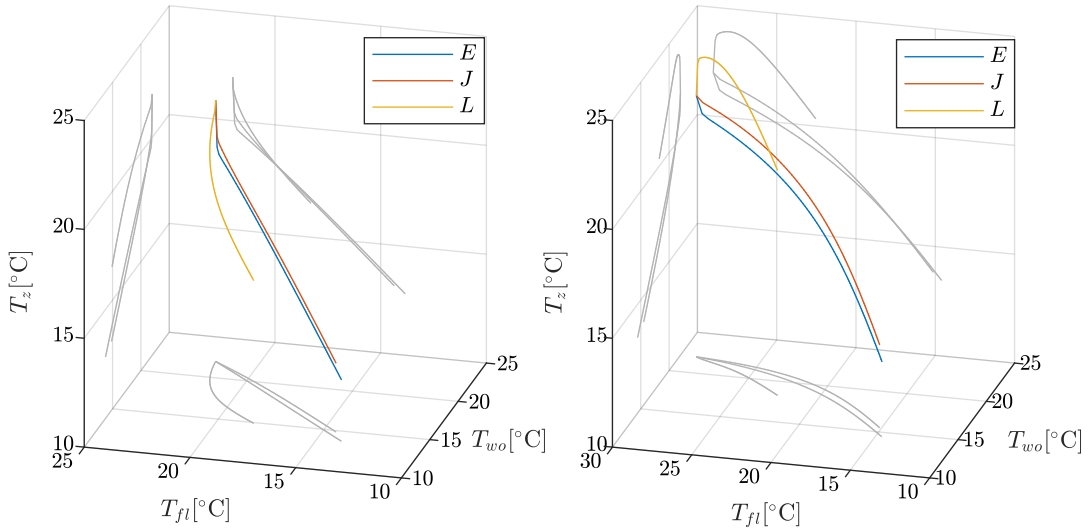

Figure 2.28: *Transient trajectories with the initial states* $x(0) = (T_z(0), T_{wi}(0), T_{wo}(0), T_{fl}(0))^T$ *for the cases* $(22, 22, 22, 22)^T$ *and* $(22, 22, 22, 29)^T$ *in* °C *over 24 hours.*

Figures 2.29 and 2.30 show the step responses of RC-model R for the three building types for either a sudden increase from zero to an ambient temperature of $T_a = 1\,°\text{C}$, solar gains of $\varphi_{sg} = 100\,\text{W}$ or a heating input of $\varphi_h = 100\,\text{W}$. All states are zero for $t = 0$ and the scaled Heaviside step function is assumed at $t \geq 0$ for the respective input while the other inputs remain zero throughout time. The step responses within the first hours in Figure 2.29 show the fast reaction of T_z to the ambient temperature increase, followed by the other states. A similar but less pronounced response can be observed for the solar gains input. The step response to a sudden heating input in the floor causes a fast reaction in T_{fl}, followed by the zone and wall temperatures. Figure 2.30 shows that buildings E and J have a similar behavior with a higher absolute response to the temperature increase compared to building L. A thermal gain of 100 W results in a higher final steady state for type L due to the better insulation standard. Building L needs roughly around twice the time to arrive at it's new steady state when the rise (the time of the step response to rise from 10% to 90% of its final value) and peak times are compared to those of buildings J and E.

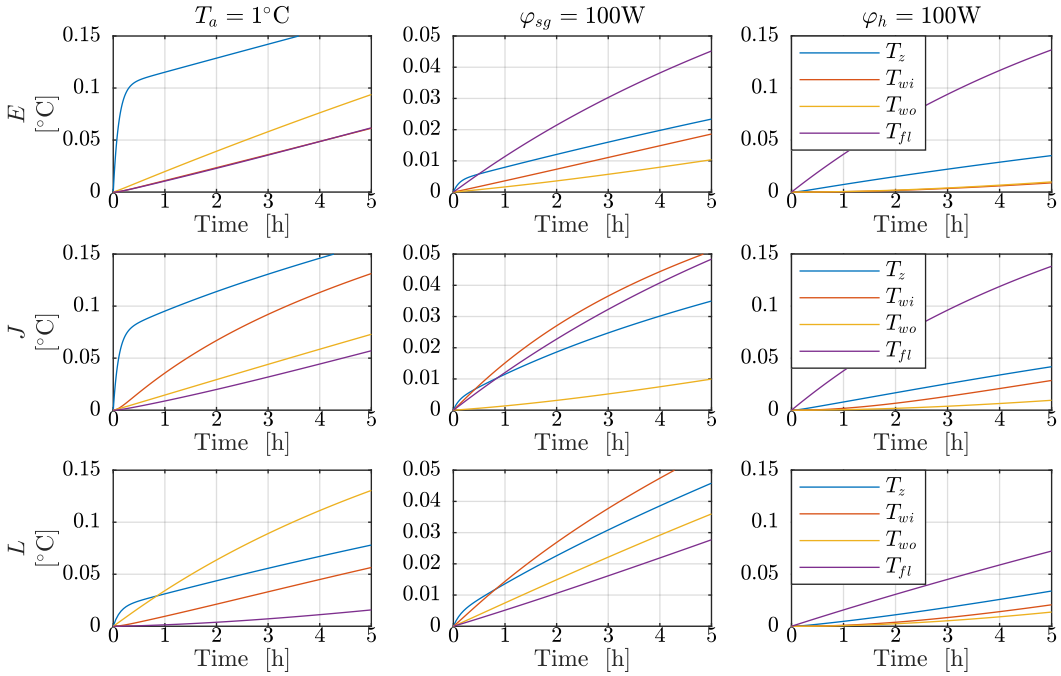

Figure 2.29: *Step responses of all states of the continuous-time RC-model R for building type E, J and L.*

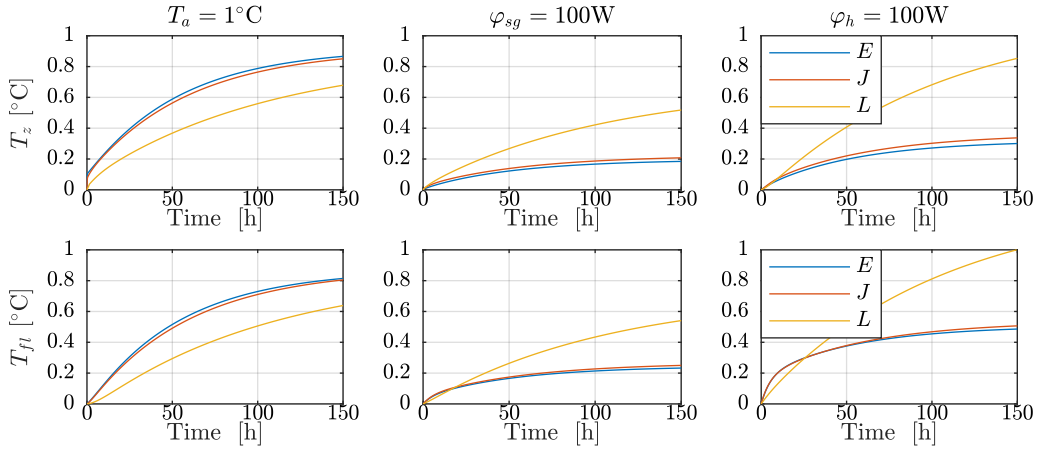

Figure 2.30: *Step responses of T_z and T_{fl} of the continuous-time RC-model R for building type E, J and L.*

2.4 Design Heat Load and Heat Pump System

The DIN EN 12831 [DIN14] defines methods for the calculation of the design heat load for a building or a zone. The transmission and ventilation heat losses are computed based on the envelope areas and total heat transfer coefficients to quantify the total heat loss to the outside to be compensated by the heating system. The calculation is carried out for a given zone air standard temperature of 20 °C and a location-specific extreme ambient temperature. Solar radiation and inner thermal gains are neglected. In this thesis, the system of the differential

Equations (A.51)-(A.54) for model R is solved for its steady state

$$\dot{x}_{RC} = 0 \tag{2.46}$$

with a fixed set point temperature $T_z = 20\,°\text{C}$ and fixed ambient conditions for the calculation of the design heat load. The heat load gives a limit for the maximum thermal power of the heat pump to select. The value of the heat load at the local norm ambient temperature, e.g. $-16\,°\text{C}$ for Munich, is commonly used to dimension the heating system. Figure 2.31 shows the heat load for the building types over the ambient temperature T_a with fixed $T_g = 10\,°\text{C}$ and the points of operation for the annual 1-step simulation. In Munich, systems of 2.9 kW, 9.3 kW and 10.6 kW would be chosen to cover the space heating demands. The maximum power $\varphi_{h,max}$ of the input is limited to the values specified above. Due to the solar gains, power is not always required at the heat load defined value for a given temperature. Similarly, sudden changes in temperature may require the heating system to operate above the heat load value. In contrast to types E and J, building L does not operate at ambient temperatures above 10 °C due to it's good insulation. When temperatures become very cold, type L operates mainly at $\varphi_{h,max}$.

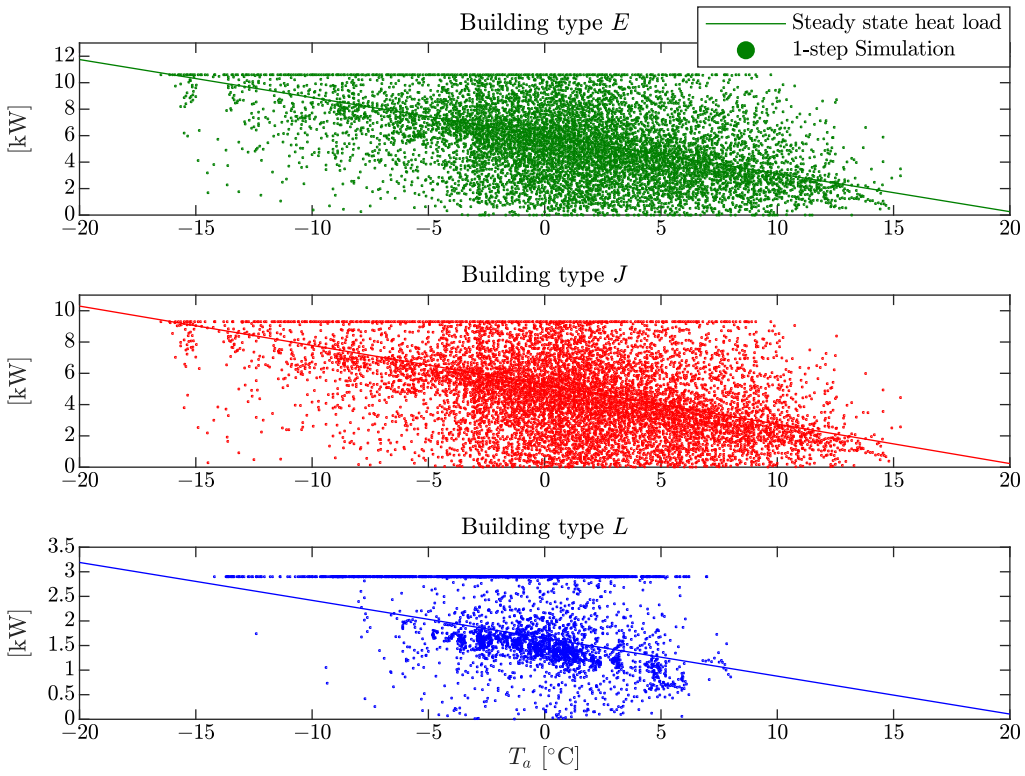

Figure 2.31: *1-step simulation results versus the steady state heat load.*

2.4.1 Heat Pump Model

The instantaneous efficiency of the operation of a heat pump is measured by its coefficient of performance η (COP), which is defined as the ratio of the heat delivered to a building for space heating and domestic hot water to the electrical demand of the heat pump. In case of an air-to-water heat pump, the thermal power provided for heating is the sum of the extracted heat from

the ambient at the evaporator and the electrical demand of the compressor of the heat pump:

$$\dot{Q}_{hp} = \dot{Q}_{amb} + P_{hp,el} \tag{2.47}$$

$$\eta = \frac{\dot{Q}_{hp}}{P_{hp,el}} = \xi \eta_C. \tag{2.48}$$

A theoretical upper bound for the COP η of a heat pump working at Carnot efficiency is given by

$$\eta_C = \frac{T_{supply}}{T_{supply} - T_{source}} \tag{2.49}$$

in absolute temperatures [VDL+12]. The supply and source temperatures are located at the evaporator and condenser side. Equation (2.49) demonstrates how the efficiency of a heat pump increases with a decreasing difference between the source and supply temperatures. For a constant supply temperature, the COP decreases for lower ambient temperatures in the winter, requiring more compressor power to deliver the same amount of thermal power. With increasing ambient temperatures, both the COP and the heating capacity of the heat pump increase [DB13]. Heat pumps are preferably combined to modern floor heating systems with relatively low supply temperatures to maintain efficient operation in cold climates accordingly. Such systems have common supply temperatures of $30 - 35\,^{\circ}\mathrm{C}$, but it is possible to efficiently use heat pumps for supply temperatures up to $55\,^{\circ}\mathrm{C}$ in older buildings [Bru06]. In contrast, domestic hot water provision and radiators usually require higher supply temperatures.
The COP in real operating conditions deviates from the theoretical upper bound by the loss factor ξ, resulting from the system dependent losses of the heat pump. The real COP is a nonlinear function of the states of the source and supply temperatures, the compressor frequency in case modulation is possible and other variables to take the overall losses in the evaporator, compressor, condenser and expansion valve into account. When the COP from Equation (2.48) is used in an optimal control problem, the resulting optimization problem becomes non-convex due to the product of the supply temperature (as a state of the system itself) and the controllable electrical power. To ensure a convex formulation of the heat pump efficiency in the optimal control problem, complex models with numerous additional states within the heat pump are often avoided and only the most dominant processes considered.
The authors in [Wim04, Bia06] concluded that in the case of an on-off air-to-water heat pump, a COP prediction based on the ambient temperature and the heat pump's characteristic curve of operation for given nominal supply temperatures is sufficient, since the ambient temperature has the strongest impact on the COP. By neglecting the COP's dependency on the state of the supply temperature, convexity of the optimal control problem was guaranteed. The COP was predicted beforehand over the prediction horizon, based on the weather forecast and the fixed nominal supply temperature. The works in [VDL+12] and [VLvH12] were based on the low-order building models identified in [Wim04, Bia06] and investigated the impact of different COP formulations on the controller's performance for a variable-speed air-to-water heat pump directly connected to a floor heating system. Modulation impacts the COP due to frequency dependent losses in the compressor and heat exchangers. The most detailed COP formulation in [VLvH12] considered the nonlinear dependency on the source and supply temperatures and the compressor frequency based on a fitting on manufacturer data, whereas the most simple formulation was a constant approximation of the COP over the prediction horizon. The resulting differences in electricity costs and discomfort for each COP formulation were evaluated and compared to a reference heating curve control. While the nonlinear model resulted in continuous part-load operation, the convexified COP formulations led to stronger power peaks and an increase in energy consumption ranging between 7%-16%. Nevertheless, similar operational behavior and efficiency

could be achieved by additionally penalizing power peaks in the controller's cost function with a quadratic term, allowing for the use of the convexified COP formulations. Interestingly, even though all COP formulations were tested in an MPC strategy to make use of the operational flexibility, only the nonlinear COP formulations could achieve a reduction of the electricity cost compared to the heating curve operation in an on-off peak tariff scenario, since the relaxed formulations led to an on-off operation of the heat pump resulting in deterioration of the real COP. The authors in [VLOA13] treated the nonlinearity between the supply temperature and heat pump's power in a single building study by iteratively solving the complete continuous-time dynamics at the steady state over the prediction horizon to obtain a current approximation of the supply temperature. This is not considered here to avoid the additional computational burden to be carried out at each time instant. A detailed model of a variable-speed air-to-water heat pump connected to a stratified storage was presented in [FBMW17] to test MPC for a multi-family house supplied by radiators. The COP's dependency on the compressor frequency was taken into account by the definition of two operational ranges and a Taylor linearization of the COP within these ranges. Variable-speed heat pumps achieve the best COP's during part load operation. Measurements for different operating conditions of the modulating heat pump showed an increase of the COP up to the optimal compressor frequency and an almost linear decrease of the efficiency beyond the optimal frequency. A convexified model was used and the computed control signals were forwarded to a detailed reference model to receive the storage temperatures. Even though a realistic performance of the heat pump could be modeled in a convex optimization problem, the linearization and definition of operational ranges came at the cost of additional decision variables.

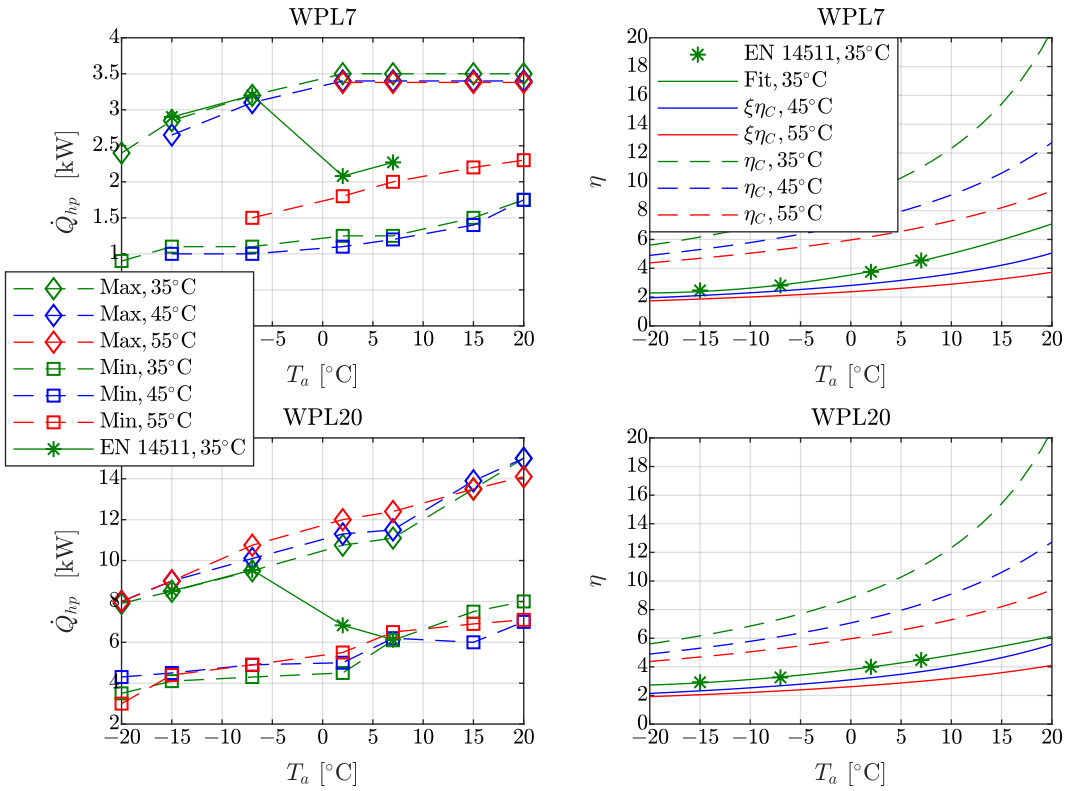

Figure 2.32: *Heat pump heating capacity range and the COPs η for different supply temperatures based on manufacturer data [Sti17] for two air-to-water heat pumps.*

To conclude, the use of convexified COP formulations can lead to an underestimation of the

energy consumption and higher power peaks, when the latter is not penalized. In order to keep the number of decision variables per building low, a time-varying, precalculated COP depending on the ambient temperature and a fixed supply temperature is used here. Figure 2.32 shows the maximum and minimum thermal capacity characteristics for two variable-speed air-to-water heat pumps and the COPs from manufacturer data taken from [Sti17]. The manufacturers' COPs are measured based on the testing procedure of the DIN EN 14511 [DIN18] for certain ambient temperature points when the supply temperature is fixed at 35 °C. The points are used here for a polynomial fitting and the COP curves for higher supply temperatures are then estimated based on the relationship between the upper bound and system COP in Equation (2.48). The fitted COP model at the supply temperature of 35 °C is

$$\eta_{35°\mathrm{C}}\Big(T_a(t)\Big) = a_1 T_a(t)^2 + a_2 T_a(t) + a_3 \tag{2.50}$$

with the parameters in Table 2.10.

Table 2.10: *Polynomial fitting coefficients for the COP model.*

Heat pump	a_1	a_2	a_3
WPL7	0.0029	0.1198	3.534
WPL20	0.0015	0.0851	3.811

ξ from Equation (2.48) can now be estimated by dividing $\eta_{35°\mathrm{C}}$ by $\eta_{C,35°\mathrm{C}}$ and the functions for other supply temperatures are obtained by scaling with ξ accordingly. This assumes the same systematic efficiency loss for all supply temperatures. The COP's dependency of the modulation frequency is neglected. Currently available manufacturer data does not provide information regarding the COP and the modulation frequency. The maximum heating capacity of the heat pumps increases with increasing ambient temperatures but is regulated for WPL7. The limits are similar for different supply temperatures. One can also observe how the EN 14511 test points are close to the maximum capacity for low ambient temperatures. Thus, the error introduced with the COP model in Equation (2.50) will be larger for milder, part-load operation conditions then for cold full-load conditions. As can be seen in Figure 2.32, the COP approaches a value of 2 for cold conditions, which is close to the value of 1.8 used in the study in [BDI18].
Since the minimum heating capacity increases with increasing ambient temperatures, the system of choice must not be overdimensioned to keep the part-load operation during milder conditions feasible [Sti17]. The minimum heating capacity for the variable-speed heat pumps is neglected in the problem formulation since the dead band of operation requires modeling of a semi-continuous function including a binary decision variable. A fully continuous range of operation from zero to the maximum ambient temperature dependent value is assumed here for convexity:

$$0 \leq \dot{Q}_{hp}(t) \leq \dot{Q}_{hp,max}(t). \tag{2.51}$$

Since the simultaneous operation at different supply temperature levels is not possible, systems in practice prioritize domestic hot water provision $\dot{Q}_{hp,dhw}$ over the supply for space heating $\dot{Q}_{hp,sh}$ in rule-based control. Again, binary decision variables would be required, see also the discussion in [PH14]. A hybrid operation to supply water at different temperature levels in

parallel is assumed here to keep the problem convex:

$$0 \leq \dot{Q}_{hp,sh}(t) + \dot{Q}_{hp,dhw}(t) \leq \dot{Q}_{hp,max}(t) \tag{2.52}$$
$$0 \leq \dot{Q}_{hp,sh}(t) \tag{2.53}$$
$$0 \leq \dot{Q}_{hp,dhw}(t). \tag{2.54}$$

The relationship to the electrical demands of the heat pump for space heating and domestic hot water is then given by

$$\dot{Q}_{hp,sh}(t) = \eta_{sh}\Big(T_a(t)\Big) P_{hp,sh}(t) \tag{2.55}$$
$$\dot{Q}_{hp,dhw}(t) = \eta_{50°\mathrm{C}}\Big(T_a(t)\Big) P_{hp,dhw}(t). \tag{2.56}$$

Delays due to on- and off-switching were considered in [Wim04] but are neglected here. Such effects occur in the range of seconds to minutes and thus will not be captured by the 15 minutes discretization intervals used here.
The extreme cold temperatures which define the design heat load for a building occur only a few times during the heating season. A heat pump dimensioned to supply the demand at the design temperature is usually overdimensioned for the most time of the year. While on-off heat pumps will result in frequent switching, modulating systems might still require a too high minimum heating capacity and not work efficiently during part-load conditions. As an alternative to the monovalent setup, bivalent monoenergetic systems are equipped with a direct electric back-up heater, located in the heat pump itself or in a buffer storage. The heat pump is dimensioned to fully cover the heat load until the so-called bivalence temperature. The back-up heater then supports at temperatures below the bivalence temperature, usually below $-5\,°\mathrm{C}$. In standard rule-based control, the total operating hours of the back-up heater are limited to a few hours per year to not impair the overall efficiency of the heating system. See [Sti17] for heat pump planning principles. Modeling such a constraint is not required for the predictive energy management strategy developed in Chapter 3, since the controller will decide whether or not the back-up heater has to be used in the optimal control strategy.
Analogously to the constraints (2.52)-(2.54), it must hold for the back-up heater that

$$0 \leq \dot{Q}_{bh,sh}(t) + \dot{Q}_{bh,dhw}(t) \leq \dot{Q}_{bh,max}(t) \tag{2.57}$$
$$0 \leq \dot{Q}_{bh,sh}(t) \tag{2.58}$$
$$0 \leq \dot{Q}_{bh,dhw}(t). \tag{2.59}$$

It is assumed that the delivered heat equals the electrical demand:

$$\dot{Q}_{bh,sh}(t) = P_{bh,sh}(t) \tag{2.60}$$
$$\dot{Q}_{bh,dhw}(t) = P_{bh,dhw}(t). \tag{2.61}$$

Finally, heat pump WPL7 is selected for building type L, WPL20 for building types J and E and the back-up heater is always dimensioned to 8.8 kW. Table 2.11 shows the reference supply temperatures selected for the computation of the COPs and maximum heating capacities for each building type. The choice of temperatures for the COP for space heating η_{sh} can be considered a conservative estimate, since lower temperatures will be possible most of the time. T_{fl} is limited to maximum temperatures of $30, 34$ and $37\,°\mathrm{C}$ for the three building types to limit the possibility to overheat or pre-charge the floor. The two older building types require such high floor temperatures to maintain T_z above $20\,°\mathrm{C}$ during very cold days. The resulting surface

temperature of the floor[25] is never above the limit of 29 °C for type L, but exceeds it at certain times when the two other types are looked at. Especially the high surface temperature for type E indicates that additional radiators or heating surfaces might be an option to heat the zone on very cold days, but the floor heating system model is kept here for simplicity.

Table 2.11: *Temperatures selected for the calculation of the heat pump efficiencies and maximum heating capacities.*

	Heat pump	η_{sh}	η_{dhw}	$\dot{Q}_{hp,max}$
L	WPL7	30 °C	50 °C	35 °C
J	WPL20	35 °C	50 °C	35 °C
E	WPL20	40 °C	50 °C	45 °C

2.4.2 Buffer Storage Model

A buffer storage enables decoupling of the heat production from the demand. Due to the following reasons, a buffer storage is assumed to be optional for the buildings considered in this thesis. Buffer storages are often used with on-off switching heat generation units like older heat pumps or combined heat and power units. Since monovalent systems are typically dimensioned to cover extreme ambient conditions, they are oversized for milder, average heating days. To avoid frequent on-off switching and premature wearout of the compressor, buffer storages are used between the heat pump and the heat emission system. In contrast to radiator systems do floor heating systems not need a buffer due to their own thermal inertia [HM09,Huc15]. An additional parallel buffer storage often requires higher operating temperatures, which negatively impacts the coefficient of performance. Also can additional mixing valves and the control technology make a buffer an expensive investment for a single family house, why storages are either connected in series to the heating circuit or completely omitted [Wim04]. Especially the variable-speed inverter technology in modern heat pumps allows to adjust the thermal power of a heat pump to the current heat load conditions. Due to the possible part load operation, typical on/off-cycling is no longer an issue and no buffer storage is needed [Huc15]. As already discussed in the heat pump section, for variable-speed heat pumps it is only important to not overdimension the system due to the minimum thermal output greater zero, which is no issue after the relaxed range of operation in Equations (2.52)-(2.54).
The simplest, temperature dependent and lossless formulation of a thermal storage model for a building supplied by a heat pump is given in [RGZ88]. Adapted to a single water storage node with heat capacity C_{sto}, the uniform temperature T_{sto} in the storage is heated up by the heat pump and back-up heater with $\dot{Q}_{hp,sh} + \dot{Q}_{bh,sh}$ and the load of the building is supplied by the storage with $\dot{Q}_{sto}$:

$$C_{sto}\dot{T}_{sto} = \dot{Q}_{hp,sh} + \dot{Q}_{bh,sh} - \dot{Q}_{sto}. \tag{2.62}$$

Adding losses towards the environment with temperature T_{env} where the buffer storage is located and rearranging leads to the following differential equation:

$$\dot{T}_{sto} = \frac{\dot{Q}_{hp,sh}}{C_{sto}} + \frac{\dot{Q}_{bh,sh}}{C_{sto}} - \frac{\dot{Q}_{sto}}{C_{sto}} - \frac{(UA)_{sto}}{C_{sto}}(T_{sto} - T_{env}). \tag{2.63}$$

Both C_{sto} and the heat loss parameter $(UA)_{sto}$ depend on the volume of the buffer storage. The thermal transmittance over the surface of the storage is assumed to be $0.3\,\frac{\mathrm{W}}{\mathrm{m^2\,K}}$. The calculation

[25] Calculated based on Equation (A.61) in the Appendix.

of the parameters is carried out as for the domestic hot water storage introduced in Section 2.5.2. The authors in [BDI18] assume a volume of 250 l for a four person SFH in order to provide enough inertia to switch the heat pump off for 1-2 hours during winter days. 100 l are recommended in [Sti17] for the optional buffer storage setup for the two modulating heat pumps considered in this thesis. A study in [Huc15] found only a small impact of the thermal inertia of the building construction on the heat pump performance when a buffer storage was used. The uniform temperature model in Equation (2.63) is a strong simplification and might not be sufficient for larger volumes and stratification effects. In this thesis it is only used for smaller volumes and helps to investigate effects of additional thermal inertia without the need of further complex modeling.

2.5 Domestic Hot Water Model

The following two subsections introduce the domestic hot water demand model used for each building considered in the simulations in Chapter 6. The model consists of a demand model to relate activities of occupants to hot water draw events and a storage model to couple the demand to the operation of the heat pump and back-up heater.

2.5.1 Domestic Hot Water Demand Model

The demand model for the domestic hot water consumption generates daily profiles for draw events for each household. Stochastic bottom-up models in the literature are based on detailed field study data [Lut08, VKA12], derived from smart meter household records [PMLC09] or generated based on general time use survey data [FWSWH16]. A commonly used tool to create user defined profiles for German households was presented in [JV05] based on the previous work in [JV01]. To achieve consistency with the residential electricity demand profiles presented in Section 4.4 based on the author's previous work in [JKC15], a model based on the same time use survey (TUS) data for Germany from [FDZa, FDZb] was developed.
The daily average domestic hot water demand for a household varies slightly in the literature. The tool in [JV05] assumes an average daily tapping of 200 l/d for a single family house. [HDR+13] review country specific studies and assume an average draw off demand for an average single family house of around 140 l/d provided at 45 °C with cold water temperature at 10 °C. This results in an amount of energy of approximately 5.684 kW h/d. Thus, the daily demand per person breaks down to 1.42 kWh per day and person in a 4 person household. The norm [DIN07] suggests to assume a demand of 25 l/d or 1.45 kW h/d per person delivered at 60 °C for the dimensioning of heat pump systems when no further specifications are available.
Domestic hot water demand can be divided into longer and shorter draw events, triggered by different occupant activities. The VDI norm 2067 [VDI17] differentiates between showering, bathing, other personal hygiene and the washing of clothes and dishes. In a simple breakdown, showering and bathing account for events of longer draws with relatively few events per day while the usage of hot water taps in the kitchen and the bathrooms account for shorter, but more frequent events. Automated dishwashing and the washing of clothes is considered in the residential electricity model and thus neglected here. Table 2.12 shows the range of flow rates, durations, the frequency per day and supply temperature assumed for the activities showering, bathing and sink usage for cooking, dishwashing or handwashing and other personal hygiene. The values are partially taken from [VDI17]. The daily frequencies for showering and bathing are altered based on survey statistics from [Wag15]. While a daily shower per person was likely, a bath was taken less than once a week.

Table 2.12: *DHW model parameters, partially based on [VDI17].*

	Flow $\dot{V}$ [$\frac{\text{l}}{\text{min}}$]	Duration Δt [min]	Frequency [1/d]	$T_{service}$ [°C]
Shower	6-10	2-6	0.85	40
Bath	10-13	6-10	0.11	40
Sink usage				
- Handwash & other hygiene	1-6	1-2	2	40
- Cooking & dishes	1-6	1-2	0.6	50

The flow rate and duration are assumed to be uniformly distributed between the specified ranges

$$\dot{V} \sim U(\dot{V}_{min}, \dot{V}_{max}) \qquad \Delta t \sim U(\Delta t_{min}, \Delta t_{max}) \tag{2.64}$$

and the tapped liters and total energy required per event can be computed as

$$V = \dot{V}\Delta t \tag{2.65}$$

$$Q = V\rho_w c_w (T_{service} - T_{cold}) \tag{2.66}$$

with V being the drawn volume in liters, $\rho_w \approx 1\,\frac{\text{kg}}{\text{l}}$ the density of water and $c_w = 4\,176\,\frac{\text{J}}{\text{kg K}} = 1.16 \cdot 10^{-3}\,\frac{\text{kW h}}{\text{kg K}}$ the specific heat capacity of water. $T_{service}$ is the preferred water temperature of the event.
The domestic hot water draw events are distributed with varying probability over the course of the day. The events for showering are assumed to be linked to the TUS activities "washing and dressing", including personal hygiene for children. Bathing events are distributed according to the same probability density function, but with the restriction of taking place after noon. The model takes into account the required occupancy of at least one household member and guarantees that the shower and bathtub are not over-occupied. Even though it is common in smaller households to find the shower integrated in the bathtub, separate devices are assumed for simplicity. Warm water draws for cooking are assumed to follow the temporal distribution of the TUS activities "preparation of meals" and "washing dishes, clearing the table". Random handwash events are assumed to be uniformly distributed during the day, with increasing and decreasing probabilities in the early morning and late evening hours. The distribution is similar to the one used in [JV05] for small and medium draws. This distribution is not based on TUS data but constructed manually, the same distribution is assumed for all households. Figure 2.33 shows the underlying probability density functions in a minute resolution for each household size and simulated draw events for one, ten and one hundred four person households.
The DHW demand may vary throughout the year, due to seasonal consumer behavior, more vacation days taken in the summer and warmer cold water temperatures in the summer [HDR+13]. The model in this work accounts for a varying cold water temperature to reflect seasonal variation and applies the formula from [HH07]. Equation (2.67) describes the daily variation of the cold water temperature $T_{cold,d}$ on day d_{dhw} as a cosinusoidal function with an amplitude of 3K around the local mean annual ambient temperature:

$$T_{cold,d} = \overline{T_{amb}} - 3\cos((d_{dhw} - d_{dhw,min(T_{amb})})\frac{2\pi}{365}). \tag{2.67}$$

$d_{dhw,min(T_{amb})}$ is the day of the lowest ambient temperature. The flow rate of draw events which require a temperature below 45 °C are corrected to account for water mixing.

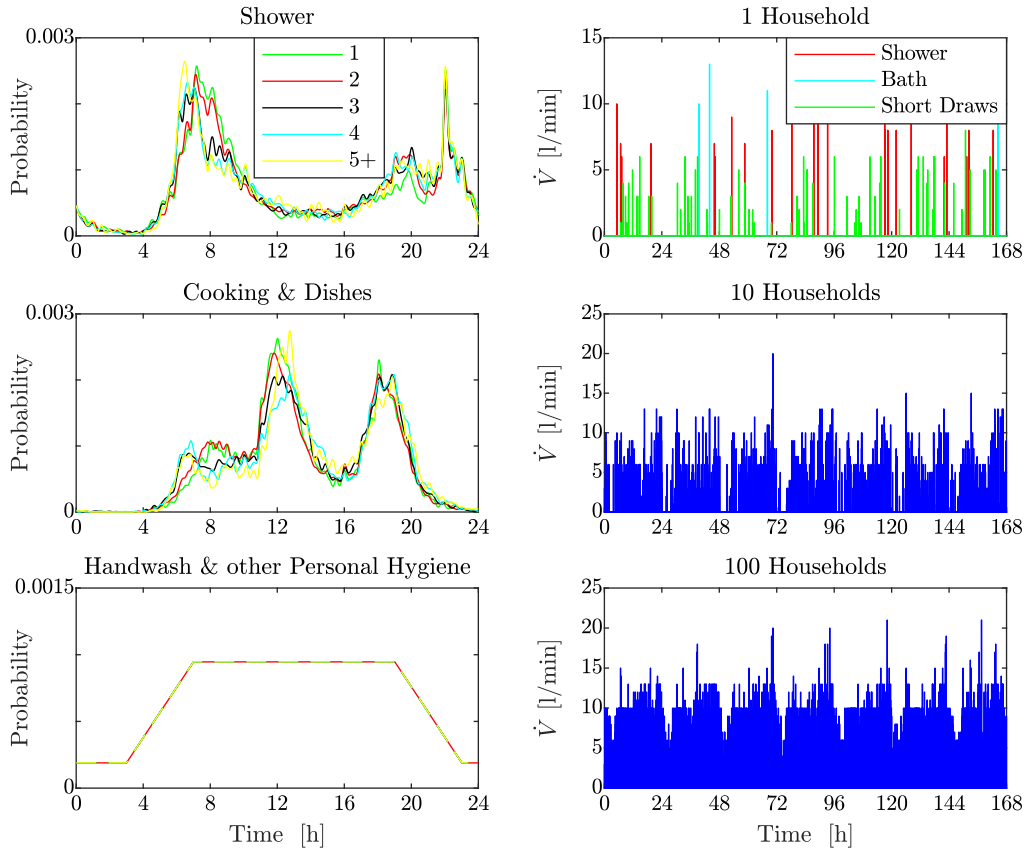

Figure 2.33: *Left column: Probability density functions per activity for 1 to 5 and more person households. Right column: DHW flow rate profiles simulated for 1 to 100 four person households.*

Figure 2.34 shows the generated results from an annual simulation of 100 four person households at a location with a mean ambient temperature of 8 °C. The mean daily consumption per person results in 45 l and 1.9 kWh. Compared to the values in [VDI17], this energy estimate is located at the upper end of the range for a medium daily per person demand.

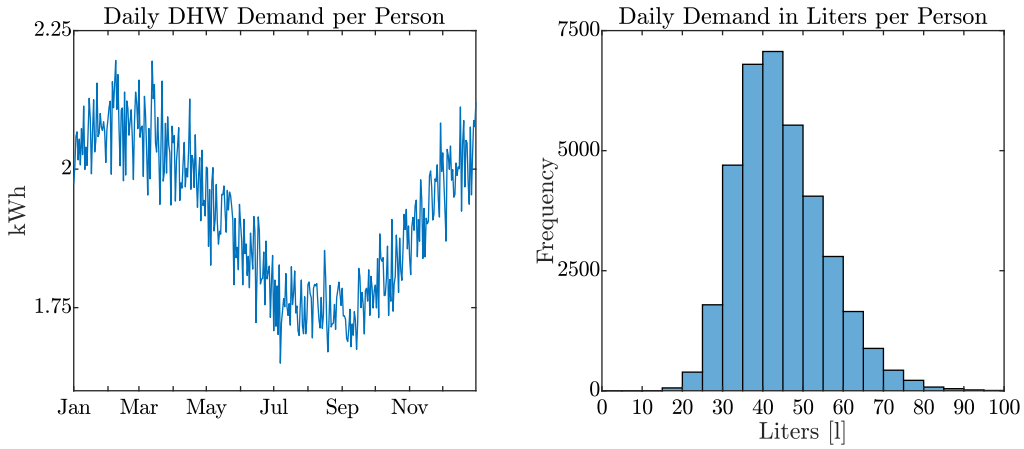

Figure 2.34: *Simulation results for the per person daily DHW demand and drawn liters of 100 four person households.*

2.5.2 Domestic Hot Water Storage Model

The water storage to supply the DHW demand is modeled as a single temperature node due to the small size of the storage. The thermal capacity C_{dhw} can be scaled by the volume of the storage. The temperature of the water T_{dhw} has to be equal or higher than 45 °C to satisfy the occupants' comfort. DHW storages can usually handle temperatures of up to 90 °C [Sti17], but the maximum storage temperature allowed here is limited by the heat pump's maximum supply temperature. $\dot{Q}_{hp,dhw}$ is the power delivered to the storage by the heat pump[26]. Heat losses result from the demand water draws $\dot{V}$ and transmission losses over the surface area of the storage to the environment at temperature T_{env} where the device is located. A constant temperature of 15 °C is assumed throughout the whole year. The continuous-time heat flow equation becomes

$$C_{dhw}\dot{T}_{dhw} = \dot{Q}_{hp,dhw} - \dot{V}\rho_w c_w(T_{dhw} - T_{cold}) - (UA)_{dhw}(T_{dhw} - T_{env}). \tag{2.68}$$

Equation (2.68) results in a time-variant system since the flow rate disturbance $\dot{V}$ varies in time and is multiplied with the state T_{dhw}. To avoid the additional discretization effort at each time step for each profile used in simulations, the power drawn from the storage is approximated to be supplied at a constant temperature of 45 °C:

$$\dot{Q}_{dhw} = \dot{V}\rho_w c_w(45\,°\text{C} - T_{cold}). \tag{2.69}$$

The profile for $\dot{Q}_{dhw}$ is precalculated and treated as a disturbance in the final model.
Table 2.13 shows the default storage parameters for a four person household. Based on the required volume, a storage with an optimal volume to surface area is computed. The thermal transmittance value matches different insulation materials discussed in [Kan17]. Standard sizing procedures for the DHW storage double the reference value per person and day in liters at e.g. 60 °C and correct the volume for the service temperature set point to match the energy contents,

[26] Power from the back-up heater for DHW operation is neglegted here for brevity.

see [Sti17,DIN07]. In this work, a security margin of 25% is added to the mean daily per person demand in a four person household.

Table 2.13: *DHW storage parameters*

Volume [l]	Capacity C_{dhw} $[\frac{\text{J}}{\text{K}}]$	Transmittance U_{dhw} $[\frac{\text{W}}{\text{m}^2\,\text{K}}]$	Surface area A_{dhw} $[\text{m}^2]$	Range T_{dhw} [°C]
225	$9.4 \cdot 10^5$	0.3	2.05	45-55

The additional required heat pump power for DHW is often estimated with the maximum energy drawn off over a short period of time and the remaining time to recharge the storage tank between two such events, see e.g. [DIN07]. Charging the 225 l storage tank to the minimum temperature within 8 h leads to additional 1.2 kW. This is sufficient to supply the average demand, but single extreme events can still require use of a back-up heater, especially when the remaining heat pump capacity is simultaneously used for space heating. The heat pumps selected in Section 2.4.1 together with the back-up heater are sufficiently dimensioned to provide power for both space heating and DHW.

2.6 Internal Gains

While the TABULA reference calculation assumed general constant internal gains of $3\,\frac{\text{W}}{\text{m}^2}$ to account for possible sources, the model used in this thesis provides a time-varying, occupancy-dependent internal gains profile. The VDI 2078 [VDI15a] states estimates of the human heat transfer for sedentary and other activities of different intensity. The total internal gains for a household of H members are calculated as

$$\varphi_{ig}(t) = o(t)r(t)\sum_{i=1}^{H}\varphi_{ig,i}(t) \tag{2.70}$$

with

$$\varphi_{ig,i}(t) = \begin{cases} \sim U(100,125)\text{W/person} & \text{from 6 a.m. to 11 p.m.} \\ 80\text{W/person} & \text{otherwise} \end{cases} \tag{2.71}$$

and occupancy indicated by

$$o(t) = \begin{cases} 1 & \text{if at least one person is present} \\ 0 & \text{otherwise.} \end{cases} \tag{2.72}$$

$r(t)$ is a stochastic process to randomly vary the occupancy during the day between one and the maximum number of household members. A more sophisticated approach would take occupancy dependencies between individual household members into account, but since individual occupancy profiles are not derivable from the available TUS data sets in [FDZa, FDZb], this simplification is used. The resulting profiles lead to a value of $1.8\,\frac{\text{W}}{\text{m}^2}$ in average for a four person household. The occupancy profile $o(t)$ is consistent with the time-series used in the household electricity and DHW models. Gains from electrical appliances and lighting are neglected.

Chapter 3

Prosumer Energy Management

This chapter develops the model predictive controller for the purpose of energy management. The control strategy allows to minimize energy consumption or energy costs and maximizes PV self-consumption when local PV generation is available. The final dynamic model of the building and heating system components is introduced and the prediction of the states and the boundary conditions are defined. Finally, the MPC optimal control problem for a single prosumer is presented.

3.1 Building Energy System Model

The following section rearranges the system matrices of the building structure and the buffer and DHW storage units for the design of the predictive controller. The final building dynamics of model R with the heating input to the floor (see derivation in Appendix A.6) are

$$\begin{aligned}\dot{T}_z &= \frac{1}{R_{vent}C_z}(T_a - T_z) + \frac{1}{R_{wi}C_z}(T_{wi} - T_z) \\ &+ \frac{1}{R_{starA}C_z}\Big((\frac{1}{SR_{starA}} - 1)T_z + \frac{1}{SR_{wo,1}}T_{wo} + \frac{1}{SR_{fl,1}}T_{fl}\Big) + \frac{s_z}{C_z}\varphi_{sg} + \frac{g_z}{C_z}\varphi_{ig} \qquad (3.1)\\ \dot{T}_{wi} &= \frac{1}{R_{wi}C_{wi}}(T_z - T_{wi}) + \frac{s_{wi}}{C_{wi}}\varphi_{sg} + \frac{g_{wi}}{C_{wi}}\varphi_{ig} \qquad (3.2)\\ \dot{T}_{wo} &= \frac{1}{R_{wo,2}C_{wo}}(T_{a,eq} - T_{wo}) + \frac{1}{R_{wo,1}C_{wo}}\Big(\frac{1}{SR_{starA}}T_z + (\frac{1}{SR_{wo,1}} - 1)T_{wo} + \frac{1}{SR_{fl,1}}T_{fl}\Big) \\ &+ \frac{s_{wo}}{C_{wo}}\varphi_{sg} + \frac{g_{wo}}{C_{wo}}\varphi_{ig} \qquad (3.3)\\ \dot{T}_{fl} &= \frac{1}{R_{fl,2}C_{fl}}(T_g - T_{fl}) + \frac{1}{R_{fl,1}C_{fl}}\Big(\frac{1}{SR_{starA}}T_z + \frac{1}{SR_{wo,1}}T_{wo} + (\frac{1}{SR_{fl,1}} - 1)T_{fl}\Big) \\ &+ \frac{s_{fl}}{C_{fl}}\varphi_{sg} + \frac{g_{fl}}{C_{fl}}\varphi_{ig} + \frac{1}{C_{fl}}(\dot{Q}_{hp,sh} + \dot{Q}_{bh,sh}) \qquad (3.4)\end{aligned}$$

for the case that the heat pump and back-up heater power for space heating ($\dot{Q}_{hp,sh} + \dot{Q}_{bh,sh}$) are direct input to the floor. If a buffer storage is considered, the generated heat is decoupled from the delivered heat to the floor $\dot{Q}_{sto}$ and the additional state T_{sto} in the water storage volume is

added to the overall dynamics:

$$(3.1), \dots, (3.3)$$

$$\dot{T}_{fl} = \frac{1}{R_{fl,2}C_{fl}}(T_g - T_{fl}) + \frac{1}{R_{fl,1}C_{fl}}\Big(\frac{1}{SR_{starA}}T_z + \frac{1}{SR_{wo,1}}T_{wo} + (\frac{1}{SR_{fl,1}} - 1)T_{fl}\Big) + \frac{s_{fl}}{C_{fl}}\varphi_{sg} + \frac{g_{fl}}{C_{fl}}\varphi_{ig} + \frac{1}{C_{fl}}\dot{Q}_{sto} \tag{3.5}$$

$$\dot{T}_{sto} = \frac{\dot{Q}_{hp,sh}}{C_{sto}} + \frac{\dot{Q}_{bh,sh}}{C_{sto}} - \frac{\dot{Q}_{sto}}{C_{sto}} - \frac{(UA)_{sto}}{C_{sto}}(T_{sto} - T_{env}). \tag{3.6}$$

The system matrix A_{RC-R} and the controllable and uncontrollable input matrices B_{RC-R} and E_{RC-R} are obtained from the rearranged dynamics of the building model with Equations (3.1)-(3.3),(3.5):

$$A_{RC-R} = \begin{pmatrix} \frac{1}{C_z}(-\frac{1}{R_{vent}} - \frac{1}{R_{wi}} + \frac{1}{R_{starA}}(\frac{1}{SR_{starA}} - 1)) & \frac{1}{R_{wi}C_z} & \frac{1}{R_{starA}C_z}\frac{1}{SR_{wo,1}} & \frac{1}{R_{starA}C_z}\frac{1}{SR_{fl,1}} \\ \frac{1}{R_{wi}C_{wi}} & -\frac{1}{R_{wi}C_{wi}} & 0 & 0 \\ \frac{1}{R_{wo,1}C_{wo}}\frac{1}{SR_{starA}} & 0 & \frac{1}{C_{wo}}(-\frac{1}{R_{wo,2}} + \frac{1}{R_{wo,1}}(\frac{1}{SR_{wo,1}} - 1)) & \frac{1}{R_{wo,1}C_{wo}}\frac{1}{SR_{fl,1}} \\ \frac{1}{R_{fl,1}C_{fl}}\frac{1}{SR_{starA}} & 0 & \frac{1}{R_{fl,1}C_{fl}}\frac{1}{SR_{wo,1}} & \frac{1}{C_{fl}}(-\frac{1}{R_{fl,2}} + \frac{1}{R_{fl,1}}(\frac{1}{SR_{fl,1}} - 1)) \end{pmatrix}$$

$$B_{RC-R} = \begin{pmatrix} 0 \\ 0 \\ 0 \\ \frac{1}{C_{fl}} \end{pmatrix} \qquad E_{RC-R} = \begin{pmatrix} 0 & \frac{1}{R_{vent}C_z} & 0 & \frac{s_z}{C_z} & \frac{g_z}{C_z} \\ 0 & 0 & 0 & \frac{s_{wi}}{C_{wi}} & \frac{g_{wi}}{C_{wi}} \\ \frac{1}{R_{wo,2}C_{wo}} & 0 & 0 & \frac{s_{wo}}{C_{wo}} & \frac{g_{wo}}{C_{wo}} \\ 0 & 0 & \frac{1}{R_{fl,2}C_{fl}} & \frac{s_{fl}}{C_{fl}} & \frac{g_{fl}}{C_{fl}} \end{pmatrix}.$$

The corresponding states, controllable input and disturbance inputs are

$$x_{RC-R} = \begin{pmatrix} T_z \\ T_{wi} \\ T_{wo} \\ T_{fl} \end{pmatrix} \qquad u_{RC-R} = \dot{Q}_{sto} \qquad d_{RC-R} = \begin{pmatrix} T_{a,eq} \\ T_a \\ T_g \\ \varphi_{sg} \\ \varphi_{ig} \end{pmatrix}.$$

The system and input matrices, state and inputs for the buffer storage model in Equation (3.6) are

$$A_{sto,sh} = -\frac{(UA)_{sto}}{C_{sto}} \qquad B_{sto,sh} = \begin{pmatrix} -\frac{1}{C_{sto}} & \frac{1}{C_{sto}} & \frac{1}{C_{sto}} \end{pmatrix} \qquad E_{sto,sh} = \frac{(UA)_{sto}}{C_{sto}}$$

$$x_{sto,sh} = T_{sto} \qquad u_{sto,sh} = \begin{pmatrix} \dot{Q}_{sto} \\ \dot{Q}_{hp,sh} \\ \dot{Q}_{bh,sh} \end{pmatrix} \qquad d_{sto,sh} = T_{env}.$$

The dynamics for the domestic hot water storage from Equation (2.68) expanded by the back-up heater input lead to

$$A_{sto,dhw} = -\frac{(UA)_{dhw}}{C_{dhw}} \qquad B_{sto,dhw} = \begin{pmatrix} \frac{1}{C_{dhw}} & \frac{1}{C_{dhw}} \end{pmatrix} \qquad E_{sto,dhw} = \begin{pmatrix} \frac{(UA)_{dhw}}{C_{dhw}} & -\frac{1}{C_{dhw}} \end{pmatrix}$$

$$x_{sto,dhw} = T_{dhw} \qquad u_{sto,dhw} = \begin{pmatrix} \dot{Q}_{hp,dhw} \\ \dot{Q}_{bh,dhw} \end{pmatrix} \qquad d_{sto,dhw} = \begin{pmatrix} T_{env} \\ \dot{Q}_{dhw} \end{pmatrix}.$$

The complete state-space representation of the continuous linear time-invariant dynamic system composed of the subsystems building, buffer storage and DHW storage is

$$\begin{aligned} \dot{x}(t) &= A_c x(t) + B_c u(t) + E_c d(t) \\ y(t) &= C x(t). \end{aligned} \tag{3.7}$$

$A_c \in \mathbb{R}^{n_x \times n_x}$ is the block diagonal matrix of the system matrices of the subsystems:

$$A_c = \begin{pmatrix} A_{RC-R} & & \\ & A_{sto,sh} & \\ & & A_{sto,dhw} \end{pmatrix}.$$

Accordingly, matrices $B_c \in \mathbb{R}^{n_x \times n_u}$ and $E_c \in \mathbb{R}^{n_x \times n_d}$ are composed of the subsystems' input and disturbance matrices $B_{sto,sh}, B_{sto,dhw}, E_{sto,sh}, E_{sto,dhw}$ and appropriately filled with zeros. n_x, n_u and n_d are the total number of states, controllable inputs and disturbances. The final states, controllable inputs and disturbances vectors are

$$x = \begin{pmatrix} T_z \\ T_{wi} \\ T_{wo} \\ T_{fl} \\ T_{sto} \\ T_{dhw} \end{pmatrix} \qquad u = \begin{pmatrix} \dot{Q}_{sto} \\ \dot{Q}_{hp,sh} \\ \dot{Q}_{bh,sh} \\ \dot{Q}_{hp,dhw} \\ \dot{Q}_{bh,dhw} \end{pmatrix} \qquad d = \begin{pmatrix} T_{a,eq} \\ T_a \\ T_g \\ \varphi_{sg} \\ \varphi_{ig} \\ T_{env} \\ \dot{Q}_{dhw} \end{pmatrix}.$$

The states of the system are assumed to be fully observable and known ($C = I_{n_x}$) and the output $y(t)$ neglected in the further notation. However, this is not the case for real systems in practice, e.g. the temperatures of the floor and walls are usually not measured.

3.2 Prediction

The dynamic system in (3.7) is discretized at every $t = k\Delta_t$, where $k \in \mathbb{N}$ is the sample number referring to the MPC time step and $\Delta_t = 15\text{min}$ the sample time. The resulting discrete linear time-invariant system is

$$x(k+1) = Ax(k) + Bu(k) + Ed(k). \tag{3.8}$$

With the measurement of $x(k) = x_0$ the controller utilizes model (3.8) to compute the predictions of the states for the next N_P time steps of the prediction horizon. The $n_x N_p$ predicted states

$(\hat{x}(k+1|k), \ldots, \hat{x}(k+N_P|k))$ computed at time k are:

$$\begin{aligned}
\hat{x}(k+1|k) &= Ax_0 + Bu(k|k) + E\hat{d}(k|k) \\
\hat{x}(k+2|k) &= A\hat{x}(k+1|k) + Bu(k+1|k) + E\hat{d}(k+1|k) \\
&= A^2x_0 + ABu(k|k) + Bu(k+1|k) + AE\hat{d}(k|k) + E\hat{d}(k+1|k) \\
&\vdots \qquad (3.9) \\
\hat{x}(k+N_P|k) &= A^{N_P}x_0 + A^{N_P-1}Bu(k|k) + A^{N_P-2}Bu(k+1|k) + \ldots + Bu(k+N_P-1|k) \\
&\quad + A^{N_P-1}E\hat{d}(k|k) + A^{N_P-2}E\hat{d}(k+1|k) + \ldots + E\hat{d}(k+N_P-1|k). \qquad (3.10)
\end{aligned}$$

Thus, the estimation at every time instant of the prediction horizon $j = 1, \ldots, N_P$ is given by

$$\hat{x}(k+j|k) = A^j x_0 + \sum_{i=1}^{j} A^{i-1}Bu(k+j-i|k) + \sum_{i=1}^{j} A^{i-1}E\hat{d}(k+j-i|k) \qquad (3.11)$$

and leads to the compact matrix form of (3.8) over the prediction horizon:

$$\hat{\boldsymbol{x}}_k = \mathcal{A}x_0 + \mathcal{B}\boldsymbol{u}_k + \mathcal{E}\hat{\boldsymbol{d}}_k \qquad (3.12)$$

with

$$\mathcal{A} = \begin{pmatrix} A \\ A^2 \\ \vdots \\ A^{N_P} \end{pmatrix} \qquad (3.13)$$

$$\mathcal{B} = \begin{pmatrix} B & 0 & 0 & \ldots & 0 \\ AB & B & 0 & \ldots & 0 \\ A^2B & AB & B & \ldots & 0 \\ \vdots & \vdots & \vdots & \ddots & 0 \\ A^{N_P-1}B & A^{N_P-2}B & A^{N_P-3}B & \ldots & B \end{pmatrix}$$

$$\mathcal{E} = \begin{pmatrix} E & 0 & 0 & \ldots & 0 \\ AE & E & 0 & \ldots & 0 \\ A^2E & AE & E & \ldots & 0 \\ \vdots & \vdots & \vdots & \ddots & 0 \\ A^{N_P-1}E & A^{N_P-2}E & A^{N_P-3}E & \ldots & E \end{pmatrix}$$

and

$$\hat{\boldsymbol{x}}_k := \hat{\boldsymbol{x}}(k) = (\hat{x}(k+1|k)^T, \hat{x}(k+2|k)^T, \ldots, \hat{x}(k+N_P|k)^T)^T \qquad (3.14)$$

$$\boldsymbol{u}_k := \boldsymbol{u}(k) = (u(k|k)^T, u(k+1|k)^T, \ldots, u(k+N_P-1|k)^T)^T \qquad (3.15)$$

$$\hat{\boldsymbol{d}}_k := \hat{\boldsymbol{d}}(k) = (\hat{d}(k|k)^T, \hat{d}(k+1|k)^T, \ldots, \hat{d}(k+N_P-1|k)^T)^T. \qquad (3.16)$$

The progression of the predicted states is fully explained by the current initial measurement, the disturbance predictions and the chosen controllable input. Throughout this thesis, perfect

predictions are assumed, which allows for

$$\boldsymbol{d}(k) = \hat{\boldsymbol{d}}(k) \tag{3.17}$$
$$\boldsymbol{x}(k) = \hat{\boldsymbol{x}}(k). \tag{3.18}$$

This is also referred to as deterministic or certainty equivalence MPC [OPJ+12]. The additional indexing to indicate the time of the prediction k is omitted for ease of notation, thus $\boldsymbol{x}(k) = \boldsymbol{x}(k|k)$ is used in the problem formulation and must not be mistaken for the final realization of x at time k.

3.3 System Boundary Constraints

The system's states are limited by possibly time-varying upper and lower bounds to guarantee thermal comfort. This leads to

$$\underline{\boldsymbol{x}}_k \leq \boldsymbol{x}_k \leq \overline{\boldsymbol{x}}_k \tag{3.19}$$

with

$$\underline{\boldsymbol{x}}_k := \underline{\boldsymbol{x}}(k) = (\underline{x}(k+1|k)^T, \underline{x}(k+2|k)^T, \ldots, \underline{x}(k+N_P|k)^T)^T \tag{3.20}$$
$$\overline{\boldsymbol{x}}_k := \overline{\boldsymbol{x}}(k) = (\overline{x}(k+1|k)^T, \overline{x}(k+2|k)^T, \ldots, \overline{x}(k+N_P|k)^T)^T. \tag{3.21}$$

The system's inputs are bounded to account for operational limits of the components in the heating system:

$$\overline{\mathcal{B}}\boldsymbol{u}_k \leq \overline{\boldsymbol{u}}_k \tag{3.22}$$
$$\boldsymbol{0} \leq \boldsymbol{u}_k. \tag{3.23}$$

Matrix $\overline{\mathcal{B}}$ couples the inputs to account for the constraints (2.52) and (2.57) on the hybrid operation of the heat pump and back-up heater with[1,2]

$$\overline{\mathcal{B}} = \begin{pmatrix} I_{N_P} \otimes (1\,0\,0\,0\,0) \\ I_{N_P} \otimes (0\,1\,0\,1\,0) \\ I_{N_P} \otimes (0\,0\,1\,0\,1) \end{pmatrix}, \tag{3.25}$$

and

$$\overline{\boldsymbol{u}}_k := \overline{\boldsymbol{u}}(k) = (\dot{Q}_{sto,max}, \ldots, \dot{Q}_{sto,max}, \dot{Q}_{hp,max}(k|k), \ldots, \dot{Q}_{hp,max}(k+N_P-1|k), \tag{3.26}$$
$$+ \dot{Q}_{bh,max}(k|k), \ldots, \dot{Q}_{bh,max}(k+N_P-1|k))^T. \tag{3.27}$$

The constraints allow to include the temperature dependent heating capacity. Standard operational behavior can be enforced, e.g. the back-up heater must only operate at ambient temperatures below $-7\,°\mathrm{C}$, but also a permanent availability can be investigated.

[1] Here for the case with buffer storage.

[2] $\otimes$ is the Kronecker product:

$$A \otimes B = \begin{pmatrix} a_{1,1}B & \ldots & a_{1,n}B \\ \vdots & \ddots & \vdots \\ a_{m,1}B & \ldots & a_{m,n}B \end{pmatrix}. \tag{3.24}$$

3.4 Coupling to the Power System

The total electric power of the heating system from Equations (2.55),(2.56),(2.60) and (2.61) becomes

$$P_{el}(k) = P_{hp,sh}(k) + P_{bh,sh}(k) + P_{hp,dhw}(k) + P_{bh,dhw}(k) \tag{3.28}$$

$$= \frac{\dot{Q}_{hp,sh}(k)}{\eta_{sh}(T_a(k))} + \dot{Q}_{bh,sh}(k) + \frac{\dot{Q}_{hp,dhw}(k)}{\eta_{50°\mathrm{C}}(T_a(k))} + \dot{Q}_{bh,dhw}(k). \tag{3.29}$$

The COPs are precalculated based on the ambient temperature predictions and a coupling matrix $\mathcal{B}_C$ can be defined as

$$\mathcal{B}_k^C = \begin{pmatrix} \mathcal{B}^C(k) & & & \\ & \mathcal{B}^C(k+1) & & \\ & & \ddots & \\ & & & \mathcal{B}^C(k+N_P-1) \end{pmatrix} \quad \mathcal{B}^C(k) = \begin{pmatrix} 0 \\ \eta_{sh}(T_a(k))^{-1} \\ 1 \\ \eta_{50°\mathrm{C}}(T_a(k))^{-1} \\ 1 \end{pmatrix}^T \tag{3.30}$$

to relate the thermal inputs of the heating system to the total electric load of the building energy system.
The coupling variable in case of the building energy systems connected to the power system is the total electric load $r(k)$, i.e. the total load seen by the grid. The total load can be computed based on the controllable inputs $u(k)$ and the fixed electricity load $l(k)$:

$$r(k) = \mathcal{B}^C(k)u(k) + l(k). \tag{3.31}$$

$l(k)$ is the disturbance signal on the coupling variable, representing the non-controllable electrical appliances in a building. The profiles used are reviewed in Section 4.4. The heat pump, back-up heater and electrical appliances are pure power consumers. Thus, in absence of local electricity generation, the total load will be either zero or positive. For the predictions of the residual load $\boldsymbol{r}_k$ over the prediction horizon in compact form one obtains

$$\boldsymbol{r}_k = \mathcal{B}_k^C \boldsymbol{u}_k + \boldsymbol{l}_k \tag{3.32}$$

with

$$\boldsymbol{r}_k := \boldsymbol{r}(k) = (r(k), r(k+1), \ldots, r(k+N_P-1))^T$$
$$\boldsymbol{l}_k := \boldsymbol{l}(k) = (l(k), l(k+1), \ldots, l(k+N_P-1))^T$$

analogously. Note that in contrast to $\boldsymbol{x}_k$, $\boldsymbol{u}_k$ and $\boldsymbol{d}_k$, both vectors $\boldsymbol{r}_k$ and $\boldsymbol{l}_k$ are assumed to be of dimension $\mathbb{R}^{N_P}$, corresponding to a one-dimensional variable per time step.
A prosumer is defined as a building energy system equipped with a resource for local electricity generation like a rooftop PV plant. In this case the prosumer may both consume and produce power, restricted by the total electrical demand of the building and the availability of solar irradiation for PV generation $g(k)$. The total load becomes the residual load

$$r(k) = \mathcal{B}^C(k)u(k) + l(k) - g(k) \tag{3.33}$$

and equivalently

$$\boldsymbol{r}_k = \mathcal{B}_k^C \boldsymbol{u}_k + \boldsymbol{l}_k - \boldsymbol{g}_k \tag{3.34}$$

over the prediction horizon with

$$\boldsymbol{g}_k := \boldsymbol{g}(k) = (g(k), g(k+1), \ldots, g(k+N_P-1))^T. \tag{3.35}$$

Note that the PV generation enters the residual load as an additional disturbance. Controllability on $\boldsymbol{g}_k$ within the interval $[\boldsymbol{0}, \boldsymbol{g}_k]$ might be available if the PV inverter allows curtailment. Curtailment is not considered in the simulations of this work. In the remaining sections, the total load is always referred to as the residual load, independent of its sign (whether or not PV generation is available).

3.5 Cost Functions

The controller of the building energy system tries to minimize the total energy consumption or energy costs over time. When no local generation is assumed, the resulting cost function f is defined as

$$f(\boldsymbol{r}_k) = \boldsymbol{c}_k^T \boldsymbol{r}_k \tag{3.36}$$

$$= \boldsymbol{c}_k^T (\mathcal{B}_k^C \boldsymbol{u}_k + \boldsymbol{l}_k), \tag{3.37}$$

with

$$\boldsymbol{c}_k \in \mathbb{R}^{N_P} = \boldsymbol{\Delta}_t \quad \text{for energy consumption,} \tag{3.38}$$

or

$$\boldsymbol{c}_k \in \mathbb{R}^{N_P} = \Delta_t \boldsymbol{\pi_k} \quad \text{for energy costs.} \tag{3.39}$$

$\boldsymbol{\Delta}_t$ is a vector with the discretization time step Δ_t in each entry and $\boldsymbol{\pi}_k$ denotes a possibly time-varying purchasing price for electricity. Since $\boldsymbol{l}_k$ is non-controllable, $\boldsymbol{c}_k^T \boldsymbol{l}_k$ is a constant cost term which cannot be influenced by the control policy of the MPC.
The cost function of the prosumer has to be modified when local electricity generation is available. Assuming that it is economically beneficial or a regulatory requirement to consume locally generated electricity first, a minimization of energy costs has to reflect the prioritized usage of the local PV generation. According to the chosen sign convention, a negative residual load represents feed-in into the grid, meaning that the local generation outweighs the electrical demand of the heat pump, back-up heater and appliances. The prosumer's cost function to increase self-consumption without the option to sell excess electricity would be

$$f(\boldsymbol{r}_k) = \begin{cases} \boldsymbol{c}_k^T \boldsymbol{r}_k & \text{if } \boldsymbol{r}_k > 0 \\ 0 & \text{otherwise.} \end{cases} \tag{3.40}$$

Excess PV generation is just fed into the grid, causing neither costs nor profits from selling in this case. The auxiliary variable $\boldsymbol{r}_k^+$ is introduced to denote the positive part of the residual load and the above case is enforced through the additional constraints

$$\boldsymbol{r}_k^+ \geq 0 \tag{3.41}$$

$$\boldsymbol{r}_k^+ \geq \boldsymbol{r}_k \tag{3.42}$$

which are added to the prosumer's optimization problem. The minimization of $\boldsymbol{r}_k^+$ in

$$f(\boldsymbol{r}_k^+) = \boldsymbol{c}_k^T \boldsymbol{r}_k^+ \tag{3.43}$$

leads to the exact value of the positive part of $\boldsymbol{r}_k$, which in return will be minimized with respect to an optimal feasible operation. Operational flexibility of the heating system will be used to integrate as much local PV generation by optimizing $\boldsymbol{u}_k$, the only controllable variable. Thus the self-consumption of the PV generation is maximized to minimize the net energy demand.
Further cost functions for MPC of building energy systems are possible but not considered in this thesis. E.g., comfort optimization can be achieved by penalizing the deviation of temperature trajectories from a reference. The cost term can be added and weighted against economic criteria as defined above in a multi-objective optimization, see [VDL+12,KJC16,ETP+17] for studies on comfort optimization in predictive control.

3.6 Prosumer MPC Optimization Problem

The final optimization problem to be solved at time k can now be stated, including the system model over the prediction horizon, constraints and the cost function. The optimization problem solved by the prosumer is composed of (3.44)-(3.51).
To proceed in the receeding horizon fashion of MPC, the controllable inputs $u(k|k)^*$ for the next time step, i.e. the first entry in the optimal solution $\boldsymbol{u}_k^*$, are applied to the system and problem (3.44)-(3.51) solved again with new x_0 and updated predictions $\boldsymbol{d}$.

$$\begin{aligned}
\underset{(\boldsymbol{u},\boldsymbol{r},\boldsymbol{r}^+)}{\text{minimize}} \quad & f(\boldsymbol{r}_k^+) && (3.44)\\
\text{subject to} \quad & \boldsymbol{x}_k = \mathcal{A}x_0 + \mathcal{B}\boldsymbol{u}_k + \mathcal{E}\boldsymbol{d}_k && (3.45)\\
& \underline{\boldsymbol{x}}_k \leq \boldsymbol{x}_k \leq \overline{\boldsymbol{x}}_k && (3.46)\\
& \overline{\mathcal{B}}\boldsymbol{u}_k \leq \overline{\boldsymbol{u}}_k && (3.47)\\
& \boldsymbol{u}_k \geq \boldsymbol{0} && (3.48)\\
& \boldsymbol{r}_k = \mathcal{B}_k^C \boldsymbol{u}_k + \boldsymbol{l}_k - \boldsymbol{g}_k && (3.49)\\
& \boldsymbol{r}_k^+ \geq \boldsymbol{r}_k && (3.50)\\
& \boldsymbol{r}_k^+ \geq \boldsymbol{0}. && (3.51)
\end{aligned}$$

Chapter 4

Power Flow and Distribution Grid Model

This chapter begins with a review on power flow models and the linearized model used in this thesis is introduced. The model is then applied to German reference grids in order to quantify the approximation error and to investigate the sensitivity to line overloading and undervoltages. Finally, the residential electricity demand model used for non-controllable household appliances is briefly reviewed.

4.1 Power Flow Models

To investigate the impact of loads and renewable generation on the distribution grid, a model to represent the state of operation of the power system is required. A *Power Flow* model describes the state of the system in terms of voltages, currents and phase angles. In the case of optimal operation with respect to generation costs or system losses, a so-called *Optimal Power Flow* problem is solved. The following power flow models are a balanced single-phase representation of the system, since unbalanced operation is not considered in this work. However, all models are extendable to the three-phase unbalanced case. While common household appliances are usually connected to a single phase[1], charging stations for electric vehicles and electrified heating equipment are required to have a three-phase connection when the rated apparent power is > 4.6 kVA [BDE19]. The recommended connection of the inverter heat pump WPL20 is three-phase, the smaller WPL7 can be connected to a single phase. The 8.8 kW back-up heater is always connected to three phases [Sti17]. This means, that the impact on the grid might only be underestimated with respect to single-phase standard electrical household appliances and smaller heat pumps in better insulated buildings.

4.1.1 AC Power Flow

Consider a power system with $|\mathcal{N}|$ buses in set $\mathcal{N} = \{0, 1, \dots, n\}$ and $|\mathcal{E}|$ branches in set $\mathcal{E} = \{1, \dots, e\}$ for distribution lines and transformers. The branch impedance between buses i and j is $Z_{ij} = R_{ij} + \mathrm{j}X_{ij}$ with resistance R_{ij}, reactance X_{ij} and imaginary unit $\mathrm{j} = \sqrt{-1}$. The branch admittance is $Y_{ij} = \frac{1}{Z_{ij}} = G_{ij} + \mathrm{j}B_{ij}$ with conductance G_{ij} and susceptance B_{ij}. Let $E_i = V_i e^{\mathrm{j}\theta_i}$ be the complex voltage of bus i with magnitude V_i and voltage angle θ_i and I_i be the complex net current injection at i defined accordingly. Further, let s_i be the apparent power injection at bus i with active power $p_i = \mathrm{Re}(s_i)$ and reactive power $q_i = \mathrm{Im}(s_i)$.
Based on Kirchhoff's law, the net apparent power injection s_i at bus i is given as [And12]:

$$s_i = p_i + \mathrm{j}q_i = E_i I_i^* \tag{4.1}$$

[1] Approximately 70% of all photovoltaic systems are single-phase connected in Germany [WW17].

$$s_i = V_i e^{\mathrm{j}\theta_i} \sum_{k \in \Omega_i^+} V_k e^{-\mathrm{j}\theta_k} (G_{ik} - \mathrm{j}B_{ik}). \tag{4.2}$$

The net injection here refers to local generation minus load. Ω_i^+ is the set of neighbor buses of i including bus i itself. The active and reactive power parts of s_i are obtained by:

$$p_i = V_i \sum_{k \in \Omega_i^+} V_k (G_{ik} \cos(\theta_i - \theta_k) + B_{ik} \sin(\theta_i - \theta_k)) \tag{4.3}$$

$$q_i = V_i \sum_{k \in \Omega_i^+} V_k (G_{ik} \sin(\theta_i - \theta_k) - B_{ik} \cos(\theta_i - \theta_k)). \tag{4.4}$$

Equations (4.3) and (4.4) state the nonlinear alternating current power flow ($ACPF$) problem depending on the variables V_i, θ_i, p_i and q_i when stated for each bus of $\mathcal{N}$. The system buses can be of $V\theta$-, pq- or pV-type, denoting which of the variables are specified and which have to be calculated. $V\theta$-buses serve as reference or slack buses with a fixed voltage and angle. pq-buses are load or generation buses without voltage control. Since the $ACPF$ cannot be solved analytically for realistic grid topologies, the solution has to be found with help of iterative approaches like the Newton-Raphson method, see [And12] for details.

4.1.2 DistFlow

In the case of balanced radial distribution grids, an alternative formulation to the above *bus injection model* can be given. The *DistFlow* model was developed in [BW89a,BW89c] for optimal capacitor placement in distribution grids and represents the power flow in a *branch flow model* form. In contrast to the *bus injection model*, we assume a directed graph $\mathcal{G} := (\mathcal{N}, \mathcal{E})$ with a tree structure established between the buses, numbered in increasing order starting from substation bus 0. A branch $(i, j) \in \mathcal{E}$ combines two buses in directed form $i \to j$. Accordingly, the active and reactive power flows P_{ij} and Q_{ij} denote the sending-end flows on the corresponding branch pointing to bus j. They are composed of the corresponding losses of branch $i \to j$, the load served at bus j and the aggregate power leaving bus j to its neighbor buses. The *DistFlow* equations are

$$P_{ij} = R_{ij} \frac{P_{ij}^2 + Q_{ij}^2}{U_i} + p_j + \sum_{k \in \mathcal{C}_j} P_{jk} \qquad \forall j \in \mathcal{N}^+ \tag{4.5}$$

$$Q_{ij} = X_{ij} \frac{P_{ij}^2 + Q_{ij}^2}{U_i} + q_j + \sum_{k \in \mathcal{C}_j} Q_{jk} \qquad \forall j \in \mathcal{N}^+ \tag{4.6}$$

$$U_j = U_i - 2(R_{ij} P_{ij} + X_{ij} Q_{ij}) + (R_{ij}^2 + X_{ij}^2) l_{ij} \qquad \forall i \to j \in \mathcal{E} \tag{4.7}$$

$$l_{ij} U_i = P_{ij}^2 + Q_{ij}^2 \qquad \forall i \to j \in \mathcal{E}. \tag{4.8}$$

$\mathcal{N}^+ = \mathcal{N} \setminus \{0\}$ is the set of buses without the substation bus. Since a tree structure is assumed, each bus j has a unique parent bus i with a smaller index and a set of child buses, the latter defined as $\mathcal{C}_j = \{k \in \mathcal{N}^+ \,|\, k : j \to k\}$. Consequently, $\mathcal{C}_j = \emptyset$ when j is an end bus. p_j and q_j denote the net or residual load at pq-bus j. $R_{ij} + \mathrm{j}X_{ij}$ is the branch's series impedance. There are neither flows pointing at the substation (root) bus, nor are loads considered, thus $P_{i0} = Q_{i0} = 0, p_0 = q_0 = 0$ and the elements are excluded from the enumeration. The substation bus (primary side of the transformer) is assumed to be the reference bus with a fixed constant

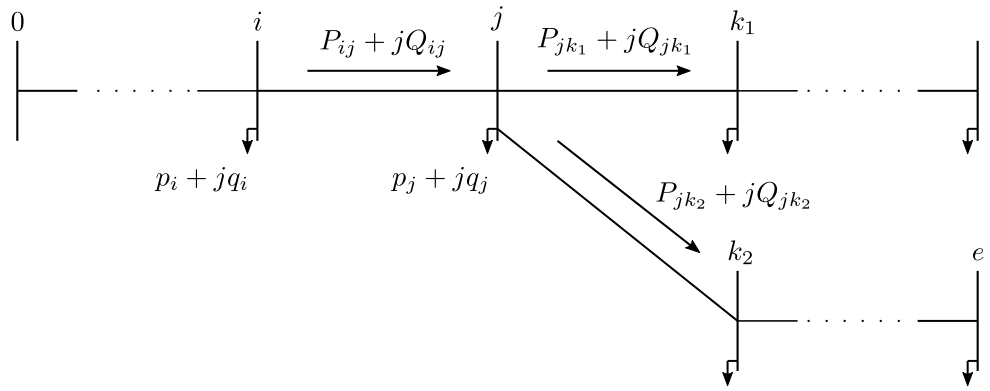

Figure 4.1: *The DistFlow grid model, drawing based on [BW89c].*

voltage $E_0 = V_0 e^{j0}$, $V_0 = V_{ref}$ and the voltage angle neglected. $U_j = V_j^2$ is introduced as the squared voltage magnitude. $l_{ij} = |I_{ij}|^2$ is the squared magnitude of the current flowing from bus i to j. A drawing of the radial *DistFlow* grid model is shown in Figure 4.1.
A proof for the general equivalence between the *bus injection model* and the *branch flow model* is given in [Low14a, Low14b]. In case of a balanced radial grid, Equations (4.5)-(4.8) give an equivalent representation of the previous AC power flow model. The bus phase angles can be omitted in the computation for balanced radial grids and can be uniquely recovered based on the power flows and bus voltages. A further extension of the model allows for the application of the *branch flow model* to meshed networks by introducing an additional cycling condition. The approach and equivalence is shown in [FL13], see [MDS+17] for an overview in power flow models. In [BW89a], an iterative nonlinear programming method is used to solve the placement problem and superior numerical robustness compared to the *bus injection model* is shown for distribution grids with typically high R/X ratios. Still, due to Equation (4.8), an optimization using the *DistFlow* equations results in a non-convex optimization problem. The authors in [FL13] relax Equation (4.8) to an inequality constraint and obtain a convex second-order cone program. They also show exactness of the relaxed OPF.

4.1.3 Linearized DistFlow

Alternatively, a linearized version of the *DistFlow*, the *Linearized DistFlow* model can be obtained by neglecting the losses in (4.5)-(4.7) and setting $l_{ij} = 0$. Hence, the active and reactive power losses are assumed to be small compared with the power flows. The *LinDistFlow* equations are

$$P_{ij} = p_j + \sum_{k \in \mathcal{C}_j} P_{jk} \qquad \forall j \in \mathcal{N}^+ \tag{4.9}$$

$$Q_{ij} = q_j + \sum_{k \in \mathcal{C}_j} Q_{jk} \qquad \forall j \in \mathcal{N}^+ \tag{4.10}$$

$$U_j = U_i - 2(R_{ij}P_{ij} + X_{ij}Q_{ij}) \qquad \forall i \to j \in \mathcal{E}. \tag{4.11}$$

The linear approximation was first stated in [BW89a, BW89c]. Without the losses taken into account, the total active and reactive power demand of the grid is underestimated. In contrast to the *DistFlow* model, the *LinDistFlow* equations are linear and can be solved directly. These favorable properties guarantee computational efficiency for the optimization problem discussed

in Chapter 5.
As mentioned earlier, the operation of a power system can be performed with respect to a certain cost function. Common cost functions for grid operators enforce peak load reduction or the minimization of power losses. For the case of loss minimization, the *DistFlow* losses for the whole grid equal the resistive losses summarized over all branches:

$$\mathcal{L}_{DistFlow} = \sum_{(i,j)\in\mathcal{E}} R_{ij}\frac{P_{ij}^2 + Q_{ij}^2}{V_i^2}. \tag{4.12}$$

Assuming $V_i^2 \approx V_0^2$ in (4.12), the losses in the *LinDistFlow* case can be further simplified to avoid the nonlinearity [BW89b]:

$$\mathcal{L}_{LinDistFlow} = \sum_{(i,j)\in\mathcal{E}} R_{ij}\frac{P_{ij}^2 + Q_{ij}^2}{V_0^2}. \tag{4.13}$$

Another common linear approximation of the *ACPF* is the DC power flow method, where only active power is considered, the line resistances are neglected, voltage angle differences are assumed to be small and the voltage profile in the grid is assumed to be flat. Those assumptions are often used in market applications where voltages are of minor importance [SJA09], but are usually not justified for applications in distribution grids [MDS+17].
Equations (4.9)-(4.11) result in a system of linear equations of form $Ax = b$. To simplify the notation for a more compact expression, the index pair (i, j) for branch flows and line parameters is reduced to j if the power flow and corresponding branch point to bus j, i.e.
$(P_{ij}, Q_{ij}, R_{ij}, X_{ij}) = (P_j, Q_j, R_j, X_j)$. Thus, all branch flows are indexed by the set $\mathcal{N}^+$. $|\mathcal{E}| = |\mathcal{N}^+|$ holds in the case of a radial grid, but both sets are kept for an intuitive understanding of the structure of the following matrices and vectors. The grid topology is stated in form of connected branch flows, with sorted vectors $P \in \mathbb{R}^{|\mathcal{E}|}$, $Q \in \mathbb{R}^{|\mathcal{E}|}$, $U \in \mathbb{R}^{|\mathcal{N}|}$ of form

$$P = (P_1, P_2, \ldots, P_e)^T \qquad Q = (Q_1, Q_2, \ldots, Q_e)^T \qquad U = (U_0, U_1, \ldots, U_n)^T$$

and the connectivity given by matrices $C_P, C_Q \in \mathbb{R}^{|\mathcal{N}^+|\times|\mathcal{E}|}$ and $C_U \in \mathbb{R}^{|\mathcal{E}|\times|\mathcal{N}|}$ with rows sorted by the power flows:

$$C_{P|Q}(i,j) = \begin{cases} 1 & \text{if } i = j \\ -1 & \text{if branch flow } i \text{ connects with branch flow } j \\ 0 & \text{otherwise} \end{cases} \tag{4.14}$$

$$C_U(i,j) = \begin{cases} -1 & \text{if bus } j \text{ is sending end of flow } i \\ 1 & \text{if bus } j \text{ is receiving end of flow } i \\ 0 & \text{otherwise.} \end{cases} \tag{4.15}$$

The branch resistances and reactances are saved in $R \in \mathbb{R}^{|\mathcal{E}|\times|\mathcal{E}|}$ and $X \in \mathbb{R}^{|\mathcal{E}|\times|\mathcal{E}|}$ with

$$R = \mathrm{diag}(R_1, R_2, \ldots, R_e) \qquad X = \mathrm{diag}(X_1, X_2, \ldots, X_e).$$

The above defined matrices lead to a compact expression of the line flows and bus voltages

$$C_P P = p \qquad C_Q Q = q \qquad C_U U = \mathbf{0}_{|\mathcal{E}|}, \tag{4.16}$$

with vectors $p \in \mathbb{R}^{|\mathcal{N}^+|}$ and $q \in \mathbb{R}^{|\mathcal{N}^+|}$

$$p = (p_1, p_2, \ldots, p_n)^T \qquad q = (q_1, q_2, \ldots, q_n)^T$$

corresponding to the active and reactive loads at the buses. Depending on the given scenario, both active and reactive power might be consumed and/or generated at a given bus, leading to

$$p_j = p_j^{(c)} - p_j^{(g)} \qquad q_j = q_j^{(c)} - q_j^{(g)}.$$

To obtain a solution of the linear equation system $Ax = b$ from (4.16) with $x = (P^T, Q^T, U^T)^T$, the voltage at the substation can be fixed to $U_0 = U_{ref}$. This can be achieved by adding an additional constraint to the system of equations or by deleting the first column of C_U, removing U_0 from solution vector U and changing the first entry in the right-hand side zeros vector to U_{ref}. From now on, the voltage vector is defined as

$$U = (U_1, U_2, \ldots, U_n)^T, \in \mathbb{R}^{|\mathcal{N}^+|}. \tag{4.17}$$

With given loads p and q and the fixed voltage at the substation, the *LinDistFlow* model determines a solution for the active and reactive branch flows and the voltage profile of the grid. Finally, the compact form

$$\Pi x = \delta \tag{4.18}$$

of the *LinDistFlow* model is given with the vectors $x \in \mathbb{R}^{2|\mathcal{E}|+|\mathcal{N}^+|}$, $\delta \in \mathbb{R}^{2|\mathcal{N}^+|+|\mathcal{E}|}$ and matrix $\Pi \in \mathbb{R}^{(2|\mathcal{N}^+|+|\mathcal{E}|)\times(2|\mathcal{E}|+|\mathcal{N}^+|)}$ as

$$\Pi = \begin{pmatrix} C_P & \mathbf{0}_{|\mathcal{N}^+|\times|\mathcal{E}|} & \mathbf{0}_{|\mathcal{N}^+|\times|\mathcal{N}^+|} \\ \mathbf{0}_{|\mathcal{N}^+|\times|\mathcal{E}|} & C_Q & \mathbf{0}_{|\mathcal{N}^+|\times|\mathcal{N}^+|} \\ 2R & 2X & C_U \end{pmatrix} \qquad x = \begin{pmatrix} P \\ Q \\ U \end{pmatrix} \qquad \delta = \begin{pmatrix} p \\ q \\ c_u \end{pmatrix}, \tag{4.19}$$

with

$$c_u = \begin{pmatrix} U_{ref} \\ \mathbf{0}_{|\mathcal{E}|-1} \end{pmatrix}. \tag{4.20}$$

4.1.4 Operational Constraints

The quadratic cost function (4.13) in combination with the linear equations (4.9)-(4.11) results in a convex quadratic optimization problem. Further operational constraints for voltages and line currents can be included in the optimization. Bus voltages are usually operated within a specified tolerance band $\underline{V} \leq V \leq \overline{V}$. Assuming a symmetric tolerance of $\pm\varepsilon$ for the bus voltage V_j, the voltage constraint becomes

$$\begin{aligned} V_{ref}(1-\varepsilon) \leq V_j \leq V_{ref}(1+\varepsilon) \\ V_{ref}^2(1-\varepsilon)^2 \leq U_j \leq V_{ref}^2(1+\varepsilon)^2 \qquad \forall j \in \mathcal{N}^+, \end{aligned} \tag{4.21}$$

with $U_j = V_j^2$. Typical values for the tolerated deviation from the reference are $\pm 10\%$ [DIN02]. It is important to note that the distribution grid operator might split up the total tolerance band over both the medium- and low-voltage grids. This can lead to a situation where for example only 5% of the tolerance band remains for the low-voltage grid due to a strong voltage drop in the medium-voltage grid. Typical values of the split DSOs use in operation can be found in [Ruf18]. Further operational constraints state that the branch currents must not exceed their ther-

Table 4.1: *Parameters of the radial synthetic low-voltage grids from [LAW+16].*

	Rural 1	**Rural 2**	**Village 1**	**Village 2**	**Suburb**
Transformer rating	250 kVA	250 kVA	250 kVA	400 kVA	400 kVA
# buses	36	18	80	74	204
# load buses	17	8	39	36	101
Feeder					
# feeders	5	4	4	4	11
longest feeder	664 m	228 m	544 m	520 m	414 m
main type	cable	overhead line	cable	cable & overhead line	cable
cross section	150 mm^2	70 mm^2	150 mm^2	70 − 150 mm^2 & 50 − 120 mm^2	150 mm^2
House connection					
length	29 m	4 m	21 m	17 m	18 m
cross-section	50 mm^2	35 mm^2	50 mm^2	35 mm^2	35 mm^2

mal rating, i.e. $l_{ij} \leq \overline{I_{ij}}$. Grid assets state apparent power limits $\overline{S}$, which allows to directly derive operational limits for the power flows used in the *LinDistFlow* model. With $S = \sqrt{P^2 + Q^2}$, $Q = P\tan(\varphi)$ and a constant power factor $pf = \cos(\varphi)$ assumed, the apparent power can be expressed only depending on the active power flow $S = \sqrt{P^2 + (P\tan(\varphi))^2} = P\sqrt{1 + \tan^2(\arccos(pf))}$. The operational limits on the possibly bidirectional active power flows can be derived:

$$P \leq \overline{P} = \frac{\overline{S}}{\sqrt{1 + \tan^2(\arccos(pf))}} \tag{4.22}$$

$$P \geq \underline{P} = -\overline{P}. \tag{4.23}$$

4.2 Distribution Grid Model

Studies on the impact of distributed energy resources on distribution grids are often based on either strongly simplified grid models or on segments of real grids with limited transferability of the results as a consequence [LAW+16]. The German research project *U − Control* classified real low-voltage grids by the mean geographical distance between households to develop reference grids to investigate static voltage stability. 358 real distribution grids were classified as a rural, village or suburban grid. A transformer's apparent power rating was no longer found to be a useful parameter for classification, since many rural grids have received transformer upgrades with the expansion of renewable energies [LAW+16].

Table 4.1 shows the characteristics of the five residential synthetic reference grids developed in the project. All grids are radial. *Rural Grid 1* is of type cable and has larger cross sections than *Rural Grid 2*, which is composed by overhead lines. However, the higher number of load buses and the longer distances between the households lead to stronger voltage drops compared with *Rural Grid 2*.

Figure 4.2 shows the topology of *Rural Grid 1*, which is primarily used for the simulations in Chapter 6. In contrast to the grids with more buses, *Rural Grid 1* still allows to solve the central optimization problems introduced in Section 5.4.4 on the local simulation machine without running into memory issues.

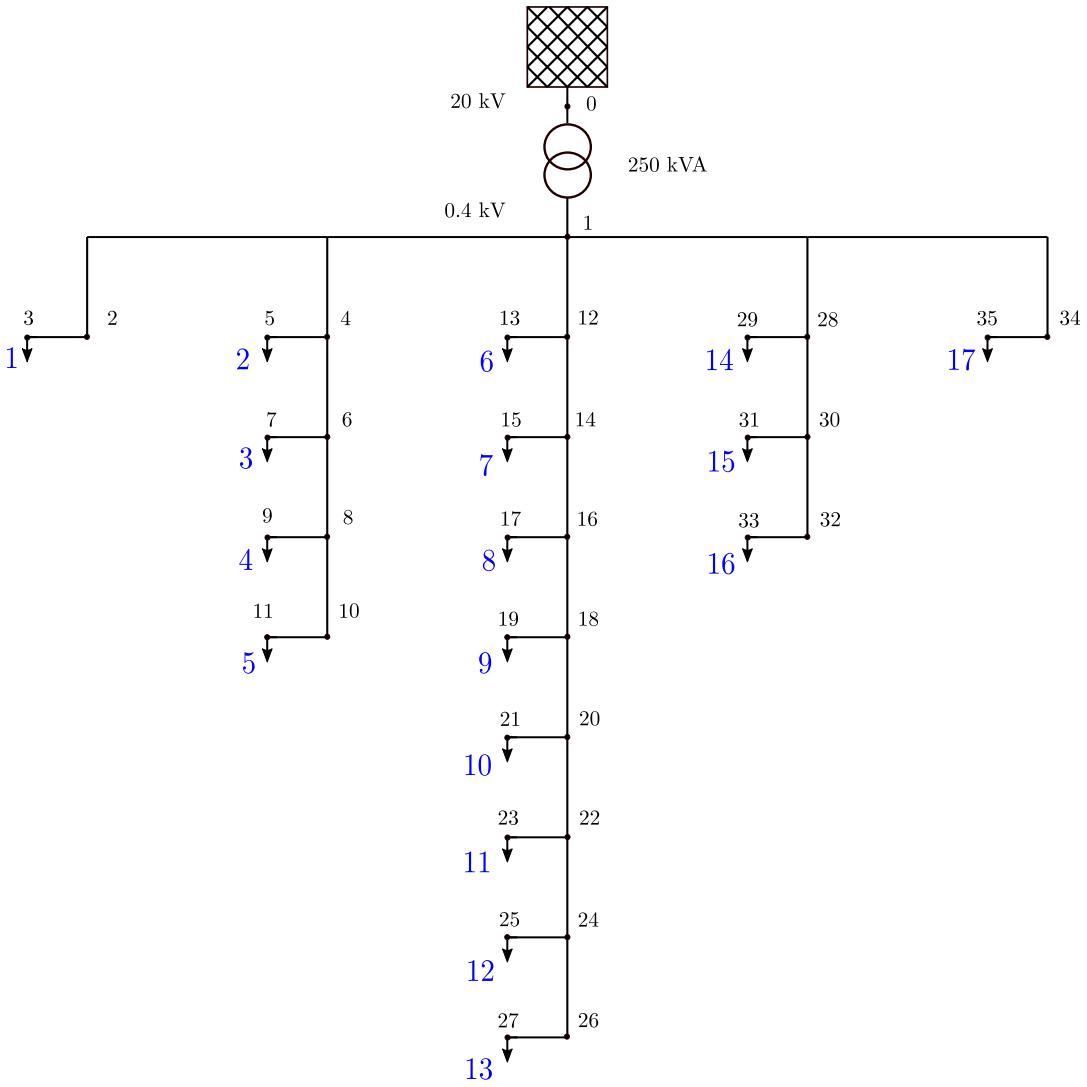

Figure 4.2: *Topology of Rural Grid 1 based on [LAW+16], bus numbers indicated in black, load/prosumer numbers in blue.*

4.3 LinDistFlow Approximation Error

This section investigates at which level of coincident load grid violations occur in the above introduced distribution grids and how well the *LinDistFlow* model approximates the reference solution from the nonlinear *ACPF* model.

Figure 4.3 shows the per unit bus voltages and branch loadings relative to the apparent power branch limits $\overline{S}$ for active power levels varied from 1 to 15 kW at all load buses for *Rural Grid 1* from [LAW+16]. The same active load p is assumed at all load buses and a constant power factor of 0.9 is assumed. The solutions are computed with Newton's method in MATPOWER from [ZMST11]. Slack bus 0 at the primary side of the transformer remains always at $1\,p.u.$. Bus 27 is the first bus to violate the lower voltage limit of $\underline{V} = 0.9\,p.u.$, followed by the neighbor buses with decreasing distance to the substation. Due to the high impedance as a result of the long distance from the substation, the buses at the ends of the feeders are affected first. Overloading occurs at a similar power level on branch 1 (transformer), which transfers the grid's total active and reactive power demands. The next branches to be potentially overloaded when

the coincident power is further increased would be the ones transferring power to the longest feeder of the grid, see e.g. branch 12.
The bottom plot in Figure 4.3 shows the approximation error resulting from the implementation of the *LinDistFlow* model when compared with the *ACPF* model. At the critical power level of 12.25 kW, the *ACPF* model shows undervoltage at bus 27, while the respective bus voltage has not yet fallen below 0.9 *p.u.* in the *LinDistFlow* model. This results from the negligence of the active and reactive power losses.
The *LinDistFlow* model becomes slightly less accurate when the reference voltage at bus 0 is reduced from 1 *p.u.* to 0.95 *p.u.* to simulate peak-load conditions in the medium-voltage grid. The difference between the voltages at bus 27 increases from 0.0046 *p.u.* to 0.0056 *p.u.*. Increased currents to serve the same load at a lower voltage level lead to higher losses, which are not considered in the *LinDistFlow* model.

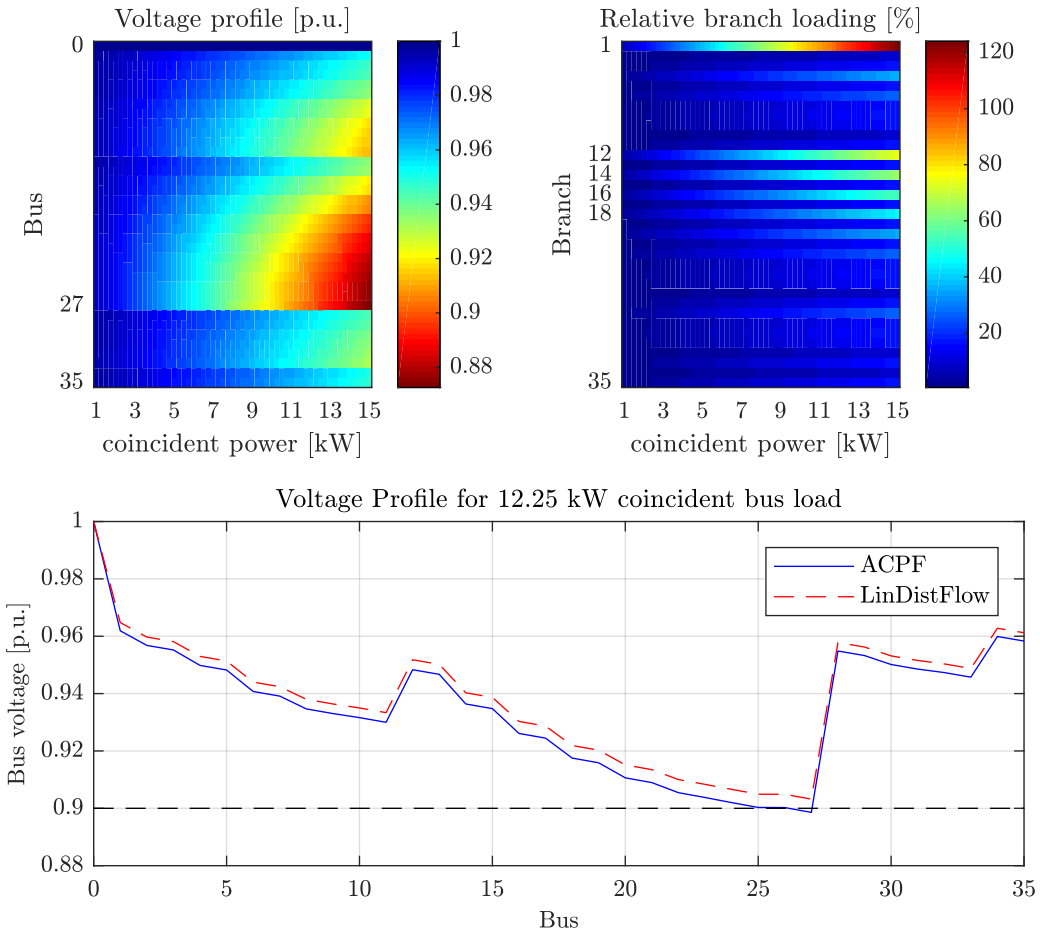

Figure 4.3: *Top: ACPF voltage profiles and branch loadings in percentage apparent power for Rural Grid 1 for increasing coincident power levels at all load buses. Bottom: Voltage difference between the ACPF and LindDistFlow solutions for coincident active power of* 12.25 kW *at all load buses. Power factor* $\cos(\varphi) = 0.9$ *assumed.*

Table 4.2 shows for which coincident active bus load condition grid violations occur in all of the test grids from [LAW+16]. The gradual increase in steps of 0.25 kW leads to either a bus voltage violation, i.e. the voltage falls below 0.9 *p.u.*, or to exceedance of the apparent power limit of a branch. The table displays the level of active power per bus at which a violation occurs and of which type the violation is. The second violation is defined as the next violation which takes

Table 4.2: *Violation of grid constraints, i.e. bus voltage below 0.9 p.u. or branch flow above the maximum apparent power $\overline{S}$ for the ACPF and LinDistFlow (LDF) models. The p.u. difference between the voltages at the most critical bus and the relative difference of the apparent power flow S_1 at the transformer are stated for 1st violation conditions in ACPF. Grid parameters from [LAW+16].*

	1st violation		**2nd violation**		$V^{LDF} - V^{ACPF}$
	ACPF	*LDF*	*ACPF*	*LDF*	$\frac{S_1^{LDF} - S_1^{ACPF}}{S_1^{ACPF}}$
Rural 1	12.25 kW	12.75 kW	12.5 kW	13 kW	
-bus	27	27	{27,26,25,24}	{27,26,25}	0.0046 p.u.
-branch			1		-6.8%
Rural 2	26.25 kW	28.25 kW	28.5 kW	30 kW	
-bus			{8,9,14,15}	{9,15}	0.0049 p.u.
-branch	1	1	1	1	-7.2%
Village 1	5.5 kW	6 kW	6.75 kW	7 kW	
-bus			{46-51}	{49,51}	0.0034 p.u.
-branch	1	1	1	1	-5.9%
Village 2	9 kW	9.25 kW	9.25 kW	9.5 kW	
-bus	{40-43}	43	{38-43}	{39-43}	0.0047 p.u.
-branch					-6.6%
Suburb	3.5 kW	3.75 kW	6 kW	6.5 kW	
-bus			{155-159}	{155-159}	0.0024 p.u.
-branch	1	1	1	1	-4.7%

place at a bus or branch in addition to the first violation.
Whether undervoltage or congestion occurs first, depends on the type of grid. When looking at high load scenarios, violations either first occur at the buses with longest distance to the substation or at the transformer due to overloading. The *LinDistFlow* model correctly replicates the type of violation. The level of coincident active power to trigger the first violation is in the range of 0.25−2 kW higher in the *LinDistFlow* model, since it neglects line losses. The simplification is also reflected in the sometimes lower total number of affected buses in the *LinDistFlow* model. As a result, grid violations are detected slightly too late in *LinDistFlow* model, but the use of a security margin can avoid this. It can be observed how the level of coincident power to cause a violation is lower for the grids with a higher number of buses. The coincident maximum operation of heat pump WPL20 and the back-up heater during cold ambient temperatures would lead to violations in all grids except *Rural Grid 2*.

4.4 Residential Electricity Demand Model

This chapter closes with a short review of the model published by the author in [JKC15] to generate time-varying residential electricity demand profiles for multi-period simulations. The random bottom-up model generates power profiles for a population of households with a specified size and annual electricity consumption. The profiles account for the non-controllable fixed electricity demand of appliances ($\boldsymbol{l}_k$ in Equation (3.49)) and are resampled to a temporal resolution of 15 minutes. The model was initially based on the occupancy and activity statistics from the TUS data in [FDZa]. The profile statistics were successfully validated against smart meter

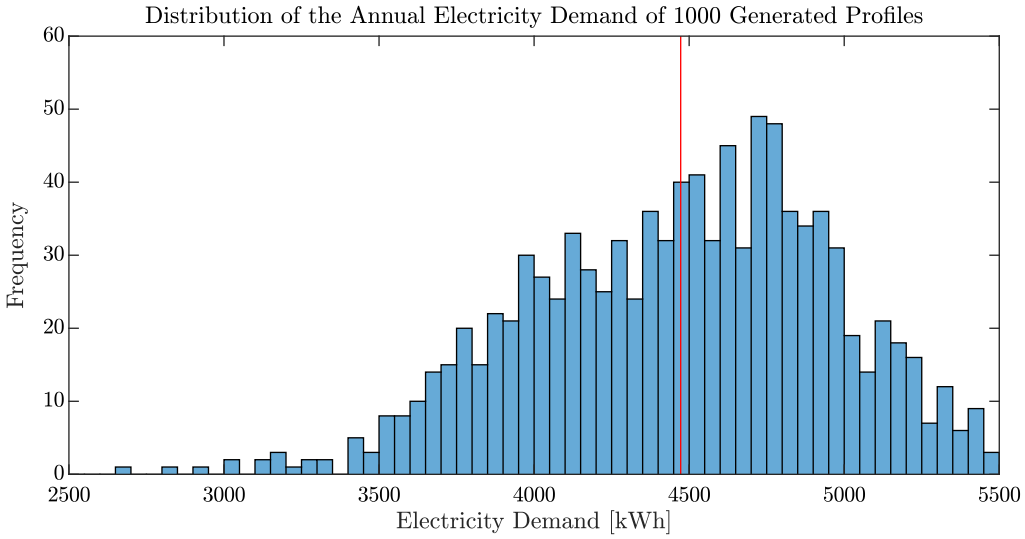

Figure 4.4: *Distribution of the annual electricity demand for 1000 4-person households generated with the REM.*

data and the residential electricity demand model (REM) achieves realistic coincident factors. Figure 4.4 shows the distribution of the annual electricity demand for 1000 4-person households. The average demand is 4 473 kWh. Profiles from this population are used for the simulations in Chapter 6.

Chapter 5

Hierarchical Distributed MPC of Prosumers in Distribution Grids

This chapter begins with a review of the ADMM algorithm, followed by the introduction of a general central MPC problem statement. Thereafter, a decomposition is carried out to facilitate a distributed hierarchical control architecture. Finally, the coordination problem is adapted to the setting of a distribution grid hosting multiple prosumers. All MPC cost functions and constraints are defined in this context.

5.1 Review of ADMM

The literature review in Chapter 1 has shown that different methods exist and are used in the smart grid and control communities to decompose and solve large-scale optimization problems in a distributed fashion. The methods involve the reformulation and decomposition of the initial central optimization problem, followed by the execution of a coordination algorithm to find the optimal solution to the initial optimization problem in an iterative and distributed procedure. The alternating direction method of multipliers (ADMM) and dual decomposition are two methods often applied in the literature reviewed. ADMM has received increased attention in recent years, significantly caused by the popular review paper on ADMM in [BPC+10]. Applications of the method beyond smart girds an controls can be found, e.g., in machine learning and image processing, where optimization problems include large data sets. A detailed review of ADMM and a discussion of its origin and connection with other decomposition methods is given in [BPC+10]. The success of ADMM results from its convergence under milder mathematical conditions and its better rate of convergence in practice when compared with other methods. Dual decomposition methods require conditions like strict convexity and finiteness of local cost functions and are not robust in the sense that a poor parameter selection may lead to algorithm divergence. In contrast, ADMM converges under milder conditions for any positive value of its penalty parameter [BPC+10, Kra14, GTSJ15, SL12]. Nevertheless, the choice of the penalty parameter has a strong impact on the performance of ADMM, i.e., on the final number of iterations and total time needed to converge to a solution of predefined accuracy required in practice. Algorithm tuning and the development of enhanced parameter selection methods is an ongoing field of research in order to speed up ADMM, see [GTSJ15, XFG17]. A more detailed discussion is given in Section 5.4.5. The remainder of this review gives a brief introduction to the dual ascent algorithm, the dual decomposition algorithm, the method of multipliers and ADMM to motivate the development and use of the latter.

5.1.1 Dual Ascent, Dual Decomposition and the Method of Multipliers

The following section is based on the review of the algorithm in [BPC+10]. *Dual ascent* is an optimization algorithm to solve problems of the form

$$\begin{aligned} \underset{x}{\text{minimize}} \quad & f(x) \\ \text{subject to} \quad & Ax = b \end{aligned} \tag{5.1}$$

with $x \in \mathbb{R}^n$, $A \in \mathbb{R}^{m \times n}$, $b \in \mathbb{R}^m$ and $f : \mathbb{R}^n \to \mathbb{R}$ is a convex function. The *Lagrangian* of problem (5.1) is

$$\mathcal{L}(x, \lambda) = f(x) + \lambda^T (Ax - b) \tag{5.2}$$

with the dual variable $\lambda \in \mathbb{R}^m$. The dual ascent method then solves problem (5.1) by iterating through the following steps until convergence:

$$x^{\ell+1} := \underset{x}{\operatorname{argmin}}\ \mathcal{L}(x, \lambda^\ell) \tag{5.3}$$

$$\lambda^{\ell+1} := \lambda^\ell + \rho^\ell (Ax^{\ell+1} - b). \tag{5.4}$$

ℓ is the iteration counter and $\rho^\ell > 0$ is the step size for the update of the dual variable.
The dual ascent method enables a distributed optimization for problems with a separable cost function. It is assumed that f is separable in a partition of $x = (x_1^T, x_2^T, \ldots, x_N^T)^T$ with

$$f(x) = \sum_{i=1}^{N} f_i(x_i) \tag{5.5}$$

and matrix A is partitioned as $A = [A_1, \ldots, A_N]$ corresponding to the $x_i \in \mathbb{R}^{n_i}$. The new Lagrangian becomes

$$\mathcal{L}(x, \lambda) = f(x) + \lambda^T (Ax - b) \tag{5.6}$$

$$= \sum_{i=1}^{N} f_i(x_i) + \sum_{i=1}^{N} (\lambda^T A_i x_i - \frac{1}{N} \lambda^T b) \tag{5.7}$$

$$= \sum_{i=1}^{N} (f_i(x_i) + \lambda^T A_i x_i - \frac{1}{N} \lambda^T b) \tag{5.8}$$

$$= \sum_{i=1}^{N} \mathcal{L}_i(x_i, \lambda) \tag{5.9}$$

and thus is separable itself. This allows for the x-update in (5.3) to be carried out in parallel for N distributed subproblems. Afterwards, a central entity collects the results and computes and broadcasts the updated dual variables like in (5.4). The dual ascent method applied to a separable problem like above is referred to as *dual decomposition*. The dual decomposition updates finally are:

$$x_i^{\ell+1} := \underset{x_i}{\operatorname{argmin}}\ \mathcal{L}_i(x_i, \lambda^\ell) \tag{5.10}$$

$$\lambda^{\ell+1} := \lambda^\ell + \rho^\ell (Ax^{\ell+1} - b). \tag{5.11}$$

Dual decomposition enables a distributed optimization, but convergence requires rather strict properties of the optimization problem, i.e. f must be strictly convex and convergence depends

on the choice of the step size ρ^ℓ, see [BPC+10, SL12, GTSJ15].
The *method of multipliers* overcomes those strong assumptions with an additional penalty term, which provides robustness to the convergence and allows for a broader range of cost functions. The method of multipliers considers the augmented problem of (5.1), given by

$$\begin{aligned} \underset{x}{\text{minimize}} \quad & f(x) + \frac{\rho}{2}\|Ax - b\|_2^2 \\ \text{subject to} \quad & Ax = b. \end{aligned} \tag{5.12}$$

$\rho \in \mathbb{R}_{>0}$ is the penalty parameter to penalize equality constraint violations. Problem (5.1) and (5.12) are equivalent, since the penalty term vanishes for a feasible solution of x. The augmented Lagrangian is

$$\mathcal{L}_\rho(x, \lambda) = f(x) + \lambda^T(Ax - b) + \frac{\rho}{2}\|Ax - b\|_2^2 \tag{5.13}$$

and applying dual ascent leads to the steps of the method of multipliers:

$$x^{\ell+1} := \underset{x}{\text{argmin}}\ \mathcal{L}_\rho(x, \lambda^\ell) \tag{5.14}$$

$$\lambda^{\ell+1} := \lambda^\ell + \rho(Ax^{\ell+1} - b). \tag{5.15}$$

In fact, the cost function f no longer has to be strictly convex or finite for the algorithm to converge. Unfortunately, even if the cost function f is separable, the penalty term may lead to products between the decision variables x_i, depending on A. This prevents the x-update to be separated across subsystems. In this case, a decomposition for a distributed optimization is not possible with the method of multipliers [BPC+10].

5.1.2 General Form ADMM

The ADMM algorithm finally blends the decomposability of dual ascent with the superior convergence of the method of multipliers [BPC+10]. The initial problem is slightly changed by splitting vector x in x and z and by separating the cost function f in f and g. In its standard variant, ADMM solves optimization problems of the form

$$\begin{aligned} \underset{x,z}{\text{minimize}} \quad & f(x) + g(z) \\ \text{subject to} \quad & Ax + Bz = c \end{aligned} \tag{5.16}$$

where $x \in \mathbb{R}^n$, $z \in \mathbb{R}^m$, $A \in \mathbb{R}^{p\times n}$, $B \in \mathbb{R}^{p\times m}$ and $c \in \mathbb{R}^p$ and $f : \mathbb{R}^n \to \mathbb{R}$ and $g : \mathbb{R}^m \to \mathbb{R}$ are assumed to be two convex functions. The augmented Lagrangian of problem (5.16) becomes

$$\mathcal{L}_\rho(x, z, \lambda) = f(x) + g(z) + \lambda^T(Ax + Bz - c) + \frac{\rho}{2}\|Ax + Bz - c\|_2^2 \tag{5.17}$$

with $\rho \in \mathbb{R}_{>0}$ and the dual variable λ. The ADMM iterations are

$$x^{\ell+1} := \underset{x}{\text{argmin}}\ \mathcal{L}_\rho(x, z^\ell, \lambda^\ell) \tag{5.18}$$

$$z^{\ell+1} := \underset{z}{\text{argmin}}\ \mathcal{L}_\rho(x^{\ell+1}, z, \lambda^\ell) \tag{5.19}$$

$$\lambda^{\ell+1} := \lambda^\ell + \rho(Ax^{\ell+1} + Bz^{\ell+1} - c) \tag{5.20}$$

The sequential evaluation of the augmented Lagrangian at the x- and z-update leads to an alternating solution scheme. Due to the decomposition in the objective, the primal updates are carried out separately with respect to their respective cost function and a quadratic term, instead

of a joint minimization over x and z.
It is convenient to reformulate $\mathcal{L}_\rho(x,z,\lambda)$ in order to combine the linear and quadratic terms in the x- and z-updates. With $a=\frac{\lambda}{\rho}$, $b=Ax+Bz-c$ and the help of the identity $\|a+b\|_2^2-\|b\|_2^2=2a^Tb+\|a\|_2^2$, the Lagrangian in (5.17) can be written as

$$\mathcal{L}_\rho(x,z,\lambda)=f(x)+g(z)+\frac{\rho}{2}\|Ax+Bz-c+\frac{\lambda}{\rho}\|_2^2-\frac{\rho}{2}\|\frac{\lambda}{\rho}\|_2^2 \tag{5.21}$$

$$\mathcal{L}_\rho(x,z,\nu)=f(x)+g(z)+\frac{\rho}{2}\|Ax+Bz-c+\nu\|_2^2-\frac{\rho}{2}\|\nu\|_2^2, \tag{5.22}$$

with the scaled dual variable $\nu=\frac{\lambda}{\rho}$. The scaled form of ADMM is then given by

$$x^{\ell+1}:=\underset{x}{\operatorname{argmin}}\left(f(x)+\frac{\rho}{2}\|Ax+Bz^\ell-c+\nu^\ell\|_2^2\right) \tag{5.23}$$

$$z^{\ell+1}:=\underset{z}{\operatorname{argmin}}\left(g(z)+\frac{\rho}{2}\|Ax^{\ell+1}+Bz-c+\nu^\ell\|_2^2\right) \tag{5.24}$$

$$\nu^{\ell+1}:=\nu^\ell+Ax^{\ell+1}+Bz^{\ell+1}-c. \tag{5.25}$$

Changing problem (5.16) to

$$\begin{aligned}\underset{x\in\mathcal{X},z\in\mathcal{Z}}{\text{minimize}}\quad & f(x)+g(z)\\ \text{subject to}\quad & Ax+Bz=c,\end{aligned} \tag{5.26}$$

where the decision variables $x\in\mathcal{X}$ and $z\in\mathcal{Z}$ are restricted by constrained convex sets, does not impact the ADMM procedure. The x- and z-updates involve now solving constrained convex optimization problems:

$$x^{\ell+1}:=\underset{x\in\mathcal{X}}{\operatorname{argmin}}\left(f(x)+\frac{\rho}{2}\|Ax+Bz^\ell-c+\nu^\ell\|_2^2\right) \tag{5.27}$$

$$z^{\ell+1}:=\underset{z\in\mathcal{Z}}{\operatorname{argmin}}\left(g(z)+\frac{\rho}{2}\|Ax^{\ell+1}+Bz-c+\nu^\ell\|_2^2\right) \tag{5.28}$$

(5.25).

Convergence to an optimal solution is guaranteed for convex optimization problems, see also the discussions in [BPC+10, Bra16, BFG+18]. All implementations in this thesis involve constrained convex optimization problems. We omit such restriction in the following section for clarity, but introduce constraints in Section 5.3, where the ADMM algorithm is applied to the coordination problem between the prosumers and the DSO.

5.1.3 Convergence and Stopping Criteria

A convergence proof for ADMM is given in the appendix of [BPC+10], and an in-depth discussion of the convergence is presented in [EY15]. According to [BPC+10], f and g must be convex functions for the ADMM algorithm to converge. The corresponding x- and z-updates must be solvable and a solution to the minimization of the augmented Lagrangian. The ADMM iterations $\ell\to\infty$ then lead to convergence of

- the residual $\Delta_{prim}^\ell=Ax^\ell+Bz^\ell-c$ to zero: $\Delta_{prim}^\ell\to 0$ (approaching feasibility),
- the objective to its optimal value: $f(x^\ell)+g(z^\ell)\to p^*$, $p^*=\min\{f(x)+g(z)|Ax+Bz=c\}$,
- the dual to the optimal dual point: $\lambda^\ell\to\lambda^*$.

Note that the convergence for convex problems does not depend on the value of the penalty parameter ρ, but the choice of ρ may impact the speed of convergence, i.e. the change in difference between an intermediate solution and the optimal solution after a finite number of iterations. The optimal choice of ρ for superior speed of convergence is problem-specific and a near-optimal selection is in general found by trial and error. Looking at the x- and z-updates in (5.23) and (5.24), one sees that ρ weights feasibility against the cost function, which means that a large value of ρ may enforce early global feasibility, but the solution may be far from the optimum. [BPC+10] finally discusses extensions for the penalty parameter ρ to vary in each iteration to achieve superior convergence. At the same time it is also argued, that many practical applications do not need high accuracy solutions, which may require many iterations, but one may be satisfied with solutions of modest accuracy found after only few iterations. Based on this observation, stopping criteria are derived to allow termination of the algorithm for a predefined tolerance. The primal residual $\Delta_{prim}^{\ell+1}$ and dual residual $\Delta_{dual}^{\ell+1}$ (the latter derived in [BPC+10] from the optimality conditions) track the primal and dual feasibility over iterations:

$$\Delta_{prim}^{\ell+1} = Ax^{\ell+1} + Bz^{\ell+1} - c \tag{5.29}$$

$$\Delta_{dual}^{\ell+1} = \rho A^T B(z^{\ell+1} - z^{\ell}). \tag{5.30}$$

The quantities approach zero with the number of algorithm iterations. Termination criteria are then given by sufficiently small residuals

$$\|\Delta_{prim}^{\ell+1}\|_2 \leq \varepsilon_{\text{prim}} \qquad\qquad \|\Delta_{dual}^{\ell+1}\|_2 \leq \varepsilon_{\text{dual}}, \tag{5.31}$$

where the values of the tolerances $\varepsilon_{\text{prim}} > 0$ and $\varepsilon_{\text{dual}} > 0$ can be chosen problem specific, see also the suggestion in [BPC+10].

5.1.4 Block-Separable ADMM

In case of a partition $x = (x_1^T, x_2^T, \ldots, x_N^T)^T$ of possibly different size x_i and a separable cost function $f(x)$ with respect to that partition, the primal updates of x can be carried out by solving subproblems over the partitions when matrix A^TA is block diagonal [BPC+10]. With

$$f(x) = f_1(x_1) + f_2(x_2) + \cdots + f_N(x_N)$$

the $x-$update of (5.23) becomes

$$\begin{aligned} x^{\ell+1} &:= \underset{x}{\operatorname{argmin}} \left(f_1(x_1) + f_2(x_2) + \cdots + f_N(x_N) + \frac{\rho}{2}\|Ax + \tilde{c}\|_2^2 \right) \\ x^{\ell+1} &:= \underset{x}{\operatorname{argmin}} \left(f_1(x_1) + f_2(x_2) + \cdots + f_N(x_N) + \frac{\rho}{2}(\|Ax\|_2^2 + 2\tilde{c}^TAx + \|\tilde{c}\|_2^2) \right), \end{aligned} \tag{5.32}$$

where $\tilde{c} = Bz^{\ell} - c + \nu^{\ell}$ is a vector of constants. Since the constant in (5.32) is irrelevant to the minimization and $2\tilde{c}^TAx$ is separable with respect to the partition in $x = (x_1^T, \ldots, x_N^T)^T$, the x-update can be split into

$$
\begin{aligned}
x_1^{\ell+1} &:= \underset{x_1}{\operatorname{argmin}} \left(f_1(x_1) + \frac{\rho}{2} \| A_1 x_1 + (B z^\ell - c + \nu^\ell)_1 \|_2^2 \right) \\
&\vdots \\
x_N^{\ell+1} &:= \underset{x_N}{\operatorname{argmin}} \left(f_N(x_N) + \frac{\rho}{2} \| A_N x_N + (B z^\ell - c + \nu^\ell)_N \|_2^2 \right),
\end{aligned}
$$

where $(\tilde{c})_i$ refers to the component of the $i-$th partition of vector $\tilde{c}$. A problem with such a structure enables the minimizations for the $1 \dots N$ components to be carried out in parallel. Thinking of the partition as a structure on the local variables of subproblems, the block diagonal structure enables a distributed optimization among the subproblems and preserves the subproblems' privacy since neither f_i nor x_i have to be shared with the other subproblems. In the first phase of the algorithm, each subsystem computes its decision variable $x_i^{\ell+1}$ in parallel and communicates the solution to a central entity, which then solves for $z^{\ell+1}$ and updates the dual variables in the second phase.
Note that the setting of subsystems in one layer and a central entity in another is a special case of the multi-block minimization problem. Imagine a setting with a second entity (third block) in addition to the subsystems (first block) and the central entity (second block). Even though a direct extension of problem (5.16) by a third cost function and a new decision variable leads to a convenient extension of the algorithm, general convergence depends on the coupling matrices. The authors in [CHYY16] discuss sufficient convergence properties of such an extension dependent on the coupling matrices. More sophisticated modifications of the ADMM algorithm are presented in [LH15] for the multi-block case.

5.1.5 Sharing ADMM

The so-called *sharing problem* is another useful variant of the initial problem statement solvable via the ADMM algorithm. A cost function $g(x)$ depends on the aggregated decision variables $x = (x_1^T, x_2^T, \dots, x_N^T)^T$ of the subsystems. Additionally, the subsystems' cost functions are separable, as discussed in the previous section. The total cost minimization of the *sharing problem* is stated as in [BPC+10]:

$$
\underset{x}{\text{minimize}} \quad \sum_{i=1}^{N} f_i(x_i) + g(\sum_{i=1}^{N} x_i). \tag{5.33}
$$

The problem is of high relevance to this work, since it represents an optimization problem with both local costs for subsystems and a global shared cost function taking into account costs arising from the aggregated decision variable. As an example, one can think of subsystems trying to both minimize their individual electricity consumption and aggregated load at a transfomer. This problem must be solved by a central entity provided with full information of the optimization problem, due to the coupling of the decision variables in the shared cost function g. Decomposition is achieved by the introduction of an auxiliary variable $z_i \in \mathbb{R}^n$ to create local copies of the decision variables $x_i \in \mathbb{R}^n$. The sharing problem solved via ADMM is

$$
\begin{aligned}
\underset{x}{\text{minimize}} \quad & \sum_{i=1}^{N} f_i(x_i) + g(\sum_{i=1}^{N} z_i) \\
\text{subject to} \quad & x_i - z_i = 0 \quad \forall i = 1, \dots, N
\end{aligned} \tag{5.34}
$$

The augmented Lagrangian of problem (5.34) becomes

$$\mathcal{L}_\rho(x,z,\nu) = \sum_{i=1}^{N} f_i(x_i) + g(\sum_{i=1}^{N} z_i) + \frac{\rho}{2}\sum_{i=1}^{N}\|x_i - z_i + \nu_i\|_2^2 - \frac{\rho}{2}\sum_{i=1}^{N}\nu_i^T\nu_i \tag{5.35}$$

The primal and dual updates in scaled form become

$$x_i^{\ell+1} := \underset{x_i}{\operatorname{argmin}} \left(f_i(x_i) + \frac{\rho}{2}\|x_i - z_i^\ell + \nu_i^\ell\|_2^2 \right) \qquad \forall i = 1,\dots,N \tag{5.36}$$

$$z^{\ell+1} := \underset{z}{\operatorname{argmin}} \left(g(\sum_{i=1}^{N} z_i) + \frac{\rho}{2}\sum_{i=1}^{N}\|x_i^{\ell+1} - z_i + \nu_i^\ell\|_2^2 \right) \tag{5.37}$$

$$\nu_i^{\ell+1} := \nu_i^\ell + x_i^{\ell+1} - z_i^{\ell+1} \qquad \forall i = 1,\dots,N \tag{5.38}$$

In each iteration the x_i-updates can be parallelized among the subsystems. The resulting decision variables are sent to a central entity to compute the z-update with respect to the shared cost function and the error term. The current iteration ends with the update of the scaled dual, which has to be computed for each subsystem.

5.2 General Central MPC Problem Statement

The following section introduces the complete optimization problem of the central model predictive controller and derives the decompostion based on the ADMM algorithm to obtain a distributed MPC. The controller includes the dynamics of prosumers and the grid constraints resulting from the power flow approximation. The control-oriented notation is based on [Bra16, BFG+18], where the ADMM algorithm was applied to general dynamic systems, but without a power flow representation. A general form of the central minimization problem including local system dynamics and global constraints for a given time index $k \in \mathbb{N}$ can be stated as

$$\underset{(x,u,z,x_g)}{\text{minimize}} \quad \sum_{i=1}^{\mathcal{I}} \sum_{j=k}^{k+N_P-1} \mathcal{F}_i(z_i(j)) + \sum_{j=k}^{k+N_P-1} \mathcal{G}_s(z(j)) + \sum_{j=k}^{k+N_P-1} \mathcal{G}_g(x_g(j)) \tag{5.39}$$

$$\text{subject to} \quad x_i(k) = x_{i,0} \tag{5.40}$$

$$x_i(j+1) = A_i x_i(j) + B_i u_i(j) + E_i d_i(j) \tag{5.41}$$

$$z_i(j) = D_i x_i(j) + H_i u_i(j) + F_i e_i(j) \tag{5.42}$$

$$x_i(j+1) \in \mathbb{X}_i, u_i(j) \in \mathbb{U}_i \tag{5.43}$$

$$Dx_g(j) = Hz(j) + Fe_g(j) \tag{5.44}$$

$$x_g(j) \in \mathbb{X}_g \tag{5.45}$$

$$\forall j = k,\dots,k+N_P-1 \quad \forall i = 1,\dots,\mathcal{I}.$$

with $\mathbb{X}_i \subset \mathbb{R}^{n_{x_i}}, \mathbb{U}_i \subset \mathbb{R}^{n_{u_i}}, \mathbb{X}_g \subset \mathbb{R}^{n_{x_g}}, z_i(j) \in \mathbb{R}^{n_{z_i}}, z(j) \in \mathbb{R}^{\sum_{i=1}^{\mathcal{I}} n_{z_i}}, d_i(j) \in \mathbb{R}^{n_{d_i}}, e_i(j) \in \mathbb{R}^{n_{e_i}}, e_g(j) \in \mathbb{R}^{n_{e_g}}$ and the matrices of appropriate size. The objective function (5.39) is composed of the running cost $\mathcal{F}_i : \mathbb{R}^{n_{z_i}} \to \mathbb{R}$ for each subsystem, shared running costs $\mathcal{G}_s : \mathbb{R}^{\sum_{i=1}^{\mathcal{I}} n_{z_i}} \to \mathbb{R}$ and a separate running cost $\mathcal{G}_g : \mathbb{R}^{n_{x_g}} \to \mathbb{R}$ at the global system level. Equation (5.40) initializes the local systems at time k with the latest measurement. Equation (5.41) states the subsystem dynamics. The state variables x_i depend on the controllable inputs u_i and disturbances d_i. Both state variables and controllable variables may further be restricted by (possibly) time-dependent

constraint sets $\mathbb{X}_i(j), \mathbb{U}_i(j)$. Equation (5.42) defines a local coupling variable $z_i(j)$, which might depend on the states, inputs or an additional disturbance signal e_i. The vector $z(j)$ stacks the subsystems' coupling variables $z_i(j)$:

$$z(j) := (z_1(j)^T, \dots, z_{\mathcal{I}}(j)^T)^T \tag{5.46}$$

and enables coupling of the subsystems in the shared cost function and the global level constraint (5.44). Thus the global system state variables $x_g(j)$ are linearly dependent on the coupling variables $z_i(j)$ and global level disturbances $e_g(j)$. The global system state variables might further be constrained by the set $\mathbb{X}_g$.
The central optimization problem can be solved for a small number of subsystems, but coupling at the global system level and in the shared cost function might be an obstacle for scalability, privacy and flexibility [BFG+18]. Specifically, the central optimization involves:

- possibly bad scalability due to a large number of subsystems and/or long prediction horizons,
- full disclosure of cost functions and systems dynamics of all subsystems to a central entity responsible at the global system level,
- predictions of all local and global disturbances carried out by the central entity or at least communicated to it, knowledge of all measured states of the subsystems at the central entity,
- adaption of the central optimization problem whenever a subsystem changes its configuration (cost function, system dynamics, coupling).

5.3 Distributed MPC

A distributed optimization algorithm using ADMM helps to avoid the drawbacks mentioned above and maintains the privacy of the subsystems involved. A more compact formulation helps to prepare problem (5.39)-(5.45) for the decomposition carried out in ADMM. Let the cost functions $f_i(\boldsymbol{z}_i) : \mathbb{R}^{n_{z_i} N_P} \to \mathbb{R}, g_s(\boldsymbol{z}) : \mathbb{R}^{\sum_{i=1}^{\mathcal{I}} n_{z_i} N_P} \to \mathbb{R}$ and $g_g(\boldsymbol{x}_g) : \mathbb{R}^{n_{x_g} N_P} \to \mathbb{R}$ be the sums over the running costs over the prediction horizon from (5.39), with vectors $\boldsymbol{z}_i$, $\boldsymbol{z}$ and $\boldsymbol{x}_g$, defined as

$$\begin{aligned}
\boldsymbol{z}_i &:= \boldsymbol{z}_i(k) = (z_i(k)^T, \dots, z_i(k+N_P-1)^T)^T \\
\boldsymbol{z} &:= \boldsymbol{z}(k) = (z(k)^T, \dots, z(k+N_P-1)^T)^T \\
\boldsymbol{x}_g &:= \boldsymbol{x}_g(k) = (x_g(k)^T, \dots, x_g(k+N_P-1)^T)^T.
\end{aligned}$$

The additional sets $\mathbb{P}_i$ and $\mathbb{D}$ are introduced to simplify the notation further, similar to [BFG+18]. The sets of constraints are expressed with respect to the optimization variables subject to a cost function. Let $\mathbb{P}_i$ be the set of feasible trajectories of subsystem i evaluated at time k:

$$\mathbb{P}_i = \left\{ \boldsymbol{z}_i \in \mathbb{R}^{n_{z_i} N_P} \;\middle|\; \begin{array}{l} \exists\, x_i(j+1) \in \mathbb{X}_i, u_i(j) \in \mathbb{U}_i \text{ such that} \\ x_i(k) = x_{i,0} \\ x_i(j+1) = A_i x_i(j) + B_i u_i(j) + E_i d_i(j) \\ z_i(j) = D_i x_i(j) + H_i u_i(j) + F_i e_i(j) \\ \forall j = k, \dots, k+N_P-1 \end{array} \right\}. \tag{5.47}$$

The set $\mathbb{D}$ correspondingly denotes solutions of feasible points of operation at the global system level for $\boldsymbol{z}$ and $\boldsymbol{x}_g$:

$$\mathbb{D} = \left\{ (\boldsymbol{x}_g, \boldsymbol{z}) \in \mathbb{R}^{n_{x_g} N_P} \times \mathbb{R}^{\sum_{i=1}^{\mathcal{I}} n_{z_i} N_P} \;\middle|\; \begin{array}{l} x_g(j) \in \mathbb{X}_g \\ Dx_g(j) = Hz(j) + Fe_g(j) \\ \forall j = k, \ldots, k + N_P - 1 \end{array} \right\}. \tag{5.48}$$

Problem (5.39)-(5.45) solved at time k can now be rewritten as

$$\underset{(\boldsymbol{z}, \boldsymbol{x}_g)}{\text{minimize}} \quad \sum_{i=1}^{\mathcal{I}} f_i(\boldsymbol{z}_i) + g_s(\boldsymbol{z}) + g_g(\boldsymbol{x}_g) \tag{5.49}$$

$$\text{subject to} \quad \boldsymbol{z}_i \in \mathbb{P}_i \quad \forall i = 1, \ldots, \mathcal{I} \tag{5.50}$$

$$(\boldsymbol{x}_g, \boldsymbol{z}) \in \mathbb{D}. \tag{5.51}$$

The above notation indicates that the function $f_i(\boldsymbol{z}_i)$ is explicitly optimized over $\boldsymbol{z}_i$ instead of $\boldsymbol{x}_i, \boldsymbol{u}_i$ and $\boldsymbol{z}_i$. From the definition of the set $\mathbb{P}_i$ in (5.47) it becomes clear that a given optimal local solution $\boldsymbol{z}_i^*$ can be translated into a local feasible solution $\boldsymbol{x}_i^*, \boldsymbol{u}_i^*$ for each subsystem. However, $\boldsymbol{z}_i^*$ and the related solution pair $(\boldsymbol{x}_i^*, \boldsymbol{u}_i^*)$ are in general not unique [BFG+18]. The above notation is mainly used for brevity to apply the ADMM algorithm, the actual implementation for this thesis does not consider an explicit statement of the set $\mathbb{P}_i$, but simultaneously computes a solution $(\boldsymbol{z}_i^*, \boldsymbol{x}_i^*, \boldsymbol{u}_i^*)$.
A further remark addresses possible extensions of the sub- and global system cost functions. The subsystems might include additional local cost functions with respect to local decision variables, similar is conceivable for the global system. The following procedure holds for such extensions, as long as the structure between local, global and coupling variables and their associated cost function is preserved. The implementations presented in Section 5.4.4 consider such functions.
To this point, the subsystems are still coupled in both $\mathbb{D}$ and the shared cost function $g_s(\boldsymbol{z})$. Recalling the decomposition procedure of ADMM to enable a distributed optimization, the structure of the sharing ADMM introduced in Section 5.1.5 can be used to separate problem (5.49)-(5.51) among the subsystems. Decoupling is achieved by introducing auxiliary copies $\boldsymbol{a}_i \in \mathbb{R}^{n_{z_i} N_P}$ for the variables $\boldsymbol{z}_i$, leading to

$$\underset{(\boldsymbol{z}, \boldsymbol{a}, \boldsymbol{x}_g)}{\text{minimize}} \quad \sum_{i=1}^{\mathcal{I}} f_i(\boldsymbol{z}_i) + g_s(\boldsymbol{a}) + g_g(\boldsymbol{x}_g) \tag{5.52}$$

$$\text{subject to} \quad \boldsymbol{z}_i \in \mathbb{P}_i \tag{5.53}$$

$$\boldsymbol{z}_i - \boldsymbol{a}_i = 0 \quad \forall i = 1, \ldots, \mathcal{I} \tag{5.54}$$

$$(\boldsymbol{x}_g, \boldsymbol{a}) \in \mathbb{D}. \tag{5.55}$$

$\boldsymbol{a} \in \mathbb{R}^{\sum_{i=1}^{\mathcal{I}} n_{z_i} N_P}$ has the same stacked structure as $\boldsymbol{z}$, i.e.:

$$\boldsymbol{a} := \boldsymbol{a}(k) = (a(k)^T, \ldots, a(k + N_P - 1)^T)^T,$$

with

$$a(j) := (a_1(j)^T, \ldots, a_{\mathcal{I}}(j)^T)^T.$$

The problem is no longer explicitly coupled in the global system dynamics and the shared cost function, but coupling is still enforced through the equality constraints in (5.54).

The augmented Lagrangian of problem (5.52)-(5.55) becomes

$$\mathcal{L}_\rho(\boldsymbol{z},\boldsymbol{a},\boldsymbol{\nu}) = \sum_{i=1}^{\mathcal{I}} f_i(\boldsymbol{z}_i) + g_s(\boldsymbol{a}) + g_g(\boldsymbol{x}_g) + \frac{\rho}{2}\sum_{i=1}^{\mathcal{I}}\|\boldsymbol{z}_i - \boldsymbol{a}_i + \boldsymbol{\nu}_i\|_2^2 - \frac{\rho}{2}\sum_{i=1}^{\mathcal{I}}\boldsymbol{\nu}_i^T\boldsymbol{\nu}_i \tag{5.56}$$

with scaled dual variable $\boldsymbol{\nu}_i = \frac{\boldsymbol{\lambda}_i}{\rho}$. Equation (5.56) is optimized in a distributed fashion, the primal and dual ADMM-updates in scaled form become

$$\boldsymbol{z}_i^{\ell+1} := \underset{\boldsymbol{z}_i\in\mathbb{P}_i}{\operatorname{argmin}} \left(f_i(\boldsymbol{z}_i) + \frac{\rho}{2}\|\boldsymbol{z}_i - \boldsymbol{a}_i^\ell + \boldsymbol{\nu}_i^\ell\|_2^2\right) \qquad \forall i = 1,\dots,\mathcal{I} \tag{5.57}$$

$$(\boldsymbol{a}^{\ell+1}, \boldsymbol{x}_g^{\ell+1}) := \underset{(\boldsymbol{a},\boldsymbol{x}_g)\in\mathbb{D}}{\operatorname{argmin}} \left(g_s(\boldsymbol{a}) + g_g(\boldsymbol{x}_g) + \frac{\rho}{2}\sum_{i=1}^{\mathcal{I}}\|\boldsymbol{z}_i^{\ell+1} - \boldsymbol{a}_i + \boldsymbol{\nu}_i^\ell\|_2^2\right) \tag{5.58}$$

$$\boldsymbol{\nu}_i^{\ell+1} := \boldsymbol{\nu}_i^\ell + \boldsymbol{z}_i^{\ell+1} - \boldsymbol{a}_i^{\ell+1} \qquad \forall i = 1,\dots,\mathcal{I}. \tag{5.59}$$

The iterative optimization scheme consists of the following steps. After a onetime arbitrary initialization of $\boldsymbol{a}_i^0, \boldsymbol{\nu}_i^0$ and a feasible initialization for $x_i(k) = x_{i,0}$, the subsystems compute (5.57) and communicate their solutions $\boldsymbol{z}_i^{\ell+1}$ to the central entity. The central entity then computes the pair $(\boldsymbol{a}^{\ell+1}, \boldsymbol{x}_g^{\ell+1})$, treating $\boldsymbol{z}_i^{\ell+1}$ as a fixed parameter in the squared norm summation. Finally the scaled dual variables $\boldsymbol{\nu}_i^{\ell+1}$ are updated and communicated back to the subsystems, where the procedure is repeated with updated variables.
The requirements for convergence of the iterative scheme were already given in Section 5.1.3. In the context of dynamic systems, convergence requires

- feasible solutions for each of the problems solved in (5.57) and (5.58), satisfying the corresponding subsystems and global level constrained convex sets $\mathbb{P}_i$ and $\mathbb{D}$,
- existence of $\boldsymbol{z}_i \in \mathbb{P}_i\ \forall i = 1,\dots,\mathcal{I}$ such that there exist local feasible solutions that are also feasible at the global level, i.e. $(\boldsymbol{z}, \boldsymbol{x}_g) \in \mathbb{D}$,

Consequently, the algorithm will not converge if no global feasible solution exists. The cost functions f_i, g_s and g_g are assumed to be convex. With the above assumptions fulfilled, the iterative scheme converges for $\ell \to \infty$ to a global optimal solution:

- the iteration's residual $(\boldsymbol{z}^\ell - \boldsymbol{a}^\ell)$ converges to zero for $\ell \to \infty$
- (5.52) converges to the optimal value of problem (5.49)-(5.51) for $\ell \to \infty$
- the $\boldsymbol{\nu}_i^\ell$ converge to the optimal dual values $\boldsymbol{\nu}_i^*$ for $\ell \to \infty$.

The reader is referred to [BPC+10] and [Bra16] regarding details on the assumptions for convex optimization problems and the proofs for convergence.
The procedure ensures privacy at the level of the subsystems, since only the coupling variable $\boldsymbol{z}_i$ has to be communicated to the central entity. Private cost functions and systems dynamics are not disclosed and may be changed during operation, since the internal change in configuration will be reflected in $\boldsymbol{z}_i$. The knowledge of global system constraints and cost functions remains in the domain of the central entity, since only $\boldsymbol{\nu}_i - \boldsymbol{a}_i$ is communicated to the subsystems. A shared cost function can be managed by the central entity on behalf of the subsystems, who have to agree to it in advance.
While the central entity has to bear the whole computational burden in the central MPC problem and the subsystems just receive the controllable input signals for execution in the low-level

controllers, the hierarchical distributed MPC procedure spreads the computation among all participating systems. This maintains privacy but also requires computational capabilities located at the subsystems. The size of the optimization problem of the central entity in (5.58) depends on the number of global system variables, constraints, the number of subsystems connected and the length of the prediction horizon. It is independent of the number of variables of the subsystems. Finally, a bidirectional communication infrastructure must exist for the exchange of the iterative solutions.

5.4 Prosumer-DSO Coordination

The previously introduced distributed MPC scheme is applied to coordinate the prosumers with respect to the distribution grid. The central optimization problem is rewritten for the case of $\mathcal{I}$ building energy systems with potential prosumer capabilities. The global system level is represented by the distribution grid and its operator, the DSO, as the central entity.

5.4.1 Building Energy Systems

The subsystem dynamics in (5.41) correspond to the dynamics of the thermal building models introduced in Chapter 3.1. In Equation (3.33) the total or residual load $r_i(j)$ of one prosumer was computed based on the controllable inputs $u_i(j)$, the fixed electricity load $l_i(j)$ and the generation $g_i(j)$, which corresponds to the coupling variable $z_i(j)$ in Equation (5.42). The constraints in (5.43) represent the constraints on the buildings' states and controllable inputs, as shown in (3.19), (3.22) and (3.23).

5.4.2 Distribution System Operator

The DSO takes the role of the central entity in the present coordination problem, contributing its own cost function and the global system constraints. Constraints (5.44)-(5.45) correspond to the operational limits of the distribution grid, represented by the *LinDistFlow* model introduced in Section 4.1.3. An extended multi-period power flow based on the *LinDistFlow* approximation is derived for the optimization problem to integrate coordination. Recalling the compact definition of the *LinDistFlow* model from (4.18), the instantaneous power flow can be determined by the system of equations

$$\Pi x_g = \delta, \tag{5.60}$$

with the matrices and vectors from (4.19):

$$\Pi = \begin{pmatrix} C_P & \mathbf{0}_{|\mathcal{N}^+|\times|\mathcal{E}|} & \mathbf{0}_{|\mathcal{N}^+|\times|\mathcal{N}^+|} \\ \mathbf{0}_{|\mathcal{N}^+|\times|\mathcal{E}|} & C_Q & \mathbf{0}_{|\mathcal{N}^+|\times|\mathcal{N}^+|} \\ 2R & 2X & C_U \end{pmatrix} \qquad x_g = \begin{pmatrix} P \\ Q \\ U \end{pmatrix} \qquad \delta = \begin{pmatrix} p \\ q \\ c_u \end{pmatrix}, \tag{5.61}$$

with

$$c_u = \begin{pmatrix} U_{ref} \\ \mathbf{0}_{|\mathcal{E}|-1} \end{pmatrix}. \tag{5.62}$$

The static power flow equations of the *LinDistFlow* model are extended to distinguish participating and non-participating buses. We define the set $\mathcal{N}_{\not c}$ for static, non-participating load buses and the set $\mathcal{N}_c$ for participating buses in addition to the set $\mathcal{N}^+$ of all buses excluding the reference bus. A bus might serve as a static load or just serve as a point of connection between branches. The load at such a bus cannot be manipulated for coordination in this case. In contrast, other buses might offer a certain degree of participation, e.g., when a prosumer has

agreed to participate in a coordination program with the DSO. This leads to the relation of the subsets $\mathcal{N}_{\not c} \subset \mathcal{N}^+$, $\mathcal{N}_c \subset \mathcal{N}^+$, $\mathcal{N}_c \cap \mathcal{N}_{\not c} = \emptyset$ and $\mathcal{N}_c \cup \mathcal{N}_{\not c} = \mathcal{N}^+$. The number of buses in the set of participating buses is equal to the number of prosumers who have consented to coordination with the DSO, i.e., $|\mathcal{N}_c| = \mathcal{I}$. The scenario-dependent matrix $C_\mathcal{I}$ specifies to which bus a participating prosumer or building energy system is connected to:

$$C_\mathcal{I}(i,j) \in \mathbb{R}^{|\mathcal{N}^+| \times \mathcal{I}} = \begin{cases} 1 & \text{if bus } i \text{ hosts participating prosumer } j, \\ 0 & \text{otherwise.} \end{cases} \tag{5.63}$$

Then, the simple summation over $C_\mathcal{I}$ with $C_\mathcal{I}\mathbf{1}_\mathcal{I} \in \mathbb{R}^{|\mathcal{N}^+|}$ leads to the participation vector with entries i

$$(C_\mathcal{I}\mathbf{1}_\mathcal{I})_{(i)} = \begin{cases} 1 & \text{if } i \in \mathcal{N}_c, \\ 0 & \text{if } i \in \mathcal{N}_{\not c}, \end{cases} \tag{5.64}$$

which specifies participation at each bus. In the next step, the power flow equations are extended by aggregation of the prosumers over the participating buses in the coupling variable $r \in \mathbb{R}^\mathcal{I}$

$$r(j) := (r_1(j), \dots, r_\mathcal{I}(j))^T$$

to separate the participating from non-participating buses.[1] Written for all time steps of the prediction horizon, this leads to the extended version of (5.60):

$$\Pi x_g(j) = \tilde{\Pi} r(j) + \delta(j) \quad \forall j = k, \dots, k + N_P - 1, \tag{5.65}$$

with updated

$$\delta(j) = \begin{pmatrix} p(j) = (\mathbf{1}_{|\mathcal{N}^+|} - C_\mathcal{I}\mathbf{1}_\mathcal{I}) \circ (l(j) - g(j)) \\ q(j) \\ c_u(j) \end{pmatrix}.^{2} \tag{5.66}$$

The active power variable $p(j)$ of the *LinDistFlow* model is replaced by $l(j) - g(j)$, a vector over all buses. In case of participation, the corresponding active power entry in δ becomes zero. In case of non-participation, $l(j) - g(j)$ can be the residual load of all non-participating electrical systems connected to a bus, but might also be zero in case no system is present. Since the focus is on active power control, a further distinction for reactive power is possible, but not required here. It is assumed that the DSO is capable to predict the reactive power at each bus. Since no detailed reactive power models are used in this thesis, a constant power factor is applied to derive the reactive power demand based on the active power.
$\tilde{\Pi} \in \mathbb{R}^{(2|\mathcal{N}^+| + |\mathcal{E}|) \times \mathcal{I}}$ finally relates the participating buses to the nodal balance and voltage equations based on $C_\mathcal{I}$ and is expanded by appropriately dimensioned zero matrices for the remaining reactive power and voltage equality constraints:

$$\tilde{\Pi} = \begin{pmatrix} C_\mathcal{I} \\ \mathbf{0}_{|\mathcal{N}^+| \times \mathcal{I}} \\ \mathbf{0}_{|\mathcal{E}| \times \mathcal{I}} \end{pmatrix}. \tag{5.67}$$

Note that Equation (5.65) is the manifestation of the general dependency between the global system variables, coupling variables and disturbances in equation (5.44).

[1] Note that the entries in $r(j)$ are one-dimensional, i.e. $n_{z_i} = 1$ for the z_i in $z(j)$ in (5.46).

[2] Hadamard product or element-wise multiplication of two matrices
$A = (a_{ij}) \in \mathbb{R}^{m \times n}$ and $B = (b_{ij}) \in \mathbb{R}^{m \times n}$: $(A \circ B)_{ij} = (a_{ij} \cdot b_{ij})$.
Using r, l and g here as vectors over multiple buses involves a slight abuse of notation, since the variables where previously introduced in Chapter 3 on the single prosumer level.

Finally, Equation (5.65) in compact notation is the multi-period power flow over the prediction horizon of length N_P

$$\boldsymbol{\Pi} \boldsymbol{x}_{g,k} - \tilde{\boldsymbol{\Pi}} \boldsymbol{r}_k = \boldsymbol{\delta}_k, \tag{5.68}$$

with matrices and vectors

$$\boldsymbol{\Pi} = I_{N_P} \otimes \Pi \qquad\qquad \tilde{\boldsymbol{\Pi}} = I_{N_P} \otimes \tilde{\Pi},$$

$$\begin{aligned}
\boldsymbol{x}_{g,k} :&= \boldsymbol{x}_g(k) = (x_g(k)^T, x_g(k+1)^T, \dots, x_g(k+N_P-1)^T)^T \\
&= \left(\begin{pmatrix} P(k) \\ Q(k) \\ U(k) \end{pmatrix}^T, \begin{pmatrix} P(k+1) \\ Q(k+1) \\ U(k+1) \end{pmatrix}^T, \dots, \begin{pmatrix} P(k+N_P-1) \\ Q(k+N_P-1) \\ U(k+N_P-1) \end{pmatrix}^T \right)^T \\
\boldsymbol{r}_k :&= \boldsymbol{r}(k) = (r(k)^T, r(k+1)^T, \dots, r(k+N_P-1)^T)^T \\
\boldsymbol{\delta}_k :&= \boldsymbol{\delta}(k) = (\delta(k)^T, \delta(k+1)^T, \dots, \delta(k+N_P-1)^T)^T.
\end{aligned}$$

of dimension $\boldsymbol{\Pi} \in \mathbb{R}^{N_P(2|\mathcal{N}^+|+|\mathcal{E}|) \times N_P(2|\mathcal{E}|+|\mathcal{N}^+|)}$, $\tilde{\boldsymbol{\Pi}} \in \mathbb{R}^{N_P(2|\mathcal{N}^+|+|\mathcal{E}|) \times N_P\mathcal{I}}$, $\boldsymbol{x}_{g,k} \in \mathbb{R}^{N_P(2|\mathcal{E}|+|\mathcal{N}^+|)}$, $\boldsymbol{r}_k \in \mathbb{R}^{N_P\mathcal{I}}$, $\boldsymbol{\delta}_k \in \mathbb{R}^{N_P(2|\mathcal{N}^+|+|\mathcal{E}|)}$. The power flows and voltages of two consecutive time steps are assumed to be independent of each other and thus decoupled in time.
The global variable constraint (5.45) corresponds to the voltage and thermal restrictions during grid operation. Inequality (4.21) leads to compact inequality equations

$$\mathbf{1}_{N_P|\mathcal{N}^+|} V_{ref}^2 (1-\varepsilon)^2 \leq \boldsymbol{U}_k \leq \mathbf{1}_{N_P|\mathcal{N}^+|} V_{ref}^2 (1+\varepsilon)^2 \tag{5.69}$$

$$\underline{\boldsymbol{U}} \leq \boldsymbol{U}_k \leq \overline{\boldsymbol{U}} \tag{5.70}$$

to consider bus voltage constraints. For brevity, only the bus voltage limits are considered in the set $\mathbb{X}_g$ in this example. For now the active and reactive line flows face no operational limits, but this can be easily changed by adding constraints based on the inequalities (4.22)-(4.23).

5.4.3 DSO Cost Functions

The shared and global system cost functions $g_s(\boldsymbol{r})$ and $g_g(\boldsymbol{x}_g)$ from (5.49) can be used for peak-shaving/valley-filling and loss minimizaion in the distribution grid. Not all of the presented cost functions are typical objectives of a DSO, but in the hierarchical setting assumed here the DSO is the entity to handle such cost functions.

Valley-Filling

In case of peak-shaving/valley-filling, the aggregated residual load is flattened to avoid power peaks during operation. In practice, this could be the objective of an aggregator or the DSO who tries to limit the volatility of the active power flow over the transformer. This is equivalent to the aggregation over the residual loads at each bus using *LinDistFlow*, where the active and reactive line losses are neglected in the nodal balance equations. From the power flow equations in (4.16), the active power flow P_1 over the transformer can be obtained by solving

$$P_1 = C_{P(1)}^{-1} p = \mathbf{1}_{|\mathcal{E}|}^T p = \sum_{i=1}^{|\mathcal{N}^+|} p_i, \tag{5.71}$$

where $C_{P(j)}^{-1}$ denotes row j of matrix C_P^{-1}. Clearly, $C_{P(1)}^{-1}$ is a vector of ones, since all loads are served via the power flow over the first line. Recalling the separation for participation in vector δ, the final cost function quantifies both the residual load of participating and non-participating buses such that the prosumers operation is adjusted with respect to the total unflexible load and generation. With $\boldsymbol{p}_k = (p(k)^T, \dots, p(k+N_P-1)^T)^T$ the valley-filling cost function is defined as

$$g_s(\boldsymbol{r}_k) = \|H_{\mathcal{I}}\boldsymbol{r}_k + H_{\mathcal{N}^+}\boldsymbol{p}_k\|_2^2 \tag{5.72}$$

with matrices $H_{\mathcal{I}} \in \mathbb{R}^{N_P \times N_P \mathcal{I}}$ and $H_{\mathcal{N}^+} \in \mathbb{R}^{N_P \times N_P|\mathcal{N}^+|}$ to aggregate the prosumers' residual loads and the non-participating residual loads at each time instant:

$$H_{\mathcal{I}} = I_{N_P} \otimes \mathbf{1}_{\mathcal{I}}^T \qquad\qquad H_{\mathcal{N}^+} = I_{N_P} \otimes \mathbf{1}_{|\mathcal{N}^+|}^T. \tag{5.73}$$

Depending on the weighting with respect to remaining cost functions, the above cost function can have a strong impact on the operation of the prosumers. The DSO could alternatively limit P_1 with an additional constraint to enforce that the tranformer's power flow never exceeds its maximum capacity. This would not affect the volatility of the aggregated residual load in a comparable way. Such a procedure is less invasive, since the operation of the prosumers is only adapted when global system constraints are active.

Loss Minimization

Minimization of the grid losses is achieved by rewriting (4.13) over the prediction horizon:

$$g_g(\boldsymbol{P}_k, \boldsymbol{Q}_k) = \frac{1}{V_0^2}(\boldsymbol{P}_k^T \boldsymbol{R} \boldsymbol{P}_k + \boldsymbol{Q}_k^T \boldsymbol{R} \boldsymbol{Q}_k). \tag{5.74}$$

$\boldsymbol{R} \in \mathbb{R}^{N_P|\mathcal{E}| \times N_P|\mathcal{E}|}$ is the block diagonal matrix of the line resistance matrix R:

$$\boldsymbol{R} = I_{N_P} \otimes R. \tag{5.75}$$

Community Self-Consumption

Another goal could be to minimize the imported electricity and to cover the local demand as much as possible by local PV generation. This could be formulated as a shared goal of the prosumers, but it is here assumed that the DSO handles the objective and formulates it with respect to a global level variable. Therefore, the power flow over the transformer $\boldsymbol{P}_{1,k}$ is selected and costs only associated to the positive parts of the line flow, i.e. no community-generated PV can be sold. Excess is fed back into the grid without compensation, which is similar to the prosumer costs as defined in Equation (3.43). The additional variable $\boldsymbol{P}_{1,k}^+$ is defined for the global-level optimization with

$$\boldsymbol{P}_{1,k}^+ \geq \mathbf{0}, \tag{5.76}$$

$$\boldsymbol{P}_{1,k}^+ \geq \boldsymbol{P}_{1,k}, \tag{5.77}$$

and the cost function

$$g_g(\boldsymbol{P}_{1,k}^+) = \boldsymbol{c}_k^T \boldsymbol{P}_{1,k}^+. \tag{5.78}$$

Increasing self-consumption is not a typical task of a DSO, but rather the operational goal of a community aggregator who is authorised to coordinate the prosumers to maximize self-consumption.

5.4.4 Decoupling of the Central Optimization Problem

The central optimization problem for the optimal prosumer-DSO coordination at time k based on the general problem formulation (5.49)-(5.51) becomes[3]

$$\underset{(\boldsymbol{u},\boldsymbol{r},\boldsymbol{r}^+,\boldsymbol{P},\boldsymbol{Q},\boldsymbol{U})}{\text{minimize}} \quad \sum_{i=1}^{\mathcal{I}} f_i(\boldsymbol{r}_{i,k}^+) + g_s(\boldsymbol{r}_k) + g_g(\boldsymbol{P}_k, \boldsymbol{Q}_k) \tag{5.79}$$

$$\text{subject to} \quad \boldsymbol{x}_{i,k} = \mathcal{A}_i x_{i,0} + \mathcal{B}_i \boldsymbol{u}_{i,k} + \mathcal{E}_i \boldsymbol{d}_{i,k} \tag{5.80}$$

$$\underline{\boldsymbol{x}}_{i,k} \leq \boldsymbol{x}_{i,k} \leq \overline{\boldsymbol{x}}_{i,k} \tag{5.81}$$

$$\overline{\mathcal{B}}_i \boldsymbol{u}_{i,k} \leq \overline{\boldsymbol{u}}_{i,k} \tag{5.82}$$

$$\boldsymbol{u}_{i,k} \geq \boldsymbol{0} \tag{5.83}$$

$$\boldsymbol{r}_{i,k} = \mathcal{B}_{i,k}^C \boldsymbol{u}_{i,k} + \boldsymbol{l}_{i,k} - \boldsymbol{g}_{i,k} \tag{5.84}$$

$$\boldsymbol{r}_{i,k}^+ \geq 0 \tag{5.85}$$

$$\boldsymbol{r}_{i,k}^+ \geq \boldsymbol{r}_{i,k} \quad \forall i = 1, \ldots, \mathcal{I}, \tag{5.86}$$

$$\boldsymbol{\Pi} \boldsymbol{x}_{g,k} - \tilde{\boldsymbol{\Pi}} \boldsymbol{r}_k = \boldsymbol{\delta}_k \tag{5.87}$$

$$\underline{\boldsymbol{U}} \leq \boldsymbol{U}_k \leq \overline{\boldsymbol{U}}. \tag{5.88}$$

Feasibility of central problem (5.79)-(5.88) has to be given to ensure the existence of a solution of the central optimization and to guarantee convergence of the ADMM algorithm to a global optimal feasible solution. The hard constraints on the states of the building energy systems in (5.81) and the voltage limits in (5.88) are relaxed with the introduction of the slack variables $s_i \in \mathbb{R}_{\geq 0}^{n_{x_i}}$ and $s_g \in \mathbb{R}_{\geq 0}^{|\mathcal{N}^+|}$ to allow for violation of temperature and voltage limits at very high associated costs

$$f_{i,f}(\boldsymbol{s}_{i,k}) = M_i \boldsymbol{1}_{N_P n_{x_i}}^T \boldsymbol{s}_{i,k} \quad \forall i = 1, \ldots, \mathcal{I} \tag{5.89}$$

$$g_f(\boldsymbol{s}_{g,k}) = M_g \boldsymbol{1}_{N_P |\mathcal{N}^+|}^T \boldsymbol{s}_{g,k} \tag{5.90}$$

for the prosumers and the DSO respectively. Sufficiently large values for the scalars $M_i, M_g \in \mathbb{R}_{>0}$ are chosen to avoid violations of constraints under standard operation conditions. The relaxed central optimization problem becomes

$$\underset{(\boldsymbol{u},\boldsymbol{r},\boldsymbol{r}^+,\boldsymbol{s},\boldsymbol{P},\boldsymbol{Q},\boldsymbol{U},\boldsymbol{s}_g)}{\text{minimize}} \quad \sum_{i=1}^{\mathcal{I}} f_i(\boldsymbol{r}_{i,k}^+) + f_{i,f}(\boldsymbol{s}_{i,k}) + g_s(\boldsymbol{r}_k) + g_g(\boldsymbol{P}_k, \boldsymbol{Q}_k) + g_f(\boldsymbol{s}_{g,k}) \tag{5.91}$$

$$\text{subject to} \quad (5.80), (5.82), (5.83), (5.84), (5.85), (5.86)$$

$$\underline{\boldsymbol{x}}_{i,k} - \boldsymbol{s}_{i,k} \leq \boldsymbol{x}_{i,k} \leq \overline{\boldsymbol{x}}_{i,k} + \boldsymbol{s}_{i,k} \tag{5.92}$$

$$\boldsymbol{s}_{i,k} \geq \boldsymbol{0}_{n_{x_i} N_P} \quad \forall i = 1, \ldots, \mathcal{I} \tag{5.93}$$

$$(5.87)$$

$$\underline{\boldsymbol{U}} - \boldsymbol{s}_{g,k} \leq \boldsymbol{U}_k \leq \overline{\boldsymbol{U}} + \boldsymbol{s}_{g,k}. \tag{5.94}$$

$$\boldsymbol{s}_{g,k} \geq \boldsymbol{0}_{N_P |\mathcal{N}^+|} \tag{5.95}$$

[3] The explicit prosumer states $\boldsymbol{x}_{i,k}$ are kept in the problem formulation for illustration, but can be disregarded in the implementation of the optimization by substitution of the variable in (5.81) by the right-hand side of Equation (5.80).

The sets $\mathbb{P}_i$ and $\mathbb{D}$ from Section 5.3 are defined analogously to separate the prosumer and DSO constraints and to reduce the notation to the variables relevant to the optimization. The set $\mathbb{P}_i$ of a prosumer's feasible solutions of the residual load trajectories and slack variable over the prediction horizon is given by

$$\mathbb{P}_i = \left\{ (\boldsymbol{r}_{i,k}, \boldsymbol{r}^+_{i,k}, \boldsymbol{s}_{i,k}) \in \mathbb{R}^{N_P} \times \mathbb{R}^{N_P}_{\geq 0} \times \mathbb{R}^{n_{x_i} N_P}_{\geq 0} \;\middle|\; \begin{array}{l} \boldsymbol{x}_{i,k} = \mathcal{A}_i x_{i,0} + \mathcal{B}_i \boldsymbol{u}_{i,k} + \mathcal{E}_i \boldsymbol{d}_{i,k} \\ \underline{\boldsymbol{x}}_{i,k} - \boldsymbol{s}_{i,k} \leq \boldsymbol{x}_{i,k} \leq \overline{\boldsymbol{x}}_{i,k} + \boldsymbol{s}_{i,k} \\ \overline{\mathcal{B}}_i \boldsymbol{u}_{i,k} \leq \overline{\boldsymbol{u}}_{i,k} \\ \boldsymbol{u}_{i,k} \geq \boldsymbol{0} \\ \boldsymbol{r}_{i,k} = \mathcal{B}^C_{i,k} \boldsymbol{u}_{i,k} + \boldsymbol{l}_{i,k} - \boldsymbol{g}_{i,k} \\ \boldsymbol{r}^+_{i,k} \geq \boldsymbol{r}_{i,k} \\ \boldsymbol{r}^+_{i,k} \geq 0 \end{array} \right\}. \tag{5.96}$$

Equivalently, the DSO's constraint set expressed in the optimization variables subject to a cost function is

$$\mathbb{D} = \left\{ \begin{pmatrix} \boldsymbol{P}_k \\ \boldsymbol{Q}_k \\ \boldsymbol{r}_k \\ \boldsymbol{s}_{g,k} \end{pmatrix}^T \in \mathbb{R}^{N_P|\mathcal{N}^+|} \times \mathbb{R}^{N_P|\mathcal{N}^+|} \times \mathbb{R}^{\mathcal{I} N_P} \times \mathbb{R}^{N_P|\mathcal{N}^+|}_{\geq 0} \;\middle|\; \begin{array}{l} \boldsymbol{\Pi} \boldsymbol{x}_{g,k} - \tilde{\boldsymbol{\Pi}} \boldsymbol{r}_k = \boldsymbol{\delta}_k \\ \underline{\boldsymbol{U}} - \boldsymbol{s}_{g,k} \leq \boldsymbol{U}_k \leq \overline{\boldsymbol{U}} + \boldsymbol{s}_{g,k} \end{array} \right\}. \tag{5.97}$$

The complete central optimization problem can be stated as

$$\underset{(\boldsymbol{r}, \boldsymbol{r}^+, \boldsymbol{s}, \boldsymbol{P}, \boldsymbol{Q}, \boldsymbol{s}_g)}{\text{minimize}} \quad \sum_{i=1}^{\mathcal{I}} f_i(\boldsymbol{r}^+_{i,k}) + f_{i,f}(\boldsymbol{s}_{i,k}) + g_s(\boldsymbol{r}_k) + g_g(\boldsymbol{P}_k, \boldsymbol{Q}_k) + g_f(\boldsymbol{s}_{g,k}) \tag{5.98}$$

$$\text{subject to} \quad (\boldsymbol{r}_{i,k}, \boldsymbol{r}^+_{i,k}, \boldsymbol{s}_{i,k}) \in \mathbb{P}_i \quad \forall i = 1, \ldots, \mathcal{I} \tag{5.99}$$

$$(\boldsymbol{P}_k, \boldsymbol{Q}_k, \boldsymbol{r}_k, \boldsymbol{s}_{g,k}) \in \mathbb{D}. \tag{5.100}$$

As outlined in Section 5.3, coupling exists via the prosumers' residual load $\boldsymbol{r}_k$ in the shared cost function g_s and in the *LinDistFlow* representation in the set $\mathbb{D}$. Again, decoupling is achieved with the introduction of copies of the prosumers' residual load vectors and application of the optimization steps of the ADMM. Introducing the auxiliary variable $\boldsymbol{a}_k$ leads to the following problem:

$$\underset{(\boldsymbol{r}, \boldsymbol{r}^+, \boldsymbol{s}, \boldsymbol{P}, \boldsymbol{Q}, \boldsymbol{a}, \boldsymbol{s}_g)}{\text{minimize}} \quad \sum_{i=1}^{\mathcal{I}} f_i(\boldsymbol{r}^+_{i,k}) + f_{i,f}(\boldsymbol{s}_{i,k}) + g_s(\boldsymbol{a}_k) + g_g(\boldsymbol{P}_k, \boldsymbol{Q}_k) + g_f(\boldsymbol{s}_{g,k}) \tag{5.101}$$

$$\text{subject to} \quad (\boldsymbol{r}_{i,k}, \boldsymbol{r}^+_{i,k}, \boldsymbol{s}_{i,k}) \in \mathbb{P}_i \quad \forall i = 1, \ldots, \mathcal{I} \tag{5.102}$$

$$\boldsymbol{r}_{i,k} - \boldsymbol{a}_{i,k} = 0 \quad \forall i = 1, \ldots, \mathcal{I} \tag{5.103}$$

$$(\boldsymbol{P}_k, \boldsymbol{Q}_k, \boldsymbol{a}_k, \boldsymbol{s}_{g,k}) \in \mathbb{D}. \tag{5.104}$$

The complete cost function $\mathcal{F}$ with new variable $\boldsymbol{a}_k$

$$\mathcal{F} := \sum_{i=1}^{\mathcal{I}} f_i(\boldsymbol{r}^+_{i,k}) + f_{i,f}(\boldsymbol{s}_{i,k}) + g_s(\boldsymbol{a}_k) + g_g(\boldsymbol{P}_k, \boldsymbol{Q}_k) + g_f(\boldsymbol{s}_{g,k}) \tag{5.105}$$

is introduced to further simplify notation. According to (5.56) the augmented Lagrangian can

be written as

$$\mathcal{L}_\rho(\boldsymbol{r}, \boldsymbol{r}^+, \boldsymbol{s}, \boldsymbol{P}, \boldsymbol{Q}, \boldsymbol{s}_g, \boldsymbol{a}, \boldsymbol{\nu}) = \mathcal{F} + \frac{\rho}{2}\sum_{i=1}^{\mathcal{I}} \|\boldsymbol{r}_{i,k} - \boldsymbol{a}_{i,k} + \boldsymbol{\nu}_{i,k}\|_2^2 - \frac{\rho}{2}\sum_{i=1}^{\mathcal{I}} \boldsymbol{\nu}_{i,k}^T \boldsymbol{\nu}_{i,k}, \tag{5.106}$$

and the computation steps per ADMM iteration become

$$(\boldsymbol{r}_{i,k}^{\ell+1}, \boldsymbol{r}_{i,k}^{+,\ell+1}, \boldsymbol{s}_{i,k}^{\ell+1}) := \underset{(\boldsymbol{r}_i, \boldsymbol{r}_i^+, \boldsymbol{s}_i) \in \mathbb{P}_i}{\operatorname{argmin}} \Big(f_i(\boldsymbol{r}_{i,k}^+) + f_{i,f}(\boldsymbol{s}_{i,k}) + \frac{\rho}{2}\|\boldsymbol{r}_{i,k} - \boldsymbol{a}_{i,k}^\ell + \boldsymbol{\nu}_{i,k}^\ell\|_2^2 \Big) \tag{5.107}$$
$$\forall i = 1, \ldots, \mathcal{I}$$

$$(\boldsymbol{a}_k^{\ell+1}, \boldsymbol{P}_k^{\ell+1}, \boldsymbol{Q}_k^{\ell+1}, \boldsymbol{s}_{g,k}^{\ell+1}) := \underset{(\boldsymbol{a}, \boldsymbol{P}, \boldsymbol{Q}, \boldsymbol{s}_g) \in \mathbb{D}}{\operatorname{argmin}} \Big(g_s(\boldsymbol{a}_k) + g_g(\boldsymbol{P}_k, \boldsymbol{Q}_k) + g_f(\boldsymbol{s}_{g,k}) + \frac{\rho}{2}\sum_{i=1}^{\mathcal{I}} \|\boldsymbol{r}_{i,k}^{\ell+1} - \boldsymbol{a}_{i,k} + \boldsymbol{\nu}_{i,k}^\ell\|_2^2 \Big) \tag{5.108}$$

$$\boldsymbol{\nu}_{i,k}^{\ell+1} := \boldsymbol{\nu}_{i,k}^\ell + \boldsymbol{r}_{i,k}^{\ell+1} - \boldsymbol{a}_{i,k}^{\ell+1} \quad \forall i = 1, \ldots, \mathcal{I}. \tag{5.109}$$

The optimization in (5.107) can be carried out in parallel among all participating prosumers and only the solutions $\boldsymbol{r}_{i,k}^{\ell+1} \forall i = 1, \ldots, \mathcal{I}$ are communicated to the DSO, keeping the other internal optimization variables private. The DSO carries out the optimization in (5.108), the suggested residual loads from the prosumers enter the cost function as constant vectors. After the computation of $\boldsymbol{a}_k^{\ell+1}$, the scaled dual variable $\boldsymbol{\nu}_{i,k}^{\ell+1}$ is updated in (5.109) by the difference between the suggested residual load of the prosumers and the DSO for each prosumer individually and broadcasted to each participant to repeat the procedure until consensus between the residual load schedules is achieved. The communication between the prosumers and the DSO during one ADMM iteration is depicted in Figure 5.1 for an example in *Rural Grid 1*.

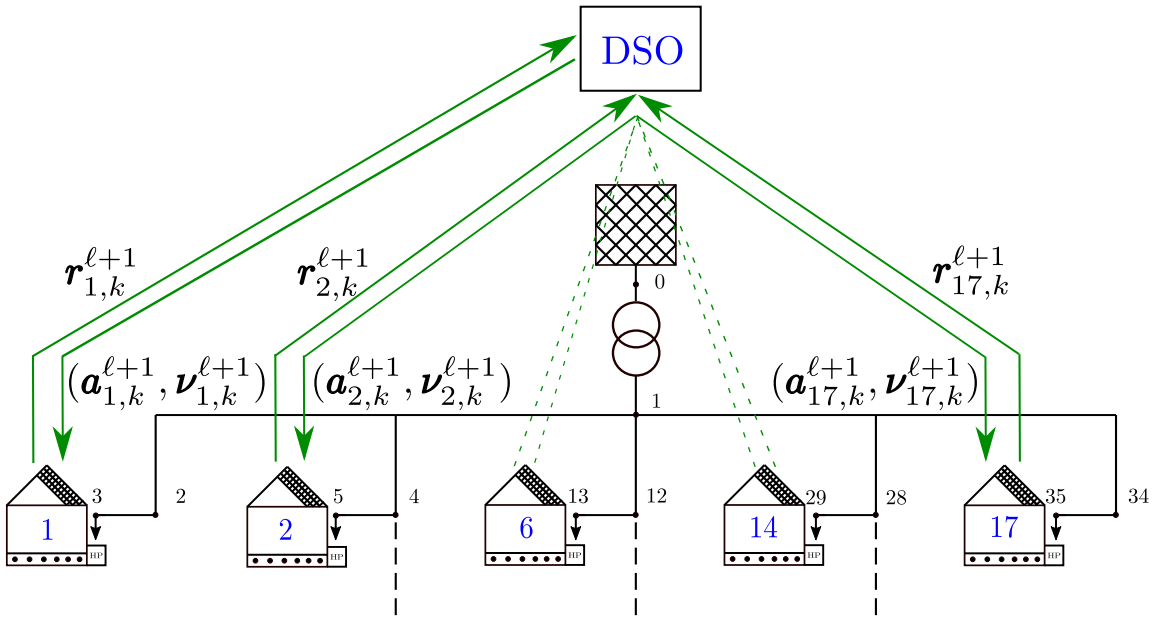

Figure 5.1: *Exchange of communication variables between 17 prosumers and the DSO for one ADMM iteration of the DMPC algorithm.*

The distributed MPC (DMPC) algorithm consists of three phases and is summarized below. The result obtained after convergence of ADMM at time step k is referred to as the open-loop result in the remainder of the thesis. Closed-loop then refers to the DMPC algorithm performed over multiple time steps, including the application of the optimal controllable inputs to the systems in phase 3, new states measurements, updated predictions and the re-execution of ADMM until convergence. Initializing $\boldsymbol{a}_{i,k}^0, \boldsymbol{\nu}_{i,k}^0$ not with zeros or arbitrary values, but with the corresponding entries of $\boldsymbol{a}_{i,k-1}^{\ell^*}, \boldsymbol{\nu}_{i,k-1}^{\ell^*}$ (here filled with zeros for the new time step in the prediction horizon) from the converged solution of the previous time step is referred to as *warm-starting*. The general idea of warm-starting is that the optimal solutions obtained at k and $k-1$ are not too different from each other, since only a new measurement of the states and predictions shifted by one time step enter the new optimal control problem. Warm-starting might then lead to faster convergence of ADMM, see also [Bra16] for a discussion of warm-starting in predictive control.

Algorithm DMPC

At time step k during DMPC operation:

Phase (1): Initialization

Prosumers $i = 1, \dots, \mathcal{I}$

- define f_i and $f_{i,f}$, measure $x_{i,0}$
- predict disturbances

$$\begin{aligned}\boldsymbol{d}_{i,k} &:= \boldsymbol{d}_i(k) = (d_i(k)^T, d_i(k+1)^T, \dots, d_i(k+N_P-1)^T)^T \\ \boldsymbol{g}_{i,k} &:= \boldsymbol{g}_i(k) = (g_i(k), g_i(k+1), \dots, g_i(k+N_P-1))^T \\ \boldsymbol{l}_{i,k} &:= \boldsymbol{l}_i(k) = (l_i(k), l_i(k+1), \dots, l_i(k+N_P-1))^T\end{aligned}$$

DSO

- define g_s, g_g and g_f
- predict active and reactive residual loads for buses of $\mathcal{N}_\ell$ in

$$\boldsymbol{\delta}_k := \boldsymbol{\delta}(k) = (\delta(k)^T, \delta(k+1)^T, \dots, \delta(k+N_P-1)^T)^T$$

Phase (2): ADMM

Initialize $\boldsymbol{a}_{i,k}^0, \boldsymbol{\nu}_{i,k}^0, \ell = 0$

while $\ell \leq \overline{\ell}$ (or other stopping criteria)

- **Prosumers** $i = 1, \dots, \mathcal{I}$ compute $\boldsymbol{r}_{i,k}^{\ell+1}$ with (5.107) and communicate to DSO
- **DSO** compute $\boldsymbol{a}_{i,k}^{\ell+1}$ with (5.108)
- **DSO** update $\boldsymbol{\nu}_{i,k}^{\ell+1}$ with (5.109) and communicate $(\boldsymbol{a}_{i,k}^{\ell+1}, \boldsymbol{\nu}_{i,k}^{\ell+1})$ back to prosumers $i = 1, \dots, \mathcal{I}$

$\ell \leftarrow \ell + 1$

Phase (3): Execution

Prosumers $i = 1, \dots, \mathcal{I}$ extract $\boldsymbol{u}_{i,k}^*$ from $\boldsymbol{r}_{i,k}^*$ and apply inputs $u_i^*(k)$ to system i

$k \leftarrow k + 1$

5.4.5 Stopping Criteria

Robust stopping criteria for ADMM are crucial for multi-period DMPC simulations to reduce the computational time whilst ensuring global feasible and close-to-optimal solutions. The authors in [CSZ+12] tested dual decomposition and ADMM as distributed optimization methods in MPC and found that a higher coupling strength (the connectivity) of the network topology between the participating dynamic systems led to an increase of necessary ADMM iterations. Moreover, the methods were relatively insensitive to the initial states of the systems. The authors found ADMM to consistently require a lower number of iterations than dual decomposition and pointed out that ADMM can be further tuned in speed by varying the penalty parameter ρ. Two update schemes for a varying ρ are introduced here besides keeping the value constant as assumed in the standard ADMM algorithm.
The primal and dual residuals from Equations (5.29) and (5.30) were introduced in Section 5.1.3 to track ADMM's progression towards convergence. The algorithm is stopped when the quantities fall below their problem-specific thresholds. The standard termination criteria applied to the DMPC algorithm are[4]

$$\|\Delta_{prim}^{\ell+1}\|_2 = \|\boldsymbol{r}_k^{\ell+1} - \boldsymbol{a}_k^{\ell+1}\|_2 \leq \varepsilon_{\text{prim}} \tag{5.110}$$

$$\|\Delta_{dual}^{\ell+1}\|_2 = \|-\rho(\boldsymbol{a}_k^{\ell+1} - \boldsymbol{a}_k^{\ell})\|_2 \leq \varepsilon_{\text{dual}}. \tag{5.111}$$

$\varepsilon_{\text{prim}}$ and $\varepsilon_{\text{dual}}$ have to be chosen to account for the absolute and relative tolerance allowed, see [BPC+10].

Residual Balancing and Adaptive ADMM

Whether the choice of ρ leads to a good rate of convergence is problem specific. While ADMM is said to achieve approximate solutions within few iterations, a high number of iterations may be required for high accuracy solutions [BPC+10]. Slow convergence can be avoided by tuning ρ during progression of the algorithm. A good choice of ρ has to balance the tradeoff between a higher weight of the penalty terms in the cost functions in (5.107) and (5.108) and the increase in the dual residual in (5.111). A standard approach to tune ρ online for faster convergence is suggested in [BPC+10] and has been applied to a distributed power system optimization in [BG16]. Penalty $\rho^{\ell+1}$ in ADMM's next iteration is defined as

$$\rho^{\ell+1} := \begin{cases} \tau\rho^{\ell} & \text{if } \|\Delta_{prim}^{\ell}\|_2 > \mu\|\Delta_{dual}^{\ell}\|_2 \\ \tau^{-1}\rho^{\ell} & \text{if } \|\Delta_{dual}^{\ell}\|_2 > \mu\|\Delta_{prim}^{\ell}\|_2 \\ \rho^{\ell} & \text{otherwise,} \end{cases} \tag{5.112}$$

to balance the residuals. Parameters $\tau = 2$ and $\mu = 10$ are suggested in [BPC+10]. The online variation of ρ requires to rescale the quadratic and linear terms resulting from the squared norm penalty terms in the cost functions in (5.107) and (5.108). Convergence is only guaranteed when ρ is no longer changed after a certain number of iterations [HYW00].
While it might be difficult to make a good choice for a fixed ρ, standard adaptive parameter scaling with residual balancing might perform poorly when ρ^0 is close to the optimal value but τ is too coarse for a proper increase, or many iterations might be required when τ is small and ρ^0 a bad initial choice. Another general flaw of residual balancing is its sensitivity to problem scaling, since the residuals might be of very different magnitude and thus commonly

[4] The primal and dual residuals in standard ADMM notation from Section 5.1.3 are $\Delta_{prim}^{\ell+1} = Ax^{\ell+1} + Bz^{\ell+1} - c$ and $\Delta_{dual}^{\ell+1} = \rho A^T B(z^{\ell+1} - z^{\ell})$. The residuals for algorithm DMPC are obtained with $A = I_{N_P\mathcal{I}}, B = -I_{N_P\mathcal{I}}$ and $c = \mathbf{0}_{N_P\mathcal{I}}$.

chosen parameters arbitrary. Several contributions in the literature address those issues. The penalty parameter update scheme in [Woh17] is formulated based on relative residuals to avoid compensation for problem scaling. The *adaptive ADMM* algorithm introduced in [XFG17] is automated to speed up ADMM and has proven to be fairly insensitive to initial ρ^0 and problem scaling, and outperformed other variants of ADMM in benchmark experiments. In [XTL+17] adaptive ADMM is further improved for consensus problems.
Adaptive ADMM is used in the simulation study in Section 6.3 to identify the optimal ρ in an open-loop optimization to be later used as a fixed parameter in a closed-loop simulation over multiple days. It is assumed that the ρ which was identified in the single optimization for the specific problem structure on a sample day is not far away from the optimal values corresponding to other time steps during a simulated week. The update scheme of adaptive ADMM applied to the DMPC problem of this thesis is given in Appendix A.12.

Chapter 6

Simulation Results

This chapter demonstrates the functionality of the hierarchical distributed MPC algorithm on the basis of three simulation studies. The first study investigates the coordination of the prosumers in a distribution grid to maintain voltage stability. The second study investigates valley-filling as a shared cost function to flatten the aggregated power demand and to avoid possible transformer overloading. The third study demonstrates how the distributed MPC algorithm can be utilized to reduce total costs and increase the PV self-consumption within the community.

6.1 Simulation Setup

The simulation environment and coordination algorithms of each study are implemented in MATLAB 2017b. All optimizations are solved with Gurobi 8.0.0.[1] The computer used for a single MPC iteration is equipped with an Intel Xeon E3-1270 3.5 GHz CPU and 16 GB memory. The computer used for closed-loop simulations and the test of larger problems is equipped with an Intel i7-7700 CPU at 3.6 GHz and 32 GB RAM. The prosumer updates in Equation (5.107) are parallelized in the implementation with the *parfor* command to distribute the $i = 1, \dots, \mathcal{I}$ optimizations on the available number of workers. The simulation computer offers a maximum of four workers, which is lower than any of the total number of prosumers considered in this chapter. Nevertheless, parallelizing reduces the computation time for larger grids compared to a serial implementation, i.e. a simple *for-loop* to carry out prosumer updates.

Central MPC Optimization Problem

The simulation studies on voltage stability and valley-filling differ only in the cost functions and are based on the same central optimization problem (5.91)-(5.95) solved at each time step during closed-loop operation. The prosumers minimize local costs for energy and the costs associated with a violation of the temperature limits:

$$f_i(\boldsymbol{r}_{i,k}^+) = \boldsymbol{c}_k^T \boldsymbol{r}_{i,k}^+ = \Delta_t \boldsymbol{\pi}_k^T \boldsymbol{r}_{i,k}^+ \qquad f_{i,f}(\boldsymbol{s}_{i,k}) = M_i \mathbf{1}^T \boldsymbol{s}_{i,k}. \tag{6.1}$$

$\Delta_t = 0.25$h due to the discretization step, $\boldsymbol{\pi}_k$ is a scenario-dependent price. The DSO minimizes the shared costs of valley-filling and the costs of a voltage band violation to guarantee feasible distribution grid operation:

$$g_s(\boldsymbol{r}_k) = \|H_{\mathcal{I}} \boldsymbol{r}_k + H_{\mathcal{N}^+} \boldsymbol{p}_k\|_2^2 \qquad g_f(\boldsymbol{s}_{g,k}) = M_g \mathbf{1}^T \boldsymbol{s}_{g,k}. \tag{6.2}$$

Parameter ω is introduced in the total cost function of the following complete optimization problem and is used as a weighting factor for the shared cost function g_s against the local

[1] www.gurobi.com

prosumer cost functions. $\omega = 0$ switches the shared cost function off. $M_g = M_i = 10^5$ is set to a high value to ensure that the slack variables are only used when feasibility cannot be achieved with the operational flexibility of the prosumers. The complete central optimization problem can be stated as:

$$\underset{(\boldsymbol{u},\boldsymbol{r},\boldsymbol{r}^+,\boldsymbol{s},\boldsymbol{P},\boldsymbol{Q},\boldsymbol{U},\boldsymbol{s}_g)}{\text{minimize}} \quad \sum_{i=1}^{\mathcal{I}} \Delta_t \boldsymbol{\pi}_k^T \boldsymbol{r}_{i,k}^+ + M_i \mathbf{1}^T \boldsymbol{s}_{i,k} + \omega \| H_{\mathcal{I}} \boldsymbol{r}_k + H_{\mathcal{N}^+} \boldsymbol{p}_k \|_2^2 + M_g \mathbf{1}^T \boldsymbol{s}_{g,k} \tag{6.3}$$

$$\text{subject to} \quad \boldsymbol{x}_{i,k} = \mathcal{A}_i x_{i,0} + \mathcal{B}_i \boldsymbol{u}_{i,k} + \mathcal{E}_i \boldsymbol{d}_{i,k} \tag{6.4}$$

$$\underline{\boldsymbol{x}}_{i,k} - \boldsymbol{s}_{i,k} \leq \boldsymbol{x}_{i,k} \leq \overline{\boldsymbol{x}}_{i,k} + \boldsymbol{s}_{i,k} \tag{6.5}$$

$$\boldsymbol{s}_{i,k} \geq \mathbf{0} \tag{6.6}$$

$$\overline{\mathcal{B}}_i \boldsymbol{u}_{i,k} \leq \overline{\boldsymbol{u}}_{i,k} \tag{6.7}$$

$$\boldsymbol{u}_{i,k} \geq \mathbf{0} \tag{6.8}$$

$$\boldsymbol{r}_{i,k} = \mathcal{B}_{i,k}^C \boldsymbol{u}_{i,k} + \boldsymbol{l}_{i,k} - \boldsymbol{g}_{i,k} \tag{6.9}$$

$$\boldsymbol{r}_{i,k}^+ \geq \mathbf{0} \tag{6.10}$$

$$\boldsymbol{r}_{i,k}^+ \geq \boldsymbol{r}_{i,k} \quad \forall i = 1, \ldots, \mathcal{I}, \tag{6.11}$$

$$\boldsymbol{\Pi} \boldsymbol{x}_{g,k} - \tilde{\boldsymbol{\Pi}} \boldsymbol{r}_k = \boldsymbol{\delta}_k \tag{6.12}$$

$$\underline{\boldsymbol{P}} \leq \boldsymbol{P}_k \leq \overline{\boldsymbol{P}} \tag{6.13}$$

$$\underline{\boldsymbol{Q}} \leq \boldsymbol{Q}_k \leq \overline{\boldsymbol{Q}} \tag{6.14}$$

$$\underline{\boldsymbol{U}} - \boldsymbol{s}_{g,k} \leq \boldsymbol{U}_k \leq \overline{\boldsymbol{U}} + \boldsymbol{s}_{g,k} \tag{6.15}$$

$$\boldsymbol{s}_{g,k} \geq \mathbf{0}. \tag{6.16}$$

Note that constraints (6.13) and (6.14) on the active and reactive power line flows are added to the final problem. Allowing a violation of constraints through slack variables was only required for the voltages in order to test stricter voltage scenarios. The central optimization problem is slightly changed for the study on community PV self-consumption and separately stated in Section 6.4 to not complicate notation.

Table 6.1 shows the standard temperatures limits chosen per building type to guarantee thermal comfort. The maximum temperature for type L is sightly higher than for J and E to avoid excessive use of local slack variables when overheating results from stronger solar gains which leads to higher temperatures due to the strong insulation standard. In the simulations, the constraint of the maximum zone temperature was never active during overheating by the heating system since the maximum floor temperature was usually reached earlier. In the following sections, slack variable costs are excluded from the total costs presented to keep the results interpretable.

Table 6.1: *Standard temperature limits used in the simulation studies.*

	$\underline{T}_z - \overline{T}_z$	$\overline{T}_{fl}$	$\underline{T}_{sto} - \overline{T}_{sto}$	$\underline{T}_{dhw} - \overline{T}_{dhw}$
L	20–27 °C	30 °C	25–30 °C	45–55 °C
J	20–25 °C	34 °C	30–35 °C	45–55 °C
E	20–25 °C	37 °C	35–40 °C	45–55 °C

The same meteorological time series which was used for the validation of the thermal building models in Section 2.2.7 is used for all simulations presented in this section. The ground temper-

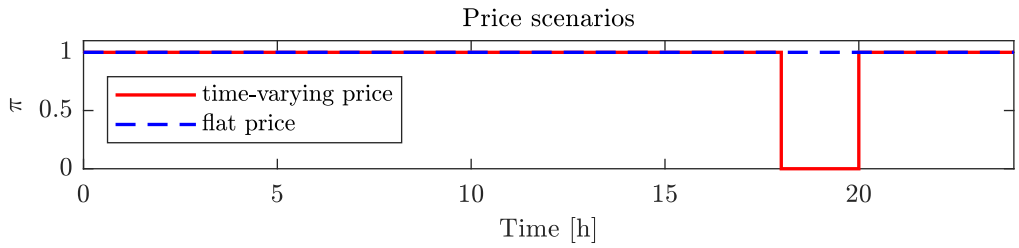

Figure 6.1: *Price scenarios considered in the study on voltage stability.*

ature is fixed at $T_g = 10°C$. If available, the buffer storage is located in the basement, which is assumed to have a constant surrounding temperature of $T_{env} = 15°C$.

Reference Operation

A reference operation is defined here as a benchmark to investigate the change in operation when coordination is required, e.g. due to a violation of the distribution grid constraints. The reference operation is defined as the optimal schedule of each prosumer with respect to its local constraints and cost functions, neglecting its impact on the distribution grid and the operation of other prosumers. The reference operation is obtained by solving only the i-indexed parts of the central optimization problem, i.e. Problem (6.3)-(6.11) for each prosumer consecutively. The result is the reference operation of each prosumer to minimize his costs in a selfish, uncoordinated and completely decentralized setting.

6.2 Voltage Stability

The first simulation study demonstrates how the operational flexibility of the prosumers can be utilized to avoid undervoltages during peak load times. Central problem (6.3)-(6.16) is solved by the DMPC algorithm when coordination is investigated. Only the linear cost terms are considered, i.e. $\omega = 0$ and the DSO costs consist only of costs associated with slack variable use for voltage feasibility in constraint (6.15). It is assumed that a prosumer is connected at each load bus and no PV generation is available to investigate low voltage conditions, i.e. $\boldsymbol{g}_{i,k} = \mathbf{0}$ for all prosumers. The following examples consider the operation of the prosumers with both a constant flat price over time and a scenario which has a price of zero for two hours between 6 and 8 pm on cold winter days in February. Figure 6.1 shows the price for both scenarios. The time-varying price scenario is motivated by a situation where an arbitrary (price) signal incentivises shifting electricity demand to a certain time of the day, e.g. due to strong wind production which leads to low market prices. Such a price signal could come from the spot market or be communicated by an aggregator. The zero cost evening hours are chosen here to coincide with lower heat pump efficiencies and relatively high electricity demands of consumer appliances, which potentially leads to a violation of the operational limits of the distribution grid. The price signal causes a high coincidence of the residual load of the prosumers.
Simulations for the coldest week of the year show that independent of the building type assumed, neither in *Rural Grid 1* nor in *Rural Grid 2* violations of the grid limits occur when a flat price is considered, not even if the reference voltage is lowered to $V_0 = 0.95$ p.u.. The time-varying price scenario and zero back-up heater capacity does not lead to violations of the grid limits either. Voltage violations start to occur in *Rural Grid 1* for the time-varying price, full back-up heater capacity and all prosumers of building type E and J with $V_0 = 1$ p.u.. Building type L leads to violations for the same assumptions but at a lower reference voltage, e.g. $V_0 = 0.95$

Table 6.2: *Occurrence of violations of grid limits for the coldest week of the year. All buildings with fully available back-up heater capacity and without buffer storage.*

	Rural Grid 1		***Rural Grid 2***	
	flat price	time-varying price	flat price	time-varying price
L	/	voltage violation for $V_0 = 0.95$ p.u.	/	/
J	/	voltage violation for $V_0 = 1$ p.u.	/	/
E	/	voltage violation for $V_0 = 1$ p.u.	/	/

p.u.. Table 6.2 summarizes these results. The first conclusion is that only specific building, price and reference voltage scenarios lead to voltage violations. The other distribution grids discussed in Section 4.3 will potentially lead to violations for a flat price scenario. Since the larger grids would add unnecessary complexity to the analysis and require higher computational cost[2], the following section is limited to *Rural Grid 1*.
The simulation results are presented in the following order to demonstrate the effectiveness of the DMPC algorithm in a comprehensive way, but also to provide insight into the response of the thermal systems: First, the open-loop results for the uncoordinated reference operation are shown to investigate the reaction of the prosumers to the time-varying price and the effect on voltage stability for one day. Afterwards, the effect of coordination with the DMPC algorithm is shown and resulting energy and cost statistics presented. Section 6.2.2 then presents the closed-loop results of the DMPC algorithm and confirms the open-loop observations. An analysis of the resulting cost increase per prosumer and the effect of additional buffer storage volumes follows. The section ends with an analysis of the number of iterations required to converge.

6.2.1 Open-loop Solutions for a Winter Day

A total of 17 prosumers are assumed to be connected to all load buses. Figures 6.2 and 6.3 show the open-loop solutions of the optimal reference operations of all buildings of either type L or E, computed in the beginning of an exemplary day (February 10) of the coldest week and both price scenarios. The temperatures of all prosumers are initialized with $x_0 = (23°\text{C}, 22°\text{C}, 22°\text{C}, 23°\text{C}, 50°\text{C})^T$ for type L and $x_0 = (24°\text{C}, 22°\text{C}, 22°\text{C}, 24°\text{C}, 50°\text{C})^T$ for type E, no buffer storages are assumed. The prediction horizon is 24 h and the systems are discretized at 15 minutes time steps. The voltage at the slack bus is fixed at $V_0 = 1$ p.u..
For type L, the zone temperatures fall slowly towards the lower limit of 20 °C and the individual trajectories start to differ slightly when the occupants of the four-person households begin to carry out different activities leading to different internal gains. While the heat pumps start to operate for space heating around noon in the flat price scenario, significant heating takes place between 6 and 8 pm when the time-varying price is available. Moderate early preheating allows to reschedule the remaining heating demand of the day in such a way that the operation can partially be shifted to the cheap hours. The aggregated residual load $\sum_{i=1}^{\mathcal{I}} \boldsymbol{r}_i$ shows a distinct increase during the zero price hours. The lower plots in Figure 6.2 show the resulting voltage profile over all buses in the grid at each quarter-hour of the day. While the flat price scenario leads to a rather flat voltage profile, the time-varying price scenario leads to a stronger but not critical voltage drop during the eight quarter-hours when the price is zero.

[2] The size of the matrices generated in the central optimization as a benchmark for ADMM exceeds the available amount of computer memory.

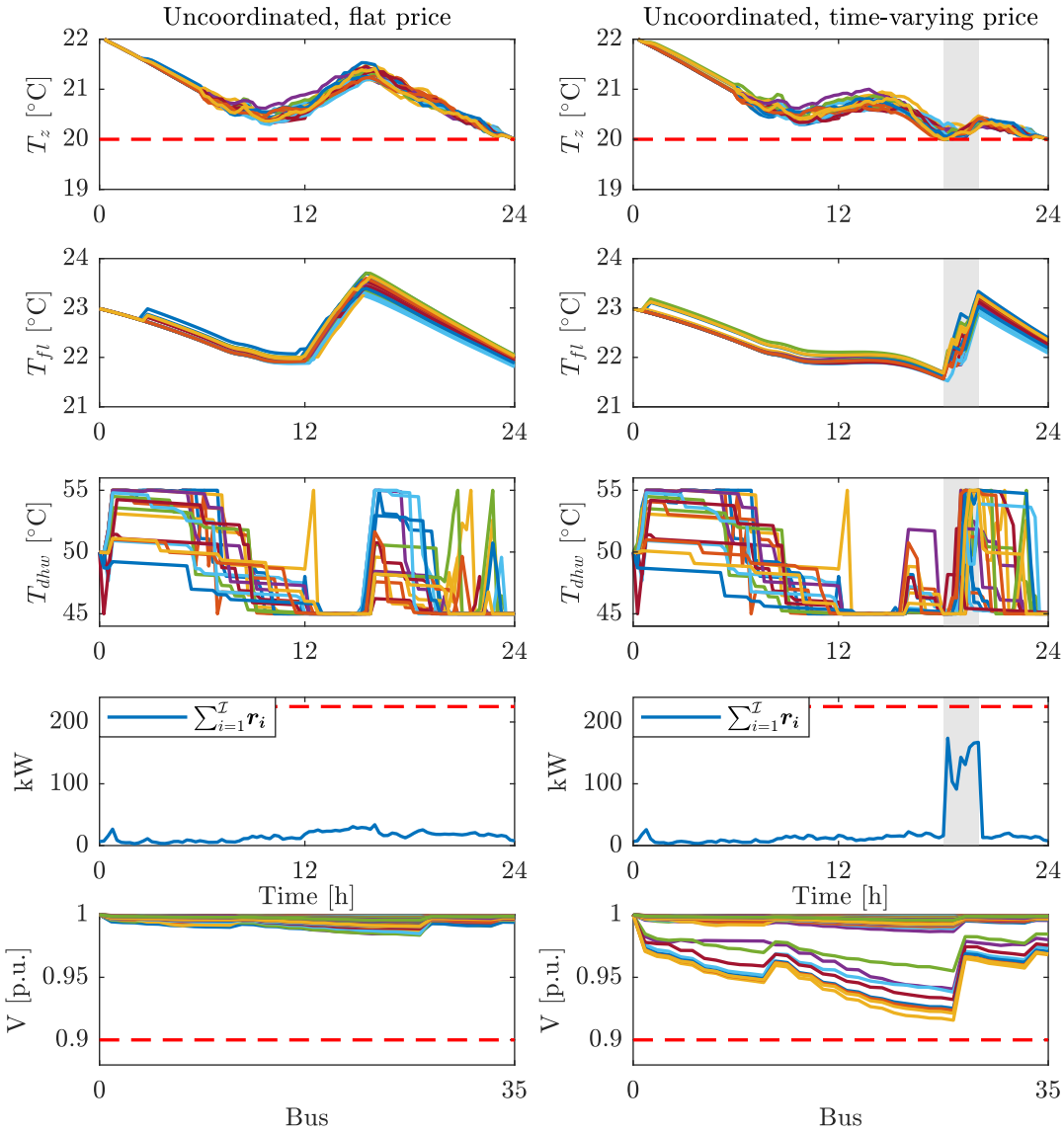

Figure 6.2: *Uncoordinated reference operation of 17 prosumers with building type L for both price scenarios in Rural Grid 1. Red dashed lines indicate the closest operational limit, i.e.* 20 °C *for* T_z*, transformer limit* $\overline{P}_1 = 225\,\text{kW}$ *and the lower voltage limit. The gray area indicates zero price hours.*

In contrast, the lower voltage limit is violated in the time-varying price scenario when all prosumers are of building type E, as can be seen in Figure 6.3. The aggregated residual load also exceeds the transformer limit $\overline{P}_1$, which reflects the sensitivity of *Rural Grid 1* observed in Section 4.3. The zone and floor temperatures show an increase before and during the zero price hours. The price advantage is exploited in such a way that the temperatures of the floors are increased until their maximum temperature limit. The zone temperatures show significantly more variation in time, which stands in contrast to the energy efficient operation close to the lower zone temperature limit in the flat price scenario[3]. The temperatures in the domestic hot water storages remain always in the required range from 45-55 °C. They are operated in such a way that a part of the charging can take place when the price is zero. This can be seen in the

[3]The internal gains from occupants are almost not recognizable in T_z for type E compared to building type L, due to the higher heat loss.

low temperatures just before the end of the zero price period, allowing for charging at zero cost. In the flat price scenario, charging mainly takes place when the COPs of the heat pumps reach a peak in the afternoon around 4 pm.
The above investigation of the reference operation for different prices and building types shows that a violation of the grid constraints is scenario dependent.

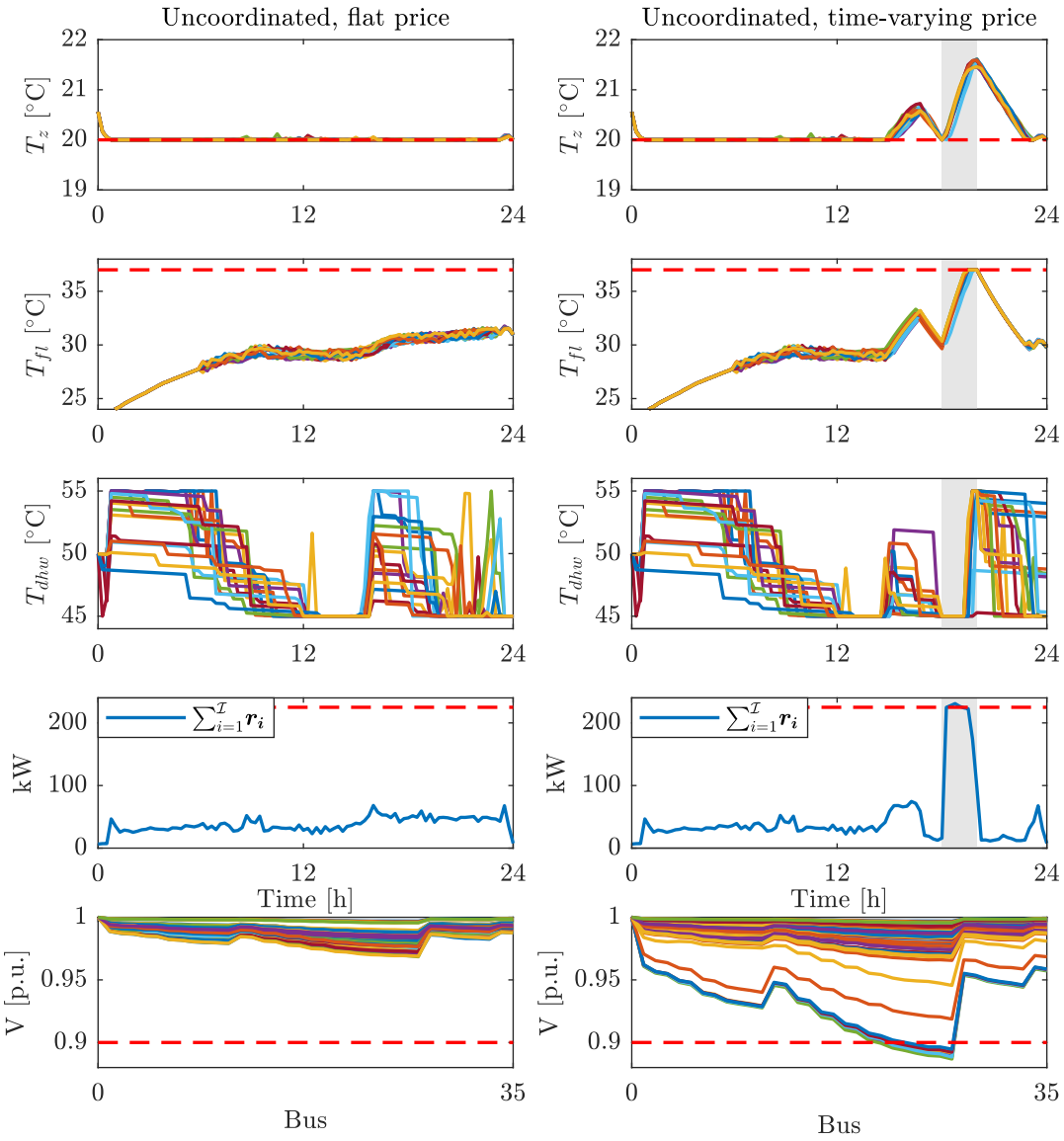

Figure 6.3: *Uncoordinated reference operation of 17 prosumers with building type E for both price scenarios in Rural Grid 1. Red dashed lines indicate the closest operational limit, i.e.* 20 °C *for* T_z, 37 °C *for* T_{fl}, *transformer limit* $\overline{P}_1 = 225\,\text{kW}$ *and lower voltage limit. The gray area indicates zero price hours.*

The following simulation results demonstrate how the DMPC algorithm can now be used to coordinate the prosumers in such a way that they can still benefit from zero price hours without jeopardizing voltage stability. Full participation of the 17 prosumers is assumed for coordination. Figure 6.4 shows the open-loop simulation results for the type E prosumers after 100 ADMM iterations, the penalty parameter was set to $\rho = 0.01$. The results are shown for the case of $V_0 = 1\,\text{p.u.}$ and the more restrictive case of $V_0 = 0.95\,\text{p.u.}$. The fourth row in Figure 6.4 shows

both the aggregated residual load computed with ADMM and the solution obtained by solving the central optimization (CO) for comparison. The power profiles are very similar and result in the same values of the objective function when evaluated at the optimal solution.

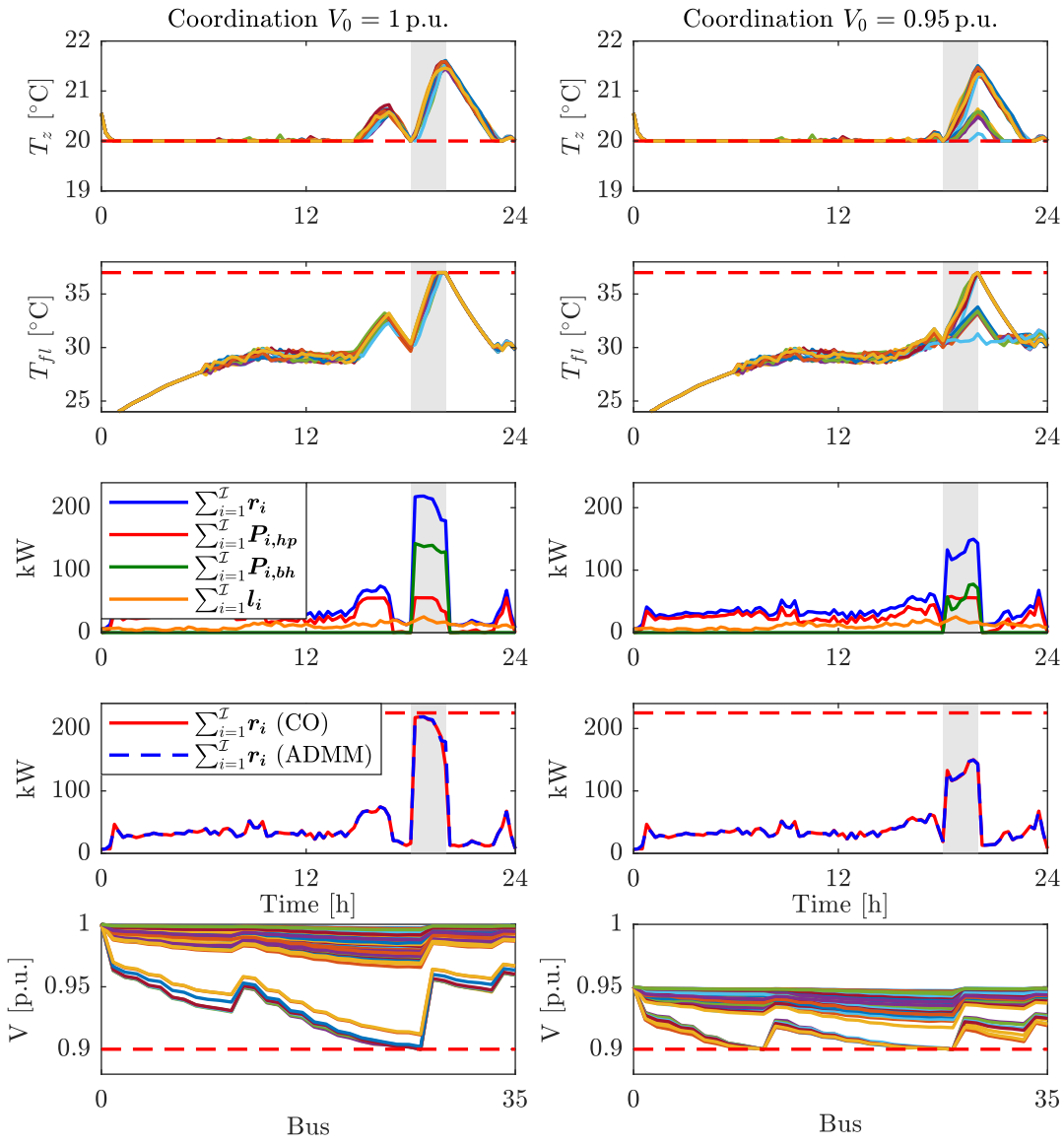

Figure 6.4: *Results for the coordination of 17 prosumers of type E in Rural Grid 1 via the distributed MPC algorithm based on ADMM. 100 Iterations, $\rho = 0.01$, central optimization (CO) profile for comparison.*

Only a small change in operation is required in the case of $V_0 = 1$ p.u., since only a relatively small undervoltage occurred in the uncoordinated case. A difference is hardly noticeable when compared with the reference operation with the time-varying price in Figure 6.3. A larger change in operation is required when the reference voltage is set to 0.95 p.u.. The temperatures in the zone and floor differ among the prosumers as a result of different operational schedules. While some participants can still increase the floor temperature to its maximum value to benefit from the reduced price, prosumers located at buses with critically low voltages have to change their operation to maintain voltage stability. This concerns mainly the prosumers located at the long feeder number 3 in Figure 4.2. The change in operation is primarily achieved through a reduction

of the back-up heater power, which was initially increased to exploit low prices. This results in a decreased aggregated residual load and a feasible voltage profile in the distribution grid.
Table 6.3 shows the aggregated electricity demands, costs, performance factors and extreme values of the active power flows, voltages and zone temperatures for the considered scenarios in *Rural Grid 1* for type E. The performance factor (PF) is derived from the seasonal performance factor to quantify the average efficiency of all heating systems over the prediction horizon:

$$PF = \frac{\mathbf{1}^T \boldsymbol{u}_k}{\mathbf{1}^T (\boldsymbol{r}_k - \mathbf{l}_k)} = \frac{\sum_{i=1}^{\mathcal{I}} \sum_{j=0}^{N_P-1} \dot{Q}_{hp,sh,i}(j) + \dot{Q}_{bh,sh,i}(j) + \dot{Q}_{hp,dhw,i}(j) + \dot{Q}_{bh,dhw,i}(j)}{\sum_{i=1}^{\mathcal{I}} \sum_{j=0}^{N_P-1} r_i(j) - l_i(j)}. \tag{6.17}$$

The time-varying price scenario without coordination results in a higher total electricity demand when compared with the flat price scenario. This is in part caused by an additional back-up heater operation, which reduces the performance factor from 3.26 to 2.57. The lower costs[4] are achieved due to the zero price hours. The aggregate costs increase when coordination takes place to maintain voltage stability. While the cost increase is negligible for $V_0 = 1\,\text{p.u.}$, an increase of 3.6% occurs for the more challenging scenario with $V_0 = 0.95\,\text{p.u.}$. The back-up heater operation is reduced by over 50%, which also leads to a better performance factor. The total electricity demand is reduced by around 10% and the maximum power flow (occurs at P_1 over the transformer) is reduced by over a third. Finally, the distributed MPC algorithm converges to the correct value of the objective function, the costs computed with the central optimization match those obtained after the 100 ADMM iterations.

Table 6.3: *Aggregated electricity demands, costs, performance factor and maximum values for all prosumers of type E over the scenarios. The first two cost entries for flat price and time-varying price without coordination result from the reference operation. Percentage change based on scenario time-varying price without coordination.*

		Flat price	**Time-varying price**		
Coordination		No	No	Yes	Yes
V_0	[p.u.]	1	1	1	0.95
residual load	[kWh]	907.2	1109.7	1114 (+0.4%)	994 (-10.4%)
heat pump	[kWh]	652.2	590.8	586.6 (-0.7%)	623.4 (+5.5%)
back-up heater	[kWh]	0	263.9	272.4 (+3.2%)	115.7 (-56.2%)
fixed demand	[kWh]	255	255	255	255
Costs	[kWh]	907.2	703	703.3 (+0.0%)	728.2 (+3.6%)
Costs CO	[kWh]			703.3	728.2
PF		3.26	2.57	2.55	2.91
$\max(\boldsymbol{P})$	[kW]	68.2	230.9	218.6 (-5.3%)	149.6 (-35.2%)
$\min(\boldsymbol{V})$	[p.u.]	0.9685	0.8868	0.9	0.9
$\max(\boldsymbol{T}_z)$	[°C]	20.6	21.6	21.6	21.5

The total increase in costs due to coordination for scenarios of undervoltage is unequally distributed among the individual prosumers participating in the DMPC scheme. While the total costs of all participants increase only by 3.6% for $V_0 = 0.95\,\text{p.u.}$, prosumers located at feeder 3 (includes prosumers {6, 7, 8, 9, 10, 11, 12, 13}) face cost increases above this value, except for prosumer 6. Prosumer 13 located at bus 27, where undervoltage was found to occur first in the

[4] Costs are expressed in kWh since π is assumed dimensionless.

analysis in Section 4.3, faces a cost increase by 13.6% in the scenario with $V_0 = 0.95$ p.u..
The results for *Rural Grid 1* and prosumer buildings of type J are similar to those of type E. The total costs increase by 2.3% when compared with the uncoordinated time-varying price scenario and $V_0 = 0.95$ p.u.. The complete results for type J are provided in Table B.1 in the Appendix. The aggregated results for type L are shown in Table 6.4, significant changes in operation of the back-up heaters and heat pumps are required when coordination takes place in the challenging scenario with $V_0 = 0.95$ p.u. (no voltage limit was violated for $V_0 = 1$ p.u.). The solution obtained after 100 ADMM iterations is only 0.04% higher than the cost obtained from the CO and could be further improved with more iterations. The increase in costs of 0.3% is relatively small when the total costs of all prosumers are considered. Flexible operation allows the systems to maintain voltage stability at low costs.

Table 6.4: *Aggregated electricity demands, costs, performance factor and maximum values for all prosumers of type L in the scenario $V_0 = 0.95$ p.u. where coordination is required. The first two cost entries for flat price and time-varying price without coordination result from the reference operation. Percentage change based on scenario time-varying price without coordination.*

		Flat price	**Time-varying price**	
Coordination		No	No	Yes
V_0	[p.u.]	1	1	0.95
residual load	[kWh]	353.6	532.3	447.6 (-15.9%)
heat pump	[kWh]	96.4	31.7	61.1 (+92.7%)
back-up heater	[kWh]	2.2	245.7	131.5 (-46.5%)
fixed demand	[kWh]	255	255	255
Costs	[kWh]	353.6	248.6	249.4 (+0.3%)
Costs CO	[kWh]			249.3
PF		3.12	1.18	1.69
$\max(\boldsymbol{P})$	[kW]	33.8	173.9	102.5 (-41.1%)
$\min(\boldsymbol{V})$	[p.u.]	0.9837	0.9157	0.9
$\max(\boldsymbol{T}_z)$	[°C]	22.2	22.2	22.2

6.2.2 Closed-loop Simulation for a Week in Winter

The following section demonstrates the functionality of the DMPC algorithm for coordination during winter time from February 9 to February 15. The second day of the 7 days was used for the demonstration of the single-shot open-loop results investigated in the previous section. This procedure is now repeated at each time step to simulate realistic operation over a longer period of time.
Figure 6.5 shows the simulation results for the 7 days closed-loop DMPC operation of the 17 prosumers of type L without a buffer storage in *Rural Grid 1*. The distributed optimization has been carried out at each time instant to coordinate the operation for the time-varying price and $V_0 = 0.95$ p.u.. At each time instant the ADMM iterations were stopped when both the Euclidean norms of the primal and dual residuals in Equations (5.110) and (5.111) were below

$$\varepsilon_{\text{prim}} = \varepsilon_{\text{dual}} = 10^{-3}\sqrt{N_P \mathcal{I}} = 10^{-3}\sqrt{96 \times 17} = 0.0404. \tag{6.18}$$

As an example, this threshold corresponds to a maximum disagreement between the residual load profiles of the DSO and the prosumers of 40 W in a single entry of the vector $(\boldsymbol{a}_k^\ell - \boldsymbol{r}_k^\ell)$, i.e. for a single instant of time and prosumer when the disagreement is zero for all other times and prosumers. A maximum number of $\overline{\ell} = 100$ iterations is set as a second termination criterion to avoid lengthy simulation time when the first criterion has not been reached yet. Independent of whether or not the algorithm's latest solution has reached the above stated accuracy, after 100 iterations the DMPC algorithm will proceed to the next time step and the latest solution is applied to the prosumers' building systems. After either of the termination criteria is met, the algorithm proceeds 15 minutes in time and ADMM begins to iterate to a new solution for the updated 24 hours prediction window. Warm-start is used for initialization.
The first diagram shows the ambient temperature and solar gains input over the 7 days. After three days of temperatures around 0 °C, the temperature drops to a record low. This is accompanied by clear sky conditions which lead to relatively high solar gains during the day. The zone and floor temperatures show how overheating is carried out by some prosumers during the first days during zero price hours, leading to recognizable peak loads in the aggregated residual load profile. The tight insulation of building type L allows to optimally integrate the daily solar gains, which primarily enter through the large south-facing window. The inertia of the system was already identified in Section 2.3 and allows for almost no space heating operation during days five and six. The remaining residual load covers mainly the domestic hot water demand and fixed electricity load during this time. The zone and floor temperatures show similarity among the prosumers since they are dominated by either coincident inactivity in the night or solar gains during the day. The fifth diagram shows the sum of the residual loads of all prosumers for the uncoordinated case, the central optimization result and the DMPC result computed with ADMM at each time instant. Load peaks are reduced to maintain global feasible operation when compared with the uncoordinated reference operation. ADMM achieves a very similar aggregated operation compared with the central optimization result, especially during times when the voltage constraints are active. The last diagram shows how the voltage is always kept between 0.9 and 0.95 p.u.. Coordination allows the voltage at the worst buses to drop to 0.9 p.u. to maximize the benefit from reduced prices.
Table 6.5 shows the corresponding aggregated results for the simulation over 7 days with buildings of type L. The results are calculated with the realized operation over the full simulation period, in contrast to the open-loop single 24 hours prediction analyzed in the previous section. The peak load is more than quadrupled for the uncoordinated time-varying price scenario compared with the flat reference operation, even exceeding the maximum value of the previous open-loop result. Like in the open-loop simulation, the back-up heater operation has to be reduced drastically to maintain voltage stability for $V_0 = 0.95$ p.u.. The costs increase by 3.4%. In the coordinated case, back-up heater reduction leads to limitation of the transformer peak load by around a fifth.

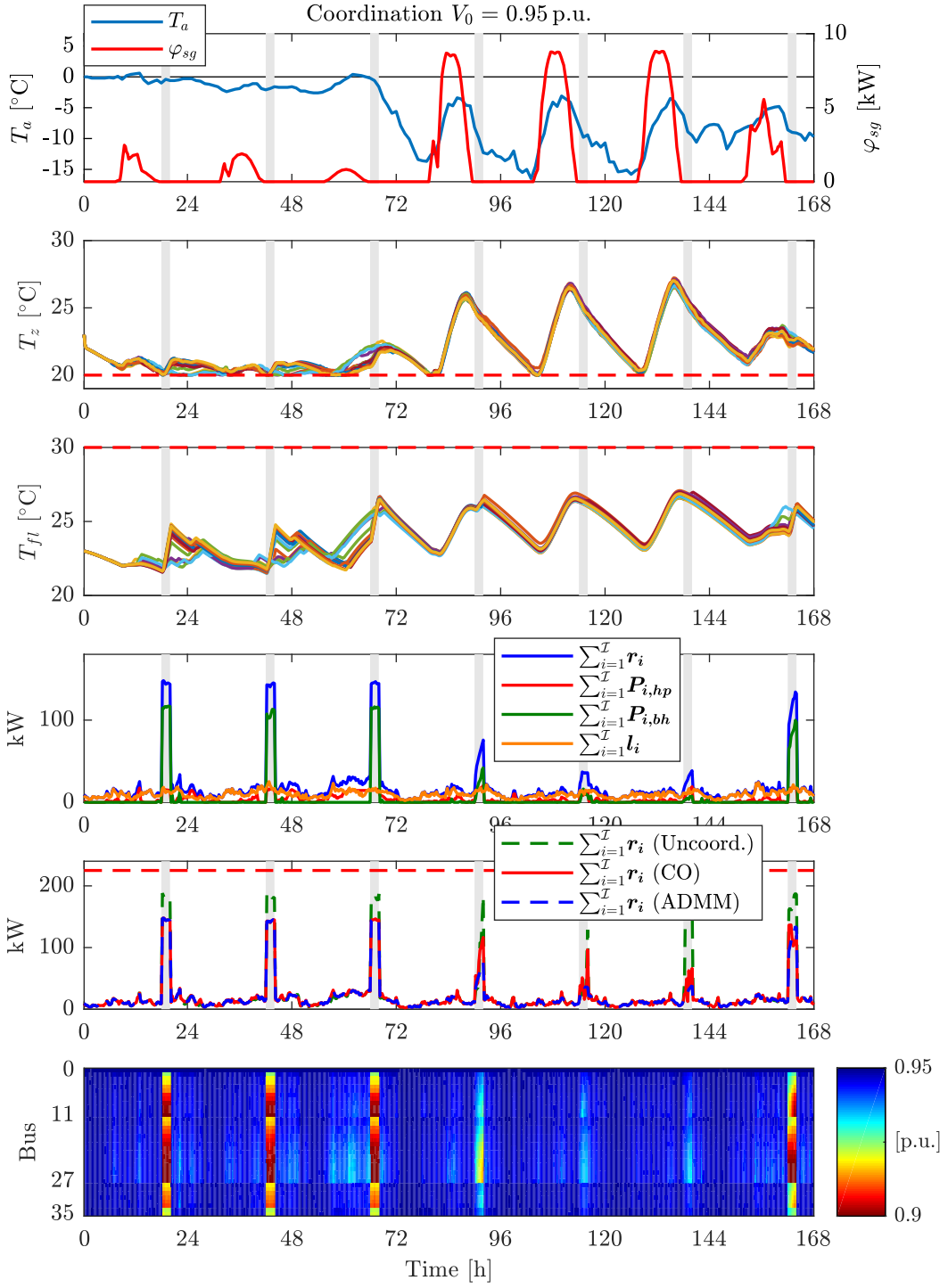

Figure 6.5: *Closed-loop results for the coordination of 17 prosumers of type L in Rural Grid 1 via the distributed MPC algorithm based on ADMM with $\rho = 0.01$. Uncoordinated reference operation (Uncoord.) and central optimization (CO) profile for comparison.*

Table 6.5: *Aggregated electricity demands, costs, performance factor and maximum values for all prosumers of type L over the scenarios in closed-loop simulation. The first two cost entries for flat price and time-varying price without coordination result from the reference operation. Percentage change based on scenario time-varying price without coordination.*

		Flat price	**Time-varying price**	
Coordination		No	No	Yes
V_0	[p.u.]	1	1	0.95
residual load	[kWh]	2587.4	3850.8	3237.6 (-15.9%)
heat pump	[kWh]	913.6	546.4	641.8 (+17.5%)
back-up heater	[kWh]	26.3	1656.9	948.3 (-42.8%)
fixed demand	[kWh]	1647.5	1647.5	1647.5
Costs	[kWh]	2587.4	1832.6	1894.8 (+3.4%)
Costs CO	[kWh]			1895.9
PF		3.06	1.5	1.82
$\max(\boldsymbol{P})$	[kW]	39.6	190.5	148 (-22.3%)
$\min(\boldsymbol{V})$	[p.u.]	0.9815	0.9062	0.9
$\max(\boldsymbol{T}_z)$	[°C]	27.1	27.1	27.2

Figure 6.6 shows the results for the same setting but building type E (no buffer storage). Similar to the observations made in Figure 6.4, coordination requires primarily the prosumers of the long feeder 3 to limit the heat pump and back-up heater operation during zero price hours to maintain voltage stability. This can be seen in the partially weaker increase in the floor and zone temperatures during the first two days. The high solar gains lead to an increase of the zone temperature during days 4, 5, and 6. In contrast to building L, space heating must be provided during the night when the temperature drops severely due to the weaker insulation. The heat pumps then often operate at maximum capacity to keep the floor temperature at a high level to maintain the zone temperature above 20 °C. The fifth diagram shows how the solutions of the ADMM algorithm have converged to an aggregated residual load profile very similar to the one obtained from the central optimization. The residual load peaks are clearly reduced compared with the uncoordinated reference operation, which at times leads to transformer overloading (see peak above 225 kW in the aggregated residual load during zero price hours on day two). The voltages never drop below 0.9 p.u.. The lowest voltages regularly occur at buses 11 and 27, at the ends of the feeders 2 and 3.

Figure 6.7 shows the change in the residual load when the uncoordinated reference operation is compared with the coordinated operation for $V_0 = 0.95$ p.u. The residual load is again mainly reduced by prosumers $7-13$ at feeder 3 during zero price hours, but also prosumer 5 at the end of feeder 2 is affected. The change in operation is often accompanied by an increase of the residual load during the hours right before the low price and another reduction just before that time. The pattern is well recognizable for 6 out of the 7 days and demonstrates how the operational flexibility allows to redistribute the residual load to maintain feasible distribution grid operation.

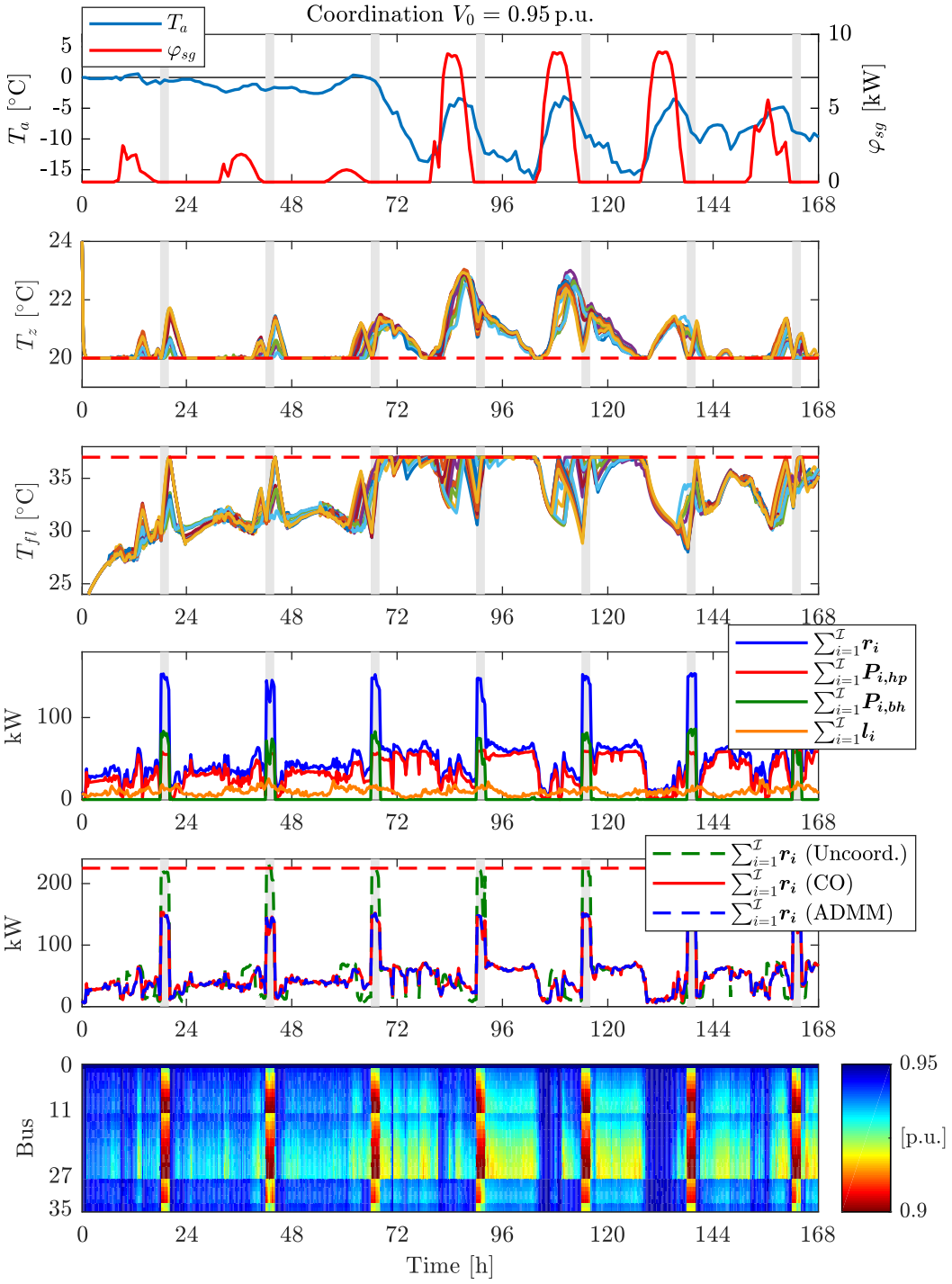

Figure 6.6: *Closed-loop results for the coordination of 17 prosumers of type E in Rural Grid 1 via the distributed MPC algorithm based on ADMM with $\rho = 0.01$. Uncoordinated reference operation (Uncoord.) and central optimization (CO) profile for comparison.*

Table 6.6 shows the aggregated results for the simulation over 7 days with buildings of type E. The operation in the flat price scenario achieves the highest energy efficiency by exploiting times of a high COP, the back-up heater operation is limited to few instances when it is used to maintain domestic hot water comfort. This operation leads to the highest performance factor. The change in operation to maintain voltage stability is similar to the previous results. The

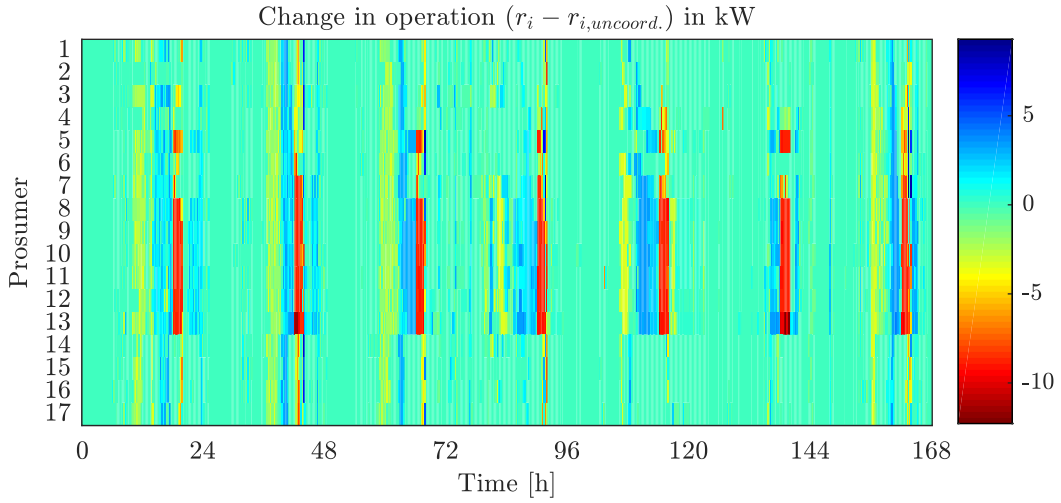

Figure 6.7: *Change in the residual load in* kW *for all prosumers of type E compared with the uncoordinated operation for* $V_0 = 0.95$ *p.u.*

increase in total electricity demand due to the time-varying price has to be reduced by 7.7% in the restrictive case of $V_0 = 0.95$ p.u., mainly caused by a 50% reduction of the demand of the back-up heaters. This also increases the overall performance factor. The active power flow over the transformer exceeds its line flow limit in the uncoordinated case and is reduced by 3.9% and 33.4% in the coordination scenarios. The maximum zone temperatures are now determined by the solar gains input over the sunny days. The aggregated costs over all prosumers are very close to those obtained from the central optimization. The relative increase in total costs of 3.8% for $V_0 = 0.95$ p.u. is in the order of the previous open-loop result of 3.6%.

Table 6.6: *Aggregated electricity demands, costs, performance factor and maximum values for all prosumers of type E over the scenarios in closed-loop simulation. The first two cost entries for flat price and time-varying price without coordination are the result of the reference operation. Percentage change based on scenario time-varying price without coordination.*

		Flat price	**Time-varying price**		
Coordination		No	No	Yes	Yes
V_0	[p.u.]	1	1	1	0.95
residual load	[kWh]	7815.8	9208.3	9238.7 (+0.3%)	8495.4 (-7.7%)
heat pump	[kWh]	6164.1	5590.3	5571.4 (-0.3%)	5861.4 (+4.8%)
back-up heater	[kWh]	4.2	1970.6	2019.9 (+2.5%)	986.5 (-49.9%)
fixed demand	[kWh]	1647.5	1647.5	1647.5	1647.5
Costs	[kWh]	7815.8	6265.9	6270.4 (+0.1%)	6502.6 (+3.8%)
Costs CO	[kWh]			6269.7	6502.4
PF		2.93	2.42	2.41	2.65
$\max(\boldsymbol{P})$	[kW]	80.5	230.9	222 (-3.9%)	153.7 (-33.4%)
$\min(\boldsymbol{V})$	[p.u.]	0.9631	0.8868	0.9	0.9
$\max(\boldsymbol{T}_z)$	[°C]	24	24	24	24

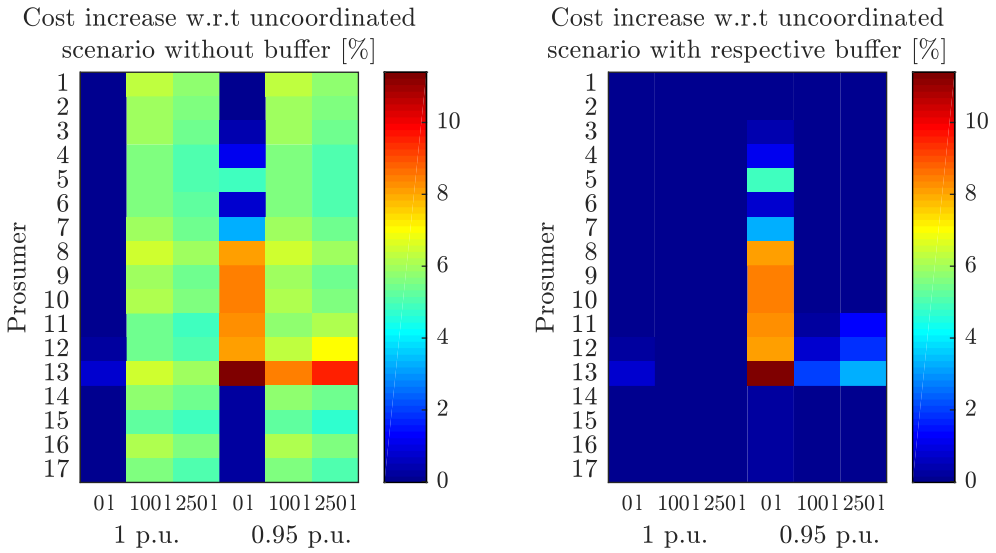

Figure 6.8: *Percentage increase in costs per prosumer of building type E over the 7 days for different buffer storage volumes from* 0 l *to* 250 l *in Rural Grid 1 when coordination is required for time-varying prices and* $V_0 = 1\,p.u.$ *or* $V_0 = 0.95\,p.u.$*. Cost increases are calculated relative to the uncoordinated case without any buffer volume (left) and relative to the uncoordinated case with the respective buffer volume (right).*

Cost Increase Per Prosumer and Additional Buffer Volume

Figure 6.8 shows the relative increase in costs per prosumer of type E due to coordination in the closed-loop simulation for different buffer storage volumes. Storage losses lead to an increase in costs for both volumes and for all prosumers for $V_0 = 1\,\text{p.u.}$ when compared with the uncoordinated operation without a buffer (left diagram). The larger buffer storage leads to higher losses, but the additional volume allows the prosumers to operate at slightly lower costs. The more restrictive scenario with $V_0 = 0.95\,\text{p.u.}$ leads to an increase in costs of 11.4% for prosumer 13 over the simulation period when no buffer storage is used. The increase can be reduced by around 25% when a 100 l volume is used. Mainly prosumer 5 at the end of feeder 2 and prosumers 7-13 along feeder 3 face increased costs for $V_0 = 0.95\,\text{p.u.}$ when no buffer storage is available. Prosumers 11, 12 and 13 do not benefit from more storage volume. Since their operation during zero price hours is strongly limited to maintain voltage stability, additional volume cannot be utilized to reduce costs further and additional losses dominate the result.
Coordination for $V_0 = 1\,\text{p.u.}$ does only lead to marginal increases in costs below 1% when compared with the costs of the reference operation with the respective volume (right diagram). It must be noted that the uncoordinated reference operation with a buffer storage results in less back-up heater operation during zero prices and fewer voltage violations per se, but the lower voltage limit was still violated at certain times in all cases. The relative cost increase for $V_0 = 0.95\,\text{p.u.}$ is only 2% for prosumer 13 and even lower for the other participants when they are equipped with a small volume of 100 l. The results indicate that a small buffer volume allows to adapt operation at a low increase of costs for the scenario investigated here. The benefit of additional buffer storage volume depends on the location in the distribution grid. An uneven distribution of buffer volumes among the prosumers might be optimal from a planning perspective and a DSO could incentivize specific participants to invest in additional storage to support voltage stability.
The simulation results for building type J are not shown since they are similar to those of type

E, although at a lower level of demand due to the better insulation standard. The aggregated results are provided in Table B.2 in the Appendix.

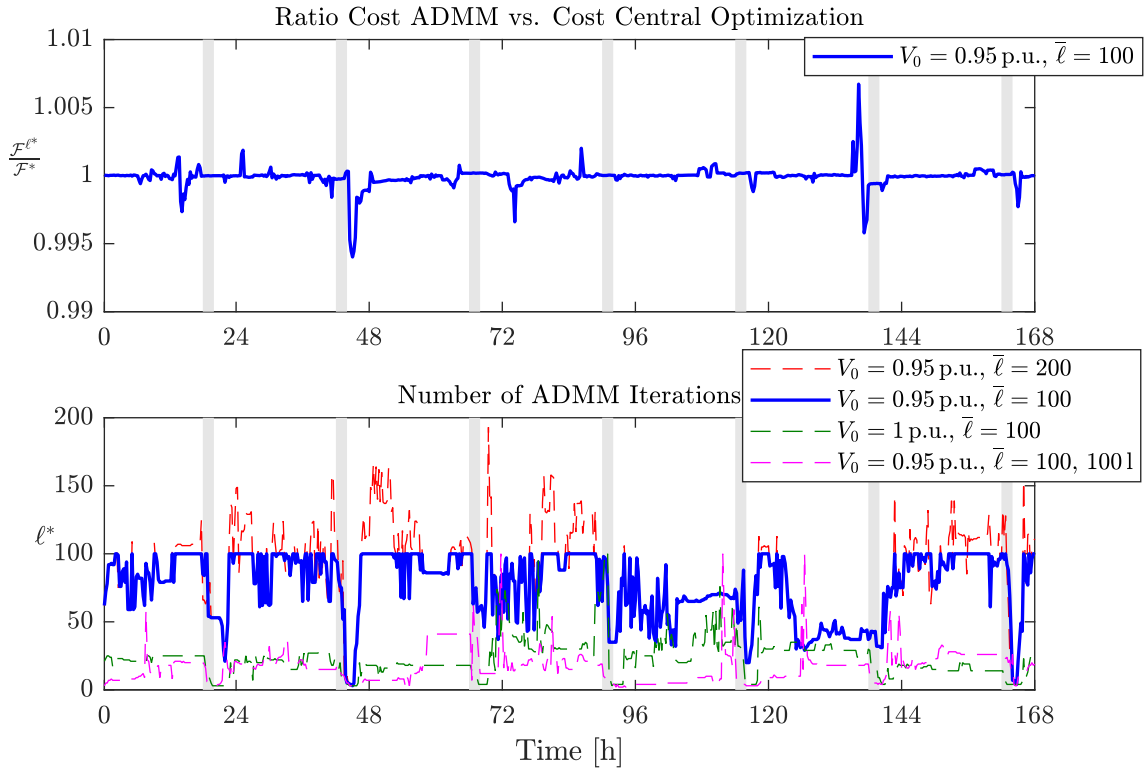

Figure 6.9: *Ratio of the objective values from ADMM ($\mathcal{F}^{\ell^*}$) and the central optimization ($\mathcal{F}^*$) at each time step over the simulation period of 7 days for building type E without the buffer and $V_0 = 0.95$ p.u. (top). ℓ^* denotes the iteration when either of the termination criteria are met. The bottom diagram shows the corresponding number of iterations required at each time step (bottom). $\rho = 0.01$ in all cases.*

Convergence

The top diagram in Figure 6.9 shows the ratio of the cost function evaluated at the last ADMM iteration and the optimal solution obtained from the central optimization at each time step over the simulated week for type E. $\mathcal{F}^{\ell^*}$ denotes the objective value of cost function (6.3) obtained via ADMM after ℓ^* iterations, $\mathcal{F}^*$ is the objective value at the optimal solution of the central optimization. The stopping criteria with $\varepsilon_{\text{prim}} = \varepsilon_{\text{dual}} = 10^{-3}\sqrt{N_P \mathcal{I}}$ and maximum iterations $\overline{\ell} = 100$ leads to costs very close to those of the central optimization, the DMPC solutions are within the range $\pm 1\%$. The small remaining difference to the central optimization can be attributed to either suboptimality or global infeasibility[5] of the last solution ℓ^*, or remaining numerical errors.
The bottom diagram shows the corresponding number of iterations required at each time step to meet the termination criteria. The scenario of $V_0 = 0.95$ p.u. requires substantial coordination, i.e. the uncoordinated residual load schedules of some prosumers have to be significantly altered to enable a global feasible operation. This is reflected in the relatively high number of iterations

[5]Since the stopping criterion requires only limited consensus between $\boldsymbol{a}_k^\ell$ and $\boldsymbol{r}_k^\ell$, the last solution might not be exactly global feasible.

Table 6.7: *Total number of iterations, average number of iterations per time step and the highest number of iterations for coordination scenarios in Rural Grid 1 and type E buildings.* $\rho = 0.01$ *in all simulations.*

	Iterations		
	total number	average	maximum
$V_0 = 0.95\,\text{p.u.}$, $\bar{\ell} = 200$	55,733	82.94	193
$V_0 = 0.95\,\text{p.u.}$, $\bar{\ell} = 100$	51,831	77.13	100
$V_0 = 0.95\,\text{p.u.}$, $\bar{\ell} = 100$, Cold-Start	53,117	79.04	100
$V_0 = 1\,\text{p.u.}$, $\bar{\ell} = 100$	15,776	23.48	100
$V_0 = 0.95\,\text{p.u.}$, $\bar{\ell} = 100$, 100 l	11,514	17.13	100

required: the maximum number of iterations $\bar{\ell} = 100$ is reached in 33% of all time steps.[6] At certain times, more iterations have to be carried out to achieve the required accuracy, as can be seen in the result for the case when the maximum iterations limit is relaxed to 200 iterations. The less restrictive scenario with $V_0 = 1\,\text{p.u.}$ requires fewer iterations most of the time. A similar situation is observed for the stricter scenario but with a 100 l buffer storage. The uncoordinated reference operation with the buffer volume already leads to almost 50 % less incidents of undervoltage[7] when compared to the scenario without a buffer. This is likely to impact the number of iterations required for coordination.

Table 6.7 shows the total number of iterations, the average and maximum number per time step for the different simulations carried out for coordination. Increasing the maximum number of iterations to 200 allows the algorithm to always reach the required accuracy within this limit, but it also results in slightly more iterations on average. Warm-starting has a positive but relatively small effect, the total number of iterations can be reduced by 2.4% for the simulated week. The average number of iterations is reduced by approximately two iterations. It is important to note that dynamic scaling of ρ can further improve the rate of convergence at each time step. Since the optimal penalty parameter may change for each time step, fixing it to a certain value will not necessarily result in the fastest implementation. Even though the 17 prosumer updates would be completely parallelized in a real-world setting, improving the speed is crucial for practical implementations. An obvious time limit is given by the control horizon, which defines for how many time steps ahead the last computed controllable inputs are used. Since only the first solution is used in the closed-loop simulation here, 15 minutes would be the maximum time window to convergence to a feasible solution.

[6] A maximum of 100 iterations per time step leads in the setting of 17 prosumers and one DSO to a worst case of $(17 + 1) \times 100 \times 96 \times 7 = 1.209.600$ optimizations to be carried out over one week with a discretization of 15 minutes.

[7] A single bus voltage violation at one time instant is counted as one incident.

6.3 Valley-Filling

The following section demonstrates the functionality of the DMPC algorithm to achieve valley-filling. The sum over the squared aggregated residual load is minimized in addition to the individual cost functions, i.e. ω in the total cost function (6.3) is no longer zero. As a result, the aggregate residual load is flattened out depending on the weighting scaled by ω. The price π for electricity is assumed to be flat. The price for usage of the temperature slack variable is increased to $M_i = 10^6$ to avoid comfort violations for a flatter profile with large ω. No PV generation is available. Results are not discussed for type J since they were similar to type E.

6.3.1 Open-loop Solutions for a Winter Day

Figure 6.10 shows the open-loop simulation results of February 10 for $\omega = 10^{-3}$ and $\omega = 1$ for 17 prosumers of type E and L in *Rural Grid 1*. The first row shows the sum of the fixed loads, the heat pumps and back-up heaters and the residual loads over all prosumers after 50 ADMM iterations. As expected, there is a strong difference between the aggregated residual load after coordination compared with the uncoordinated case. A larger ω results in a flatter profile. Operation is rescheduled to optimally add to the inflexible fixed load to avoid peak loads in the aggregated profile. This is especially well noticeable for type L, where the electricity demand for heating perfectly adds to the fixed demand without causing new peaks. The aggregated residual load after 50 ADMM iterations matches well the profile obtained from the central optimization. The second row in Figure 6.10 shows the zone temperatures of the prosumers. Stronger overheating is noticeable for building type E and $\omega = 1$ when compared with the temperature trajectories for $\omega = 10^{-3}$. The third and fourth row show the progression of the residuals over the iterations, the ratio of the total cost compared with the central optimization and the updated penalty parameter ρ. The adaptive ADMM penalty parameter scheme from [XFG17] allows to tune ρ in every other iteration and approaches its optimal value relatively fast. With arbitrary chosen $\rho^0 = 0.01$ from the previous section, the final values ρ^{50} differ depending on the problem scaling with ω. A period of a fast decrease of the residuals is followed by slower progress after a certain amount of iterations. The residuals when ρ remains fixed at 0.01 are also shown. The adaptive scheme is highly beneficial when the initial value of ρ is far away from the optimal value, see e.g. the very slow progress in the primal residuals for both building types with $\omega = 1$. The objective value $\mathcal{F}^\ell$ obtained via ADMM approaches quickly the total costs $\mathcal{F}^*$ of the solution obtained from the central optimization.
Any feasible deviation from the uncoordinated reference operation causes increased energy costs, since it is the benchmark for the lowest total energy consumption in the flat-price scenario. Thus, rescheduling the heating system for the shared goal of a flatter aggregated profile results in increased energy demands and costs of the prosumers. Figure 6.11 shows the objective values of the prosumer and shared cost functions, mean and standard deviation of the aggregated residual load and mean of each prosumer's zone temperature for different ω and building types E and L without a buffer. The open-loop results are obtained after 50 ADMM iterations with adaptive penalty parameter ρ. The total costs (here energy demands) over all prosumers increase with increasing ω but also saturate for a larger weighting factor. The increase in total electricity demand in kWh is below 1% for both building types when the case $\omega = 10^2$ is compared with the reference operation ($\omega = 0$). The largest increases in the prosumers' individual demands are 1.12% for type E and 0.46% for type L. As a larger ω puts more emphasis on minimizing the squared aggregated residual load profile, the associated objective value of cost function g_s decreases for a larger weighting factor. The second row of Figure 6.11 shows the mean and standard deviation of the aggregated profile $\sum_{i=1}^{\mathcal{I}} \boldsymbol{r}_i$. The standard deviation is reduced by over 50% for type E and by over two thirds for type L for $\omega = 10^2$, the mean of the aggregated residual load remains

almost unchanged. The operational flexibility to deviate from the reference schedule leads to a small increase below 0.5 °C of the mean temperatures of all prosumers when ω is increased for a flatter profile. A similar increase was observed for the floor temperature.

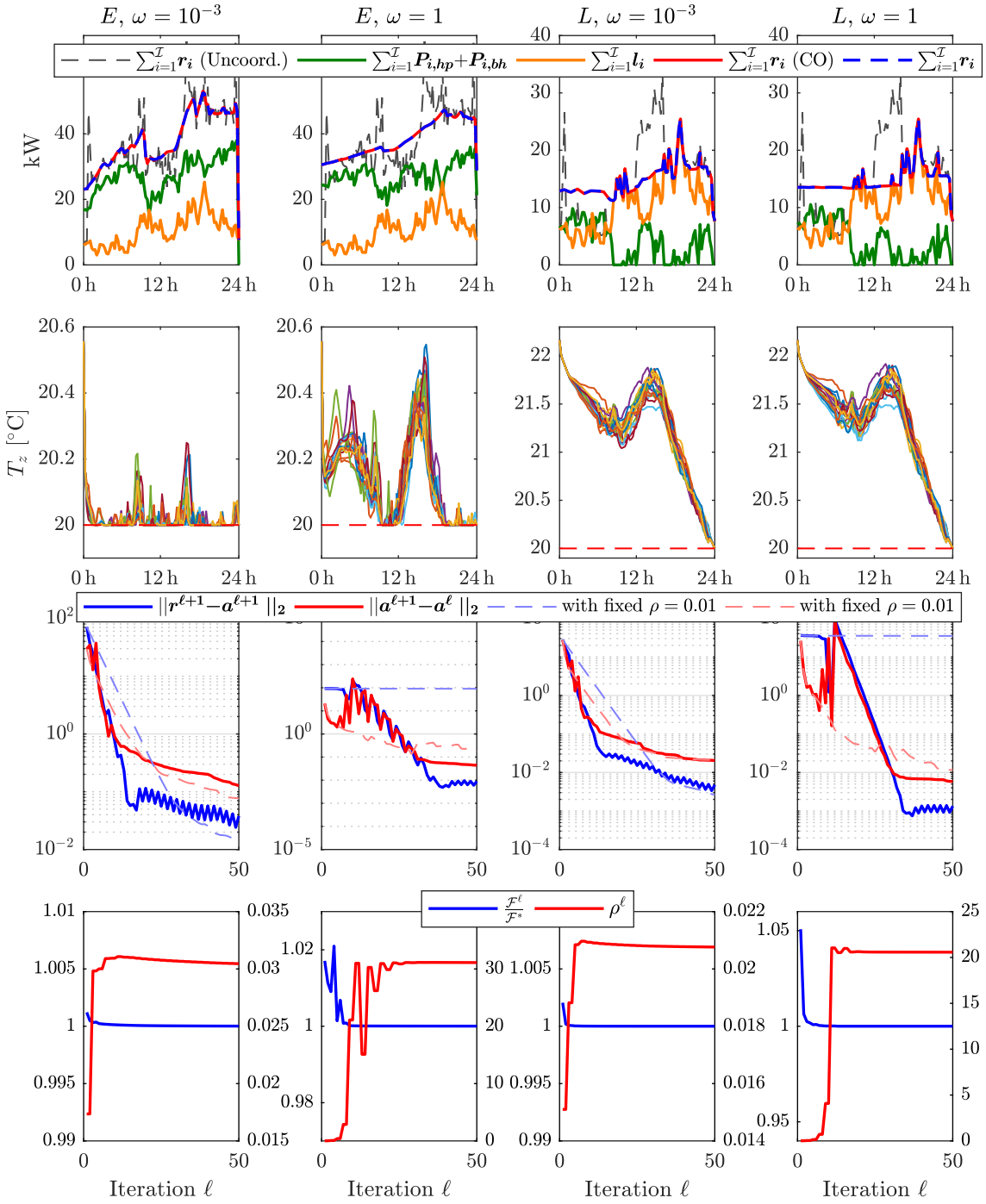

Figure 6.10: *Open-loop results for valley-filling with* $\omega = 10^{-3}$ *and* $\omega = 1$ *for 17 prosumer of type E and L. ADMM initialized with* $\rho = 0.01$.

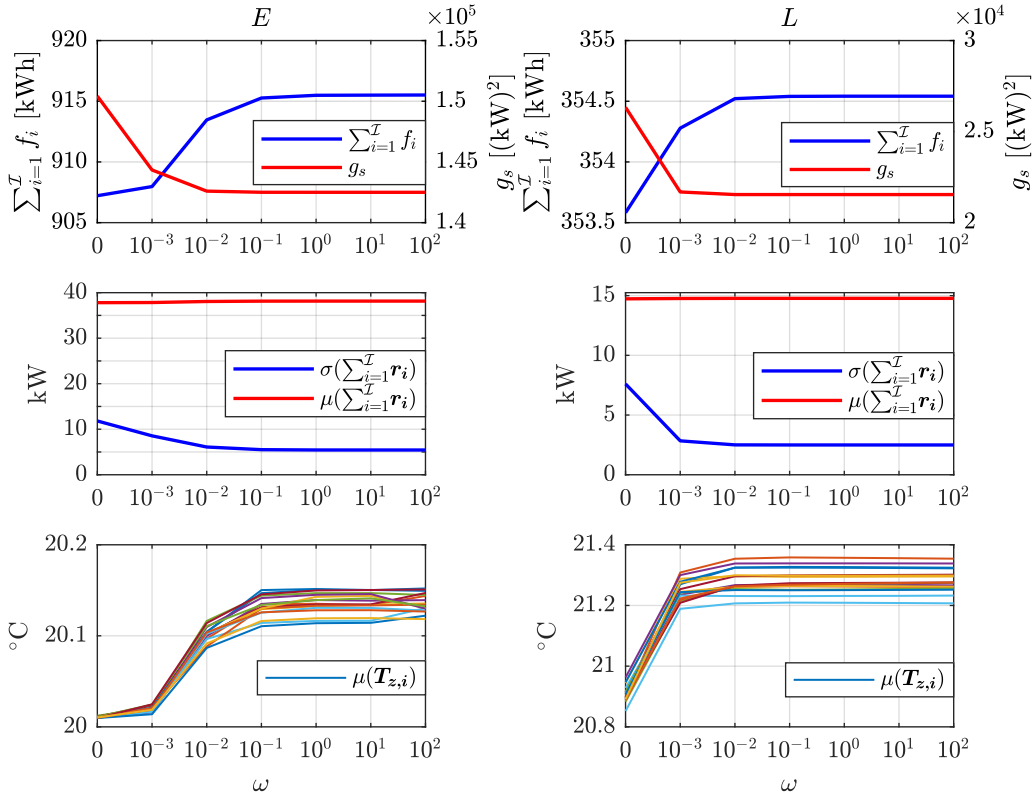

Figure 6.11: *Change in the aggregate prosumer and shared cost funtions (top), mean and standard deviation of the aggregated residual load (middle) and mean of each prosumers zone temperature for different ω and building types E and L without a buffer.*

6.3.2 Closed-loop Simulation for a Week in Winter

A closed-loop simulation run is carried out for the same week in winter as was used for the analysis on voltage stability. The simulations for both building types E and L are carried out for $\omega = 1$ and the penalty parameter is fixed to $\rho = 31$ and $\rho = 20.5$ respectively for the building types based on the values identified in Figure 6.10. The maximum number of iterations is set to $\overline{\ell} = 50$ and the stopping criteria is set to $\varepsilon_{\text{prim}} = 10^{-2}\sqrt{N_P \mathcal{I}}$ and $\varepsilon_{\text{dual}} = 10^{-2}\rho\sqrt{N_P \mathcal{I}}$. This guarantees sufficient accuracy since the coordinated operation results in line flows and bus voltages with good distance to the operational limits.

Table 6.8 shows the aggregated results of the closed-loop simulation for the reference operation with a constant flat-price and the coordinated operation for valley-filling with $\omega = 1$. The electricity demand (and thus costs) of the aggregated residual load increases only slightly to achieve a flattened profile, i.e. +1.1% for type E and +0.3% for type L. The heat pumps demand slightly more electricity, but the performance factors remain almost unchanged. The objective value of the shared cost function over the realized operation[8] decreases for both building types, which confirms the open-loop results. The objective values of the coordinated operation with $\omega = 1$ increase strongly due to the quadratic term in cost function (6.3). Inserting the realized operational schedules from the DMPC operation with ADMM and the central optimization in the total cost function yields the total costs. The objective values from ADMM are very close to those obtained from the central optimization. Valley-filling has a strong impact on the maximum and standard deviation of the aggregated residual load, e.g. the maximum peak caused by the

[8] Stated as g_s in the table with a slight abuse of notation.

prosumers of building type L is reduced by over a quarter. The resulting bus voltages are not critical and the increase in the mean temperature is moderate.
The dynamic simulation results for valley-filling for the two building types are shown in Figure 6.12 and Figure 6.13. The operation of the heat pumps is to a certain extent a mirror image of the predicted fixed load, i.e. the heat pumps are mainly operating when the fixed load is low and vice versa. It is well recognizable for building type L how the operation of the heating systems does almost not create new peaks in the aggregated residual load profile. The resulting profile is strongly flattened out when compared with the more volatile uncoordinated operation. In summary, the aggregated load at the transformer can be significantly altered in shape and volatility with only a marginal increase in the operational costs and a marginal impact on the comfort of the participants.

Table 6.8: *Aggregated electricity demands, costs, performance factor and system metrics for the uncoordinated reference operation with a flat price and for coordination of valley-filling with $\omega = 1$ for the seven days closed-loop simulation. With a slight abuse of notation, the shared costs g_s are here computed by the realized residual load schedules of the closed-loop simulation and are stated to show the composition of the total costs. Function g_s is also evaluated for the scenario when no coordination takes place (values in brackets).*

		Building type E		**Building type L**	
Coordination		No	$\omega = 1$	No	$\omega = 1$
V_0	[p.u.]	1	1	1	1
residual load	[kWh]	7815.8	7900.3 (+1.1%)	2587.4	2595.7 (+0.3%)
heat pump	[kWh]	6164.1	6249.3 (+1.4%)	913.6	921.9 (+0.9%)
back-up heater	[kWh]	4.2	3.5 (-16.7%)	26.3	26.3 (+0.0%)
fixed demand	[kWh]	1647.5	1647.5	1647.5	1647.5
g_s		(1,673,949.6)	1,550,579 (-7.4%)	(208,948)	170,019.8 (-18.6%)
Costs		7815.8	1,558,479.3	2587.4	172,615.5
Costs CO			1,558,246.4		172,495.8
PF		2.93	2.93	3.06	2.96
$\max\left(\sum_{i=1}^{\mathcal{I}} \boldsymbol{r}_i\right)$	[kW]	80.5	69.7 (-13.4%)	39.6	29.4 (-25.8%)
$\sigma(\sum_{i=1}^{\mathcal{I}} \boldsymbol{r}_i)$	[kW]	18.1	9.8 (-45.9%)	8.6	3.8 (-55.8%)
$\mu(\sum_{i=1}^{\mathcal{I}} \boldsymbol{r}_i)$	[kW]	46.5	47 (+1.1%)	15.4	15.5 (+0.6%)
$\min(\boldsymbol{V})$	[p.u.]	0.9631	0.9685	0.9815	0.9834
$\mu(\boldsymbol{T}_z)$	[°C]	20.5	20.7	21.9	22

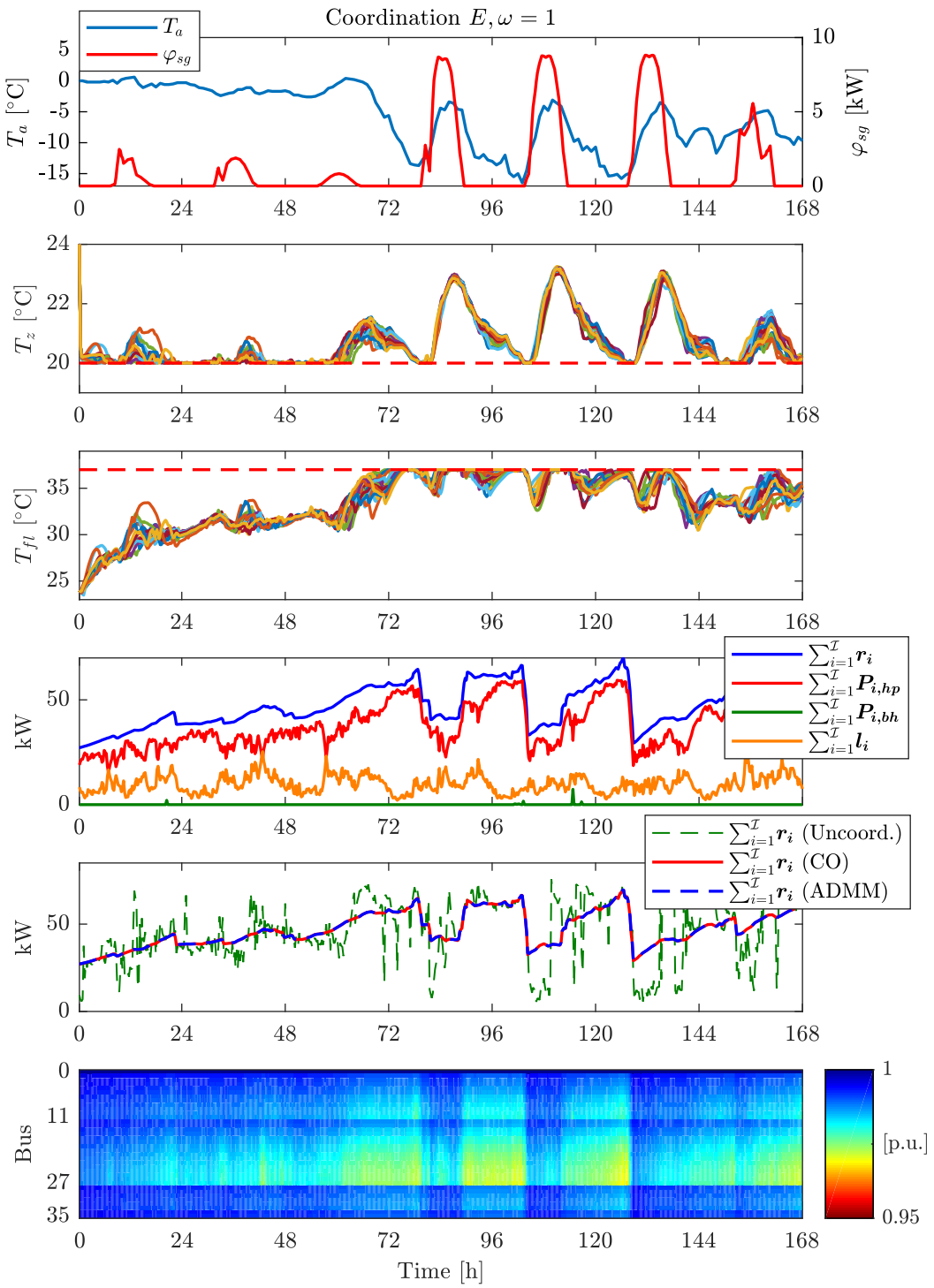

Figure 6.12: *Closed-loop results for valley-filling coordination of 17 prosumers of type E in Rural Grid 1 via the distributed MPC algorithm based on ADMM with* $\rho = 31$. *Uncoordinated reference operation (Uncoord.) and central optimization (CO) profile for comparison.*

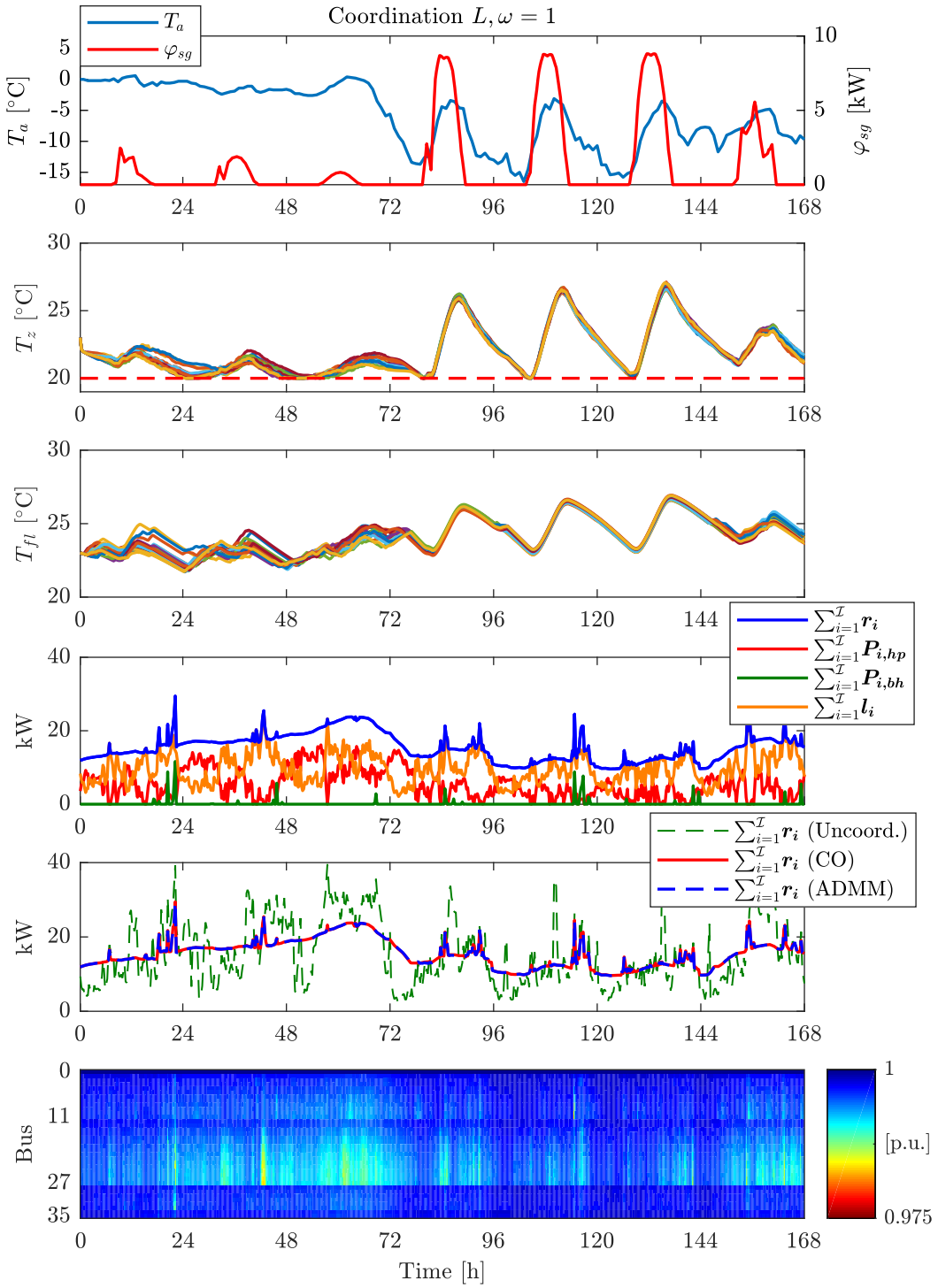

Figure 6.13: *Closed-loop results for valley-filling coordination of 17 prosumers of type L in Rural Grid 1 via the distributed MPC algorithm based on ADMM with $\rho = 20.5$. Uncoordinated reference operation (Uncoord.) and central optimization (CO) profile for comparison.*

6.4 Community Self-Consumption

The last study demonstrates the ability of the DMPC implementation to increase the consumption of local PV generation on the community level. The reference operation assumed for the study on community self-consumption remains the same as it was in the previous two studies, i.e. the reference operation is obtained by solving only the i-indexed parts in (6.3)-(6.11) consecutively to optimize individual prosumer energy costs while maintaining local feasible operation. This is achieved by each prosumer with a PV plant by consuming as much local generation as possible since PV feed-in is assumed to not be compensated. Buildings without generation minimize their individual costs by operating the heating system in the most energy efficient way. The central optimization problem for coordination to achieve minimum costs on the community level is changed to the cost function from (5.78) and extended in the constraints by (5.76)-(5.77) to account for the new optimization variable $\boldsymbol{P}_1^+$:

$$\underset{(\boldsymbol{u},\boldsymbol{r},\boldsymbol{r}^+,\boldsymbol{s},\boldsymbol{P},\boldsymbol{P}_1^+,\boldsymbol{Q},\boldsymbol{U},\boldsymbol{s}_g)}{\text{minimize}} \quad \Delta_t \boldsymbol{\pi}_k^T \boldsymbol{P}_{1,k}^+ + M_g \mathbf{1}^T \boldsymbol{s}_{g,k} + \sum_{i=1}^{\mathcal{I}} M_i \mathbf{1}^T \boldsymbol{s}_{i,k} \tag{6.19}$$

$$\text{subject to} \quad (6.4) - (6.16) \tag{6.20}$$

$$\boldsymbol{P}_{1,k}^+ \geq \mathbf{0} \tag{6.21}$$

$$\boldsymbol{P}_{1,k}^+ \geq \boldsymbol{P}_{1,k}. \tag{6.22}$$

A flat price is assumed and the community has to pay for the positive parts of the aggregated residual load transfer over the transformer, i.e. $\boldsymbol{P}_1^+$. The prosumers $\{1, 4, 5, 12, 13, 15, 16, 17\}$ located at the ends of the feeders in Figure 4.2 of *Rural Grid 1* are assumed to be equipped with PV panels of roughly 7 kW installed capacity per roof.[9] The stopping criteria from Section 6.2.2 are also used here to abort ADMM iterations.

Figure 6.14 shows the closed-loop simulation results for the seven days in winter. All buildings and prosumers participate in the coordination and are of building type E without a buffer storage. The zone and floor temperatures are kept within their limits. The floor temperatures are increased during the severe temperature drop over the night from the third to the forth day which also involves an increase in the zone temperatures. The increase in the temperatures during the following days are caused by both heating system operation and higher solar gains. The fourth plot shows how parts of the aggregated heat pump operation are located at times when PV generation occurs to reduce the community's energy costs. Back-up heaters are rarely used. The fifth subplot shows the resulting aggregated residual load profile (equivalent to $\boldsymbol{P}_1$ over the transformer) resulting from the DMPC simulation. Two further aggregated residual load profiles are plotted to demonstrate the impact of coordination. The first additional profile results from the uncoordinated reference operation without anticipation of the PV generation, i.e. buildings with a PV plant do not predict their local generation in the predictive controller and only optimize the heating system in an energy efficient way. The residual load of the prosumers is then just the post-operation subtraction of the local generation from the local total electricity demand. Local generation is only consumed when it naturally coincides in time with the local electricity demand (no PV prediction, Uncoord.). The second additional aggregated profile shows the result for the uncoordinated reference operation when local PV generation is

[9] The PV panels are south-facing and have a tilt angle of 30°. A module efficiency of 15% and a system performance ratio of 85% is assumed. The earlier chapters referred to all buildings as *prosumers* due to the general problem formulation introduced earlier to account for local generation, despite PV availability in the simulation scenarios. In the following a distinction is made between buildings with PV (*prosumers*) and those without (*buildings*).

predicted within each prosumer's MPC and the heating system operation can be adjusted with respect to the additional information (Uncoord.).

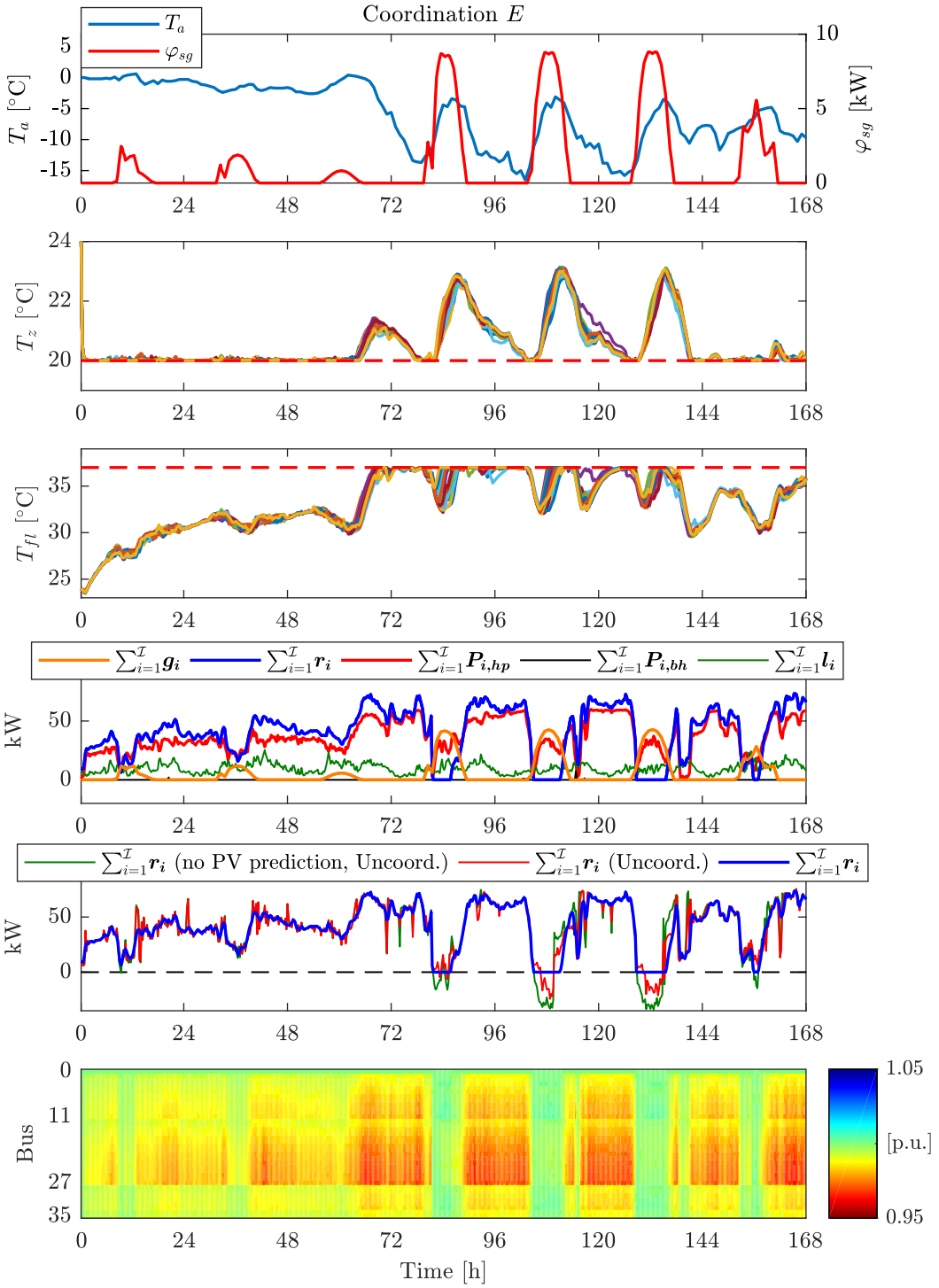

Figure 6.14: *Closed-loop results for the coordinated community cost optimization with type E buildings in Rural Grid 1 via the DMPC algorithm based on ADMM with $\rho = 0.1$. 8 buildings are equipped with a PV plant. Aggregated residual load profiles for the uncoordinated reference operation without (no PV prediction, Uncoord.) and with PV prediction (Uncoord.) for comparison.*

The resulting aggregated profiles have more spikes when the operation is not coordinated. Local anticipation of the PV prediction reduces the individual costs of the prosumers and in this case the negative residual load when compared with the aggregated residual load from the reference operation without PV prediction. The coordinated DMPC operation achieves almost always a non-negative residual load throughout the simulation by placing the heat pump operation at times of high PV generation. The bus voltages are never critical, they drop during peak load times and increase slightly at midday when PV generation peaks.
Figure 6.15 shows for day six how the operation of the individual building energy systems is adjusted to lower the aggregated costs by a better utilization of the available PV generation. Prosumer 13 is equipped with a PV plant. When no coordination takes place (Uncoord.), its heat pump operation follows the local available PV generation for the first hours until the floor temperature reaches its operational maximum for a second time. When coordination takes place, the heat pump operation is rescheduled and, especially during the first hours when PV generation is available, reduced. At the same time, building 11 without PV generation increases its heat pump operation to coincide with the PV generation of the prosumers.

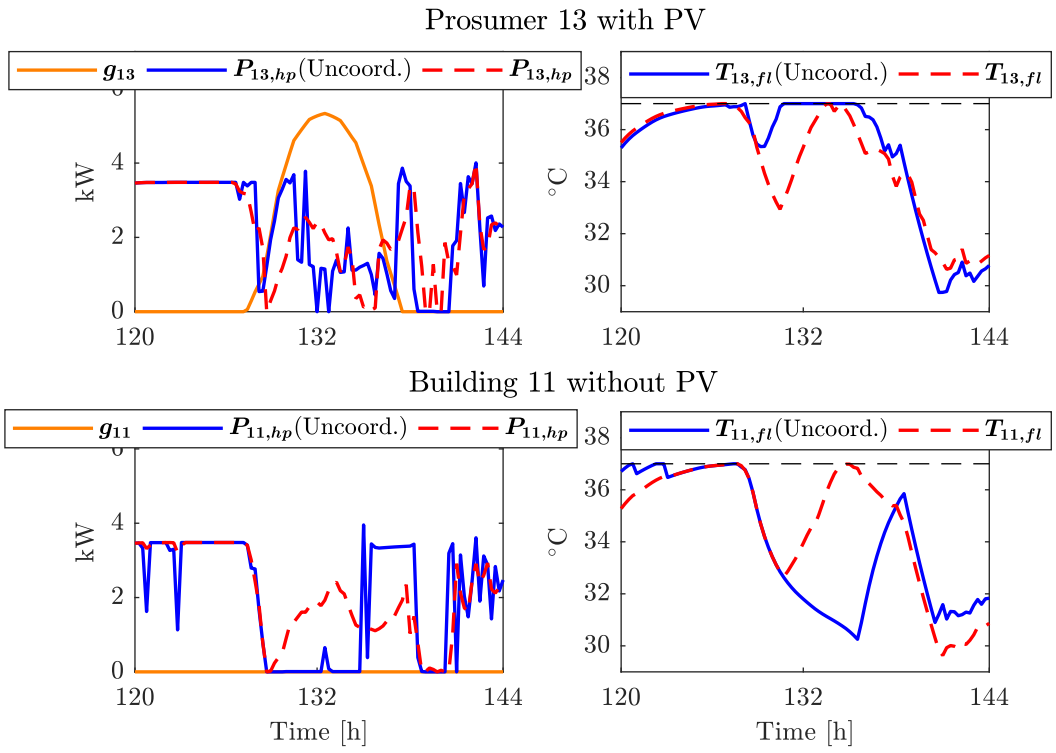

Figure 6.15: *Closed-loop simulation results for prosumer 13 equipped with PV and building 11 without PV for day six. Operation of the heat pumps from the reference operation with PV prediction (Uncoord.) and the coordinated operation via the DMPC algorithm.*

In the following, a closer look at the per building level demonstrates the impact of the three different strategies of operation: uncoordinated reference operation without PV prediction, uncoordinated reference operation with PV prediction and finally coordinated operation with PV prediction to minimize community costs. The plots in the left column of Figure 6.16 show the differences in the zone, floor, domestic hot water storage temperatures and the residual loads of each building and prosumer when the results of the uncoordinated reference operation without PV prediction are subtracted from the uncoordinated operation with PV prediction. The differences are well recognizable for days four to seven, when larger amounts of PV generation

are available. The prosumers equipped with a PV plant change their individual operation in order to minimize costs. Their residual loads are increased when PV generation starts and are reduced when the generation peak has been passed. Changed heating has a similar effect on the zone, floor and domestic hot water temperatures, which are increased when PV generation occurs. Obviously, operational changes only occur for buildings equipped with PV systems since no aggregated coordination takes place. This is changed in the right column of Figure 6.16, where the calculated differences result from subtracting the temperatures and residual loads of the reference operation with local PV prediction from the coordinated operation obtained from the DMPC algorithm. In order to optimize the community's aggregate costs by increasing the overall PV consumption, buildings without a PV plant increase their heating system operation during times when PV is available. Coordination leads to increased residual loads and temperatures when PV is available, especially well recognizable for days five and six. The prosumers with PV deviate from their individual optimal reference operation and reduce their operation during those times, which leads to the opposite effect on the temperatures and residual loads.

Table 6.9 shows the aggregated results for the community in *Rural Grid 1* for the seven days closed-loop simulation. The results are shown for building types E and L, the community's self-consumption over the simulation period T is computed as

$$\Omega = 1 - \frac{\sum_{t=1}^{T} |\min(P_1(t), 0)|}{\sum_{t=1}^{T} \sum_{i=1}^{\mathcal{I}} g_i(t)}. \tag{6.23}$$

The first columns for type E and L each show the results of the uncoordinated reference operation when PV generation is not predicted by the prosumers. Predicting local generation helps the prosumers with a PV plant to alter their operation to achieve lower costs. In this case, also the total costs measured at the transformer are reduced by 1.69% for the type E buildings (second column). The level of the community's self-consumption Ω is increased from 71% when PV is not predicted to 90% when those buildings with a PV plant predict their local generation. This can be further enhanced to a 100% self-consumption of all local PV generation when coordination is carried out with the DMPC algorithm. The costs are reduced by 2.3%. The minimum residual load peak over the transformer is drastically reduced when coordination takes place.

The community's costs can be reduced by 5.2% when type L buildings with a lower heating demand are coordinated. This indicates the high flexibility of the systems to alter operation. The additional back-up heater operation is used for both space-heating and domestic hot water and results in a lowered performance factor. The community's self-consumption is increased from 65% to 83%, leaving some remaining PV generation which cannot be integrated due to the overall lower heating demands of the buildings. In contrast to the case of building type E, coordination has no effect on the minimum residual load peak over the transformer.

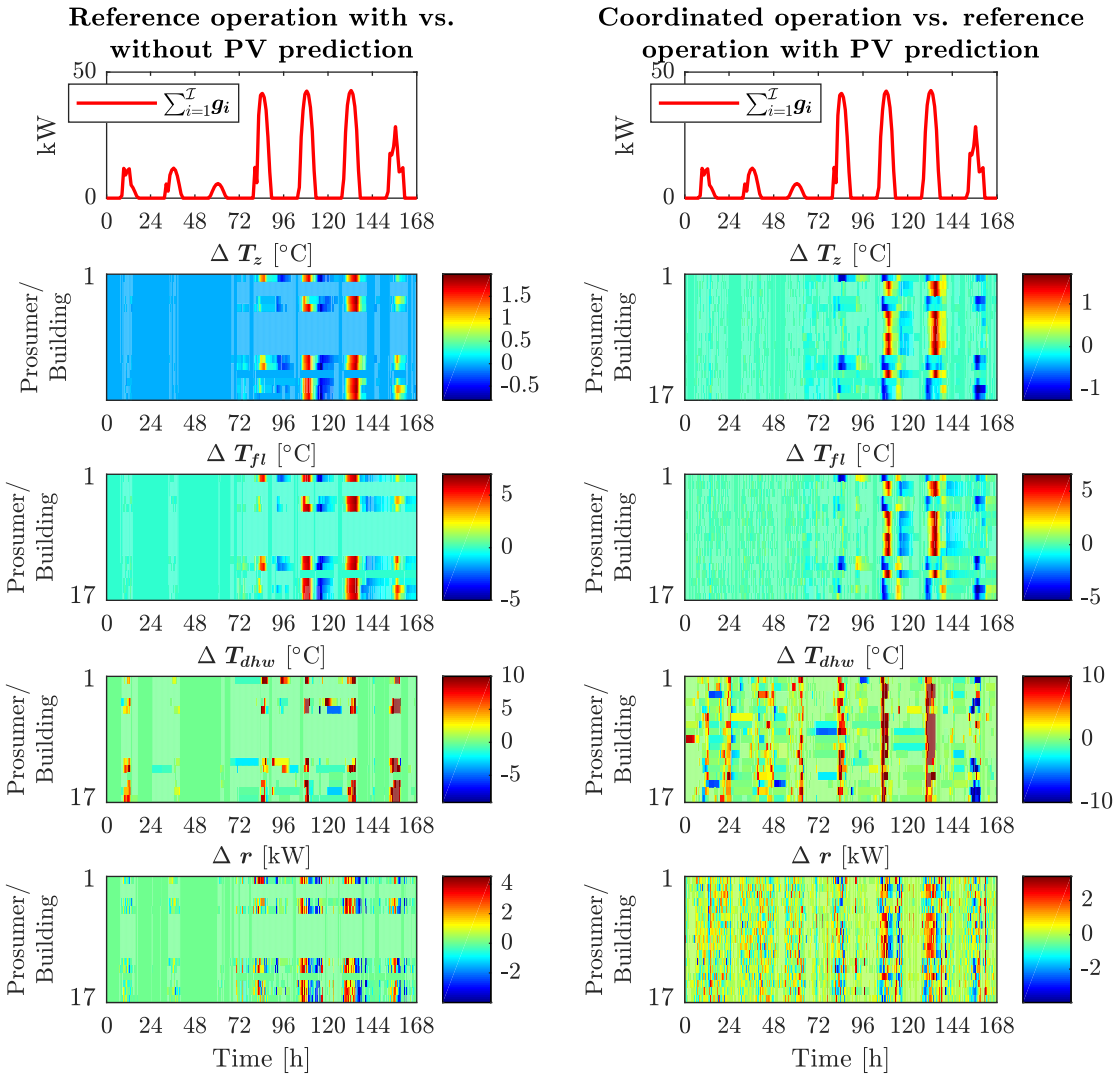

Figure 6.16: *Per time step differences between the temperatures and residual loads of the uncoordinated reference operation with and without PV prediction (left column) and the coordinated DMPC operation and the uncoordinated reference operation with PV prediction (right column) over all buildings and prosumers over the seven simulated days.*

Table 6.9: *Aggregated electricity demands, costs, performance factors, levels of self-consumption and system metrics for the uncoordinated reference operation without PV prediction, with PV prediction and for coordination to achieve minimum costs of the community by increasing self-consumption for the seven days closed-loop simulation. Percentage change with respect to the case without coordination and with PV prediction. All costs measured at the transformer.*

		Building type E			**Building type L**		
Coordination		No	No	Yes	No	No	Yes
PV prediction		No	Yes	Yes	No	Yes	Yes
cum. demand	[kWh]	6742.9	6828.6	6773.1(-0.8%)	1514.6	1622.4	1709.4(+5.4%)
heat pump	[kWh]	6164.1	6165.3	6194.6(+0.5%)	913.6	858	829.9(-3.3%)
back-up heat.	[kWh]	4.2	88.7	3.9(-95.6%)	26.3	189.8	304.9(+60.6%)
fixed demand	[kWh]	1647.5	1647.5	1647.5	1647.5	1647.5	1647.5
PV	[kWh]	1072.9	1072.9	1072.9	1072.9	1072.9	1072.9
Costs		7052.1	6932.6	6773.2(-2.3%)	1931.1	1995.5	1891.6(-5.2%)
Costs CO				6769.9			1906.8
PF		2.93	2.9	2.93	3.06	2.76	2.58
Ω		0.71	0.9	1	0.61	0.65	0.83
$\max(\boldsymbol{P}_1)$	[kW]	75.4	75.4	73.3	39.2	40.5	38.9
$\min(\boldsymbol{P}_1)$	[kW]	-34.3	-24.3	-0.1	-33.4	-33.4	-33.4

6.5 Conclusion

The three simulation studies on voltage stability, valley-filling and community cost reduction through optimized PV self-consumption have demonstrated the mechanism and effectiveness of the DMPC algorithm to coordinate the operation of prosumers or building energy management systems in distribution grids. Medium sized *Rural Grid 1* was chosen to simplify the analysis of the simulation results.

A time-varying price scenario was introduced to cause undervoltages in the study on voltage stability. While the uncoordinated reference operation of 17 older and weaker insulated buildings of type E already caused undervoltages below 0.9 p.u. for a slack bus voltage of $V_0 = 1$ p.u. during the zero price hours, modern buildings of type L caused undervoltages only for a lower slack bus voltage level such as $V_0 = 0.95$ p.u.. The DMPC algorithm managed to reschedule the operation of the prosumers to avoid voltages below 0.9 p.u., while it maintained individual temperature bounds and operational limits of the heating systems of all participants. The open-loop solutions computed with the distributed optimization of ADMM matched those obtained from a reference central optimization. The closed-loop simulation results showed that coordination to maintain voltage stability led to a minimal to moderate increase of the total costs, i.e. +3.8% for type E and +3.4% for type L in the restrictive scenario with $V_0 = 0.95$ p.u.. The per prosumer cost increase was significantly higher for those participants connected to the most critical buses and feeder, i.e. where the residual load profiles had to be altered most to prevent undervoltage. As an example, DMPC coordination for feasible distribution grid operation led to a cost increase of 11.4% over the simulated week for the prosumer located at the end of the longest feeder. The use of additional buffer storage volumes led to an increase in costs per prosumer for the less restrictive scenario of $V_0 = 1$ p.u., due to the fact that additional storage losses overcompensated benefits of additional operational flexibility. In contrast, prosumers who faced the strongest undervoltages benefitted the most from a buffer storage volume in the stricter scenario with $V_0 = 0.95$ p.u.. The worst cost increase among the prosumers was reduced by 25% in the closed-loop simulation. The results indicate that buffer storages might be a reasonable investment to support voltage stability at the end of long feeders when older buildings dominate the distribution grid.

The number of necessary iterations to meet specific stopping criteria in order to guarantee feasible and close to global optimal solutions in the closed-loop DMPC simulations varied depending on the scenario and required accuracy. A smaller voltage band required more coordination and thus significantly more iterations to meet the stopping criteria, i.e. a tripling from $V_0 = 1$ p.u. to $V_0 = 0.95$ p.u.. The type E prosumers and DSO had to solve their optimization problems and exchange the communication variables for 77 times on average at each time step in the latter scenario.

The second study demonstrated how the DMPC algorithm coordinates the operation of the prosumers towards a flatter aggregate residual load, which results in a less volatile power flow over the transformer. In a single shot open-loop simulation, the standard deviation of the aggregated residual load decreased with an increasing weighting factor ω, while both the total electricity costs of the prosumers and the mean zone temperatures increased moderately. The operation of the heating systems deviated from the energy efficient uncoordinated reference operation in order to optimally add the heat pump and back-up heater loads to the non-flexible fixed electricity demand to flatten out the aggregated residual load. The total cost increase for $\omega = 10^2$ compared to the uncoordinated scenario was below 1% for both building types E and L, while the standard deviation of the aggregated residual load was reduced by over 50% and over two thirds, respectively. A closed-loop simulation over seven days with $\omega = 1$ confirmed the moderate increase in electricity costs observed in the open-loop results. The peak load over the transformer was

reduced by 13.4% (25.8%) and the standard deviation of the aggregated residual load reduced by 45.9% (55.8%) for type E (L). To conclude, a community's aggregated residual load profile can be modified significantly at a relatively low cost increase.
The third study on optimization of community costs by better self-consumption of local PV generation showed the effectiveness of the DMPC algorithm to coordinate the operation of buildings without PV together with prosumers equipped with a PV plant. While only the prosumers optimized their operation with respect to their local PV generation in the uncoordinated scenario, the DMPC coordination rescheduled buildings and prosumers based on the communicated residual loads so that the joint operational costs at the transformer were minimal. The total costs of the building type E community were reduced by 2.3% compared to the uncoordinated scenario. The aggregate residual load, i.e. the power flow over the transformer, was almost always larger or equal zero. Assuming buildings of type L resulted in a cost reduction of 5.2%. The community's self-consumption was increased from 90% to 100% for the type E scenario and from 65% to 83% for the type L scenario. In the latter case the maximum self-consumption was limited by the low heating demand of the buildings.

Chapter 7

Conclusion and Outlook

This chapter summarizes the main contributions of this thesis and draws a conclusion based on the presented models and simulation studies. An outlook provides input for future research directions based on the limitations of this work.

7.1 Conclusion

In order to demonstrate how the operational flexibility of prosumers can be exploited to achieve minimum costs of operation while guaranteeing feasible distribution grid operation, a thermal building model was developed to represent the dynamics of residential SFHs. Chapter 2 first provided an introductory overview of the German residential building stock and potential future heat pump penetration scenarios in order to reduce the selection of representative building parameterizations for the subsequent modeling tasks. While heat pumps already have a high share in new built SFHs, gas-based heating systems dominate in older buildings with usually poor thermal insulation. An investigation of different penetration scenarios has shown that in addition to installations in modern buildings, heat pumps in older buildings will have a significant share in all scenarios and years until 2050, assuming current refurbishment rates and investment choices change. The three building types E, J and L with thermal characteristics defined in the TABULA typology were selected to represent the possible range from rather weakly refurbished buildings (E) to advanced modern constructions (L). It was further assumed that all variants could be heated by a heat pump and a floor heating system. The three different types were not only selected to be able to test the worst and best case impact on a distribution grid, but also to verify the transferability of the generalized thermal building model for different parameterizations.
A single zone RC-modeling approach proved to be sufficiently accurate to predict the zone temperature, the most important state of the thermal building model in order to track thermal comfort. Different linear fourth-order models of varying complexity were validated for types J and L against a dynamic reference simulation in EnergyPlus. While the zone temperature was already well approximated with the simplest model, accurate tracking of temperatures of components of the structural thermal mass required to model the radiative heat transfer between the heated floor and outer walls. In a cross-validation over different simulation periods, a RMSE below 1 °C was achieved with such a model for all temperature states in building L and all but the inner wall temperature for building J for all considered simulation periods. The final model chosen did not only have a high accuracy to approximate the zone and floor temperatures based on a given heating system power profile and disturbances, but the model also led to reasonable close power profile and energy demand predictions when used for that purpose. The thermal building model was then extended by a heat pump model, parameterized for each of the three building types, a back-up heater and an optional buffer storage model. A DHW model and an internal gains model were the final contributions in order to represent the whole range of thermal

systems and disturbances relevant for the residential prosumer model. In Chapter 3 all models and disturbances were brought together and a model predictive controller for prosumer energy management designed. The chosen modeling approach results in two convenient features: Firstly, the complete low-order thermal model approximates the most important dynamics of the structural thermal mass and the water storages and includes the dominant disturbances affecting the thermal processes. This is achieved with a model of low complexity, which requires a relatively low parameterization effort from the user and allows to use the model to upscale to aggregations of prosumers considered in neighborhood and distribution grid studies. Secondly, the model is well applicable in the distributed control studies of this thesis, since it is linear and results in a convex optimization problem. The problem can be solved efficiently with standard solvers and is usable in distributed optimization without loosing guarantee of convergence.
In line with this, a relaxed linear power flow approximation was reviewed in Chapter 4 to approximate the non-convex AC power flow equations. A validation study for five German reference distribution grids showed acceptable bus voltage errors below 0.005 p.u. when the coincident demand at all load buses was increased to the first violation of grid constraints. Depending on the distribution grid, a too high coincident demand led to either a voltage violation at the longest feeder or to exceedance of the apparent power flow limit at the transformer. Larger grids, i.e. grids with more load buses and longer feeders showed violations for a lower level of coincident demand.
A distributed model predictive controller for the optimal coordination of prosumers in distribution grids was designed based on ADMM for the decomposition and distributed optimization of the central optimization problem in Chapter 5. After an initial problem formulation for coupled linear time-invariant dynamic systems, the formulation was adapted to the context of this thesis and the above thermal and electrical models combined. The formulation was further extended to guarantee global feasibility of the problem in order to make the algorithm robust for multi-period simulations with varying boundary conditions. The hierarchical DMPC algorithm coordinates consensus between prosumers and a DSO while preserving data privacy. The exchange of information is limited to the sharing of predicted and desired residual load profiles and dual variables. Local cost functions and local system knowledge of the prosumers is not shared with the DSO. Cost functions handled by the DSO and the distribution grid model are not revealed to the prosumers. The DSO's optimization problem grows only with respect to the incorporation of an additional residual load vector for a prosumer in his problem statement, otherwise it is independent of subsystem complexity and internal changes. ADMM was chosen for the distributed optimization since it is guaranteed to converge to a global optimal solution for convex problems and does not depend on the choice of the penalty parameter. Even though ADMM is often claimed to progress fast to approximate solutions, high accuracy solutions may require many iterations. The choice of the penalty parameter has a significant impact on the algorithm's speed and a dynamic scaling procedure from the literature was applied to the problem and selectively used in the later simulation studies. This helped to identify a good choice of the penalty parameter in order to speed up simulations.
Three simulation studies were carried out in Chapter 6 to demonstrate the effectiveness of the DMPC algorithm to coordinate the utilization of operational flexibility offered by the prosumers. Simulation studies on voltage stability, valley-filling and community PV self-consumption in a rural grid of moderate size were carried out over winter days for the different building types assuming perfect predictions. A time-varying price scenario was introduced to cause undervoltages during two zero price hours per day in the study on voltage stability, since a flat price scenario did not result in voltage violations. While the uncoordinated reference operation of 17 weaker insulated type E and type J buildings caused undervoltages below 0.9 p.u. for a slack bus voltage of $V_0 = 1$ p.u., modern buildings of type L caused undervoltages only in a more

restrictive scenario with $V_0 = 0.95\,\text{p.u.}$. The main reason for undervoltages was the use of back-up heaters to exploit low prices. The DMPC algorithm managed to reschedule the operation of the prosumers to avoid the undervoltages and simultaneously maintained individual comfort temperature bounds and operational limits of the heating systems of all participants. Results of the closed-loop simulation over one week indicated a minimal to moderate increase of the total costs, i.e. +3.8% for type E and +3.4% for type L in the restrictive scenario $V_0 = 0.95\,\text{p.u.}$. Participants connected to the most critical buses and feeder, i.e. where the residual load profiles had to be altered the most to prevent undervoltages, faced an above average per prosumer cost increase. Those prosumers could reduce the required cost increase with additional buffer storage volume in the restrictive scenario. The number of necessary iterations to meet the problem specific stopping criteria in order to guarantee feasible and close to global optimal solutions in the closed-loop DMPC simulations varied depending on the scenario and required accuracy. A smaller voltage band required more coordination and thus significantly more iterations.
The second simulation study demonstrated how the DMPC algorithm coordinates the operation of the prosumers towards valley-filling in order to achieve a less volatile aggregated electricity demand profile. During coordination with DMPC the operation of the heating systems deviated from the energy efficient uncoordinated reference operation in order to optimally add the heat pump and back-up heater loads to the non-flexible fixed electricity demand. The resulting total cost increase due to efficiency losses was low for a predefined weighting of the shared cost function against the local cost functions of the prosumers. A closed-loop simulation over seven days showed that the peak load over the transformer was reduced by 13.4% (25.8%), the standard deviation of the aggregated load reduced by 45.9% (55.8%), while the total cost increased by 1.1% (0.3%) for type E (L). The community's aggregated residual load profile was modified significantly at a relatively low cost increase.
The last study applied the DMPC algorithm to coordinate a community cost minimization through optimized self-consumption of local PV generation. While prosumers equipped with PV plants only optimized their operation with respect to their local PV generation in the uncoordinated scenario, the DMPC coordination rescheduled buildings without PV and prosumers based on the communicated residual loads so that the joint costs were minimal. This led to a total cost reduction by 2.3% for a building type E community and a reduction by 5.2% for type L buildings in a closed-loop DMPC simulation over seven days. The community's self-consumption was increased from 90% to 100% for type E scenario and from 65% to 83% for the type L scenario. The low heating demand of type L limited higher rates of self-consumption.

7.2 Outlook

An outlook for future directions of research is given with respect to possible improvements in modeling, the extension of studies and contributions to enable integration with electricity market processes.

7.2.1 Model Limitations

Every model developed in the course of this thesis is a simplification of the respective process or system in order to reduce complexity and to maintain certain mathematical properties for application in convex optimization. A strong simplification is involved in the representation of on- and off-switching systems as systems with a continuous operational range in order to avoid binary decision variables. This concerns back-up heaters and minimum power constraints of modulating heat pumps. Rounding procedures are a simple way to derive control signals from the solutions of the relaxed problem but may jeopardize feasibility on both the local and global system level.

One could also formulate the prosumer problems as mixed-integer quadratic problems and just observe how ADMM behaves. ADMM can be applied to non-convex problems but convergence is no longer guaranteed.
Improved modeling techniques might also be useful for the water storages. DHW and buffer storages were modeled each by a uniform temperature distribution via a single ordinary differential equation. Modeling multiple temperature layers seems necessary for larger volumes and might be of great importance in studies were the focus is on the flexible operation of water storages. Multi-layer formulations lead to bilinear terms of decision variables and require special treatment. McCormick envelopes have already been applied by the author in a separate study in order to relax the nonlinearity, validation of the approach requires simulation of a nonlinear reference model and is beyond the scope of this thesis.
Finally, an extension to a three-phase distribution grid model will be helpful to understand the impact of heat pumps in unbalanced grids. A lossy power flow model might be a reasonable extension to put the often moderate cost increase of the prosumers in perspective to the change in grid losses.

7.2.2 Extension of Studies and Testing

All simulation studies assumed perfect predictions, but real-world grid operation faces multiple sources of uncertainty. This concerns electricity demand predictions for small aggregations of households and prosumers will only have limited capabilities to accurately predict their electrical load, occupancy and domestic hot water demand. This motivates the application of methods to robustify the coordinated dispatch. Studies on voltage stability should further investigate how advanced reactive power control of PV inverters can be utilized to provide voltage support in combination with DSM. The previous studies have shown that DSM with thermal systems affects energy consumption and thermal comfort. Even though the effects might be small, DSM has to compete against options of nearly cost-free inverter control. Finally, a further extension of a DMPC algorithm should incorporate electric vehicle charging as another threat to grid operation.
In order to facilitate the use of distributed control concepts in future energy systems, algorithms have to be adapted and tested on real systems. This concerns a proper identification of all systems involved, since their models are a key ingredient in MPC. In the context of this thesis, it is worth repeating that the simplified thermal building models have been validated for standard operation. Whether the models provide an accurate response of the systems over the full range of possible control signal frequencies requires further system identification with the help of measurements.
Experimental tests of the distributed control strategy in a laboratory environment will provide insight into how the algorithm can be applied on real systems with possibly even stronger hardware restrictions. This concerns communication delays in iterative schemes of distributed optimization, limited processor and memory capabilities of (micro)controllers and thus specific solving techniques for convex optimization problems on embedded systems. A first version of the DMPC algorithm of this thesis was successfully tested on a network of three Raspberry Pis in a master's thesis project in preparation for possible further applications in TUM's *Center for Combined Smart Energy Systems* (CoSES). In the end, a rather complex solution like the DMPC algorithm has to compete with simpler and completely decentralized solutions, which also might be capable to solve specific coordination problems.

7.2.3 Market Process Integration

A two-way communication infrastructure between the prosumers and the DSO is required in order to enable a DMPC procedure, i.e. smart meter gateways must process and communicate

communication variables. This goes beyond the capabilities defined in the German "Smart Grid Ready Label" for heat pumps.
Coordination with respect to distribution grid limits might not be required at each time step during operation, depending on the type of grid and level of electric heat pump and vehicle penetration. Since the MPC solutions of two consecutive time steps will often not differ too much from one another, it might be possible to limit the coordination to a day-ahead procedure with security margins, followed by uncoordinated operation of the prosumers with respect to previously defined limits.
A further aspect addresses the integration of coordination schemes like presented in this thesis with existing competitive market processes. The DMPC algorithm is a cooperative mechanism which requires exact implementation and execution of the procedure of ADMM at the prosumer and DSO levels in order to find the optimal solution jointly. Compliance with the ADMM updates and truthful communication of the local temporary solutions is necessary to converge to a global optimal feasible solution and must be ensured or incentivised. On the other hand, local grid congestion and voltage band violations might not be solvable in a competitive market setting, since often only few participants can effectively mitigate the issues, leaving little bargaining power to the DSO. In order to guarantee safe grid operation, the DSO should be given a right to enforce feasible operation as a last resort.

Bibliography

[AH16] Ercan Atam and Lieve Helsen. Control-Oriented Thermal Modeling of Multizone Buildings: Methods and Issues: Intelligent Control of a Building System. *IEEE Control Systems*, 36(3):86–111, 2016. doi:10.1109/MCS.2016.2535913.

[AHH12] P. B. Andersen, J. Hu, and K. Heussen, editors. *Coordination Strategies for Distribution Grid Congestion Management in a Multi-Actor, Multi-Objective Setting: 14 - 17 Oct. 2012, Berlin, Germany*, Piscataway, NJ, 2012. IEEE.

[AHP12] A. Arteconi, N. J. Hewitt, and F. Polonara. State of the art of thermal storage for demand-side management. *Applied Energy*, 93:371–389, 2012. doi:10.1016/j.apenergy.2011.12.045.

[AHW+17] Thomas Auer, Thomas Hamacher, Ulrich Wagner, Dennis Atabay, Manuel de Borja-Torrejón, Rita Dornmair, Philipp Kuhn, Johannes Maderspacher, Florian Sänger, Johanna Laenge, and Jonathan-Leon Finkbeiner. Gebäude als intelligenter Baustein im Energiesystem. Lastmanagement-Potenziale von Gebäuden im Kontext der zukünftigen Energieversorgungsstruktur in Deutschland. *Endbericht, Technische Universität München*, 2017. doi:10.14459/2017MD1378336.

[AKG09] D. Arasteh, C. Kohler, and B. Griffith. Modeling Windows in Energy Plus with Simple Performance Indices. *Technical Report, Lawrence Berkeley National Lab. (LBNL), Berkeley*, 2009. doi:10.2172/975375.

[And12] Göran Andersson. Power System Analysis: Lecture 227-0526-00. *ITET ETH Zürich*, 2012.

[APB+16] Alessia Arteconi, Dieter Patteeuw, Kenneth Bruninx, Erik Delarue, William D'haeseleer, and Lieve Helsen. Active demand response with electric heating systems: Impact of market penetration. *Applied Energy*, 177:636–648, 2016. doi:10.1016/j.apenergy.2016.05.146.

[Arn16] M. P. Arnold. Integration of Residential Distributed Generators and Heat Pumps into the Low Voltage Grid from a Voltage Level Perspective. *Dissertation, Technische Universität Dortmund*, 2016. doi:10.17877/DE290R-17232.

[Aro14] J. Arold. Perspektiven von Strom zur Wärmeerzeugung in Niedrigstenergiegebäuden. *Dissertation, Universität Stuttgart*, 2014.

[BASB12] Benjamin Biegel, Palle Andersen, Jakob Stoustrup, and Jan Bendtsen. Congestion Management in a Smart Grid via Shadow Prices. *IFAC Proceedings Volumes*, 45(21):518–523, 2012. doi:10.3182/20120902-4-FR-2032.00091.

[BB10] Alberto Bemporad and Davide Barcelli. Decentralized Model Predictive Control. In Alberto Bemporad, Maurice Heemels, and Mikael Johansson, editors, *Networked Control Systems*, pages 149–178. Springer London, London, 2010. URL: https://doi.org/10.1007/978-0-85729-033-5_5.

[BBM15] Francesco Borrelli, Alberto Bemporad, and Manfred Morari. *Predictive control for linear and hybrid systems*. Cambridge University Press, Cambridge and New York and Port Melbourne, 2015.

[BCC+11] Radu Břlan, Joshua Cooper, Kuo-Ming Chao, Sergiu Stan, and Radu Donca. Parameter identification and model based predictive control of temperature inside a house. *Energy and Buildings*, 43(2):748–758, 2011. doi:10.1016/j.enbuild.2010.10.023.

[BDE19] BDEW Bundesverband der Energie- und Wasserwirtschaft e.V. Technische Anschlussbedingungen TAB 2019 für den Anschluss an das Niederspannungsnetz. 2019.

[BDI18] BDI. Klimapfade für Deutschland. *Federation of German Industries e. V.*, 2018.

[Beu36] L. Beuken. *Wärmeverluste bei periodisch betriebenen Öfen: Eine neue Methode zur Vorausbestimmung nicht-stationärer Wärmeströmungen*. Triltsch u. Huther, Berlin, 1936.

[BFG+16] Philipp Braun, Timm Faulwasser, Lars Grüne, Christopher M. Kellett, Steven R. Weller, and Karl Worthmann. Hierarchical Distributed ADMM for Predictive Control with Applications in Power Networks. *Preprint Universität Bayreuth*, 2016. URL: https://epub.uni-bayreuth.de/3043/.

[BFG+18] Philipp Braun, Timm Faulwasser, Lars Grüne, Christopher M. Kellett, Steven R. Weller, and Karl Worthmann. Hierarchical distributed ADMM for predictive control with applications in power networks. *IFAC Journal of Systems and Control*, 3:10–22, 2018. doi:10.1016/j.ifacsc.2018.01.001.

[BG16] Mohammadhafez Bazrafshan and Nikolaos Gatsis. Decentralized Stochastic Optimal Power Flow in Radial Networks with Distributed Generation. *IEEE Transactions on Smart Grid*, pages 1–15, 2016. doi:10.1109/TSG.2016.2518644.

[BGHL16] Kyri Baker, Junyao Guo, Gabriela Hug, and Xin Li. Distributed MPC for Efficient Coordination of Storage and Renewable Energy Sources Across Control Areas. *IEEE Transactions on Smart Grid*, 7(2):992–1001, 2016. doi:10.1109/TSG.2015.2512503.

[Bia06] Mikael Andreas Bianchi. Adaptive modellbasierte prädiktive Regelung einer Kleinwärmepumpenanlage. *Dissertation, Eidgenössische Technische Hochschule ETH Zürich, Nr. 16892*, 2006.

[BKF+14] J. Büchner, J. Katzfey, O. Flörcken, A. Moser, H. Schuster, S. Dierkes, T. van Leuuwen, L. Verheggen, M. Uslar, and M. van Amelsvoort. *Moderne Verteilernetze für Deutschland (Verteilernetzstudie): Studie im Auftrag des Bundesministeriums für Wirtschaft und Energie (BMWi): Forschungsprojekt Nr. 44/12*. 2014.

[BKHB17] T. Beck, H. Kondziella, G. Huard, and T. Bruckner. Optimal operation, configuration and sizing of generation and storage technologies for residential heat pump systems in the spotlight of self-consumption of photovoltaic electricity. *Applied Energy*, 188:604–619, 2017. doi:10.1016/j.apenergy.2016.12.041.

[BLHP09] Antonella Battaglini, Johan Lilliestam, Armin Haas, and Anthony Patt. Development of SuperSmart Grids for a more efficient utilisation of electricity from renewable sources. *Journal of Cleaner Production*, 17(10):911–918, 2009. doi:10.1016/j.jclepro.2009.02.006.

[BMU14] BMU. Aktionsprogramm Klimaschutz 2020. Eckpunkte des BMUB. *Bundesministerium für Umwelt, Naturschutz und nukleare Sicherheitgie (BMBU)*, 2014.

[BMW18] BMWi. Energieeffizienz in Zahlen. Entwicklungen und Trends in Deutschland 2018. *Bundesministerium für Wirtschaft und Energie (BMWi)*, 2018.

[BMW19] BMWi. Erneuerbare Energien in Zahlen. Nationale und internationale Entwicklung im Jahr 2018. *Bundesministerium für Wirtschaft und Energie (BMWi)*, 2019.

[BOB+13] K. Bettgenhäuser, M. Offermann, T. Boermans, M. Bosquet, J. Grözinger, B. von Manteuffel, and N. Surmeli. Heat Pump Implementation Scenarios until 2030: An analysis of the technology's potential in the building sector of Austria, Belgium, Germany, Spain, France, Italy, Sweden and the United Kingdom. *ECOFYS*, 2013.

[BPC+10] Stephen Boyd, Neal Parikh, Erik Chu, Borja Peleato, and Jonathan Eckstein. Distributed Optimization and Statistical Learning via the Alternating Direction Method of Multipliers. *Foundations and Trends® in Machine Learning*, 3(1):1–122, 2010. doi:10.1561/2200000016.

[Bra16] Philipp Braun. Hierarchical distributed optimization and predictive control of a smart grid. *Dissertation, Universität Bayreuth*, 2016. URL: https://epub.uni-bayreuth.de/2987/.

[Bru06] Johannes Brugmann. Planung von Luft/ Wasser-Wärmepumpen für Altbauten. *KI Luft- und Kältetechnik*, (5):192–197, 2006.

[BS11] Hans Dieter Baehr and Karl Stephan. *Heat and Mass Transfer*. Springer-Verlag Berlin Heidelberg, Berlin, Heidelberg, 3., rev. ed. edition, 2011. doi:10.1007/978-3-642-20021-2.

[BSBA12] B. Biegel, J. Stoustrup, J. Bendtsen, and P. Andersen. Model predictive control for power flows in networks with limited capacity. In *American Control Conference (ACC), 2012*, pages 2959–2964, Piscataway, NJ, 2012. IEEE. doi:10.1109/ACC.2012.6314854.

[Bun15] Bundesverband Wärmepumpe e.V. BWP-Branchenstudie 2015: Szenarien und politische Handlungsempfehlungen. *Bundesverband Wärmepumpe e.V. (BWP)*, 2015.

[Bun19] Bundesverband Wärmepumpe e.V. Baugenehmigungen 2018: Wärmepumpe erneut auf Platz eins. *Press release, Bundesverband Wärmepumpe e.V. (BWP)*, 2019.

[BV04] Stephen Boyd and Lieven Vandenberghe. *Convex Optimization*. Cambridge University Press, 7th printing with corrections, 2009 edition, 2004.

[BW89a] M. Baran and F. F. Wu. Optimal sizing of capacitors placed on a radial distribution system. *IEEE Transactions on Power Delivery*, 4(1):735–743, 1989. doi:10.1109/61.19266.

[BW89b] M. E. Baran and F. F. Wu. Network reconfiguration in distribution systems for loss reduction and load balancing. *IEEE Transactions on Power Delivery*, 4(2):1401–1407, 1989. doi:10.1109/61.25627.

[BW89c] M. E. Baran and F. F. Wu. Optimal capacitor placement on radial distribution systems. *IEEE Transactions on Power Delivery*, 4(1):725–734, 1989. doi:10.1109/61.19265.

[CD18] Holger Cischinsky and Nikolaus Diefenbach. Datenerhebung Wohngebäudebestand 2016: Datenerhebung zu den energetischen Merkmalen und Modernisierungsraten im deutschen und hessischen Wohngebäudebestand. *Institut Wohnen und Umwelt, Darmstadt*, 2018.

[CGB+13] Giuseppe Tommaso Costanzo, Oliver Gehrke, Daniel Esteban Morales Bondy, Fabrizio Sossan, Henrik Bindner, Jacopo Parvizi, and Henrik Madsen. A coordination scheme for distributed model predictive control: Integration of flexible DERs. In *2013 4th PES innovative smart grid technologies Europe (ISGT Europe 2013)*, pages 1–5, Piscataway, NJ, 2013. IEEE. doi:10.1109/ISGTEurope.2013.6695474.

[CGŠ+13] Jiří Cigler, Dimitrios Gyalistras, Jan Široký, Vinh-Nghi Tiet, and Lukáš Ferkl. Beyond theory: The challenge of implementing model predictive control in buildings. *Proceedings of CLIMA 2013: 11th REHVA world congress, Prague, Czech Republic*, 2013.

[CHKG05] Drury Crawley, John Hand, Michaël Kummert, and Brent Griffith. Contrasting the capabilities of building energy performance simulation programs. *Proceedings of BS2005: 9th Conference of International Building Performance Simulation Association, Montréal, Canada*, pages 231–238, 2005.

[CHYY16] Caihua Chen, Bingsheng He, Yinyu Ye, and Xiaoming Yuan. The direct extension of ADMM for multi-block convex minimization problems is not necessarily convergent. *Mathematical Programming*, 155(1):57–79, 2016. doi:10.1007/s10107-014-0826-5.

[CM14] Core Writing Team, Pachauri, R. K. and L. A. Meyer. Climate Change 2014: Synthesis Report. Contribution of Working Groups I, II and III to the Fifth Assessment Report of the Intergovernmental Panel on Climate Change. 2014.

[CSZ+12] Christian Conte, Tyler Summers, Melanie N. Zeilinger, Manfred Morari, and Colin N. Jones. Computational aspects of distributed optimization in model predictive control. In *IEEE 51st Annual Conference on Decision and Control (CDC), 2012*, pages 6819–6824, Piscataway, NJ, 2012. IEEE. doi:10.1109/CDC.2012.6426138.

[Dav94] M. G. Davies. The thermal response of an enclosure to periodic excitation: The CIBSE approach. *Building and Environment*, 29(2):217–235, 1994. doi:10.1016/0360-1323(94)90072-8.

[DB13] John A. Duffie and William A. Beckman. *Solar engineering of thermal processes*. Wiley, New York, 4. ed. edition, 2013. doi:10.1002/9781118671603.

[dCBS+14] R. de Coninck, R. Baetens, D. Saelens, A. Woyte, and L. Helsen. Rule-based demand-side management of domestic hot water production with heat pumps in zero energy neighbourhoods. *Journal of Building Performance Simulation*, 7(4):271–288, 2014. doi:10.1080/19401493.2013.801518.

[DEMM17] Dall'Anese, E., P. Mancarella, and A. Monti. Unlocking Flexibility: Integrated Optimization and Control of Multienergy Systems. *IEEE Power and Energy Magazine*, 15(1):43–52, 2017. doi:10.1109/MPE.2016.2625218.

[DEN] DENA. Definition Niedrigstenergiehaus. *Online, Deutsche Energie-Agentur*. URL: https://effizienzhaus.zukunft-haus.info/aktivitaeten/cohereno/definition-niedrigstenergiehaus/.

[DEN18a] DENA. dena-GEBÄUDEREPORT KOMPAKT 2018: Statistiken und Analysen zur Energieeffizienz im Gebäudebestand. *Bericht, Deutsche Energie-Agentur*, 2018.

[DEN18b] DENA. Integrierte Energiewende: Impulse für die Gestaltung des Energiesystems bis 2050. *Bericht, Deutsche Energie-Agentur*, 2018.

[DIN02] DIN EN. Voltage characteristics of electricity supplied by public distribution networks, 2011-02.

[DIN07] DIN EN 15450. Heizungsanlagen in Gebäuden – Planung von Heizungsanlagen mit Wärmepumpen, 12-2007.

[DIN08] DIN EN ISO 13790. Energieeffizienz von Gebäuden - Berechnung des Energiebedarfs für Heizung und Kühlung, 09-2008.

[DIN10] DIN EN ISO 10456. Baustoffe und Bauprodukte – Wärme- und feuchtetechnische Eigenschaften – Tabellierte Bemessungswerte und Verfahren zur Bestimmung der wärmeschutztechnischen Nenn- und Bemessungswerte. Building materials and products – Hygrothermal properties – Tabulated design values and procedures for determining declared and design thermal values, 05-2010.

[DIN13] DIN EN 1264. Raumflächenintegrierte Heiz- und Kühlsysteme mit Wasserdurchströmung. Water based surface embedded heating and cooling systems, 03-2013.

[DIN14] DIN EN 12831-1. Heizungsanlagen und wasserbasierte Kühlanlagen in Gebäuden – Verfahren zur Berechnung der Norm-Heizlast – Teil 1: Raumheizlast. Heating systems and water based cooling systems in buildings – Method for calculation of the design heat load – Part 1: Space heating load, 11-2014.

[DIN15a] DIN EN ISO 13370. Thermal performance of buildings – Heat transfer via the ground – Calculation methods, 07-2015.

[DIN15b] DIN EN ISO 6946. Bauteile – Wärmedurchlasswiderstand und Wärmedurchgangskoeffizient – Berechnungsverfahren.Building components and building elements – Thermal resistance and thermal transmittance – Calculation method, 06-2015.

[DIN18] DIN EN 14511. Air conditioners, liquid chilling packages and heat pumps for space heating and cooling and process chillers, with electrically driven compressors, 05-2018.

[DSM16] Michael Diekerhof, Sebastian Schwarz, and Antonello Monti. Distributed optimization for electro-thermal heating units. In Andrej Ferdo Gubina, editor, *IEEE PES Innovative Smart Grid Technologies, Europe*, pages 1–6, Piscataway, NJ, 2016. IEEE. doi:10.1109/ISGTEurope.2016.7856258.

[DVM14] Michael Diekerhof, Stefanie Vorkampf, and Antonello Monti. Distributed optimization algorithm for heat pump scheduling. In *IEEE PES Innovative Smart Grid Technologies Conference Europe (ISGT-Europe), 2014*, pages 1–6, Piscataway, NJ, 2014. IEEE. doi:10.1109/ISGTEurope.2014.7028943.

[DZG13] Emiliano Dall'Anese, Hao Zhu, and Georgios B. Giannakis. Distributed Optimal Power Flow for Smart Microgrids. *IEEE Transactions on Smart Grid*, 4(3):1464–1475, 2013. doi:10.1109/TSG.2013.2248175.

[EPMS+14] O. Edenhofer, R. Pichs-Madruga, Y. Sokona, E. Farahani, S. Kadner, K. Seyboth, A. Adler, I. Baum, S. Brunner, P. Eickemeier, B. Kriemann, J. Savolainen, S. Schlömer, C. von Stechow, T. Zwickel, and J. C. Minx. Climate Change 2014: Mitigation of Climate Change. Contribution of Working Group III to the Fifth Assessment Report of the Intergovernmental Panel on Climate Change. *Cambridge University Press, Cambridge, United Kingdom and New York, NY, USA*, 2014.

[ESJ09] Kristian Edlund, Leo Emil Sokoler, and John Bagterp Jorgensen. A primal-dual interior-point linear programming algorithm for MPC. In *Proceedings of the 48th IEEE Conference on Decision and Control (CDC)*, pages 351–356, Piscataway, NJ, 2009. IEEE. doi:10.1109/CDC.2009.5400440.

[ETP+17] Ozan Erdinc, Akin Tascikaraoglu, Nikolaos G. Paterakis, Yavuz Eren, and Joao P. S. Catalao. End-User Comfort Oriented Day-Ahead Planning for Responsive Residential HVAC Demand Aggregation Considering Weather Forecasts. *IEEE Transactions on Smart Grid*, 8(1):362–372, 2017. doi:10.1109/TSG.2016.2556619.

[EY15] Jonathan Eckstein and Wang Yao. Understanding the Convergence of the Alternating Direction Method of Multipliers: Theoretical and Computational Perspectives. 2015. URL: http://www.optimization-online.org/DB_HTML/2015/06/4954.html.

[Far10] H. Farhangi. The path of the smart grid. *IEEE Power and Energy Magazine*, 8(1):18–28, 2010. doi:10.1109/MPE.2009.934876.

[FBMW17] David Fischer, Josef Bernhardt, Hatef Madani, and Christof Wittwer. Comparison of control approaches for variable speed air source heat pumps considering time variable electricity prices and PV. *Applied Energy*, 204:93–105, 2017. doi:10.1016/j.apenergy.2017.06.110.

[FCL13] Masoud Farivar, Lijun Chen, and Steven Low. Equilibrium and dynamics of local voltage control in distribution systems. In *2013 IEEE 52nd Annual Conference on Decision and Control (CDC)*, pages 4329–4334, Piscataway, NJ, 2013. IEEE. doi:10.1109/CDC.2013.6760555.

[FDZa] FDZ der Statistischen Ämter des Bundes und der Länder. Zeitbudgeterhebung, 2001-2002, eigene Berechnungen.

[FDZb] FDZ der Statistischen Ämter des Bundes und der Länder. Zeitbudgeterhebung, 2012-2013, eigene Berechnungen.

[Fed16] Federal Statistical Office. Bautätigkeit und Wohnungen: Bautätigkeit 2015. *Statistisches Bundesamt (Destatis)*, (Fachserie 5 Reihe 1), 2016.

[Fed18a] Federal Statistical Office. Bautätigkeit und Wohnungen: Bautätigkeit 2017. *Statistisches Bundesamt (Destatis)*, Fachserie 5 Reihe 1, 2018.

[Fed18b] Federal Statistical Office. Bautätigkeit und Wohnungen: Bestand an Wohnungen. 31. Dezember 2017. *Statistisches Bundesamt (Destatis)*, Fachserie 5 Reihe 3, 2018.

[Fed19] Federal Statistical Office. Umweltnutzung und Wirtschaft. Tabellen zu den Umweltökonomischen Gesamtrechnungen. Teil 2: Energie: Berichtszeitraum 2000 - 2017. *Statistisches Bundesamt (Destatis)*, 2019.

[FL13] Masoud Farivar and Steven H. Low. Branch Flow Model: Relaxations and Convexification-Part I. *IEEE Transactions on Power Systems*, 28(3):2554–2564, 2013. doi:10.1109/TPWRS.2013.2255317.

[FLTM12] Marcus Fuchs, Moritz. Lauster, Jens Teichmann, and Dirk Müller. Modularer Modellansatz zur Simulation von Energiesystemen auf Quartiersebene. *in Proc. fourth German-Austrian IBPSA Conference BaumSIM, 2012*, pages 348–353, 2012.

[Fra13] Fraunhofer ISE. WP Monitor, 2013. URL: https://wp-monitoring.ise.fraunhofer.de/wp-monitor-plus/german/index/index.html.

[Fra17] Fraunhofer IWES/IBP. Wärmewende 2030. Schlüsseltechnologien zur Erreichung der mittel- und langfristigen Klimaschutzziele im Gebäudesektor. Studie im Auftrag von Agora Energiewende. *Fraunhofer IWES/IBP*, 2017.

[Fra18] Fraunhofer ISE. Projekt WPsmart im Bestand, 2018. URL: https://wp-monitoring.ise.fraunhofer.de/wp-smart-im-bestand/german/index/index.html.

[FWSWH16] David Fischer, Tobias Wolf, Johannes Scherer, and Bernhard Wille-Haussmann. A stochastic bottom-up model for space heating and domestic hot water load profiles for German households. *Energy and Buildings*, 124:120–128, 2016. doi:10.1016/j.enbuild.2016.04.069.

[Gel85] C. W. Gellings. The concept of demand-side management for electric utilities. *Proceedings of the IEEE*, 73(10):1468–1470, 1985. doi:10.1109/PROC.1985.13318.

[Glü08] Bernd Glück. Abschlussbericht Innovative Wärmeübertragung und Wärmespeicherung im Verbundvorhaben Heizen und Kühlen mit Niedrigexergie (LowEx). *Westsächsische Hochschule Zwickau, Clina Heiz- und Kühlelemente GmbH*, 2008.

[GML+14] Danny Günther, Marek Miara, Robert Langner, Sebastian Helmling, and Jeannette Wapler. WP Monitor: Feldmessung von Wärmepumpenanlagen. *Abschlussbericht, Fraunhofer ISE, Freiburg*, 2014.

[GSK+11] Vehbi C. Gungor, Dilan Sahin, Taskin Kocak, Salih Ergut, Concettina Buccella, Carlo Cecati, and Gerhard P. Hancke. Smart Grid Technologies: Communication Technologies and Standards. *IEEE Transactions on Industrial Informatics*, 7(4):529–539, 2011. doi:10.1109/TII.2011.2166794.

[GTSJ15] Euhanna Ghadimi, Andre Teixeira, Iman Shames, and Mikael Johansson. Optimal Parameter Selection for the Alternating Direction Method of Multipliers (ADMM): Quadratic Problems. *IEEE Transactions on Automatic Control*, 60(3):644–658, 2015. doi:10.1109/TAC.2014.2354892.

[HAS+14] G. Hausladen, T. Auer, J. Schneegans, K. Klimke, and H. Riemer. Lastverhalten von Gebäuden unter Berücksichtigung unterschiedlicher Bauweisen und technischer Systeme: Speicher- und Lastmanagementpotenziale in Gebäuden. *Kurzbericht, Technische Universität München, Lehrstuhl für Bauklimatik und Haustechnik*, 2014. URL: https://www.irbnet.de/daten/kbf/kbf_d_F_2920.pdf.

[Hau09] G. Hauser. Energieeffizeinte Gebäude - ein Muss für die Zukunftssicherung! *BMWi, Fraunhofer IBP: LowEx-Symposium - Tagungsband*, 2009. URL: http://aachen2050.isl.rwth-aachen.de/w/images/5/56/LowEx-Tagungsband_10-09.pdf.

[HBP+12] Rasmus Halvgaard, Peder Bacher, Bengt Perers, Elsa Andersen, Simon Furbo, John B. Jørgensen, Niels K. Poulsen, and Henrik Madsen. Model Predictive Control for a Smart Solar Tank Based on Weather and Consumption Forecasts. *Energy Procedia*, 30:270–278, 2012. doi:10.1016/j.egypro.2012.11.032.

[HDR+13] M. Y. Haller, R. Dott, J. Ruschenburg, F. Ochs, and J. Bony. The Reference Framework for System Simulations of the IEA SHC Task 44 / HPP Annex 38 Part A: General Simulation Boundary Conditions: A technical report of subtask C , Report C1 Part A. *International Energy Agency*, 2013.

[Hei15] Christian Heilek. Modellgestützte Optimierung des Neubaus und Einsatzes von Erzeugungsanlagen und Speichern für elektrische und thermische Energie im deutschen Energiesystem. *Dissertation,Technische Universität München*, 2015.

[HGM+17] Sarmad Hanif, H. B. Gooi, Tobias Massier, Thomas Hamacher, and Thomas Reindl. Distributed Congestion Management of Distribution Grids Under Robust Flexible Buildings Operations. *IEEE Transactions on Power Systems*, 32(6):4600–4613, 2017. doi:10.1109/TPWRS.2017.2660065.

[HGP12a] Ion Hazyuk, Christian Ghiaus, and David Penhouet. Optimal temperature control of intermittently heated buildings using Model Predictive Control: Part I – Building modeling. *Building and Environment*, 51:379–387, 2012. doi:10.1016/j.buildenv.2011.11.009.

[HGP12b] Ion Hazyuk, Christian Ghiaus, and David Penhouet. Optimal temperature control of intermittently heated buildings using Model Predictive Control: Part II – Control algorithm. *Building and Environment*, 51:388–394, 2012. doi:10.1016/j.buildenv.2011.11.008.

[HH07] Richard Heimrath and Michel Haller. The Reference Heating System, the Template Solar System of Task 32: A Report of IEA Solar Heating and Cooling programme - Task 32 "Advanced storage concepts for solar and low energy buildings". Report A2 of Subtask A. *International Energy Agency*, 2007.

[HJP+13] Rasmus Halvgaard, John B. Jorgensen, Niels K. Poulsen, Henrik Madsen, and Lieven Vandenberghe. Decentralized large-scale power balancing. In *2013 4th PES innovative smart grid technologies Europe (ISGT Europe 2013)*, pages 1–5, Piscataway, NJ, 2013. IEEE. doi:10.1109/ISGTEurope.2013.6695323.

[HM09] K. Huchtemann and D. Müller. Analyse von Wärmepumpensystemen im Wohnungsbau. *KI Kälte Luft Klima*, (03):38–42, 2009.

[HMG+17] Sarmad Hanif, Tobias Massier, Hoay Beng Gooi, Thomas Hamacher, and Thomas Reindl. Cost Optimal Integration of Flexible Buildings in Congested Distribution Grids. *IEEE Transactions on Power Systems*, 32(3):2254–2266, 2017. doi:10.1109/TPWRS.2016.2605921.

[HP15] Hans-Martin Henning and Andreas Palzer. Was kostet die Energiewende? Wege zur Transformation des deutschen Energiesystems bis 2050. *Fraunhofer ISE, Freiburg*, 2015.

[HPMJ12] Rasmus Halvgaard, Niels Kjolstad Poulsen, Henrik Madsen, and John Bagterp Jorgensen. Economic Model Predictive Control for building climate control in a Smart Grid. In *IEEE PES innovative smart grid technologies (ISGT), 2012*, pages 1–6, Piscataway, NJ, 2012. IEEE. doi:10.1109/ISGT.2012.6175631.

[Huc15] K. Huchtemann. Supply Temperature Control Concepts in Heat Pump Heating Systems. *Dissertation, RWTH Aachen*, 2015.

[HVP+16] Rasmus Halvgaard, Lieven Vandenberghe, Niels Kjolstad Poulsen, Henrik Madsen, and John Bagterp Jorgensen. Distributed Model Predictive Control for Smart Energy Systems. *IEEE Transactions on Smart Grid*, 7(3):1675–1682, 2016. doi:10.1109/TSG.2016.2526077.

[HWLN14] Shaojun Huang, Qiuwei Wu, Zhaoxi Liu, and Arne Hejde Nielsen. Review of congestion management methods for distribution networks with high penetration of distributed energy resources. In *IEEE PES Innovative Smart Grid Technologies Conference Europe (ISGT-Europe), 2014*, pages 1–6, Piscataway, NJ, 2014. IEEE. doi:10.1109/ISGTEurope.2014.7028811.

[HWO+15] Shaojun Huang, Qiuwei Wu, Shmuel S. Oren, Ruoyang Li, and Zhaoxi Liu. Distribution Locational Marginal Pricing Through Quadratic Programming for Congestion Management in Distribution Networks. *IEEE Transactions on Power Systems*, 30(4):2170–2178, 2015. doi:10.1109/TPWRS.2014.2359977.

[HYW00] B. S. He, H. Yang, and S. L. Wang. Alternating Direction Method with Self-Adaptive Penalty Parameters for Monotone Variational Inequalities. *Journal of Optimization Theory and Applications*, 106(2):337–356, 2000. doi:10.1023/A:1004603514434.

[IA09] Ali Ipakchi and Farrokh Albuyeh. Grid of the future. *IEEE Power and Energy Magazine*, 7(2):52–62, 2009. doi:10.1109/MPE.2008.931384.

[Int17] International Geothermal Centre. Analyse des deutschen Wärmepumpenmarktes: Bestandsaufnahme und Trends. *2. Aktualisierung der Studie, International Geothermal Centre, Bochum*, 2017.

[JAL+18] Rune Grønborg Junker, Armin Ghasem Azar, Rui Amaral Lopes, Karen Byskov Lindberg, Glenn Reynders, Rishi Relan, and Henrik Madsen. Characterizing the energy flexibility of buildings and districts. *Applied Energy*, 225:175–182, 2018. doi:10.1016/j.apenergy.2018.05.037.

[JAW14] Morten Juelsgaard, Palle Andersen, and Rafael Wisniewski. Distribution Loss Reduction by Household Consumption Coordination in Smart Grids. *IEEE Transactions on Smart Grid*, 5(4):2133–2144, 2014. doi:10.1109/TSG.2014.2312428.

[JKC15] Akhila Jambagi, Michael Kramer, and Vicky Cheng. Residential electricity demand modelling: Activity based modelling for a model with high time and spatial resolution. In Mohamed Essaaidi and Youssef Zaz, editors, *Proceedings of 2015 IEEE International Renewable and Sustainable Energy Conference (IRSEC'15)*, pages 1–6, Piscataway, NJ, 2015. IEEE. doi:10.1109/IRSEC.2015.7455047.

[JMPL+17] Søren Østergaard Jensen, Anna Marszal-Pomianowska, Roberto Lollini, Wilmer Pasut, Armin Knotzer, Peter Engelmann, Anne Stafford, and Glenn Reynders. IEA EBC Annex 67 Energy Flexible Buildings. *Energy and Buildings*, 155:25–34, 2017. doi:10.1016/j.enbuild.2017.08.044.

[Jun14] Johannes Jungwirth. Entwicklung einer modellprädiktiven Regelung mit einem adaptiven Gebäudemodell zur Flexibilisierung der Wärme- und Kälteversorgung von Gebäuden. *Dissertation,Technische Universität München*, 2014.

[JV01] Ulrike Jordan and Klaus Vajen. Realistic Domestic Hot-Water Profiles in Different Time Scales. *Universität Marburg*, 2001.

[JV05] Ulrike Jordan and Klaus Vajen. DHWcalc: Program to generate domestic hot water profiles with statistical means for user defined conditions. *Proc. ISES Solar World Congress, Orlando (US), 8. - 12.8.2005,*, 2005.

[Kan17] Thomas Kanig. Effizienzklassen für Warmwasserspeicher: Buderus/Huch GmbH Behälterbau. *Presentation*, 2017.

[KH17] P. Kohlhepp and V. Hagenmeyer. Technical Potential of Buildings in Germany as Flexible Power-to-Heat Storage for Smart-Grid Operation. *Energy Technology*, 53:10, 2017. doi:10.1002/ente.201600655.

[KJC16] Michael Kramer, Akhila Jambagi, and Vicky Cheng. A model predictive control approach for demand side management of residential power to heat technologies. In *2016 IEEE International Energy Conference (ENERGYCON)*, pages 1–6, Piscataway, NJ, 2016. IEEE. doi:10.1109/ENERGYCON.2016.7513903.

[KJC17a] Michael Kramer, Akhila Jambagi, and Vicky Cheng. Bottom-up Modeling of Residential Heating Systems for Demand Side Management in District Energy System Analysis and Distribution Grid Planning. *Proceedings of BS2017: 15th Conference of International Building Performance Simulation Association, San Francisco, USA*, pages 711–718, 2017. URL: http://www.ibpsa.org/proceedings/BS2017/BS2017_183.pdf.

[KJC17b] Michael Kramer, Akhila Jambagi, and Vicky Cheng. Distributed model predictive control for building energy systems in distribution grids. In *2017 IEEE PES Innovative Smart Grid Technologies Conference Europe (ISGT-Europe)*, pages 1–6, Piscataway, NJ, 2017. IEEE. doi:10.1109/ISGTEurope.2017.8260293.

[KK16] M. Killian and M. Kozek. Ten questions concerning model predictive control for energy efficient buildings. *Building and Environment*, 105:403–412, 2016. doi:10.1016/j.buildenv.2016.05.034.

[KKL18] R. Kuniyoshi, M. Kramer, and M. Lindauer. Validation of RC Building Models for Applications in Energy and Demand Side Management. *Proceedings of eSim 2018, the 10th conference of IBPSA-Canada Montréal, Canada, May 9-10, 2018*, 2018.

[KMW+13] Mikkel Urban Kajgaard, Jesper Mogensen, Anders Wittendorff, Attila Todor Veress, and Benjamin Biegel. Model predictive control of domestic heat pump. In *American Control Conference (ACC), 2013*, pages 2013–2018, Piscataway, NJ, 2013. IEEE. doi:10.1109/ACC.2013.6580131.

[KR07] Jérôme Henri Kämpf and Darren Robinson. A simplified thermal model to support analysis of urban resource flows. *Energy and Buildings*, 39(4):445–453, 2007. doi:10.1016/j.enbuild.2006.09.002.

[Kra14] Matt Kraning. Dynamic Network Energy Management via Proximal Message Passing. *Foundations and Trends® in Optimization*, 1(2):73–126, 2014. doi:10.1561/2400000002.

[Kun17] R. Kuniyoshi. Validation of RC Building Models for Application in Energy and Demand Side Management. *Master's thesis, Technische Universität München*, 2017.

[KvS12] Rick Kramer, Jos van Schijndel, and Henk Schellen. Simplified thermal and hygric building models: A literature review. *Frontiers of Architectural Research*, 1(4):318–325, 2012. doi:10.1016/j.foar.2012.09.001.

[LAW+16] M. Lindner, C. Aigner, R. Witzmann, F. Wirtz, I. Berber, M. Gödde, and R. Frings. Aktuelle Musternetze zur Untersuchung von Spannungsproblemen in der Niederspannung. *14. Symposium Energieinnovation, Graz*, 2016.

[LBD15] Emmanouil Loukarakis, Janusz W. Bialek, and Chris J. Dent. Investigation of Maximum Possible OPF Problem Decomposition Degree for Decentralized Energy Markets. *IEEE Transactions on Power Systems*, 30(5):2566–2578, 2015. doi:10.1109/TPWRS.2014.2365959.

[LBL+14] M. Lauster, M.-A. Brüntjen, H. Leppmann, M. Fuchs, J. Teichmann, R. Streblow, C. van Treeck, and D. Müller. Improving a low order building model for urban scale applications. *in Proc. Fifth German-Austrian IBPSA Conference BaumSIM, 2014*, 2014.

[LCRA95] Anders Lindfors, Anders Christoffersson, Roland Roberts, and Gunnar Anderlind. Model Based Frequency Domain Estimation of the Thermal Properties of Building Insulation. *Journal of Thermal Insulation and Building Envelopes*, 18(3):229–260, 1995. doi:10.1177/109719639501800305.

[LDB16] Emmanouil Loukarakis, Chris J. Dent, and Janusz W. Bialek. Decentralized Multi-Period Economic Dispatch for Real-Time Flexible Demand Management. *IEEE Transactions on Power Systems*, 31(1):672–684, 2016. doi:10.1109/TPWRS.2015.2402518.

[LDSB12] Tobias Loga, Nikolaus Diefenbach, Britta Stein, and Rolf Born. *TABULA: Scientific Report Germany. Further Development of the German Residential Building Typology.* IWU, Darmstadt, 2012. URL: http://www.building-typology.eu/downloads/public/docs/scientific/DE_TABULA_ScientificReport_IWU.pdf.

[LH15] Lanchao Liu and Zhu Han. Multi-block ADMM for big data optimization in smart grid. In *2015 International Conference on Computing, Networking and Communications (ICNC)*, pages 556–561, Piscataway, NJ, 2015. IEEE. doi:10.1109/ICCNC.2015.7069405.

[LHM+07] J. PeçasA. Lopes, N. Hatziargyriou, J. Mutale, P. Djapic, and N. Jenkins. Integrating distributed generation into electric power systems: A review of drivers, challenges and opportunities. *Electric Power Systems Research*, 77(9):1189–1203, 2007. doi:10.1016/j.epsr.2006.08.016.

[Lin17] M. Lindauer. Dynamische Sensitivitätsanalysemethoden energetischer Wohngebäudequartierssimulationen. *Dissertation, Technische Universität München*, 2017.

[LMB12] Yashen Lin, Timothy Middelkoop, and Prabir Barooah. Issues in identification of control-oriented thermal models of zones in multi-zone buildings. In *IEEE 51st Annual Conference on Decision and Control (CDC), 2012*, pages 6932–6937, Piscataway, NJ, 2012. IEEE. doi:10.1109/CDC.2012.6425958.

[Log02] Tobias Loga. Die EnEV und das Niedrigenergiehaus: Beispielrechnungen für ein Einfamilienhaus. *Institut Wohnen und Umwelt, Darmstadt*, pages 1–17, 2002. URL: https://www.iwu.de/fileadmin/user_upload/dateien/energie/werkzeuge/die_enev_und_das_neh.pdf.

[Low14a] Steven H. Low. Convex Relaxation of Optimal Power Flow—Part I: Formulations and Equivalence. *IEEE Transactions on Control of Network Systems*, 1(1):15–27, 2014. doi:10.1109/TCNS.2014.2309732.

[Low14b] Steven H. Low. Convex Relaxation of Optimal Power Flow—Part II: Exactness. *IEEE Transactions on Control of Network Systems*, 1(2):177–189, 2014. doi:10.1109/TCNS.2014.2323634.

[LRF+14] M. Lauster, P. Remmen, M. Fuchs, J. Teichmann, R. Streblow, and D. Müller. Modelling long-wave radiation heat exchange for thermal network building simulations at urban scale using Modelica. *Proceedings of the 10th International ModelicaConference*, pages 125–133, 2014.

[LSDB15] Tobias Loga, Britta Stein, Nikolaus Diefenbach, and Rolf Born. *Deutsche Wohngebäudetypologie: Beispielhafte Maßnahmen zur Verbesserung der Energieeffizienz von typischen Wohngebäuden ; erarbeitet im Rahmen der EU-Projekte TABULA - Typology approach for building stock energy assessment, EPISCOPE - Energy performance indicator tracking schemes for the continous optimisation of refurbishment processes in European housing stocks.* IWU, Darmstadt, 2. erw. edition, 2015.

[LTF+14] M. Lauster, J. Teichmann, M. Fuchs, R. Streblow, and D. Mueller. Low order thermal network models for dynamic simulations of buildings on city district scale. *Building and Environment*, 73:223–231, 2014. doi:10.1016/j.buildenv.2013.12.016.

[Lut08] Jim Lutz. Water heaters and hot water distribution systems. *Lawrence Berkeley National Laboratory. Prepared for California Energy Commission, PIER Buildings End-Use Energy*, 2008.

[LVK10] Ioannis Lampropoulos, Greet M. A. Vanalme, and Wil L. Kling. A methodology for modeling the behavior of electricity prosumers within the smart grid. In *IEEE PES Innovative Smart Grid Technologies Conference Europe (ISGT Europe), 2010*, pages 1–8, Piscataway, NJ, 2010. IEEE. doi:10.1109/ISGTEUROPE.2010.5638967.

[LvS13] Gunn K. H. Larsen, Nicky D. van Foreest, and Jacquelien M. A. Scherpen. Distributed Control of the Power Supply-Demand Balance. *IEEE Transactions on Smart Grid*, 4(2):828–836, 2013. doi:10.1109/TSG.2013.2242907.

[LWO14] Ruoyang Li, Qiuwei Wu, and Shmuel S. Oren. Distribution Locational Marginal Pricing for Optimal Electric Vehicle Charging Management. *IEEE Transactions on Power Systems*, 29(1):203–211, 2014. doi:10.1109/TPWRS.2013.2278952.

[LXL+12] Jing Liu, Yang Xiao, Shuhui Li, Wei Liang, and C. L. Philip Chen. Cyber Security and Privacy Issues in Smart Grids. *IEEE Communications Surveys & Tutorials*, 14(4):981–997, 2012. doi:10.1109/SURV.2011.122111.00145.

[MBB+10] Albert Molderink, Vincent Bakker, Maurice G. C. Bosman, Johann L. Hurink, and Gerard J. M. Smit. Management and Control of Domestic Smart Grid Technology. *IEEE Transactions on Smart Grid*, 1(2):109–119, 2010. doi:10.1109/TSG.2010.2055904.

[MBH+10] Yudong Ma, Francesco Borrelli, Brandon Hencey, Brian Coffey, Sorin Bengea, and Philip Haves. Model predictive control for the operation of building cooling systems. In *American Control Conference (ACC), 2010*, pages 5106–5111, Piscataway, NJ, 2010. IEEE. doi:10.1109/ACC.2010.5530468.

[MDP13] Andrea Mercurio, Alessandro Di Giorgio, and Fabio Purificato. Optimal fully electric vehicle load balancing with an ADMM algorithm in Smartgrids. In Panos Antsaklis, editor, *21st Mediterranean Conference on Control & Automation (MED), 2013*, pages 119–124, Piscataway, NJ, 2013. IEEE. doi:10.1109/MED.2013.6608708.

[MDS+17] Daniel K. Molzahn, Florian Dorfler, Henrik Sandberg, Steven H. Low, Sambuddha Chakrabarti, Ross Baldick, and Javad Lavaei. A Survey of Distributed Optimization and Control Algorithms for Electric Power Systems. *IEEE Transactions on Smart Grid*, 8(6):2941–2962, 2017. doi:10.1109/TSG.2017.2720471.

[MF15] Giancarlo Mantovani and Luca Ferrarini. Temperature Control of a Commercial Building With Model Predictive Control Techniques. *IEEE Transactions on Industrial Electronics*, 62(4):2651–2660, 2015. doi:10.1109/TIE.2014.2387095.

[MGK+11] Marek Miara, Danny Günther, Thomas Kramer, Thore Oltersdorf, and Jeannette Wapler. Wärmepumpen Effizienz: Messtechnische Untersuchung von Wärmepumpenanlagen zur Analyse und Bewertung der Effizienz im realen Betrieb. *Abschlussbericht, Fraunhofer ISE, Freiburg*, 2011.

[MH95] H. Madsen and J. Holst. Estimation of continuous-time models for the heat dynamics of a building. *Energy and Buildings*, 22(1):67–79, 1995. doi:10.1016/0378-7788(94)00904-X.

[MH99] Manfred Morari and Jay H. Lee. Model predictive control: Past, present and future. *Computers & Chemical Engineering*, 23(4-5):667–682, 1999. doi:10.1016/S0098-1354(98)00301-9.

[MKDB12] Yudong Ma, Anthony Kelman, Allan Daly, and Francesco Borrelli. Predictive Control for Energy Efficient Buildings with Thermal Storage: Modeling, Stimulation, and Experiments. *IEEE Control Systems*, 32(1):44–64, 2012. doi:10.1109/MCS.2011.2172532.

[MLMdM09] Y. V. Makarov, C. Loutan, J. Ma, and P. de Mello. Operational Impacts of Wind Generation on California Power Systems. *IEEE Transactions on Power Systems*, 24(2):1039–1050, 2009. doi:10.1109/TPWRS.2009.2016364.

[MM09] Patrick McDaniel and Stephen McLaughlin. Security and Privacy Challenges in the Smart Grid. *IEEE Security & Privacy Magazine*, 7(3):75–77, 2009. doi:10.1109/MSP.2009.76.

[MMB15] Yudong Ma, Jadranko Matusko, and Francesco Borrelli. Stochastic Model Predictive Control for Building HVAC Systems: Complexity and Conservatism. *IEEE Transactions on Control Systems Technology*, 23(1):101–116, 2015. doi:10.1109/TCST.2014.2313736.

[MMS+15] Dirk Müller, Antonello Monti, Sebastian Stinner, Tim Schlösser, Thomas Schütz, Peter Matthes, Henryk Wolisz, Christoph Molitor, Hassan Harb, and Rita Streblow. Demand side management for city districts. *Building and Environment*, 91:283–293, 2015. doi:10.1016/j.buildenv.2015.03.026.

[MSSVP14] Mehdi Maasoumy, Borhan M. Sanandaji, Alberto Sangiovanni-Vincentelli, and Kameshwar Poolla. Model Predictive Control of regulation services from commercial buildings to the smart grid. In *American Control Conference (ACC), 2014*, pages 2226–2233, Piscataway, NJ, 2014. IEEE. doi:10.1109/ACC.2014.6859332.

[MSV13] Mehdi Maasoumy and Alberto Sangiovanni-Vincentelli. Optimal Control of Building HVAC Systems in the Presence of Imperfect Predictions. In *Proceedings of the ASME 5th Annual Dynamic Systems and Control Division conference and JSME 11th Motion and Vibration Conference*, page 257, New York, NY, 2013. ASME. doi:10.1115/DSCC2012-MOVIC2012-8523.

[MT13] Benyamin Moradzadeh and Kevin Tomsovic. Two-Stage Residential Energy Management Considering Network Operational Constraints. *IEEE Transactions on Smart Grid*, 4(4):2339–2346, 2013. doi:10.1109/TSG.2013.2265313.

[NdSH04] R. R. Negenborn, B. de Schutter, and J. Hellendoorn. Multi-Agent Model Predictive Control: A Survey: Technical report 04-010. *Delft Center for Systems and Control, Delft University of Technology*, 2004. URL: https://repository.tudelft.nl/islandora/object/uuid:58d2299c-b1b7-4478-bda2-ff1c0132a8b6/datastream/OBJ.

[Nie05] T. R. Nielsen. Simple tool to evaluate energy demand and indoor environment in the early stages of building design. *Solar Energy*, 78(1):73–83, 2005. doi:10.1016/j.solener.2004.06.016.

[NMB+12] S. Nykamp, A. Molderink, V. Bakker, H. A. Toersche, J. L. Hurink, and G.J.M. Smit. Integration of heat pumps in distribution grids: Economic motivation for grid control. In *3rd IEEE PES International Conference and Exhibition on Innovative Smart Grid Technologies (ISGT Europe), 2012*, pages 1–8, Piscataway, NJ, 2012. IEEE. doi:10.1109/ISGTEurope.2012.6465605.

[NSB17] D. Bao Nguyen, Jacquelien M. A. Scherpen, and Frits Bliek. Distributed Optimal Control of Smart Electricity Grids With Congestion Management. *IEEE Transactions on Automation Science and Engineering*, 14(2):494–504, 2017. doi:10.1109/TASE.2017.2664061.

[OMSE+14] Daniel E. Olivares, Ali Mehrizi-Sani, Amir H. Etemadi, Claudio A. Canizares, Reza Iravani, Mehrdad Kazerani, Amir H. Hajimiragha, Oriol Gomis-Bellmunt, Maryam Saeedifard, Rodrigo Palma-Behnke, Guillermo A. Jimenez-Estevez, and Nikos D. Hatziargyriou. Trends in Microgrid Control. *IEEE Transactions on Smart Grid*, 5(4):1905–1919, 2014. doi:10.1109/TSG.2013.2295514.

[OPJ+12] Frauke Oldewurtel, Alessandra Parisio, Colin N. Jones, Dimitrios Gyalistras, Markus Gwerder, Vanessa Stauch, Beat Lehmann, and Manfred Morari. Use of model predictive control and weather forecasts for energy efficient building climate control. *Energy and Buildings*, 45:15–27, 2012. doi:10.1016/j.enbuild.2011.09.022.

[PBA+15] Dieter Patteeuw, Kenneth Bruninx, Alessia Arteconi, Erik Delarue, William D'haeseleer, and Lieve Helsen. Integrated modeling of active demand response with electric heating systems coupled to thermal energy storage systems. *Applied Energy*, 151:306–319, 2015. doi:10.1016/j.apenergy.2015.04.014.

[PH14] Dieter Patteeuw and Lieve Helsen. Residential buildings with heat pumps, a verified bottom-up model for demand side management studies. *in Proc. 9th International Conference on System Simulation in Buildings, Liege, December 10–12, 2014*, pages 1–19, 2014.

[PH16] Dieter Patteeuw and Lieve Helsen. Combined design and control optimization of residential heating systems in a smart-grid context. *Energy and Buildings*, 133:640–657, 2016. doi:10.1016/j.enbuild.2016.09.030.

[Pip57] Louis A. Pipes. Matrix analysis of heat transfer problems. *Journal of the Franklin Institute*, 263(3):195–206, 1957. doi:10.1016/0016-0032(57)90927-4.

[PKG+17] Matthias Pazold, Matthias Kersken, Johannes Gantner, Michael Jäger, and Herbet Sinnesbichler. Windheizung 2.0 - Energiespeicherung und Stromnetzregelung mit hocheffizienten Gebäuden: Projektphase 2017. *Fraunhofer IBP, Stuttgart, Holzkirchen*, 2017.

[PMLC09] Liam Paull, Derek MacKay, Howard Li, and Liuchen Chang. A water heater model for increased power system efficiency. *2009 Canadian Conference on Electrical and Computer Engineering*, pages 731–734, 2009. doi:10.1109/CCECE.2009.5090225.

[PS17] Christina Protopapadaki and Dirk Saelens. Heat pump and PV impact on residential low-voltage distribution grids as a function of building and district properties. *Applied Energy*, 192:268–281, 2017. doi:10.1016/j.apenergy.2016.11.103.

[QB03] S. J. Qin and T. A. Badgwell. A survey of industrial model predictive control technology. *Control Engineering Practice*, 11(7):733–764, 2003. doi:10.1016/S0967-0661(02)00186-7.

[RAB12] James B. Rawlings, David Angeli, and Cuyler N. Bates. Fundamentals of economic model predictive control. In *IEEE 51st Annual Conference on Decision and Control (CDC), 2012*, pages 3851–3861, Piscataway, NJ, 2012. IEEE. doi:10.1109/CDC.2012.6425822.

[RDS14] G. Reynders, J. Diriken, and D. Saelens. Quality of grey-box models and identified parameters as function of the accuracy of input and observation signals. *Energy and Buildings*, 82:263–274, 2014. doi:10.1016/j.enbuild.2014.07.025.

[RDS15] G. Reynders, J. Diriken, and D. Saelens. Impact of the Heat Emission System on the Identification of Grey-box Models for Residential Buildings. *Energy Procedia*, 78:3300–3305, 2015. doi:10.1016/j.egypro.2015.11.740.

[RDS17] Glenn Reynders, Jan Diriken, and Dirk Saelens. Generic characterization method for energy flexibility: Applied to structural thermal storage in residential buildings. *Applied Energy*, 198:192–202, 2017. doi:10.1016/j.apenergy.2017.04.061.

[Rey15] Glenn Reynders. Quantifying the impact of building design on the potential of structural storage for active demand response in residential buildings. *Dissertation, KU Leuven*, 2015.

[RGEC13] Alfonso P. Ramallo-González, Matthew E. Eames, and David A. Coley. Lumped parameter models for building thermal modelling: An analytic approach to simplifying complex multi-layered constructions. *Energy and Buildings*, 60:174–184, 2013. doi:10.1016/j.enbuild.2013.01.014.

[RGJ17] Jose Rivera, Christoph Goebel, and Hans-Arno Jacobsen. Distributed Convex Optimization for Electric Vehicle Aggregators. *IEEE Transactions on Smart Grid*, 8(4):1852–1863, 2017. doi:10.1109/TSG.2015.2509030.

[RGR+17] Johan Rockström, Owen Gaffney, Joeri Rogelj, Malte Meinshausen, Nebojsa Nakicenovic, and Hans Joachim Schellnhuber. A roadmap for rapid decarbonization. *Science*, 355(6331):1269–1271, 2017. doi:10.1126/science.aah3443.

[RGZ88] R. E. Rink, V. Gourishankar, and M. Zaheeruddin. Optimal control of heat-pump/heat-storage systems with time-of-day energy price incentive. *Journal of Optimization Theory and Applications*, 58(1):93–108, 1988. doi:10.1007/BF00939772.

[RM09] J. B. Rawlings and D. Q. Mayne. *Model predictive control: Theory and design*. Nob Hill Publ, Madison, Wis., 2009. URL: http://www.nobhillpublishing.com/mpc/index-mpc.html.

[RMP+10] Christel Russ, Marek Miara, Michael Platt, Danny Günther, Thomas Kramer, Holger Dittmer, Thomas Lechner, and Christian Kurz. Feldmessung von Wärmepumpen im Gebäudebestand. *Kurzfassung zum Abschlussbericht, Fraunhofer ISE, Freiburg*, 2010.

[RNS13] G. Reynders, T. Nuytten, and D. Saelens. Potential of structural thermal mass for demand-side management in dwellings. *Building and Environment*, 64:187–199, 2013. doi:10.1016/j.buildenv.2013.03.010.

[Rou72] L. Rouvel. Berechnung des wärmetechnischen Verhaltens von Räumen bei dynamischen Wärmelasten. *Brennstoff Wärme Kraft*, 24(6):245–262, 1972.

[Rou16] L. Rouvel. Test- und Validierungsbeispiele für Flächenheiz- und Flächenkühlsysteme entsprechend den Vorgaben der VDI 6020 und VDI 2078. *GEBSIMU*, 2016.

[Row02] Derek Rowell. Time-Domain Solution of LTI State Equations: 2.14 Handout Analysis and Design of Feedback Control Systems. 2002.

[RS14] G. Reynders and D. Saelens. Bottom-up modeling of the Belgian residential building stock: influence of model complexity. *Proceedings of the 9th Conference in System Simulation in Buildings, Liege, December 10-12*, 2014.

[Ruf18] Holger Ruf. Limitations for the feed-in power of residential photovoltaic systems in Germany – An overview of the regulatory framework. *Solar Energy*, 159:588–600, 2018. doi:10.1016/j.solener.2017.10.072.

[RWH+13] Jose Rivera, Philipp Wolfrum, Sandra Hirche, Christoph Goebel, and Hans-Arno Jacobsen. Alternating Direction Method of Multipliers for decentralized electric vehicle charging control. In *2013 IEEE 52nd Annual Conference on Decision and Control (CDC)*, pages 6960–6965, Piscataway, NJ, 2013. IEEE. doi:10.1109/CDC.2013.6760992.

[RZ04] L. Rouvel and F. Zimmermann. Berechnung des instationären thermischen Gebäudeverhaltens-Teil 1. *Heizung-Lüftung-Haustechnik*, (3):39–46, 2004. URL: http://www.gebsimu.de/2-K-Modell_HLH_2004.pdf.

[SAM16] Paul Stadler, Araz Ashouri, and Francois Marechal. Distributed model predictive control of energy systems in microgrids. In *10th Annual International Systems Conference proceedings*, pages 1–6, Piscataway, NJ, 2016. IEEE. doi:10.1109/SYSCON.2016.7490607.

[Sca09] Riccardo Scattolini. Architectures for distributed and hierarchical Model Predictive Control – A review. *Journal of Process Control*, 19(5):723–731, 2009. doi:10.1016/j.jprocont.2009.02.003.

[SHM16] Sebastian Stinner, Kristian Huchtemann, and Dirk Müller. Quantifying the operational flexibility of building energy systems with thermal energy storages. *Applied Energy*, 181:140–154, 2016. doi:10.1016/j.apenergy.2016.08.055.

[SJA09] B. Stott, J. Jardim, and O. Alsac. DC Power Flow Revisited. *IEEE Transactions on Power Systems*, 24(3):1290–1300, 2009. doi:10.1109/TPWRS.2009.2021235.

[SKP+] Herbet Sinnesbichler, Matthias Kersken, Matthias Pazold, Katrin Lenz, Hans Erhorn, Heike Erhorn-Kluttig, Patrick Schumacher, Sarah Doster, Michael Jäger, Florian Antretter, and Dietrich Schmidt. Windheizung 2.0 - Energiespeicherung und Stromnetzregelung mit hocheffizienten Gebäuden: Projektphase 2015/16. *Fraunhofer IBP, Stuttgart, Holzkirchen, Kassel.*

[SL12] Tyler H. Summers and John Lygeros. Distributed model predictive consensus via the Alternating Direction Method of Multipliers. In Bruce Hajek and Tamer Başar, editors, *50th Annual Allerton Conference on Communication, Control, and Computing (Allerton), 2012*, pages 79–84, Piscataway, NJ, 2012. IEEE. doi:10.1109/Allerton.2012.6483202.

[SNN+14] Pervez Hameed Shaikh, Nursyarizal Bin Mohd Nor, Perumal Nallagownden, Irraivan Elamvazuthi, and Taib Ibrahim. A review on optimized control systems for building energy and comfort management of smart sustainable buildings. *Renewable and Sustainable Energy Reviews*, 34:409–429, 2014. doi:10.1016/j.rser.2014.03.027.

[Sou12] M. Sourbron. Dynamic thermal behaviour of buildings with concrete core activation. *Dissertation, KU Leuven*, 2012.

[SQP+13] T. F. Stocker, D. Qin, G.-K. Plattner, M. Tignor, S. K. Allen, J. Boschung, A. Nauels, Y. Xia, V. Bex, and P. M. Midgley. Climate Change 2013: The Physical Science Basis. Contribution of Working Group I to the Fifth Assessment Report of the Intergovernmental Panel on Climate Change. *Cambridge University Press, Cambridge, United Kingdom and New York, NY, USA*, 2013.

[SSH13] K. Schaber, F. Steinke, and T. Hamacher. Managing Temporary Oversupply from Renewables Efficiently: Electricity Storage Versus Energy Sector Coupling. *International Energy Workshop, Paris*, 2013.

[Sti17] Stiebel Eltron. Planung und Installation Wärmepumpen. 2017.

[Sto09] Jakob Stoustrup. Plug & play control: Control technology towards new challenges. pages 1668–1683, 2009. doi:10.23919/ECC.2009.7074647.

[Str08] Goran Strbac. Demand side management: Benefits and challenges. *Energy Policy*, 36(12):4419–4426, 2008. doi:10.1016/j.enpol.2008.09.030.

[SVAS78] N. Sandell, P. Varaiya, M. Athans, and M. Safonov. Survey of decentralized control methods for large scale systems. *IEEE Transactions on Automatic Control*, 23(2):108–128, 1978. doi:10.1109/TAC.1978.1101704.

[TBS11] Klaus Trangbaek, Jan Bendtsen, and Jakob Stoustrup. Hierarchical Control for Smart Grids. *IFAC Proceedings Volumes*, 44(1):6130–6135, 2011. doi:10.3182/20110828-6-IT-1002.01977.

[TBSH15] S. Tenbohlen, M. Brunner, M. Schmidt, and T. Henzler. Be- und Entlastung elektrischer Verteilnetze durch Wärmepumpen bei der Wärmeerzeugung in Wohngebäuden. *Zentrum für Energieforschung, Universität Stuttgart*, 2015.

[The10] The European Parliament and the Council of the European Union. Directive 2010/31/EU, 2010. URL: https://eur-lex.europa.eu/LexUriServ/LexUriServ.do?uri=OJ:L:2010:153:0013:0035:DE:PDF.

[TSWB15] T. Tjaden, F. Schnorr, J. Weniger, and Berger, J. Quaschning, V. Einsatz von PV-Systemen mit Wärmepumpen und Batteriespeichern zur Erhöhung des Autarkiegrades in Einfamilienhaushalten. *30. Symposium Photovoltaische Solarenergie 2015, Kloster Banz, Bad Staffelstein*, 2015.

[UA12] A. Ulbig and G. Andersson. On operational flexibility in power systems: 2012 IEEE Power and Energy Society General Meeting. 2012. doi:10.1109/PESGM.2012.6344676.

[Uni15] United Nations Framework Convention on Climate Change. Paris Agreement. *online*, 2015. URL: https://unfccc.int/files/essential_background/convention/application/pdf/english_paris_agreement.pdf.

[U.S15] U.S. Department of Energy. EnergyPlusTM Documentation: Engineering Reference - The Reference to EnergyPlus Calculations. 2015. URL: https://energyplus.net/sites/default/files/pdfs_v8.3.0/EngineeringReference.pdf.

[U.S18] U.S. Department of Energy. EnergyPlusTM Version 9.0.1 Documentation: Input Output Reference. 2018. URL: https://energyplus.net/sites/all/modules/custom/nrel_custom/pdfs/pdfs_v9.0.1/InputOutputReference.pdf.

[VDI15a] VDI 2078. Berechnung der thermischen Lasten und Raumtemperaturen (Auslegung Kühllast und Jahressimulation).Calculation of thermal loads and room temperatures (design cooling load and annual simulation), 06-2015.

[VDI15b] VDI 6007. Berechnung des instationären thermischen Verhaltens von Räumen und Gebäuden. Calculation of transient thermal response of rooms and buildings Modelling of rooms, 06-2015.

[VDI16] VDI 6020. Anforderungen an thermisch-energetische Rechenverfahren zur Gebäude- und Anlagensimulation, 09-2016.

[VDI17] VDI 2067. Wirtschaftlichkeit gebäudetechnischer Anlagen Nutzenergiebedarf für die Trinkwassererwärmung. Economic efficiency of building installations Effective energy demands for heating drinking water, 04-2017.

[VDL+12] Clara Verhelst, David Degrauwe, Filip Logist, Jan van Impe, and Lieve Helsen. Multi-objective optimal control of an air-to-water heat pump for residential heating. *Building Simulation*, 5(3):281–291, 2012. doi:10.1007/s12273-012-0061-z.

[VGC+14] D. Vanhoudt, D. Geysen, B. Claessens, F. Leemans, L. Jespers, and J. van Bael. An actively controlled residential heat pump: Potential on peak shaving and maximization of self-consumption of renewable energy. *Renewable Energy*, 63:531–543, 2014. doi:10.1016/j.renene.2013.10.021.

[VHRW08] A. N. Venkat, I. A. Hiskens, J. B. Rawlings, and S. J. Wright. Distributed MPC Strategies With Application to Power System Automatic Generation Control. *IEEE Transactions on Control Systems Technology*, 16(6):1192–1206, 2008. doi:10.1109/TCST.2008.919414.

[VKA12] Evangelos Vrettos, Stephan Koch, and Goran Andersson. Load frequency control by aggregations of thermally stratified electric water heaters. In *3rd IEEE PES International Conference and Exhibition on Innovative Smart Grid Technologies (ISGT Europe), 2012*, pages 1–8, Piscataway, NJ, 2012. IEEE. doi:10.1109/ISGTEurope.2012.6465893.

[VKM+16a] Evangelos Vrettos, Emre Can Kara, Jason MacDonald, Goran Andersson, and Duncan S. Callaway. Experimental Demonstration of Frequency Regulation by Commercial Buildings – Part I: Modeling and Hierarchical Control Design. *IEEE Transactions on Smart Grid*, page 1, 2016. doi:10.1109/TSG.2016.2628897.

[VKM+16b] Evangelos Vrettos, Emre Can Kara, Jason MacDonald, Goran Andersson, and Duncan S. Callaway. Experimental Demonstration of Frequency Regulation by Commercial Buildings – Part II: Results and Performance Evaluation. *IEEE Transactions on Smart Grid*, page 1, 2016. doi:10.1109/TSG.2016.2628893.

[VLOA13] Evangelos Vrettos, Kuan Lin Lai, Frauke Oldewurtel, and Goran Andersson. Predictive Control of Buildings for Demand Response with Dynamic Day-ahead and Real-time Prices. *2013 European Control Conference (ECC)*, 2013. doi:10.23919/ECC.2013.6669762.

[VLvH12] Clara Verhelst, Filip Logist, Jan van Impe, and Lieve Helsen. Study of the optimal control problem formulation for modulating air-to-water heat pumps connected to a residential floor heating system. *Energy and Buildings*, 45:43–53, 2012. doi:10.1016/j.enbuild.2011.10.015.

[VRW05] A. N. Venkat, J. B. Rawlings, and S. J. Wright. Stability and optimality of distributed model predictive control. In *2005 44th IEEE Conference on Decision and Control & European Control Conference*, pages 6680–6685, Piscataway, N.J, 2005. Institute of Electrical and Electronics Engineers. doi:10.1109/CDC.2005.1583235.

[VRW06] A. N. Venkat, J. B. Rawlings, and S. J. Wright. Implementable distributed model predictive control with guaranteed performance properties. In *American Control Conference, 2006*, page 6 pp, Piscataway, NJ, 2006. IEEE Operations Center. doi:10.1109/ACC.2006.1655424.

[Wag15] Matthias Wagnitz. Ausrichtung der Heizungs-, Klima- und Lüftungstechnik an den Bedürfnissen der Nutzer im Wohnungsbau. *Dissertation, Technische Universität Dresden*, 2015.

[WDCD14] Sam Weckx, Reinhilde D'hulst, Bert Claessens, and Johan Driesensam. Multiagent Charging of Electric Vehicles Respecting Distribution Transformer Loading and Voltage Limits. *IEEE Transactions on Smart Grid*, 5(6):2857–2867, 2014. doi:10.1109/TSG.2014.2345886.

[Wim04] Roger Wilfried Wimmer. Regelung einer Wärmepumpenanlage mit Model Predictive Control. *Dissertation, Eidgenössische Technische Hochschule ETH Zürich, Nr. 15709*, 2004.

[WKB+15] Karl Worthmann, Christopher M. Kellett, Philipp Braun, Lars Grune, and Steven R. Weller. Distributed and Decentralized Control of Residential Energy Systems Incorporating Battery Storage. *IEEE Transactions on Smart Grid*, 6(4):1914–1923, 2015. doi:10.1109/TSG.2015.2392081.

[WKGW14] Karl Worthmann, Christopher M. Kellett, Lars Grüne, and Steven R. Weller. Distributed Control of Residential Energy Systems using a Market Maker. *IFAC Proceedings Volumes*, 47(3):11641–11646, 2014. doi:10.3182/20140824-6-ZA-1003.01785.

[Woh17] Brendt Wohlberg. ADMM Penalty Parameter Selection by Residual Balancing: arXiv:1704.06209v1. *arXiv*, 2017. URL: https://arxiv.org/abs/1704.06209.

[WW17] Marco Wagler and Rolf Witzmann. Effects of asymmetrically connected PV and battery systems on the node voltages and pen-conductor currents in low-voltage grids. *CIRED - Open Access Proceedings Journal*, 2017(1):2246–2249, 2017. doi:10.1049/oap-cired.2017.0315.

[XFG17] Zheng Xu, Mario Figueiredo, and Tom Goldstein. Adaptive ADMM with Spectral Penalty Parameter Selection. *Proceedings of the 20th International Conference on Artificial Intelligence and Statistics*, (PMLR 54):718–727, 2017. URL: http://proceedings.mlr.press/v54/xu17a/xu17a.pdf.

[XTL+17] Zheng Xu, Gavin Taylor, Hao Li, Mário A. T. Figueiredo, Xiaoming Yuan, and Tom Goldstein. Adaptive Consensus ADMM for Distributed Optimization. *Proceedings of the 34th International Conference on Machine Learning, Sidney*, (70):3841–3850, 2017.

[ZMPK+12] Yi Zong, Lucian Mihet-Popa, Daniel Kullmann, Anders Thavlov, Oliver Gehrke, and Henrik W. Bindner. Model Predictive Controller for Active Demand Side Management with PV self-consumption in an intelligent building. In *3rd IEEE PES International Conference and Exhibition on Innovative Smart Grid Technologies (ISGT Europe), 2012*, pages 1–8, Piscataway, NJ, 2012. IEEE. doi:10.1109/ISGTEurope.2012.6465618.

[ZMST11] Ray Daniel Zimmerman, Carlos Edmundo Murillo-Sanchez, and Robert John Thomas. MATPOWER: Steady-State Operations, Planning, and Analysis Tools for Power Systems Research and Education. *IEEE Transactions on Power Systems*, 26(1):12–19, 2011. doi:10.1109/TPWRS.2010.2051168.

Appendix A

Modeling and Validation

A.1 Convex Optimization

An introduction to convex optimization is given in [BV04]. Throughout the thesis optimization problems of the form

$$\begin{aligned} \min_{x \in \mathbb{R}^n} \quad & f(x) \\ \text{subject to} \quad & x \in D \end{aligned} \tag{A.1}$$

with cost function $f : \mathbb{R}^n \to \mathbb{R}$, decision variable $x \in \mathbb{R}^n$ and constraint set $D \subset \mathbb{R}^n$ resulting from equality and inequality constraints occur. The above problem is called convex when f is a convex function and D is a convex set.
Convex set: The set D is convex if for all $x_1, x_2 \in D$ and for all $\theta \in (0, 1)$

$$\theta x_1 + (1 - \theta) x_2 \in D \tag{A.2}$$

holds.
Convex function: The function $f : D \to \mathbb{R}$ defined on a convex set D is called convex if for all $x_1, x_2 \in D, x_1 \neq x_2$ and for all $\theta \in (0, 1)$

$$f(\theta x_1 + (1 - \theta) x_2) \leq \theta f(x_1) + (1 - \theta) f(x_2) \tag{A.3}$$

holds. A function is strictly convex if the above definition holds for the strict inequality.

A.2 Thermal Response of a Component and Chain Matrix

The derivation of the matrix representation of the thermal two-port network for a homogeneous material layer in the frequency domain can be found in [Pip57, Rou72, Dav94, LCRA95]. The ordinary differential Equation (2.11) after applying the Fourier transformation on the quantities on both sides has the general solution

$$T(\omega, x) = F_1(\omega) \cosh\left(x \sqrt{j\omega \frac{c\rho}{\lambda}}\right) + F_2(\omega) \sinh\left(x \sqrt{j\omega \frac{c\rho}{\lambda}}\right). \tag{A.4}$$

With the boundary conditions at $T(\omega, x = 0)$ and Equation (2.12) one obtains

$$F_1(\omega) = T(\omega, x = 0) \tag{A.5}$$

and

$$\dot{q}(\omega, x) = -\lambda \frac{\partial}{\partial x} T(\omega, x) \tag{A.6}$$

$$= -\lambda \left(F_1(\omega) \sqrt{j\omega \frac{c\rho}{\lambda}} \sinh\left(x \sqrt{j\omega \frac{c\rho}{\lambda}} \right) + F_2(\omega) \sqrt{j\omega \frac{c\rho}{\lambda}} \cosh\left(x \sqrt{j\omega \frac{c\rho}{\lambda}} \right) \right), \tag{A.7}$$

evaluated at $x = 0$ leads to

$$\dot{q}(\omega, x = 0) = -\lambda F_2(\omega) \sqrt{j\omega \frac{c\rho}{\lambda}} \tag{A.8}$$

$$-\dot{q}(\omega, x = 0) \frac{1}{\lambda \sqrt{j\omega \frac{c\rho}{\lambda}}} = F_2(\omega). \tag{A.9}$$

Thus $T(\omega, x)$ and $\dot{q}(\omega, x)$ become

$$T(\omega, x) = T(\omega, x = 0) \cosh\left(x \sqrt{j\omega \frac{c\rho}{\lambda}} \right) - \dot{q}(\omega, x = 0) \frac{1}{\lambda \sqrt{j\omega \frac{c\rho}{\lambda}}} \sinh\left(x \sqrt{j\omega \frac{c\rho}{\lambda}} \right) \tag{A.10}$$

$$\dot{q}(\omega, x) = -T(\omega, x = 0) \lambda \sqrt{j\omega \frac{c\rho}{\lambda}} \sinh\left(x \sqrt{j\omega \frac{c\rho}{\lambda}} \right) + \dot{q}(\omega, x = 0) \cosh\left(x \sqrt{j\omega \frac{c\rho}{\lambda}} \right) \tag{A.11}$$

and rearranging for matrix form results in

$$\begin{pmatrix} T(\omega, x = 0) \\ \dot{q}(\omega, x = 0) \end{pmatrix} = \begin{pmatrix} \cosh\left(x \sqrt{j\omega \frac{c\rho}{\lambda}} \right) & \frac{1}{\lambda \sqrt{j\omega \frac{c\rho}{\lambda}}} \sinh\left(x \sqrt{j\omega \frac{c\rho}{\lambda}} \right) \\ \lambda \sqrt{j\omega \frac{c\rho}{\lambda}} \sinh\left(x \sqrt{j\omega \frac{c\rho}{\lambda}} \right) & \cosh\left(x \sqrt{j\omega \frac{c\rho}{\lambda}} \right) \end{pmatrix} \begin{pmatrix} T(\omega, x) \\ \dot{q}(\omega, x) \end{pmatrix}. \tag{A.12}$$

With $R = \frac{x}{\lambda}$ in [m^{2}K/W] and $C = \rho c x$ in [J/(m^{2}K)] the matrix in Equation (A.12) can be rewritten as

$$\begin{pmatrix} T(\omega, x = 0) \\ \dot{q}(\omega, x = 0) \end{pmatrix} = \begin{pmatrix} \cosh\left(\sqrt{j\omega RC} \right) & \frac{R}{\sqrt{j\omega RC}} \sinh\left(\sqrt{j\omega RC} \right) \\ \frac{\sqrt{j\omega RC}}{R} \sinh\left(\sqrt{j\omega RC} \right) & \cosh\left(\sqrt{j\omega RC} \right) \end{pmatrix} \begin{pmatrix} T(\omega, x) \\ \dot{q}(\omega, x) \end{pmatrix}. \tag{A.13}$$

The real and imaginary parts of the matrix entries $\left(\begin{smallmatrix} a_{11} & a_{12} \\ a_{21} & a_{22} \end{smallmatrix}\right)$ can be further separated with $\sqrt{j} = \frac{1}{\sqrt{2}}(1 + j)$ and addition theorems with complex arguments to obtain the representation

in [Rou72]:

$$\mathrm{Re}(\underline{a}_{11}) = \mathrm{Re}(\underline{a}_{22}) = \cosh\sqrt{\frac{1}{2}\omega RC}\cos\sqrt{\frac{1}{2}\omega RC} \tag{A.14}$$

$$\mathrm{Im}(\underline{a}_{11}) = \mathrm{Im}(\underline{a}_{22}) = \sinh\sqrt{\frac{1}{2}\omega RC}\sin\sqrt{\frac{1}{2}\omega RC} \tag{A.15}$$

$$\mathrm{Re}(\underline{a}_{12}) = R\sqrt{\frac{1}{2\omega RC}}\left(\cosh\sqrt{\frac{1}{2}\omega RC}\sin\sqrt{\frac{1}{2}\omega RC} + \sinh\sqrt{\frac{1}{2}\omega RC}\cos\sqrt{\frac{1}{2}\omega RC}\right) \tag{A.16}$$

$$\mathrm{Im}(\underline{a}_{12}) = R\sqrt{\frac{1}{2\omega RC}}\left(\cosh\sqrt{\frac{1}{2}\omega RC}\sin\sqrt{\frac{1}{2}\omega RC} - \sinh\sqrt{\frac{1}{2}\omega RC}\cos\sqrt{\frac{1}{2}\omega RC}\right) \tag{A.17}$$

$$\mathrm{Re}(\underline{a}_{21}) = -\frac{1}{R}\sqrt{\frac{1}{2}\omega RC}\left(\cosh\sqrt{\frac{1}{2}\omega RC}\sin\sqrt{\frac{1}{2}\omega RC} - \sinh\sqrt{\frac{1}{2}\omega RC}\cos\sqrt{\frac{1}{2}\omega RC}\right) \tag{A.18}$$

$$\mathrm{Im}(\underline{a}_{21}) = \frac{1}{R}\sqrt{\frac{1}{2}\omega RC}\left(\cosh\sqrt{\frac{1}{2}\omega RC}\sin\sqrt{\frac{1}{2}\omega RC} + \sinh\sqrt{\frac{1}{2}\omega RC}\cos\sqrt{\frac{1}{2}\omega RC}\right) \tag{A.19}$$

A.3 $3R2C$, $2R1C$ and $1R1C$ Parameters

The equations are derived in [Rou72] and [RZ04] and are used in the VDI guidelines [VDI15b, VDI16]:

$3R2C$

$$R_1 = \frac{1}{A}\frac{(\mathrm{Re}(\underline{a}_{22})-1)\,\mathrm{Re}(\underline{a}_{12}) + \mathrm{Im}(\underline{a}_{22})\,\mathrm{Im}(\underline{a}_{12})}{(\mathrm{Re}(\underline{a}_{22})-1)^2 + \mathrm{Im}(\underline{a}_{22})^2} \quad [\mathrm{K/W}] \tag{A.20}$$

$$R_2 = \frac{1}{A}\frac{(\mathrm{Re}(\underline{a}_{11})-1)\,\mathrm{Re}(\underline{a}_{12}) + \mathrm{Im}(\underline{a}_{11})\,\mathrm{Im}(\underline{a}_{12})}{(\mathrm{Re}(\underline{a}_{11})-1)^2 + \mathrm{Im}(\underline{a}_{11})^2} \quad [\mathrm{K/W}] \tag{A.21}$$

$$R_3 = \left(\frac{1}{A}\sum_{v=1}^{n}\frac{x_v}{\lambda_v}\right) - R_1 - R_2 \quad [\mathrm{K/W}] \tag{A.22}$$

$$C_1 = \frac{A}{\omega}\frac{(\mathrm{Re}(\underline{a}_{22})-1)^2 + \mathrm{Im}(\underline{a}_{22})^2}{(\mathrm{Re}(\underline{a}_{12})\,\mathrm{Im}(\underline{a}_{22}) - (\mathrm{Re}(\underline{a}_{22})-1)\,\mathrm{Im}(\underline{a}_{12})} \quad [\mathrm{J/K}] \tag{A.23}$$

$$C_2 = \frac{A}{\omega}\frac{(\mathrm{Re}(\underline{a}_{11})-1)^2 + \mathrm{Im}(\underline{a}_{11})^2}{(\mathrm{Re}(\underline{a}_{12})\,\mathrm{Im}(\underline{a}_{11}) - (\mathrm{Re}(\underline{a}_{11})-1)\,\mathrm{Im}(\underline{a}_{12})} \quad [\mathrm{J/K}] \tag{A.24}$$

$2R1C$

$$R_w = R_1 + R_2 + R_3 \quad [\mathrm{K/W}] \tag{A.25}$$

$$\tilde{R}_2 = R_2 + R_3 \quad [\mathrm{K/W}] \tag{A.26}$$

$$\tilde{C}_1 = \frac{1}{\omega R_1}\frac{R_w A - \mathrm{Re}(\underline{a}_{12})\,\mathrm{Re}(\underline{a}_{22}) - \mathrm{Im}(\underline{a}_{12})\,\mathrm{Im}(\underline{a}_{22})}{\mathrm{Re}(\underline{a}_{22})\,\mathrm{Im}(\underline{a}_{12}) - (\mathrm{Re}\,\underline{a}_{12})\,\mathrm{Im}(\underline{a}_{22})} \quad [\mathrm{J/K}] \tag{A.27}$$

$1R1C$

$$R_1 = \frac{1}{A}\frac{(\mathrm{Re}(\underline{a}_{22})-1)\,\mathrm{Re}(\underline{a}_{12}) + \mathrm{Im}(\underline{a}_{22})\,\mathrm{Im}(\underline{a}_{12})}{(\mathrm{Re}(\underline{a}_{22})-1)^2 + \mathrm{Im}(\underline{a}_{22})^2} \quad [\mathrm{K/W}] \tag{A.28}$$

$$\tilde{C}_1 = \frac{1}{\omega R_1}\frac{R_w A - \mathrm{Re}(\underline{a}_{12})\,\mathrm{Re}(\underline{a}_{22}) - \mathrm{Im}(\underline{a}_{12})\,\mathrm{Im}(\underline{a}_{22})}{\mathrm{Re}(\underline{a}_{22})\,\mathrm{Im}(\underline{a}_{12}) - (\mathrm{Re}\,\underline{a}_{12})\,\mathrm{Im}(\underline{a}_{22})} \quad [\mathrm{J/K}] \tag{A.29}$$

A.4 Material Compositions

Table A.1: *Component composition based on the TABULA typology and own selection with [DIN10]*

Building type *E*	**density** ρ $\frac{kg}{m^3}$	**spec. heat capacity** c Ws/(kgK)	**conductivity** λ W/(mK)	**thickness** m
		Outer wall		
Plaster	1400	1000	0.7	0.02
Vert. perforated brick	600	1000	0.4	0.25
Therm. insulation 035	80	840	0.035	0.12
Lime mortar	1800	1000	0.87	0.02
		Inner wall		
Lightweight concrete	1200	1000	0.4	0.12
		Floor		
Tile	2000	1000	1	0.02
Cement screed	2000	1000	1.4	0.04
Therm. insulation 035	80	840	0.035	0.1
Concrete	1800	1000	1.15	0.24
Plaster	1200	1000	0.35	0.01
		Roof		
OSB-Plate	900	1000	0.21	0.015
Polystyrene	60	1000	0.04	0.075
Roofing tile	530	900	0.14	0.04
		Door		
Maplewood	600	2100	0.1	0.012
Foam glass granulate	200	1000	0.08	0.025
Maplewood	600	2100	0.1	0.016
Windows		**g-value** [ ]	**U-value** W/(m^{2}K)	
		0.6	1.3	

Table A.2: *Component composition based on the TABULA typology and [TBSH15]*

Building type *J*	**density ρ** $\frac{\text{kg}}{\text{m}^3}$	**spec. heat capacity c** Ws/(kgK)	**conductivity λ** W/(mK)	**thickness** m
		Outer wall		
Plaster	1200	1000	0.35	0.015
Vert. perforated brick	1500	1000	0.5	0.14
Polystyrene	15	1250	0.04	0.1
Vert. perforated brick	1500	1000	0.5	0.14
Plaster	1200	1000	0.35	0.015
		Inner wall		
Plaster	900	1000	0.21	0.013
Mineral rock wool	60	1000	0.04	0.1
Plaster	900	1000	0.21	0.013
		Floor		
Tile	2000	1000	1	0.01
Cement screed	2000	1000	1.2	0.045
Polystyrene	15	1250	0.03	0.1
Reinforced concrete	2400	840	2.2	0.14
Plaster	1200	1000	0.35	0.01
		Roof		
OSB board	600	1880	0.13	0.015
Polystyrene	15	1250	0.045	0.16
Vapor barrier	700	1000	0.13	0.02
Roofing tile	530	900	0.5	0.04
		Door		
Maplewood	700	1600	0.185	0.011
Foam glass granulate	200	1000	0.08	0.015
Maplewood	700	1600	0.185	0.016
Windows		**g-value** [ ]	**U-value** W/(m^{2}K)	
		0.6	1.4	

Table A.3: *Component composition based on the TABULA typology and [Aro14]*

Building type L	**density** ρ $\frac{kg}{m^3}$	**spec. heat capacity** c Ws/(kgK)	**conductivity** λ W/(mK)	**thickness** m
		Outer wall		
Plasterboard	900	1000	0.21	0.015
Mineral rock wool	60	1000	0.04	0.08
Mineral rock wool	60	1000	0.04	0.22
Wood	600	2100	0.1	0.1
		Inner wall		
Plasterboard	900	1000	0.21	0.015
Mineral rock wool	60	1000	0.04	0.1
Plasterboard	900	1000	0.21	0.015
		Floor		
Tile	2000	1000	1	0.02
Cement screed	2000	1000	1.4	0.12
Polystyrene	15	1250	0.03	0.22
Reinforced concrete	2400	840	2.2	0.2
Plaster	1200	1000	0.35	0.01
		Roof		
OSB board	650	1880	0.13	0.015
Polystyrene	15	1250	0.04	0.35
Vapor barrier	700	1000	0.13	0.02
Roofing tile	530	900	0.14	0.04
		Door		
Maplewood	600	2100	0.1	0.015
Foam glass granulate	200	1000	0.08	0.055
Maplewood	600	2100	0.1	0.025
Windows		**g-value** [ ]	**U-value** W/(m^{2}K)	
		0.6	0.7	

A.5 Distribution Factors

Note that the area A_{wo} contains both the outer wall and the roof areas.
Initial area-weighted s-factors

$$s_{wi} = (1 - s_z)\frac{A_{wi}}{A_{wi} + A_{wo} + A_{fl}} \tag{A.30}$$

$$s_{wo} = (1 - s_z)\frac{A_{wo}}{A_{wi} + A_{wo} + A_{fl}} \tag{A.31}$$

$$s_{fl} = (1 - s_z)\frac{A_{fl}}{A_{wi} + A_{wo} + A_{fl}} \tag{A.32}$$

Area-weighted g-factors

$$g_{wi} = (1 - g_z)\frac{A_{wi}}{A_{wi} + A_{wo} + A_{fl}} \tag{A.33}$$

$$g_{wo} = (1 - g_z)\frac{A_{wo}}{A_{wi} + A_{wo} + A_{fl}} \tag{A.34}$$

$$g_{fl} = (1 - g_z)\frac{A_{fl}}{A_{wi} + A_{wo} + A_{fl}} \tag{A.35}$$

Initial area-weighted f-factors

$$f_{wi} = (1 - f_z)\frac{A_{wi}}{A_{wi} + A_{wo} + A_{fl}} \tag{A.36}$$

$$f_{wo} = (1 - f_z)\frac{A_{wo}}{A_{wi} + A_{wo} + A_{fl}} \tag{A.37}$$

$$f_{fl} = (1 - f_z)\frac{A_{fl}}{A_{wi} + A_{wo} + A_{fl}} \tag{A.38}$$

A.6 Delta-Star Transformation

Computation of the resistances $R_{starA/B/C}$:

$$R_{starA} = \frac{R_{conv,wo}R_{conv,fl}}{R_{conv,wo} + R_{conv,fl} + R_{rad,wo-fl}} \tag{A.39}$$

$$R_{starB} = \frac{R_{conv,wo}R_{rad,wo-fl}}{R_{conv,wo} + R_{conv,fl} + R_{rad,wo-fl}} \tag{A.40}$$

$$R_{starC} = \frac{R_{conv,fl}R_{rad,wo-fl}}{R_{conv,wo} + R_{conv,fl} + R_{rad,wo-fl}}. \tag{A.41}$$

The differential equations for the RC-model from Figure 2.14 are

$$\begin{aligned}\frac{dT_z}{dt} &= \frac{1}{R_{vent}C_z}(T_a - T_z) + \frac{1}{R_{wi}C_z}(T_{wi} - T_z) + \frac{1}{R_{starA}C_z}(T_{star} - T_z) \\ &\quad + \frac{s_z}{C_z}\varphi_{sg} + \frac{g_z}{C_z}\varphi_{ig} + \frac{f_z}{C_z}\varphi_h\end{aligned} \tag{A.42}$$

$$\frac{dT_{wi}}{dt} = \frac{1}{R_{wi}C_{wi}}(T_z - T_{wi}) + \frac{s_{wi}}{C_{wi}}\varphi_{sg} + \frac{g_{wi}}{C_{wi}}\varphi_{ig} + \frac{f_{wi}}{C_{wi}}\varphi_h \tag{A.43}$$

$$\frac{dT_{wo}}{dt} = \frac{1}{R_{wo,2}C_{wo}}(T_{a,eq} - T_{wo}) + \frac{1}{R_{wo,1}C_{wo}}(T_{star} - T_{wo}) + \frac{s_{wo}}{C_{wo}}\varphi_{sg} + \frac{g_{wo}}{C_{wo}}\varphi_{ig} + \frac{f_{wo}}{C_{wo}}\varphi_h \tag{A.44}$$

$$\frac{dT_{fl}}{dt} = \frac{1}{R_{fl,2}C_{fl}}(T_g - T_{fl}) + \frac{1}{R_{fl,1}C_{fl}}(T_{star} - T_{fl}) + \frac{s_{fl}}{C_{fl}}\varphi_{sg} + \frac{g_{fl}}{C_{fl}}\varphi_{ig} + \frac{f_{fl}}{C_{fl}}\varphi_h \tag{A.45}$$

with

$$R_{wo,1} = \tilde{R}_{wo,1} + R_{starB} \tag{A.46}$$

$$R_{fl,1} = \tilde{R}_{fl,1} + R_{starC}. \tag{A.47}$$

The heat flow balance at T_{star} leads to

$$0 = \frac{1}{R_{starA}}(T_z - T_{star}) + \frac{1}{R_{wo,1}}(T_{wo} - T_{star}) + \frac{1}{R_{fl,1}}(T_{fl} - T_{star}) \tag{A.48}$$

$$T_{star} = \frac{1}{SR_{starA}}T_z + \frac{1}{SR_{wo,1}}T_{wo} + \frac{1}{SR_{fl,1}}T_{fl} \tag{A.49}$$

with

$$S = \frac{1}{R_{starA}} + \frac{1}{R_{wo,1}} + \frac{1}{R_{fl,1}}. \tag{A.50}$$

Inserting in Equations (A.42)-(A.45) results in

$$\begin{aligned}\frac{dT_z}{dt} &= \frac{1}{R_{vent}C_z}(T_a - T_z) + \frac{1}{R_{wi}C_z}(T_{wi} - T_z) \\ &+ \frac{1}{R_{starA}C_z}\Big((\frac{1}{SR_{starA}} - 1)T_z + \frac{1}{SR_{wo,1}}T_{wo} + \frac{1}{SR_{fl,1}}T_{fl}\Big) \\ &+ \frac{s_z}{C_z}\varphi_{sg} + \frac{g_z}{C_z}\varphi_{ig} + \frac{f_z}{C_z}\varphi_h\end{aligned} \tag{A.51}$$

$$\frac{dT_{wi}}{dt} = \frac{1}{R_{wi}C_{wi}}(T_z - T_{wi}) + \frac{s_{wi}}{C_{wi}}\varphi_{sg} + \frac{g_{wi}}{C_{wi}}\varphi_{ig} + \frac{f_{wi}}{C_{wi}}\varphi_h \tag{A.52}$$

$$\begin{aligned}\frac{dT_{wo}}{dt} &= \frac{1}{R_{wo,2}C_{wo}}(T_{a,eq} - T_{wo}) + \frac{1}{R_{wo,1}C_{wo}}\Big(\frac{1}{SR_{starA}}T_z + (\frac{1}{SR_{wo,1}} - 1)T_{wo} + \frac{1}{SR_{fl,1}}T_{fl}\Big) \\ &+ \frac{s_{wo}}{C_{wo}}\varphi_{sg} + \frac{g_{wo}}{C_{wo}}\varphi_{ig} + \frac{f_{wo}}{C_{wo}}\varphi_h\end{aligned} \tag{A.53}$$

$$\begin{aligned}\frac{dT_{fl}}{dt} &= \frac{1}{R_{fl,2}C_{fl}}(T_g - T_{fl}) + \frac{1}{R_{fl,1}C_{fl}}\Big(\frac{1}{SR_{starA}}T_z + \frac{1}{SR_{wo,1}}T_{wo} + (\frac{1}{SR_{fl,1}} - 1)T_{fl}\Big) \\ &+ \frac{s_{fl}}{C_{fl}}\varphi_{sg} + \frac{g_{fl}}{C_{fl}}\varphi_{ig} + \frac{f_{fl}}{C_{fl}}\varphi_h\end{aligned} \tag{A.54}$$

A.7 Computation of the Surface Temperatures

The surface temperatures are computed based on the RC-model output for a comparison with the EnergyPlus values. Derived like the surface temperature of the floor in Equations (2.38) and (2.39), the inner and outer wall temperatures for the models D and F are

$$T_{wi,s} = \frac{R_{si,wi}T_{wi} + \tilde{R}_{wi,1}T_z}{R_{wi,1}} \tag{A.55}$$

$$T_{wo,s} = \frac{R_{si,wo}T_{wo} + \tilde{R}_{wo,1}T_z}{R_{wo,1}} \tag{A.56}$$

with

$$\tilde{R}_{wi,1} = R_{wi,1} - R_{si,wi} \tag{A.57}$$

$$\tilde{R}_{wo,1} = R_{wo,1} - R_{si,wo}. \tag{A.58}$$

Model R

$$T_{wi,s} = \frac{R_{si,wi}T_{wi} + \tilde{R}_{wi,1}T_z}{R_{wi,1}} \tag{A.59}$$

$$T_{wo,s} = \frac{R_{starB}T_{wo} + \tilde{R}_{wo,1}T_{star}}{\tilde{R}_{wo,1} + R_{starB}} \tag{A.60}$$

$$T_{fl,s} = \frac{R_{starC}T_{fl} + \tilde{R}_{fl,1}T_{star}}{\tilde{R}_{fl,1} + R_{starC}} \tag{A.61}$$

with $\tilde{R}_{wi,1}$ and $\tilde{R}_{wo,1}$ as defined in Equations (A.57) and (A.46).

A.8 Cross Validation with sRMSE

$$sRMSE = \sqrt{\frac{1}{N\sigma^2_{x_{E+}}} \sum_{i=1}^{N} (x_{i,RC} - x_{i,E+})^2} \tag{A.62}$$

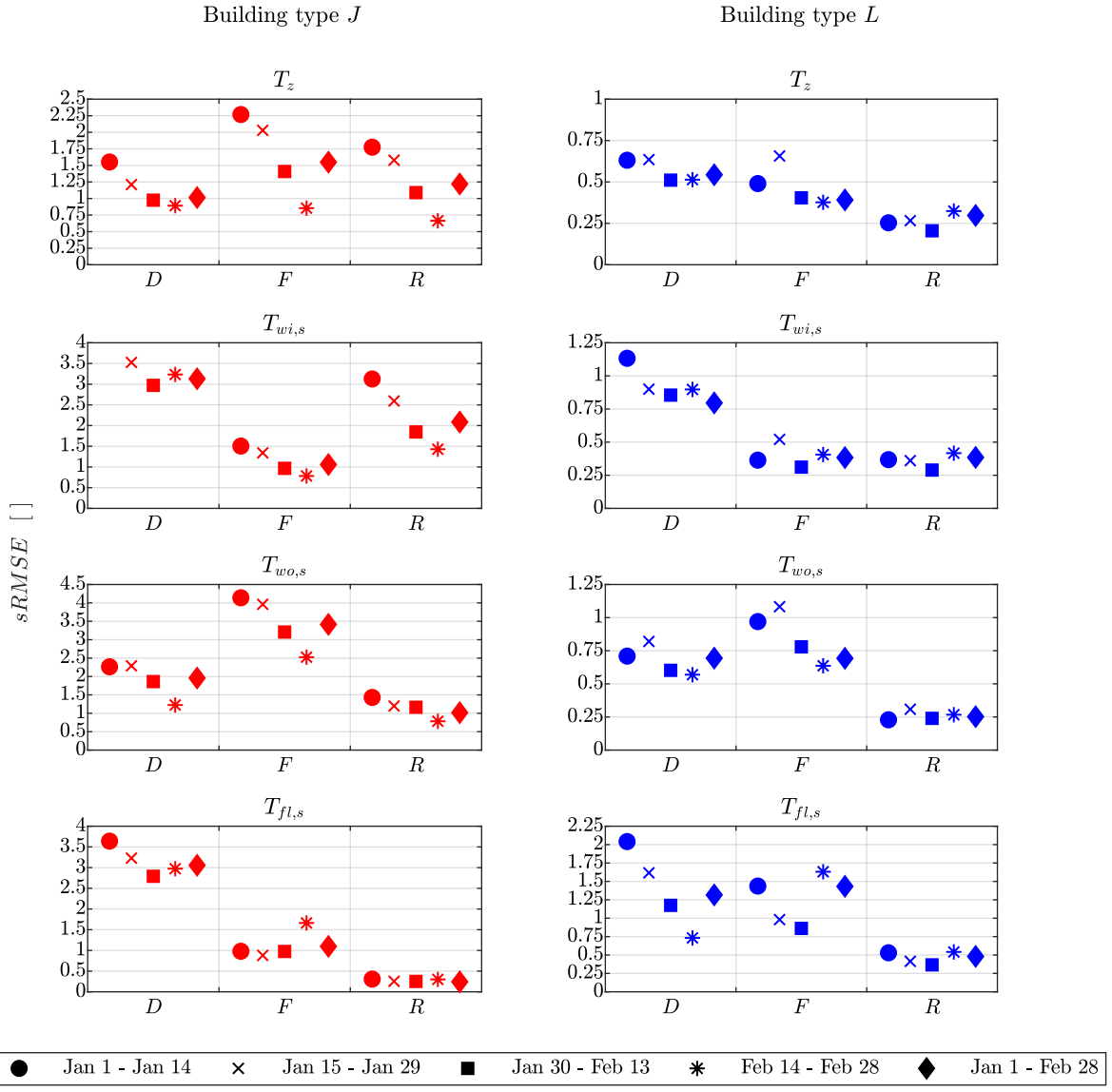

Figure A.1: *Standardized RMSE for the RC-models D,F, and R compared to the EnergyPlus(E+) reference for building type J and L.*

A.9 Back-Calculation of EnergyPlus Temperatures for 1-Step Prediction

Models D and F: The relationship from Equation (2.39) can be used to compute temperatures based on the EnergyPlus surface temperatures $T_{wi,E+}, T_{wo,E+}, T_{fl,E+}$ for application in the RC-model to update the state for the 1-step prediction:

$$T_{wi} = \frac{R_{wi,1}}{R_{si,wi}} T_{wi,E+} - \frac{\tilde{R}_{wi,1}}{R_{si,wi}} T_{z,E+} \tag{A.63}$$

$$T_{wo} = \frac{R_{wo,1}}{R_{si,wo}} T_{wo,E+} - \frac{\tilde{R}_{wo,1}}{R_{si,wo}} T_{z,E+} \tag{A.64}$$

$$T_{fl} = \frac{R_{fl,1}}{R_{si,fl}} T_{fl,E+} - \frac{\tilde{R}_{fl,1}}{R_{si,fl}} T_{z,E+}. \tag{A.65}$$

Model R: Applying the heat balance equations on the extended model leads to the following temperatures:

$$T_{wi} = \frac{R_{wi,1}}{R_{si,wi}} T_{wi,E+} - \frac{\tilde{R}_{wi,1}}{R_{si,wi}} T_{z,E+} \tag{A.66}$$

$$T_{wo} = \frac{R_{wo,1}}{R_{starB}} T_{wo,E+} - \frac{\tilde{R}_{wo,1}}{R_{starB}} T_{star} \tag{A.67}$$

$$T_{fl} = \frac{R_{fl,1}}{R_{starC}} T_{fl,E+} - \frac{\tilde{R}_{fl,1}}{R_{starC}} T_{star}. \tag{A.68}$$

T_{wi} can be directly computed. Inserting Equation (A.49) with (A.50) in Equations (A.67) and (A.68) allows to solve the equation system for the outer wall and floor temperatures after some basic algebra.

A.10 R^2 Model $D+$ and F

Table A.4: *Accuracy of the simulation with error propagation (Sim.) versus 1-step prediction error (1+) of models D+ and F for building types J and L over the period Feb 14-Feb 28.*

		D+				***F***			
		$RMSE$ [°C]		R^2 [ ]		$RMSE$ [°C]		R^2 [ ]	
		Sim.	1+	Sim.	1+	Sim.	1+	Sim.	1+
J	T_z	1.4	1.8	-2.939	-5.459	0.6	0.1	0.255	0.968
	$T_{wi,s}$	0.6	0.5	0.581	0.737	0.7	0.1	0.351	0.993
	$T_{wo,s}$	0.5	1.0	0.233	-2.557	1.3	0.0	-5.020	0.996
	$T_{fl,s}$	1.1	0.3	0.631	0.969	3.0	0.2	-1.864	0.992
L	T_z	0.9	0.6	0.797	0.898	0.7	0.2	0.869	0.993
	$T_{wi,s}$	0.9	0.2	0.803	0.986	0.8	0.1	0.837	0.998
	$T_{wo,s}$	0.7	0.5	0.870	0.935	1.2	0.1	0.632	0.998
	$T_{fl,s}$	0.5	0.2	0.886	0.990	2.4	0.1	-1.779	0.998

A.11 Homogeneous Solution and State Trajectories

The following paragraph defines the time constants and state transition of the state-space model and is based on [MH95, Row02]. The scalar differential equation

$$\dot{x}(t) = ax(t) + bu(t) + ed(t) \tag{A.69}$$

has the homogeneous response

$$x(t) = e^{at}x(0) = e^{-\frac{t}{\tau}}x(0) \tag{A.70}$$

with time constant $\tau = -\frac{1}{a}$. The homogeneous response is defined as the state response of the system with zero input $u(t) = 0, d(t) = 0$ for an arbitrary initial condition $x(0)$. The homogeneous solution to the n-th order linear system

$$\dot{x}(t) = Ax(t) + Bu(t) + Ed(t) \tag{A.71}$$

is then

$$x(t) = e^{At}x(0) \tag{A.72}$$

with the matrix exponential $e^{At} = (I + At + \frac{A^2t^2}{2!} + \frac{A^3t^3}{3!} \ldots)$ and $A \in \mathbb{R}^{n\times n}$. Since each entry in e^{At} is a sum of scalar exponential terms, so is the homogeneous response of the states. This leads to the approach

$$x_i(t) = \sum_{j=1}^{n} v_{ij}e^{\lambda_j t} \tag{A.73}$$

of each state x_i being a weighted sum with coefficients v_{ij}, which depend on the system's structure and inital values $x(0)$ [Row02]. With the derivate of Equation (A.73) and $\dot{x} = Ax$ one can show that it must hold that [Row02]

$$\lambda_i v_i = Av_i \quad \forall i = 1, ..., n. \tag{A.74}$$

λ_i and v_i are the i-th eigenvalue and corresponding eigenvector of system matrix A. Like in [MH95], the time constants in Figure 2.27 are then defined as

$$\tau_i = -\frac{1}{\lambda_i} \quad \forall i = 1, ..., n. \tag{A.75}$$

$V = [v_1|v_2|\ldots|v_n]$ is the matrix composed of the system's n eigenvectors in it's columns. In case of distinct eigenvalues, the homogeneous response of the states can be computed as [Row02]:

$$x(t) = V \begin{bmatrix} e^{\lambda_1 t} & & \\ & \ddots & \\ & & e^{\lambda_n t} \end{bmatrix} V^{-1}x(0) \tag{A.76}$$

and is as such a linear combination of the n modal components $e^{\lambda_i t}$.

A.12 Adaptive ADMM

The motivation and derivation of adaptive ADMM can be found in [XFG17]. The nomenclature of the paper is kept to avoid confusion and the steps of calculation are just repeated. The equations in (A.79)-(A.81) are adapted to the variables of the DMPC problem formulated in this thesis. The penalty parameter $\rho^{\ell+1}$ of the next ADMM iteration is updated in every other iteration (as suggested by the authors in [XFG17]) based on the results of iteration ℓ, according

to the following scheme:

$$\rho^{\ell+1} := \begin{cases} \sqrt{\hat{\alpha}_\ell \hat{\beta}_\ell} & \text{if } \alpha_\ell^{cor} > \epsilon^{cor} \text{and } \beta_\ell^{cor} > \epsilon^{cor} \\ \hat{\alpha}_\ell & \text{if } \alpha_\ell^{cor} > \epsilon^{cor} \text{and } \beta_\ell^{cor} \leq \epsilon^{cor} \\ \hat{\beta}_\ell & \text{if } \alpha_\ell^{cor} \leq \epsilon^{cor} \text{and } \beta_\ell^{cor} > \epsilon^{cor} \\ \rho^\ell & \text{otherwise.} \end{cases} \tag{A.77}$$

$\epsilon^{cor} = 0.2$ is suggested. α_ℓ^{cor} and β_ℓ^{cor} are computed as

$$\alpha_\ell^{cor} = \frac{\langle \Delta \hat{H}_\ell, \Delta \hat{\lambda}_\ell \rangle}{\|\Delta \hat{H}_\ell\| \|\Delta \hat{\lambda}_\ell\|} \qquad \beta_\ell^{cor} = \frac{\langle \Delta \hat{G}_\ell, \Delta \lambda_\ell \rangle}{\|\Delta \hat{G}_\ell\| \|\Delta \lambda_\ell\|} \tag{A.78}$$

with

$$\Delta \hat{H}_\ell = I_{N_P \mathcal{I}}(\boldsymbol{r}_k^\ell - \boldsymbol{r}_k^{\ell_0}) \qquad \Delta \hat{\lambda}_\ell = \hat{\lambda}_\ell - \hat{\lambda}_{\ell_0} \tag{A.79}$$

$$\Delta \hat{G}_\ell = -I_{N_P \mathcal{I}}(\boldsymbol{a}_k^\ell - \boldsymbol{a}_k^{\ell_0}) \qquad \Delta \lambda_\ell = \boldsymbol{\nu}_k^\ell \rho^\ell - \boldsymbol{\nu}_k^{\ell_0} \rho^{\ell_0} \tag{A.80}$$

and

$$\hat{\lambda}_\ell = (\boldsymbol{\nu}_k^\ell + \boldsymbol{r}_k^\ell - \boldsymbol{a}_k^{\ell-1}) \rho^\ell. \tag{A.81}$$

ℓ_0 denotes an older iteration, i.e. $\ell_0 < \ell$. Candidate penalty parameters $\hat{\alpha}_\ell$ and $\hat{\beta}_\ell$ are computed as follows:

$$\hat{\alpha}_\ell := \begin{cases} \hat{\alpha}_\ell^{MG} & \text{if } 2\hat{\alpha}_\ell^{MG} > \hat{\alpha}_\ell^{SD} \\ \hat{\alpha}_\ell^{SD} - \hat{\alpha}_\ell^{MG}/2 & \text{otherwise,} \end{cases} \tag{A.82}$$

$$\hat{\beta}_\ell := \begin{cases} \hat{\beta}_\ell^{MG} & \text{if } 2\hat{\beta}_\ell^{MG} > \hat{\beta}_\ell^{SD} \\ \hat{\beta}_\ell^{SD} - \hat{\beta}_\ell^{MG}/2 & \text{otherwise,} \end{cases} \tag{A.83}$$

$$\hat{\alpha}_\ell^{SD} = \frac{\langle \Delta \hat{\lambda}_\ell, \Delta \hat{\lambda}_\ell \rangle}{\langle \Delta \hat{H}_\ell, \Delta \hat{\lambda}_\ell \rangle} \qquad \hat{\alpha}_\ell^{MG} = \frac{\langle \Delta \hat{H}_\ell, \Delta \hat{\lambda}_\ell \rangle}{\langle \Delta \hat{H}_\ell, \Delta \hat{H}_\ell \rangle}, \tag{A.84}$$

$$\hat{\beta}_\ell^{SD} = \frac{\langle \Delta \lambda_\ell, \Delta \lambda_\ell \rangle}{\langle \Delta \hat{G}_\ell, \Delta \lambda_\ell \rangle} \qquad \hat{\beta}_\ell^{MG} = \frac{\langle \Delta \hat{G}_\ell, \Delta \lambda_\ell \rangle}{\langle \Delta \hat{G}_\ell, \Delta \hat{G}_\ell \rangle}. \tag{A.85}$$

Note that the iteration index ℓ is placed as a subscript in the new variables for readability.

Appendix B

DMPC Simulation Results

B.1 Voltage Stability Results Type J

Table B.1: *Aggregated electricity demands, costs, performance factor and maximum values for all prosumers of type J over the scenarios. The first two cost entries for flat price and time-varying price without coordination are the result of the reference operation. Percentage change based on scenario time-varying price without coordination.*

		Flat price	**Time-varying price**		
Coordination		No	No	Yes	Yes
V_0	[p.u.]	1	1	1	0.95
residual load	[kWh]	732.4	921.9	928.7 (+0.7%)	817.9 (-11.3%)
heat pump	[kWh]	477.4	422.3	422.9 (+0.1%)	453.4 (+7.4%)
back-up heater	[kWh]	0	244.6	250.8 (+2.5%)	109.5 (-55.2%)
fixed demand	[kWh]	255	255	255	255
Costs	[kWh]	732.4	556.7	556.9 (+0.0%)	569.6 (+2.3%)
Costs CO	[kWh]			556.9	569.6
PF		3.59	2.66	2.64	3.1
$\max(\boldsymbol{P})$	[kW]	64.4	224.4	215.4 (-4%)	135.3 (-39.7%)
$\min(\boldsymbol{V})$	[p.u.]	0.9715	0.8901	0.9	0.9
$\max(\boldsymbol{T}_z)$	[°C]	20.8	21.6	21.6	21.6

Table B.2: *Aggregated electricity demands, costs, performance factor and maximum values for all prosumers of type J over the scenarios in closed-loop simulation.*

		Flat price	**Time-varying price**		
Coordination		No	No	Yes	Yes
V_0	[p.u.]	1	1	1	0.95
residual load	[kWh]	6304	7528.3	7804.4 (+3.7%)	6980 (-7.3%)
heat pump	[kWh]	4653.7	4212.3	4091.6 (-2.9%)	4397.1 (+4.4%)
back-up heater	[kWh]	2.8	1668.6	2065.3 (+23.8%)	935.4 (-43.9%)
fixed demand	[kWh]	1647.5	1647.5	1647.5	1647.5
Costs	[kWh]	6304	4999.7	4999 (-0.0%)	5117.7 (+2.4%)
Costs CO	[kWh]			4999.9	5118.4
PF		3.26	2.61	2.49	2.86
$\max(\boldsymbol{P})$	[kW]	79.5	224.5	216.2 (-3.7%)	154 (-31.4%)
$\min(\boldsymbol{V})$	[p.u.]	0.9625	0.89	0.9	0.9
$\max(\boldsymbol{T}_z)$	[°C]	24.1	24.2	24.2	24.2

List of Supervised Theses

L. Beißwenger, Solutions for Allocating Costs for a Cooperative Energy Exchange on District Level, master's thesis, 2019.

T. Ali Zai, Implementation of a Distributed Model Predictive Control Algorithm for Prosumers on Revolution Pis, master's thesis, 2019.

R. Kuniyoshi, Validation of RC Building Models for Application in Energy and Load Management, master's thesis, 2017.

N. Joshi, Evaluation of the Potential of Devices for Domestic Hot Water Provision to Integrate Excess Production from Photovoltaic Plants, master's thesis, 2016.

M. Uddin, Parameter Fitting and Validation of a Thermal Building Model Based on EnergyPlus with Matlab, master's thesis, 2015.

U. Shahid, GIS Data Management for the City of Munich, project report, 2015.